



저작자표시-비영리-변경금지 2.0 대한민국

이용자는 아래의 조건을 따르는 경우에 한하여 자유롭게

- 이 저작물을 복제, 배포, 전송, 전시, 공연 및 방송할 수 있습니다.

다음과 같은 조건을 따라야 합니다:



저작자표시. 귀하는 원저작자를 표시하여야 합니다.



비영리. 귀하는 이 저작물을 영리 목적으로 이용할 수 없습니다.



변경금지. 귀하는 이 저작물을 개작, 변형 또는 가공할 수 없습니다.

- 귀하는, 이 저작물의 재이용이나 배포의 경우, 이 저작물에 적용된 이용허락조건을 명확하게 나타내어야 합니다.
- 저작권자로부터 별도의 허가를 받으면 이러한 조건들은 적용되지 않습니다.

저작권법에 따른 이용자의 권리는 위의 내용에 의하여 영향을 받지 않습니다.

이것은 [이용허락규약\(Legal Code\)](#)을 이해하기 쉽게 요약한 것입니다.

[Disclaimer](#)

Soft Nanoelectronic Devices Based on Novel 2D
Nanomaterials and Self-assembled Organic
Semiconductors

Eun Kwang Lee

Department of Energy Engineering
(Energy Engineering)

Graduate School of UNIST

Soft Nanoelectronic Devices Based on Novel 2D Nanomaterials and Self-assembled Organic Semiconductors

A thesis submitted to the Graduate School of UNIST in partial fulfillment of
the requirements for the degree of Doctor of Philosophy

Eun Kwang Lee

1. 11. 2017

Approved by



Advisor

Byeong-Su Kim



Advisor

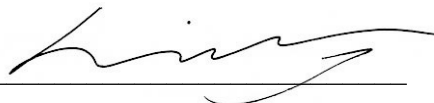
Joon Hak Oh

Soft Nanoelectronic Devices Based on Novel 2D
Nanomaterials and Self-assembled Organic
Semiconductors

Eun Kwang Lee

This certifies that the thesis of Eun Kwang Lee is approved.

1. 11. 2017



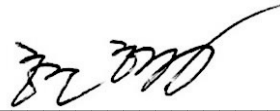
Advisor: Byeong-Su Kim



Joon Hak Oh: Thesis Committee Member #1



Jong-Beom Baek: Thesis Committee Member #2



Hyunhyub Ko: Thesis Committee Member #3



Sang Kyu Kwak: Thesis Committee Member #4;

Abstract

Recent advances in electronic device are focused on a fabrication of flexible and stretchable electronic gadgets in a low-cost and sustainable ways. The fabrication of flexible and stretchable electronic devices is highly challenging using inorganic or Si-based electronic materials due to its fragile nature upon a strain. Utilization of solution-processable organic materials including small molecules and polymer in organic field effect transistors (OFETs), light emitting diodes, and solar cells, facilitates a low-cost, large-area, cheap, and environment-friendly mass production for the fabrication of flexible and stretchable electronic devices. Conjugated small molecules and polymers continue to be studied intensively as semiconducting and conducting materials due to its tunability of their electronic and optoelectronic properties. Graphene, a single layer of two-dimensional (2D) carbon atoms in a honeycomb lattice, has attracted enormous attention due to its unique electronic, optical, thermal, and mechanical properties. It has an extremely high charge carrier mobility ($\sim 200,000 \text{ cm}^2\text{V}^{-1}\text{s}^{-1}$), an optical transmittance of 97.7%, a theoretical sheet resistance of $30 \text{ }\Omega/\text{sq}$, a high fracture strain resistance greater than 20%, and chemical stability. These features make it highly promising for applications in flexible electronics and energy conversion devices, including touch screens, field-effect transistors (FETs), capacitors, batteries, solar cells, and light-emitting diodes (LEDs). However, the zero-band gap, small optical absorption, and chemical inertness have limited its practical application in switching and optoelectronic devices. Similar to graphene, transition metal dichalcogenides (TMDCs) are 2D materials stacked by van der Waals forces. Contrary to graphene, which does not have a bandgap energy, TMDCs have tunable bandgaps unlike to graphene. Typically, bulk TMDCs show indirect bandgap. On the other hand, the bandgap of TMDCs gradually decrease to one monolayer.

Herein, I present a forward-looking my research results which are mainly focused on the interface studies between organic electronic materials and 2D nanomaterials including graphene and MoSe_2 , because of the importance of the mechanism and the behavior of electrical property change when organic electronic materials and 2D nanomaterials comes together in the electronic device system. When it comes to the interface study between heterogeneous electronic materials, doping of organic semiconductor and 2D nanomaterials is one of the important steps to enhance the electrical performance. Especially, n-doping of organic semiconductor is more challenging than p-doping because the n-dopants have to show a very low ionization potential to enable electrons to be transferred effectively, which renders most possible candidates unstable in air. Among the various doping strategies, surface transfer doping technique has been investigated for graphene and MoSe_2 to modify or enhance their electrical or optoelectrical properties without severe damage on the surface of matrix. In addition, new carbon-based materials with honey comb structure or graphitic structure applying heterogenous atoms such as nitrogen (nitrogen doped reduced graphene oxide and 2D polyaniline) are explored to figure out their unique electrical properties and potential of electronic application. The experimental results and discussion in this thesis represent a forward-looking insight in charge transport behavior when organic electronic materials and 2D nanomaterials make junction together and pave the way of the applicability of organic semiconductors in conventional microelectronic infrastructures, which will lead to progress in the realization of soft nanoelectronic devices.

Keywords: graphene, polymer semiconductors, doping, phototransistor, optoelectronic properties

Contents

Abstract	1
Contents	2
List of Figures and Tables.....	4
Chapter 1. Introduction to the Interface Between Graphene and Organic Electronic Materials.....	17
1.1. Research Background.....	17
1.2. Synthesis of Graphene and Two-Dimensional Transition Metal Dichalcogenides (2D TMDCs)	18
1.3. Electronic Properties of Graphene and 2D TMDCs	19
1.4. Surface Transfer Doping Using Organic Dopants	20
1.5. Applications Using the Combination of Organic Electronic Materials and Graphene and 2D TMDCs.....	20
1.6 References	22
Chapter 2. Graphene-ruthenium Complex Hybrid Photodetectors With Ultrahigh Photoresponsivity	26
2.1. Introduction	26
2.2. Experimental Section	27
2.3. Results and Discussion.....	28
2.4. Conclusion.....	32
2.5. References	32
Chapter 3. Flexible Organic Phototransistor Array with Enhanced Responsivity via Metal-Ligand Charge Transfer	40
3.1. Introduction	40
3.2. Experimental Section	41
3.3. Results and Discussion.....	42
3.4. Conclusion.....	47
3.5 References	48
Chapter 4. Chemically Robust Ambipolar Organic Transistor Array Directly Patterned by Photolithography.....	55
4.1. Introduction	55
4.2. Experimental Section	56
4.3. Results and Discussion.....	59
4.4. Conclusion.....	64
4.5. References	65
Chapter 5. Reduced Pyronin B Doping on Graphene and Organic Semiconductor	81
5.1. Introduction	81
5.2. Experimental Section	82

5.3. Results and Discussion.....	84
5.4. Conclusion.....	87
5.5. References	87
Chapter 6. Highly Enhanced Optoelectronic Properties in MoSe ₂ with Reduced Organic Cationic Dye as Molecular N-Dopant.....	96
6.1. Introduction.....	96
6.2. Experimental Section	97
6.3. Results and Discussion.....	98
6.4. Conclusion.....	102
6.5. References	102
Chapter 7. Nitrogen-Doped Graphene Nanoplatelets from Simple Solution Edge-Functionalization for n-Type Field-Effect Transistors	109
7.1. Introduction.....	109
7.2. Experimental Section	110
7.3. Results and Discussion.....	111
7.4. Conclusion.....	117
7.5. References	118
Chapter 8. Two-dimensional Polyaniline From Carbonized Organic Single Crystals in Solid State .	127
8.1. Introduction.....	127
8.2. Experimental Section	127
8.3. Results and Discussion.....	128
8.4. Conclusion.....	132
8.5. References	132
Chapter 9. Summary and Perspectives.....	146
Acknowledgments.....	149
감사의 글	150
Curriculum Vitae	152

List of Figures and Tables

Chapter 1

Figure 1.1. Schematic illustration of strategies to achieve soft nano electronics.

Figure 1.2. Graphene growth using CVD. (a) Photograph of CVD. (b) Detailed illustration of CVD process for the growth of graphene. CVD heater is placed on the position of Cu foil for the growth of graphene (Step 1). Heater is moved away from the Cu foil to cool down quickly (Step 2). (c) Temperature gradient versus time in CVD process and gas (CH_4 , H_2) flow condition (d) Transfer curve of CVD grown graphene measured in vacuum condition (1×10^{-6} torr).

Figure 1.3. Scheme of the doping process for molecular p-type (left) and n-type doping (right).

Figure 1.4. The configurations of organic field effect transistor.

Chapter 2

Scheme 2.1. Synthetic procedure for ruthenium complex **1**.

Figure 2.1. Chemical structure of ruthenium complex **1** and schematic depiction of graphene-ruthenium complex hybrid FET-type photodetector. In the chemical structure of complex **1**: H atoms were omitted and C, N, O, Ru atoms were represented by gray, blue, light-red and dark-red balls. For clarity, the scale of complex **1** is enlarged compared to graphene.

Figure 2.2. Raman spectra of graphene/ SiO_2/Si (Bottom) and ruthenium compound **1**/graphene/ SiO_2/Si (Top). The Raman spectra were excited at 532 nm with an incident power < 1 mW (Laser spot diameter was 500 nm).

Figure 2.3. AFM height and surface profile (white line) along the black dotted line: (a) pristine graphene/ SiO_2/Si . (b) ruthenium complex **1**/graphene/ SiO_2/Si .

Figure 2.4. XPS spectra of ruthenium compound **1**/graphene/ SiO_2/Si ($h\nu = 1486.6$ eV). Some of the characteristic peaks are marked ($\text{O}1s$, $\text{N}1s$, $\text{C}1s$, $\text{Ru}3p$ and $\text{Ru}3d$). The $\text{Ru}3d_{3/2}$ peak is merged with the $\text{C}1s$ emission.

Figure 2.5. Current-voltage characteristics and energy level change of ruthenium complex **1**/graphene FET device. (a) Transfer characteristics of pristine graphene and ruthenium complex **1**/graphene devices ($V_{\text{DS}} = 1$ V) under dark condition. (b) Transfer characteristics under dark and polychromatic incident light with different intensities ($V_{\text{DS}} = 1$ V). (c) Output characteristics coupled with light illumination under hole-enhancement mode ($V_{\text{G}} = -80$ V). (d) Output characteristics coupled with light illumination without applying gate field ($V_{\text{G}} = 0$ V). (e) Energy level changes of pristine e graphene upon functionalization with ruthenium complex **1** and optical illumination.

Figure 2.6. Hysteresis of ruthenium complex **1**/graphene device under vacuum ($\sim 10^{-5}$ torr).

Figure 2.7. Current–voltage characteristics. $I_{\text{DS}}-V_{\text{DS}}$ characteristics of pristine graphene device using incident light with different intensities under vacuum ($\sim 10^{-5}$ Torr) ($V_{\text{G}} = -80$ V).

Figure 2.8. (a) UV-vis spectra of pristine graphene/glass and ruthenium **1**/graphene/glass. (b) Transfer characteristics ($I_{\text{DS}}-V_{\text{G}}$) ($V_{\text{DS}} = 1$ V) under dark and monochromatic light illumination with different wavelengths (0.15 ~ 0.16 mW).

Figure 2.9. Photoresponse. (a) Normalized current response of graphene-ruthenium complex hybrid photodetectors upon on/off switching of illumination ($V_{\text{DS}} = 1$ V; $V_{\text{G}} = 0$ V; Irradiation: polychromatic light of 0.93 mW). (b) Responsivity as a function of gate voltage (the wavelength of incident light: $\lambda = 450$ nm).

Figure 2.10. Time response of photocurrent growth and decay for graphene-ruthenium complex hybrid photodetectors. (a) Photocurrent growth upon illumination. (b) Photocurrent decay after turning off the light. $V_{\text{DS}} = 1$ V; $V_{\text{G}} = 0$ V.

Chapter 3

Figure 3.1. Schematic depiction of Ru-complex **1**/BPE-PTCDI/Si/SiO₂ phototransistor and chemical structures of Ru-complex **1**, BPE-PTCDI.

Figure 3.2. (a) UV-vis spectra of Ru-complex **1**/glass, BPE-PTCDI/glass and Ru-complex **1**/BPE-PTCDI/glass. AFM height and surface roughness: (b) BPE-PTCDI/SiO₂/Si. (c) Ru-complex **1**/BPE-PTCDI/SiO₂/Si. SEM images of (d) BPE-PTCDI/SiO₂/Si. (e) Ru-complex **1**/BPE-PTCDI/SiO₂/Si.

Figure 3.3. AFM height images and cross-sectional profiles with the surface roughness: Ru-complex **1**/BPE-PTCDI/SiO₂/Si (The dark red part is the surface of SiO₂/Si wafer obtained by scraping off the Ru-complex **1**/BPE-PTCDI part).

Figure 3.4. XPS spectra of Ru-complex **1**-modified BPE-PTCDI/SiO₂/Si ($h\nu = 1486.6$ eV). Some of the characteristic peaks are marked (O1s, N1s, C1s and Ru3d). The Ru3d_{3/2} peak is merged with the C1s emission.

Figure 3.5. Current-voltage characteristics of BPE-PTCDI and Ru-complex **1**/BPE-PTCDI FET devices. Transfer characteristics ($V_{\text{DS}} = 100$ V) of (a) BPE-PTCDI and (b) Ru-complex **1**/BPE-PTCDI FET devices. Output characteristics of (c) BPE-PTCDI and (d) Ru-complex **1**/BPE-PTCDI FET devices. ($V_{\text{GS}} = 20, 40, 60, 80, 100$ V). Transfer characteristics of (e) BPE-PTCDI/SiO₂/Si and (f) Ru-complex **1**/BPE-PTCDI/SiO₂/Si devices under dark and monochromatic light ($\lambda = 450$ nm, $1.5\mu\text{Wcm}^{-2}$, $V_{\text{DS}} = 100$ V).

Figure 3.6. Hysteresis of Ru-complex **1**-modified BPE-PTCDI phototransistors. The red line shows the result of a device dried in N₂ condition for 1 day, while the black line exhibits the result of a device dried at room temperature for 1 day in N₂ and annealed at 100 °C in N₂ consecutively.

Figure 3.7. (a) Normalized current response of Ru-complex **1**/BPE-PTCDI/SiO₂/Si phototransistor upon on (yellow area)/off (blue area) switching of illumination ($V_{DS} = 100$ V; $V_{GS} = 0$ V; Irradiation: 1.5, 30, 100 μWcm^{-2}). (b) Photoresponsivity of Ru-complex **1**/BPE-PTCDI/SiO₂/Si and BPE-PTCDI/SiO₂/Si devices as a function of gate voltage ($\lambda = 450$ nm, 1.5 μWcm^{-2}). Time response of (c) photocurrent growth and (d) decay for Ru-complex **1**/BPE-PTCDI phototransistors and its exponential fitted results (red solid lines) using Equation (5) and (6), respectively, $V_{DS} = 100$ V; $V_{GS} = 100$ V.

Figure 3.8. External quantum efficiency (EQE) (η) of Ru-complex **1**/BPE-PTCDI and BPE-PTCDI devices as a function of V_{GS} ($\lambda = 450$ nm, 1.5 $\mu\text{W cm}^{-2}$).

Figure 3.9. (a) Schematic illustration of 10×10 Ru-complex **1**/BPE-PTCDI/SU-8 phototransistor device fabricated on a flexible transparent PI. (b) Detailed schematic structure of a single phototransistor. (c) Photograph of the 10×10 phototransistor array prepared on a PI substrate. (Inset: optical image of single device layout, S, D and G indicate source, drain and gate respectively, scale bar, 200 μm) (d) Typical 10 selected transfer curves ($V_{DS} = 3$ V) among phototransistor array under dark (pink) and illumination condition (purple). (Inset: photograph when light is incident to the device, scale bar, 1 cm) (e) Electron mobility change and its distribution (black error bars) with time for 7 days in ambient laboratory condition. (f) Photocurrent mapping of the 10×10 phototransistor array for the light spot (illumination position: column, row = 5, 5). Light wavelength and intensity were $\lambda = 450$ nm and 1.5 μWcm^{-2} , respectively.

Figure 3.10. (a) AFM height image of SU-8 dielectric layer. (Top) Surface morphology and (Bottom) the cross-sectional profile showing the thickness of 35 nm. (b) Capacitance vs. frequency of SU-8 dielectric layer.

Figure 3.11. (a) Schematic cross-sectional diagram of BPE-PTCDI on SU-8 and PI as dielectric and substrate, respectively. (b) The transfer curves ($V_{DS} = 3$ V) of the device when the light was on (purple) and off (pink). Light intensity was 1.5 μWcm^{-2} .

Figure 3.12. Calculation of tensile and compressive strains with respect to the bending radius.

Figure 3.13. Flexibility test of the phototransistor array prepared on a PI substrate. (a) The phototransistor array was placed on the top surface of PI substrate. A tensile strain was applied during upward bending (top), in contrast, a compressive strain was applied during downward bending (bottom), scale bar = 20 mm. (b) Normalized electron mobility change after tensile strain bending (black) and compressive bending (red) cycles. (Inset: schematic figures of devices during tensile (left) and compressive strain (right)) (c) Normalized electron mobility change with respect to various twisted angles from 5° to 40° (Inset: photograph of twisted device, scale bar = 35 mm). (d) Normalized mobility change with respect to $2R_{\text{bend}}$ under dark (red) and light (blue) where R_{bend} is bending radius (Inset: photograph of device measurement for investigating the effect of bending radius on the performance, scale bar = 5 mm).

Chapter 4

Figure 4.1. The specific capacitance of SU-8 dielectric (150 nm). The 1 nFcm⁻² of capacitance was obtained from the stable region (10³~10⁵ Hz).

Figure 4.2. (a) Raman spectra of graphene electrode at different positions. The color of solid line corresponds to the same color position of inset. Inset: Optical image of patterned graphene using conventional photolithography and RIE on 300 nm SiO₂/n⁺⁺Si wafer. Scale bar is 40 μm. (b) The chemical structure of **PTDPPSe-SiC4**. (c) AFM image of **PTDPPSe-SiC4** solution-sheared film on graphene electrode (left) and Si wafer (right). Dashed blue arrows indicate the transition. 2D GIXD profiles of **PTDPPSe-SiC4** on (d) SiO₂ 300 nm wafer and (e) graphene. (f) Pole figure for (010) diffraction of **PTDPPSe-SiC4** on graphene and SiO₂ (where χ is defined as the semicircular angle between the crystallite orientation and the surface normal).

Figure 4.3. (a) Graphene was grown on Cu foil using chemical vapor deposition (CVD). CVD-grown graphene was transferred on the Si wafer and patterned (c) and etched away using reactive ion etching. The sample was treated with octadecyltrichlorosilane self-assembled monolayer. (OTS-SAM) (d) The polymer semiconductor, **PTDPPSe-SiC4**, was deposited on the substrate by solution-shearing method.

Figure 4.4. High-resolution AFM images of **PTDPPSe-SiC4** on graphene (a, c, e) and the SiO₂ wafer (b, d, f) after shearing coating. The height (a, b), amplitude (c, d) and phase (e, f) images of AFM. The shearing direction corresponds x axis.

Figure 4.5. AFM images of the spin-coated **PTDPPSe-SiC4**. The **PTDPPSe-SiC4** film was coated on Si wafer (top) and graphene (bottom).

Figure 4.6. Pole figure for (010) diffraction of **PTDPPSe-SiC4** on graphene. (a) 0.08° and (b) 0.13° as X-ray incidence angles. χ is defined as the semicircular angle between the crystallite orientation and the surface normal. (c) Proposed stacking illustration of **PTDPPSe-SiC4** on graphene electrode.

Figure 4.7. (a) The p-channel (under $V_{DS} = -100V$) and (b) n-channel (under $V_{DS} = 100V$) transfer characteristics of solution-sheared **PTDPPSe-SiC4** FETs with graphene electrodes on the OTS-treated 300 nm SiO₂/n⁺⁺Si wafer. (c) Energy diagram of graphene, **PTDPPSe-SiC4** and gold. (d) OFET-based inverter characteristics of **PTDPPSe-SiC4** under $V_{DD} = 100 V$ (inset: schematic diagram of the complementary inverter structure).

Figure 4.8. Output curves of **PTDPPSe-SiC4** on Si wafer. The p-channel (left) and n-channel (right) output curves ($I_{DS}-V_{DS}$) were obtained from transistors with graphene electrodes based on **PTDPPSe-SiC4** film prepared by solution shearing method.

Figure 4.9. Transfer ($I_{DS}-V_{GS}$) characteristics of **PTDPPSe-SiC4** FETs with graphene electrodes. The **PTDPPSe-SiC4** FETs were made by spin coating for (a) p-channel and (c) n-channel, drop casting for (b) p-channel and (d) n-channel on OTS-treated 300 nm SiO₂/n⁺⁺Si wafer.

Figure 4.10. The stability test of the **PTDPPSe-SiC4** FET. The devices were stored in ambient condition and measured in vacuum condition ($\sim 10^{-6}$ torr).

Figure 4.11. OFET-based inverter characteristics of **PTDPPSe-SiC4** FETs using Au electrodes.

Figure 4.12. Width-normalized channel resistance measured using transfer line method (TLM). When channel length goes to 0, R_{total} becomes R_C which means contact resistance. The width of channel was 1000 μm . Width-normalized channel resistances of the OFET with graphene electrodes for (a) p-type and (c) n-type operations. Width-normalized channel resistances of the OFET with Au electrodes for (b) p-type and (d) n-type operations.

Figure 4.13. (a) Schematic BGBC transistor structure. (b) Graphene electrodes patterned on SU-8 dielectric layer. (c) **PTDPPSe-SiC4** film was coated on the whole area of plastic substrate using solution-shearing. (d) **PTDPPSe-SiC4** film was patterned by conventional photolithography. Insets are schematic 3D illustration (top right) and structure (bottom right) of unit device from (b) to (d). Full device fabrication procedures can be found in Figure 4.11. (e) A photograph of 10 x 10 transistor on PI film. (f) An optical image of single transistor device from the blue rectangular area of Figure 4.13e. Channel width and length were 65 μm and 50 μm , respectively. (g) Hole mobility mapping on the 10 × 10 flexible transistor arrays in ambient condition. (h) Normalized hole mobility changes with respect to the bending radius (R_{bend}) in parallel (black symbol) and perpendicular (red symbol) bending with respect to shearing direction. (Inset: a photograph of device measurement for investigating the effect of bending radius, scale bar = 30 mm).

Figure 4.14. Schematic fabrication steps of transparent 10 x 10 transistor array on PI film. (a) Transparent polyimide was coated on a glass substrate. (b) Align marker (Cr/Au, 40 nm) were formed using photolithography. (c) Gate electrodes were formed using photolithography. (d) A diluted SU-8 solution in gamma-butyrolactone was patterned for the dielectric layer. (e) CVD-grown graphene electrodes as source and drain were transferred onto the substrate and patterned by photolithography and reactive ion etching to form channel gap. (f) Gold lines was deposited to connect graphene electrodes with contacts. (g) **PTDPPSe-SiC4** as a semiconductor layer was deposited by solution shearing. (h) Photoresist (DSAM-3000) was spin-coated. (i) The substrate was irradiated with UV through photomask and developed in DPD-200 developer, forming photoresist mask. (j) Unnecessary part of **PTDPPSe-SiC4** was etched away using dry etcher under the atmosphere of CF_4 . (k) Photoresist mask was removed in acetone. The substrate was washed away with DI water and nitrogen gas. (l) The device was detached from the glass substrate.

Figure 4.15. Optical images of line-patterned **PTDPPSe-SiC4** on Si wafer using conventional photolithography. The feature sizes of line pattern were varied from 2 to 20 μm .

Figure 4.16. Transmittance of transparent devices with PI/Graphene/SU-8/ **PTDPPSe-SiC4**

Figure 4.17. Transfer curves of **PTDPPSe-SiC4** FETs prepared on flexible PI film. The transfer curve under (a) p-channel and (b) n-channel operation, respectively, was measured in an N_2 atmosphere.

Figure 4.18. P-type transfer curves of **PTDPPSe-SiC4** FET based on the flexible PI substrate measured in (a) N_2 condition and (b) ambient condition. $W/L = 65/50 \mu\text{m}$.

Figure 4.19. Calculation of tensile strain with respect to bending radius (R_{bend}).

Figure 4.20. (a) Schematic illustration for demonstration of the solvent resistance. PTDPPSe-SiC4 transistors using graphene electrode were soaked in various solvents for 24 h. Then the solvents were removed by blowing N_2 gas and heating at 220 °C in N_2 condition. (b) Photographs of **P3HT** and **PTDPPSe-SiC4** FETs after soaking in chlorobenzene (CB) for 24 h. (c) Hole and (d) electron mobility distributions of 10 measured devices after soaking in solvents for 24 h. (e) Schematic illustration for acetone sensing using a **PTDPPSe-SiC4** FET array. (f) I_D/I_{Base} changes upon on/off switching (20 cycles) of acetone vapors exposed to the device. Purple areas in the graph indicate the response upon exposing to 4 SLM of acetone vapor ($V_{\text{DS}} = V_{\text{GS}} = -100$ V).

Figure 4.21. UV-Vis spectra to test the solvent-resistance of the deposited films before and after the polymer film coated wafers were soaked into various solvents. (a) DI water, (b) ethanol, (c) acetone and (d) chlorobenzene. The devices were soaked for 24 hours.

Figure 4.22. UV-vis absorption spectra of (a) **PTDPPSe-alkyl** and (b) **PTDPPSe-SiC4** in 1 mg mL⁻¹ in chlorobenzene solution (black line) and film (red line). Insets in (a) and (b) are molecular structures of **PTDPPSe-alkyl** and **PTDPPSe-SiC4**, respectively.

Figure 4.23. The evaluation of response time (left) and recovery time (right) of the **PTDPPSe-SiC4** based acetone sensor.

Table 4.1. OFETs performance of the devices with different electrodes. The p-channel and n-channel characteristics of FETs on OTS-treated SiO_2 (300 nm)/ $n^{++}\text{Si}$ wafer were measured with $V_{\text{DS}} = -100$ and 100 V, respectively. The electrical measurement was performed in nitrogen atmosphere. In the case of spin-coating and solution-shearing method, device yield was 100%. In the case of drop-casting, device yield was 71% due to the film thickness issue (5 fabricated out of 7 devices).

Table 4.2. Comparison of electrical properties before and after soaked in various solvents for 24 hours. Properties of as-fabricated devices were measured before soaked in solvents. Then the devices properties were measured again after soaking in various solvents (DI water, ethyl alcohol, acetone and chlorobenzene) for 24 h and heating the devices at 220 °C under N_2 condition.

Chapter 5

Figure 5.1. From a to c: Synthesis of reduced pyronin B (rPyB). (a) Toluene was layered on top of the pyronin b (PyB) solution dissolved in water. (b) NaBH_4 was added to the PyB solution to synthesize rPyB. The rPyB is not charged, thus rPyB molecules were moving to toluene spontaneously. (c) After 24 hour, rPyB molecules moved to toluene completely. (d) Chemical structure of PyB. (e) Schematic illustration of rPyB solution doping on a graphene field-effect transistor (FET)

Figure 5.2. Photographs of the biphasic solution reaction to synthesize rPyB. (a) right after reduction of PyB with NaBH_4 . after 1 day, toluene and water part were separated. after 1 week of (b) toluene part, containing rPyBs and (c) water part.

Figure 5.3. (a) Absorption spectra of PyB (black) and rPyB (red) (b) Transmittance of graphene and graphene after coating of rPyB (c) Raman spectra of graphene before and after coating of rPyB Kelvin probe (KP) mapping before (d) and after (e) coating of rPyB on graphene. Work function of reference electrode was gold which is 5.1 eV. KP mapping area = $(10 \times 100 \times 635 \text{ nm}) \times (10 \times 100 \times 635 \text{ nm}) = 0.40 \text{ mm}^2$. Φ , work function.

Figure 5.4. Raman spectra of graphene with respect to the number of rPyB coating

Figure 5.5. Kelvin probe mapping of graphene with respect to the number of rPyB.

Figure 5.6. Transfer curves of graphene before (a) and after (b) rPyB coating. Transfer curves of N2200 FETs with (c) pure graphene electrodes and (d) graphene electrodes coated rPyB. Transfer curves of N2200 FET with bottom contact top gate (BCTG) configuration (e) without and (f) with rPyB coating (insets: schematic device structure)

Figure 5.7. Transfer curves of N2200 before (left) and after (right) coating of rPyB at the interface between Au electrodes and N2200.

Figure 5.8. Transfer curves of N2200 FETs. N2200 solution (3 mg/mL in chlorobenzene) was mixed with rPyB from 1 wt % to 50 wt %.

Figure 5.9. Atomic force microscopy images on N2200 film mixing with rPyB (1 ~ 10 wt %).

Figure 5.10. (a) Ultraviolet photoemission spectroscopy (UPS) of graphene electrode (black) and rPyB-doped graphene electrode (red). (b) Energy diagram of graphene electrode and rPyB-doped graphene electrode derived from UPS. (c) Comparison of energy levels of graphene, N2200, Au and rPyB-doped graphene. (d) electron mobility changes of graphene FETs in ambient condition for 90 days with respect to the number of rPyB coating (from 1 to 4 rPyB coating).

Figure 5.11. Schematic image of PDMS stamp and the detail for the preparation of stamping doping. PDMS stamp was fabricated by photolithography with SU-8 photoresist. The fabricated PDMS stamp was soaked into rPyB solution for 1 min. After drying toluene at 120 °C, PDMS stamp was placed on a position of destination.

Figure 5.12. Solution processable, selective on-demand contact doping using PDMS stamp. (a) 16×16 graphene FET array was fabricated on 300 nm $\text{SiO}_2/\text{n}^+\text{Si}$ wafer using a conventional photolithography. (b) The fabricated PDMS stamp was soaked in rPyB solution. The PDMS stamp was placed on top of the graphene FET array. On-demand selective n-type doping using PDMS stamp with fingertip. (c) PDMS stamp was placed on top of the graphene FET. Fingertip touched at the center of PDMS for the on-demand contact doping. Fingertip was detached. V_{Dirac} mapping before (d) and after (f) selective stamping doping at the center of PDMS stamp.

Figure 5.13. Transfer curves of graphene FET before (left) and after (right) rPyB stamping doping.

Chapter 6

Figure 6.1. MoSe₂ growth. By controlling growth parameters such as temperature, amount of precursors as well as growth time, MoSe₂ can be grown into (a) isolated domain with the common triangular shape or (b) continuous monolayer film.

Figure 6.2. Device fabrication. (a) Monolayer MoSe₂ was grown with CVD technique. (b) Photolithography was used to define the source and drain electrode. (c) Exposed areas for S/D electrode were treated to n-buLi for phase transition from 2H to 1T. (d – e) S/D electrodes were deposited by thermal evaporation of Cr and Au. (f) The device was doped by spin – coating with rPyB solution

Figure 6.3. Material characterization. (a) Optical microscope image of the CVD grown MoSe₂. (b) AFM image of monolayer MoSe₂ with thickness of 0.72 nm. (d) Raman spectra of as grown (2H), 1T phase and rPyB doped MoSe₂. (d) TEM image of monolayer MoSe₂. (e – f) XPS spectra of Mo 3d and Se 3d for 2H and 1T phases of MoSe₂.

Figure 6.4. AFM analysis on before and after doped MoSe₂. (a) The morphology of as grown monolayer MoSe₂ on Si/SiO₂ substrate. (b) The change in thickness of monolayer MoSe₂ to about 0.4 nm than actual thickness of monolayer MoSe₂ after being doped with rPyB

Figure 6.5. AFM analysis on before and after doped graphene. (a) The morphology of pristine graphene on Si/SiO₂ substrate with thickness of 0.69 nm. (b) The change in thickness of graphene to about 0.41 nm thicker than actual thickness of pristine graphene after being doped with rPyB.

Figure 6.6. XPS analysis. (a) and (b) show the Mo and Se peaks of rPyB doped MoSe₂. The conformity of the rPyB doped MoSe₂ to as grown MoSe₂ shows that there are no lattice defects on MoSe₂ induced by the doping.

Figure 6.7. a) and b) show the individual peaks with respect to Mo 3d_{5/2}, Mo 3d_{3/2} and Se 3d_{5/3}, Se 3d_{3/2} of as grown sample.

Figure 6.8. a) and b) show the individual peaks with respect to 2H and 1T phases in 1T sample.

Figure 6.9. Electrical performance. (a) Device configuration of 2H, 1T and rPyB devices. (b) Transfer characteristics of corresponding devices operating at $V_{DS} = 10$ V.

Figure 6.10. Output characteristics of corresponding (a) 2H, (b) 1T and (c) rPyB devices.

Figure 6.11. Wavelength dependent photoresponse of rPyB doped MoSe₂ photodetector. (a) Transfer characteristic in dark and various light conditions operating at $V_{DS} = 10$ V. (b) Photoresponsivity for wavelength of 650 and 532 nm as function of gate voltage. Photoswitching behavior at wavelength of (c) 532nm and (d) 650nm with light intensity of 300 μ W

Figure 6.12. Optoelectronic properties of undoped (1T) device. (a) The transfer characteristics of 1T device in dark as well as under various light illumination. The photoswitching behavior of the phototransistor under illumination of $\lambda = 532$ nm (b) and $\lambda = 650$ nm (c) at $V_{GS} = -20$ V.

Figure 6.13. rPyB doped MoSe₂ photodetector on a flexible substrate and its electrical characteristic. (a) Schematic depiction of the rPyB doped MoSe₂ photodetector on flexible PET film. PEDOT was coated on PET film as a flexible gate electrode. 500 nm of parylene dielectric was deposited. (b) A

photograph of the flexible MoSe₂ photodetector on flexible PET film and (c) a magnified optical image from the green rectangle of Figure 6.13a. (d) Transfer curves of the rPyB doped MoSe₂ photodetector on flexible PET film. (e) Normalized electron mobility change with respect to various bending radii (R_{bend}) (Inset: photograph of bent devices, scale bar = 20 mm).

Table 6.1. Tabulated data of FET performances of 2H, 1T and rPyB doped devices.

Table 6.2. Summary of optoelectronic performance of undoped (1T) and doped (rPyB) MoSe₂ based devices.

Chapter 7

Figure 7.1. Schematic representations: (a) the formation of imine (Schiff base) from the condensation reaction between mono-ketone (C=O) and aniline (mono-amine); (b) the formation of aromatic pyrazine rings from the double-condensation reaction between α -diketone and 1,2-diaminobenzene (*ortho*-diamine); (c) the reaction between GO and 4-fluoroaniline or 1,2-diamino-4-fluorobenzene to yield iGO or pGO, respectively. Subsequent heat-treatment of iGO and pGO under nitrogen atmosphere produced hiGO and hpGO, respectively.

Figure 7.2. Schematic representations: (a) the formation of imine (-C=N-) bond after the reaction between the mono-ketone (C=O) group and mono-amine (H₂N-); (b) the formation 6-membered pyrazine ring after the reaction between the 1,2-diketone and *ortho*-diamine. The formation energies of imine and pyrazine are +11.9 and -20.4 kcal/mol, respectively, indicating the formation of pyrazine is spontaneous reaction.

Figure 7.3. (a) Solid-state ¹³C magic-angle spinning (MAS) NMR spectra of GO, iGO and pGO; (b) FT-IR spectra; (c) TGA thermograms obtained with a heating rate of 10 °C min⁻¹; (d) XRD diffraction patterns. The numbers are *d*-spacings in angstrom (Å); (e) Raman spectra; (f) XPS survey spectra of graphite, GO, iGO, pGO, hiGO and hpGO.

Figure 7.4. High-resolution XPS spectra of C 1s peaks: (a) graphite; (b) GO; (c) iGO; (d) hiGO; (e) pGO; (f) hpGO.

Figure 7.5. High-resolution XPS spectra of N 1s peaks: (a) graphite; (b) GO; (c) iGO; (d) hiGO; (e) pGO; (f) hpGO.

Figure 7.6. High-resolution XPS spectra of F 1s peaks: (a) graphite; (b) GO; (c) iGO; (d) hiGO; (e) pGO; (f) hpGO.

Figure 7.7. UV-vis spectra of GO, iGO, hiGO, pGO and hpGO in DMF solutions.

Figure 7.8. (a, b) TEM images of pGO at different magnifications; (c) corresponding selected-area electron diffraction (SAED) pattern taken at the relatively flat area. (d, e) TEM images of hpGO at different magnifications; (f) corresponding SAED pattern.

Figure 7.9. (a) Schematic illustration of FETs using GO derivatives as the active layers; (b) a tapping-mode AFM image of hpGO film on a SiO₂/Si wafer. The embedded graph is the thickness profile along

the dashed line; (c) the typical transfer curve of hpGO FET at $V_D = 1$ V. The inset is an optical image of hpGO FET with photolithographically patterned gold electrodes ($W/L = 40$, $L = 3$ μm). Scale bar is 40 μm .

Figure 7.10. (a) Optical image of hpGO FETs with gold electrodes patterned using e-beam lithography ($W/L = 10$, $L = 500$ nm); (b) the typical transfer curve obtained at $V_D = 0.5$ V. Inset is AFM image of the active channel areas squared in (a).

Figure 7.11. Optical microscope images of (a) large area of hpGO film on SiO_2 and (b) hpGO FET devices with top-contact gold electrodes ($W/L = 1.2$). (c) The typical transfer curve obtained at $V_D = 1$ V. Average electron and hole mobilities obtained from 82 FET devices with the long channel length were 1.0 ± 0.03 and 1.4 ± 0.04 $\text{cm}^2\text{V}^{-1}\text{s}^{-1}$, respectively, with the Dirac point of -16.2 ± 3.0 V. This strongly supports our proposition on the effects of grain boundaries.

Figure 7.12. Transfer characteristics and hysteresis behaviors of hpGO FETs ($W/L = 10$, $L = 500$ nm). The sweep range of gate voltage varied with (a) -40 V \sim $+40$ V, (b) -60 V \sim $+60$ V and (c) -80 V \sim $+80$ V, respectively.

Figure 7.13. Transfer curves of hpGO FETs measured in ambient atmosphere environment: (a) $W/L = 10$, $L = 500$ nm and (b) $W/L = 40$, $L = 3$ μm .

Table 7.1. Elemental analyses of graphite, GO, iGO, hiGO, pGO and hpGO

Table 7.2. Average electrical properties of top-contact bottom-gate FET devices fabricated from various samples

Table 7.3. Summary of Dirac point shift according to forward and reverse sweeps with different gate voltage sweep ranges.

Table 7.4. Average (mean) electrical properties of the hpGO FETs measured in ambient atmosphere.

Chapter 8

Figure 8.1. Schematic representation of 2D PANI formation. (A) Single-crystal X-ray packing structure of HAB (structure 1); structure of 2D PANI unit with edge groups (C_3NH , structure 2) and the spontaneous transformation of HAB crystal unit into the 2D PANI structure (structure 3). Morphology changes of HAB crystals into 2D PANI frameworks. (B) Digital photograph of HAB crystals on butter paper. (C) Optical microscopy image of a needle-like HAB crystal before annealing. (D) SEM image of an HAB single crystal before annealing. (E) Digital image of HAB after annealing at 500 $^\circ\text{C}$. (F) Optical microscopy image of 2D PANI crystal after annealing at 500 $^\circ\text{C}$. (G) SEM image of a 2D PANI single crystal after annealing.

Figure 8.2. STM and theoretical studies of the 2D PANI structure. (A) STM image of a 2D PANI framework (2.5×2.5 nm^2 , $V_s = -1.1$ V, $I_t = 1.0$ nA). Inset structure represents C_3N repeating unit with carbon atom (grey ball) and nitrogen atom (blue ball). (B) Topographic height profile along the cyan dot line marked in A. (C) Differential conductance (dI/dV) spectrum of a 2D PANI framework. (D)

Simulated STM image with superimposed structure of C_3N repeating unit. (E) Electronic band structure. (F) PDOS of the carbon (dark-red) and nitrogen (dark-blue) atoms.

Figure 8.3. Single crystal structure of HAB. (A) The structure of HAB formula unit; (B) hydrogen-bonded three layers of HAB crystal; (C) hydrogen-bonded packing *i*-direction view in B; (D) hydrogen-bonded packing *ii*-direction view in B; (E) hydrogen-bonded packing *iii*-direction view in B.

Figure 8.4. SEM images of the pure HAB crystals before pyrolysis. (A-D) Showing well-defined hexagonal rod like framework from different crystals.

Figure 8.5. SEM EDS analysis of HAB crystals before pyrolysis. (A) SEM image; (B) SEM energy dispersive X-ray spectroscopy (EDS) showing the elemental composition of the hexaaminobenzene hydrochloride (HAB); (C) C-mapping; (D) N-mapping; (E) O-mapping; (F) Cl-mapping from the corresponding SEM image.

Figure 8.6. SEM images of the 2D PANI frameworks. (A-D) Showing the stacked layers and the prominent hexagonal rod like morphology is well maintained after annealing at 500 °C.

Figure 8.7. SEM EDS analysis of 2d PANI. (A) SEM image with energy dispersive X-ray spectroscopy (EDS) showing the elemental composition of the 2D PANI framework; (B) C-mapping; (C) N-mapping; (D) O-mapping from the corresponding SEM image, showing no chloride peak in the EDS spectrum.

Figure 8.8. Mechanistic representation for the formation of the 2D PANI framework from HAB crystals via C_3NH structure with edge groups. The 2D PANI is formed spontaneously with the removal of ammonium chloride (NH_4Cl) and ammonia (NH_3). For clarification, we have assigned dark blue color to the amine group ($-NH_2$) and the dark red color to the HCl attached amine ($-NH_3Cl$) group in the HAB molecule. When two blue and one red react and form tertiary nitrogen ($\begin{matrix} \diagup N \diagdown \\ | \end{matrix}$) linkage releasing two NH_4Cl molecules, represented by black dots (●). When two reds and one blue react and form tertiary nitrogen ($\begin{matrix} \diagup N \diagdown \\ | \end{matrix}$) linkage, releasing one NH_4Cl and one NH_3 molecules, represented by black squares (■). This reaction occurs spontaneously forming 2D PANI.

Figure 8.9. Characterisations of the 2D PANI structures. (A) TGA thermogram obtained from an HAB single crystals with a ramping rate of 10 °C/min in argon. (B) TGA thermogram obtained from a 2D PANI framework with a ramping rate of 10 °C/min in argon. TGA thermogram in air is presented in Figure 8.12. (C) Solid-state ^{13}C magic-angle spinning (MAS) NMR spectrum of 2D PANI framework showing only two carbon peaks. (D) XPS survey spectrum of 2D PANI framework. Its high-resolution XPS spectra are presented in Figure 8.13.

Figure 8.10. Detection of ammonium chloride. (A) Before addition of $AgNO_3$ to the sample solution (right vial); (B) after addition of $AgNO_3$, white precipitation appeared, indicating the presence of chloride ion $HAB + HNO_3 + AgNO_3 \rightarrow AgCl$ (white precipitation in water, right vial); (C) mixture of HAB and NaOH, before heating; (D) after heating the mixture, pH paper at the mouth of the test tube turn deep green, showing the release of ammonia gas as follow: $NH_4^+Cl^- + Na^+OH^- \rightarrow NaCl + H_2O\uparrow +$

$\text{NH}_3\uparrow$. When the HAB monomer is annealed in a quartz tube furnace, ammonium chloride is released and deposited as ammonium chloride crystals, which have a melting point of $340\text{ }^\circ\text{C}$ (sublimation), inside the tube and outside the heating zone. The deposited material was collected from the furnace tube and washed with chloroform to afford a white compound. Then, basic chemical tests were performed to detect ammonia and the chloride ion in the solution. The chloride ion was detected using a silver nitrate solution, because it forms a white precipitate after reaction with silver into silver chloride (AgCl) (Figure 8.10A and 10B). To identify ammonia, sodium hydroxide was added to the white crystals, which were then heated using a heat gun. Upon heating, ammonia is released and reacts with damp pH paper placed at the mouth of the test tube, turning it dark green (Figure 8.10C and 10D).

Figure 8.11. Estimation of the formation energy of 2D PANI structure. In this calculation, the two-dimensionally ionic-bonded lattice of $\text{C}_6\text{N}_6\text{H}_{15}\text{Cl}_3$ crystals, three-dimensional solid salt structures of ammonium chloride (NH_4Cl) and ammonia (NH_3) molecules are used for the reference of reactant and product. In this gauge, the energy gain per C_3N formula unit is calculated to be -2.03 eV in our DFT-PBE calculation.

Figure 8.12. Thermal stability of 2D PANI in air. TGA thermogram obtained from a 2D PANI crystal after annealing ($500\text{ }^\circ\text{C}$) with heating rate of $10\text{ }^\circ\text{C}/\text{min}$ in air.

Figure 8.13. Bond nature in 2D PANI framework. High-resolution XPS survey spectra of 2D PANI framework. (A) C 1s; (B) N 1s; (C) O 1s. Little amount of oxygen content is originated from physically absorbed moisture and oxygen due to hygroscopic nature of 2D PANI.

Figure 8.14. Powder XRD of the 2D PANI. (A) experimental PXRD pattern from the 2D PANI (dark green), simulated XRD after Pawley refinement (dark red) and the difference (dark blue); (B) unit cell of the 2D PANI with AB stacking.

Figure 8.15. Electrochemical analysis of 2D PANI by cyclic voltammograms in acetonitrile containing 0.1 M TBAPF_6 . (A) 2D PANI crystals; (B) 2D PANI crystal with Ferrocene; (C) pure HAB crystals were also tried to measure the electrochemical band gap, but HAB molecules were unstable in the electrochemical test condition. HAB decomposed during the process. Thus, it was not able to determine HOMO-LUMO gap by electrochemical method.

Figure 8.16. The band structure (Figure 8.2E) for the 2D triangular lattice of 2D PANI. (A) the valence band maximum state at Γ ; (B, C) the doubly degenerate conduction band minimum state at Γ ; (D) the valence band maximum state at M ($1/2,0$); (E, F) two low-lying state in the conduction band minimum at M.

Figure 8.17. Electrical performance of 2D PANI and doping study with HCl gas. (A) AFM height image from the white square marked in the inset. Inset is optical microscope image of FET using 2D PANI as active materials on Si wafer with 300 nm SiO_2 . Source and drain (channel length = 500 nm) were patterned by e-beam lithography ($W/L = 60\text{ }\mu\text{m}/0.5\text{ }\mu\text{m} = 120$). (B) Thickness profile indicates a cross-section of a cyan-dashed line in A. (C) Transfer curve of pristine 2D PANI FET (without doping) as a

function of gate voltage at $V_{DS} = 10$ mV, measured under vacuum (5×10^{-6} torr). (D) Schematic diagram of the doping set-up for 2D PANI. (E) Conductivity changes as a function of gate voltage after doping with HCl gas. The solid black line represents the electrical property of the pristine 2D PANI (undoped). The doping temperature increased from 20 to 160 °C with a step of 20 °C. (F) An average conductivity (10 FET devices) changes as a function of the doping temperature.

Figure 8.18. Optical microscope images of FET devices with channel length of 500 nm. Source and drain electrodes were defined by e-beam lithography.

Figure 8.19. Output curves of 2D PANI FET measured under a pressure of 5×10^{-5} torr.

Figure 8.20. Current-voltage curves of 2D PANI measured under a pressure of 5×10^{-5} torr with increasing the doping temperature.

Figure 8.21. Transfer curves of 2D PANI as a function of doping temperature. Doping temperature was changed from 20 to 160 °C with a step of 20 °C.

Table 8.1. Elemental composition of the 2D PANI framework from different characterization techniques.

Table 8.2. Atomistic coordinates for the refined unit cell parameters with AB stacking for the 2D PANI via Pawley refinement (space groups Triclinic P1, $a=b=4.78$ Å, $c=6.81$ Å, $\alpha=\beta=90^\circ$, $\gamma=120^\circ$)

Table 8.3. The comparison of conductivity of various materials, including metals, carbon-based materials, organic linear PANI and 2D PANI.

Chapter 1. Introduction to the Interface Between Graphene and Organic Electronic Materials

1.1. Research Background

Over the past decades, the key words for electronics based on silicon technology are ‘Large’ and ‘High-speed’. However, in recent years, the key words have been changed into anthropocentric keywords: convenient, wearable, smart, self-aware, comfortable, etc. Thus, developments of flexible and tiny electronic devices are essential part for achieving anthropocentric devices. In order to make the flexible devices, ‘Top-down approach’ (chiseled material away) such as photolithography has been extensively exploited in the fabrication of microelectronic devices. The top-down approach reached to fabrication limit in silicon-based electronics due to quantum tunneling effect,^[1] with approximately, 1 nm. Another approach called ‘Bottom-up approach’ (building material up) would be a promising method for the fabrication of next-generation electronic devices. The examples of ‘Bottom-up approach’ are usually based on molecular self-assembly, molecular recognition and supramolecular chemistry.^[2-7] However, it is not easy to fully exploit the 'Bottom-up approach' in the area of nanotechnology because of its fastidiousness of reaction. Thus, it should be elucidated the mechanisms behind the phenomenon of bottom-up approach in the interaction between molecules.

For the commercial quantity of production of electronic devices, the fabrication process should be simplified. Solution-processable approaches are one of the simplest way for commercial quantity of production of electronic devices. Solution-processable approach allows researchers to use simple techniques such as ink-jet printing, spin-coating, dip-coating and drop-casting.^[8-10] A lot of methods using solution-processability is applied to fabrication of nanodevice.

The developments of novel electronic materials are important aspects to materialize flexible electronics. Graphene is a promising single sheet of honeycomb lattice made of carbon. In addition, graphene shows extraordinary electrical, optical, thermal and mechanical properties. The properties of graphene are changed from semiconductor to conductor according to the size of graphene and the number of layers of graphene sheets. To exploit graphene as semiconductor, reliable bandgap control is required for transistor switching device, acquiring relevant high on/off ratio. Several methods for opening of bandgap in graphene have been announced, for example, applying to electrical field on bilayer graphene,^[11] applying to strain,^[12] making graphene nanoribbon,^[13-17] nanomesh,^[18] etc. However, reliable methods for high on/off ratio have not been reported so far.

As a rising material that could replace graphene, transition metal dichalcogenides (TMDCs) have attract great attention for electronic applications. TMDC crystals are composed of atomically thin layers. The layers were stacked by van-der waals force, thus TMDCs are called also ‘Van-der waals 2D materials’. TMDCs have a direct bandgap, unlike graphene, thus could be used as semiconductor in

electronics. For example, MoS₂ field effect transistor showed an on/off ratio ca. 10⁸ as well as high electron mobility ca. 50 cm²V⁻¹s⁻¹.^[19] Further interesting of TMDCs is its flexibility and optical transparency which is comparable to those of graphene for soft nanoelectronic device.

Organic semiconductor is solution-processable for fabrication of nano device, in addition, molecular functionality could be adjusted by chemical reaction. Therefore, ‘bottom up approach’, for example, molecular self-assembly, is accessible by inducing molecular force. Molecular self-assembly allows organic semiconductor to be used as single crystalline which shows high-performance for being used as semiconductor.^[20, 21] Because of reduced distance between molecules, charge transport in single crystalline organic semiconductor takes place in higher speed.

In spite of the advantages of graphene, TMDCs, organic electronic materials and solution-process, it has been barely reported the combination of those in the field of nanoelectronics so far. Thus, it is strongly desired to utilize the advantages of graphene, TMDCs, organic single crystal and solution-process in soft nanoelectronics (Figure 1.1), the impacts from the fusion technology will be tremendous for the academic society as well as practical applications.

1.2. Synthesis of Graphene and Two-Dimensional Transition Metal

Dichalcogenides (2D TMDCs)

Graphene can be obtained from various methods using liquid phase or thermal exfoliation of graphite,^[22-30] chemical vapor deposition on metal catalysis^[31, 32] and mechanical exfoliation from graphite.^[33, 34]

The simplest way to obtain graphene is mechanical exfoliation from graphite using Scotch tape. The graphene from the mechanical exfoliation results a high quality of graphene on the flat surface. However, the production yields and the scalability of mechanical exfoliation are not enough for mass production. The size of the obtained graphene sheets from mechanical exfoliation is few hundred micrometer which cannot be facilitated into practical applications.

Graphene oxide (GO) is the most investigated material to exfoliate graphite in liquid phase. GO is simply obtained using Hummer’s method.^[35-40] The pristine graphite is oxidized under the presence of a mixture of KMnO₄ and H₂SO₄. After the oxidation process, resulting GO sheets. Large numbers of oxygen-containing functional groups, for example, carboxyl, epoxides, and hydroxyl groups, are attached onto the graphene basal plane and edges. Thus, stable GO dispersions in water or polar organic solvents are obtained.^[37, 38]

Graphene can be grown through high temperature annealing of a SiC(0001) wafer which allows to grow graphene epitaxially on the SiC(0001) wafer. After the evaporation of Si atoms from the SiC wafer surface, graphene layers are formed by carbon segregations.^[41-44] Chemical vapor deposition (CVD) is utilized for graphene growth. The schematic illustration of graphene growth using CVD is depicted in Figure 1.2. The large-scale CVD-grown graphene film is formed after cooling step in which dissolved

carbon atoms into a metal catalyst substrate at high temperature are precipitated. The CVD-grown graphene film is supported by polymer films such as polystyrene (PS), polymethyl methacrylate (PMMA), the metal catalyst is etched away. The polymer-supported graphene film can be transferred to the desired substrate.^[31, 32] The size of graphene film via CVD growth is scalable with high quality for the practical application. However, the cost using this method is expensive and high temperature is required. The research for low-cost graphene film is under development.

2D TMDCs have the general formula of MX_2 , where M is a metal, X is a chalcogen atom (that is, sulfur, selenium or tellurium). Adjacent layers of TMDCs are weakly held together by van der Waals forces, which allow them to be easily exfoliate. The bandgap of most semiconducting TMDs changes with layer thickness. Bulk layered materials are indirect bandgap semiconductors, whereas single layered TMDs are direct band semiconductors. To prepare TMDCs with scalability, liquid exfoliation methods have been developed using chemical surfactants from bulk 2D TMDCs crystals.^[45, 46] However, compulsory intercalation of the chemical surfactants or sonication degrades the electronic and photonic quality of 2D TMDCs, which is not utilized to the practical application. Most 2D TMDCs have been successfully prepared using CVD process.^[47-49]

1.3. Electronic Properties of Graphene and 2D TMDCs

Graphene possess superior electrical, mechanical and optical properties. Many graphene characteristics measured in experiments have exceeded those obtained in any other material, with some reaching theoretically predicted limits: room-temperature electron mobility of $2.5 \times 10^5 \text{ cm}^2\text{V}^{-1}\text{s}^{-1}$ ^[50] (theoretical limit $2 \times 10^5 \text{ cm}^2\text{V}^{-1}\text{s}^{-1}$); a Young's modulus of 1 TPa and intrinsic strength of 130 GPa^[51] (very close to that predicted by theory); very high thermal conductivity (above $3,000 \text{ WmK}^{-1}$)^[52]; optical absorption of exactly $\pi\alpha \approx 2.3\%$ (in the infrared limit, where α is the fine structure constant)^[53]; complete impermeability to any gases,^[54] ability to sustain extremely high densities of electric current (a million times higher than copper).^[55] However, in order to utilize graphene as an active layer in transistors which are the fundamental building block of modern electronic devices, graphene is not relevant to the active layer of transistors due to the absence of bandgap in the electronic structure.

2D TMDCs, alternatively, such as MoS_2 , MoSe_2 , are interesting electronic materials with sizable ($>0.3 \text{ eV}$) bandgaps so that low off-state currents and high on-state currents can be realized unlike with graphene.^[56] In 2D TMDCs, charge carriers are confined in the atomically thin semiconductor. A narrow mobile charge carrier layer is confined in the thin film. This confinement of charge carriers allows the carriers to be easily controlled by the gate voltage, leading to excellent gate electrostatics.^[57] For example, mechanically exfoliated MoS_2 were used as an active channel material in field-effect transistors in 2007.^[58, 59] n-type transport was observed with mobilities of up to $50 \text{ cm}^2\text{V}^{-1}\text{s}^{-1}$ and an on/off ratio of $>10^5$ in the configuration of a back-gated field-effect transistor and at $V_{\text{GS}} = -50 \text{ V}$. The

monolayer MoS₂ transistors with HfO₂ as the gate dielectric demonstrated mobilities in the range of tens of cm²V⁻¹s⁻¹,^[58, 59] high on/off ratios, high on currents at a source–drain voltage of 0.5 V and a low subthreshold swing (SS) of 74 mVdec⁻¹. These initial results demonstrated that useful FET properties could be achieved from very thin semiconductor channels and provided encouragement for the community to pursue 2D materials for electronics.

1.4. Surface Transfer Doping Using Organic Dopants

The studies on the interface of 2D nanomaterials including graphene, 2D TMDCs and organic electronic materials are important to investigate futuristic smart electronic devices which are flexible, rollable and bendable. Doping is a key process to form p/n junction which is the most basic architecture in semiconductor devices. The basic principle of doping is depicted in Figure 1.3. Electron donors (n-dopants) or acceptors (p-dopants) are added to the semiconductor material, generating extra mobile hole and electron charge carriers. The n-dopants donate electrons from the ionization energy (IE) of n-dopants to the lowest unoccupied molecular orbital (LUMO) states of the semiconductor to obtain n-type doping in the semiconductor on the other hand, p-type dopants extract electrons from the highest occupied molecular orbital (HOMO) states to the electron affinity (EA) of p-dopants, therefore producing holes.

Inorganic doping with alkali metals or halides has often been used in order to enhance the conductivity and tune the types of charge carrier and display comparable performance. However, it is turned out that the inorganic-mediated doping is problematic in the growing field of futuristic smart electronic devices, where organic semiconductors and 2D TMDCs including graphene are the active component, because alkali metals and halides tend to react active layer components easily or diffuse into the channel in the semiconductor, resulting in detrimental effects on electrical performance.^[60, 61]

A new doping method, surface transfer doping, has been used to dope these materials at the near-surface regime for nondestructive effects on semiconductors. Surface transfer doping depends on an exchange of electrons at the interface between a semiconductor and dopants. Although the charge transfer process across the solid/solid interface as a result of misalignment of the Fermi levels on each side is long known to be a general phenomenon in solid state physics,^[62] utilizing the interfacial charge transfer as an effective doping scheme to control the conductivity of nanostructured materials has only recently been proposed.

1.5. Applications Using the Combination of Organic Electronic Materials and Graphene and 2D TMDCs

The fabrication of field-effect transistors using graphene and organic electronic materials and 2D TMDCs is a fundamental step to investigate futuristic devices. Typical structures of organic field-effect

transistor (OFET), top contact bottom gate (TCBG), bottom contact bottom gate (BCBG), top contact top gate (TCTG) and bottom contact top gate (BCTG), are illustrated in Figure 1.4. In both cases, the organic semiconductor is deposited on a dielectric layer and contacted with two metal contacts, called, the source and drain, and on the other side of the dielectric a third contact, the gate. Thus, the amount of source-drain current (I_{SD}) along the active channel formed at the interface between the semiconductor and dielectric can be controlled by application of a gate voltage (V_{GS}) between the source and the gate. Minimal I_{SD} is measured when no V_{GS} is applied. When a certain amount of V_{GS} is applied, mobile electrons or holes are created at the semiconductor-dielectric interface and the S–D current increases (device “on” state). The relationships describing the OFET drain current are given in following equation;

$$I_{DS} = \frac{W}{L} \mu C_i (V_{GS} - V_t - \frac{V_{DS}}{2}) V_{DS} \text{ for linear regime (1.1)}$$

$$I_{DS} = \frac{1}{2} \frac{W}{L} \mu C_i (V_{GS} - V_t)^2 \text{ for saturation regime (1.2)}$$

where μ is the field-effect mobility of the semiconductor, W the channel width, L the channel length, C_i the capacitance per unit area of the insulator layer, V_t the threshold voltage, V_{DS} the source-drain voltage, respectively. On increasing the V_{DS} and V_{GS} magnitudes, a linear regime (1.1) is initially observed at low drain voltages when $V_{DS} \ll V_{GS} - V_t$, followed by a saturation regime (1.2) when the V_{DS} exceeds the V_{GS} ($V_{DS,sat} \approx V_{GS} - V_t$), resulting in ‘pinch-off’ of the accumulation layer. The charge carrier mobilities for n-type and p-type operation can be calculated by using the equation (1.1) and (1.2).

Another application using graphene and organic electronic materials and 2D TMDCs is organic phototransistor which is designated as a semiconductor light sensor formed from a transistor that provides high levels of gain. Compared to photodiodes that have two electrodes, phototransistors enable easier control of light-detection and sensitivity without noise increment associated with conventional avalanche photodiodes. This is attributed to the presence of a third electrode for amplifying the electrical signals induced by the incoming photons.^[63]

In organic phototransistors, aside from charge-carrier mobility, light responsivity (r) and photocurrent/dark-current ratio (P) are important parameters for investigating photosensitivity for organic phototransistors and those values can be determined from transfer characteristics coupled with light irradiation. The R and P values are typically defined by the following equations;

$$R = \frac{I_{ph}}{P_{inc}} = \frac{(I_{light} - I_{dark})}{P_{inc}} \text{ (1.3)}$$

$$P = \frac{(I_{light} - I_{dark})}{I_{dark}} \text{ (1.4)}$$

Where I_{ph} is the photocurrent, P_{inc} is the incident illumination power on the channel of the device, I_{light} is the drain current under illumination, and I_{dark} is the drain current in the dark. In addition, external quantum efficiency (EQE, η) is an important parameter for investigating gain of organic phototransistors and this value can be defined as the ratio of the number of photo-generated carriers that practically

enhance the drain current to the number of photons incident onto the organic phototransistor channel area, using the following equation;

$$\eta = \frac{(I_{light} - I_{dark})hc}{eP_{inc}A\lambda_{peak}} \quad (1.5)$$

Where h is the Plank constant, c is the speed of light, e is the fundamental unit of charge, A is the area of the transistor channel and λ_{peak} is the peak wavelength of the incident light.

1.6 References

- [1] J. Appenzeller, M. Radosavljević, J. Knoch, P. Avouris, *Phys. Rev. Lett.* **2004**, *92*, 483011.
- [2] S. De Feyter, F. C. De Schryver, *Chem. Soc. Rev.* **2003**, *32*, 139.
- [3] R. Gutzler, C. Fu, A. Dadvand, Y. Hua, J. M. MacLeod, F. Rosei, D. F. Perepichka, *Nanoscale* **2012**, *4*, 5965.
- [4] R. Gutzler, O. Ivasenko, C. Fu, J. L. Brusso, F. Rosei, D. F. Perepichka, *Chem. Commun.* **2011**, *47*, 9453.
- [5] O. Ivasenko, D. F. Perepichka, *Chem. Soc. Rev.* **2011**, *40*, 191.
- [6] T. Kudernac, S. Lei, J. A. A. W. Elemans, S. De Feyter, *Chem. Soc. Rev.* **2009**, *38*, 402.
- [7] R. Otero, J. M. Gallego, A. L. V. De Parga, N. Martín, R. Miranda, *Adv. Mater.* **2011**, *23*, 5148.
- [8] S. R. Forrest, *Nature* **2004**, *428*, 911.
- [9] C. J. Drury, C. M. J. Mutsaers, C. M. Hart, M. Matters, D. M. De Leeuw, *Appl. Phys. Lett.* **1998**, *73*, 108.
- [10] G. H. Gelinck, T. C. T. Geuns, D. M. De Leeuw, *Appl. Phys. Lett.* **2000**, *77*, 1487.
- [11] Y. Zhang, T. T. Tang, C. Girit, Z. Hao, M. C. Martin, A. Zettl, M. F. Crommie, Y. R. Shen, F. Wang, *Nature* **2009**, *459*, 820.
- [12] K. Novoselov, *Nat. Mater.* **2007**, *6*, 720.
- [13] V. Barone, O. Hod, G. E. Scuseria, *Nano Lett.* **2006**, *6*, 2748.
- [14] I. Meric, M. Y. Han, A. F. Young, B. Ozyilmaz, P. Kim, K. L. Shepard, *Nat. Nanotechnol.* **2008**, *3*, 654.
- [15] K. Nakada, M. Fujita, G. Dresselhaus, M. S. Dresselhaus, *Physical Review B - Condensed Matter and Materials Physics* **1996**, *54*, 17954.
- [16] K. S. Novoselov, A. K. Geim, S. V. Morozov, D. Jiang, M. I. Katsnelson, I. V. Grigorieva, S. V. Dubonos, A. A. Firsov, *Nature* **2005**, *438*, 197.
- [17] Y. W. Son, M. L. Cohen, S. G. Louie, *Phys. Rev. Lett.* **2006**, *97*.
- [18] J. Bai, X. Zhong, S. Jiang, Y. Huang, X. Duan, *Nat. Nanotechnol.* **2010**, *5*, 190.
- [19] B. Radisavljevic, A. Radenovic, J. Brivio, V. Giacometti, A. Kis, *Nat. Nanotechnol.* **2011**, *6*, 147.
- [20] J. C. Love, L. A. Estroff, J. K. Kriebel, R. G. Nuzzo, G. M. Whitesides, *Chem. Rev.* **2005**, *105*, 1103.
- [21] E. Moulin, J. J. Cid, N. Giuseppone, *Adv. Mater.* **2013**, *25*, 477.
- [22] J. N. Coleman, *Adv. Funct. Mater.* **2009**, *19*, 3680.
- [23] Y. Hernandez, V. Nicolosi, M. Lotya, F. M. Blighe, Z. Sun, S. De, I. T. McGovern, B. Holland, M. Byrne, Y. K. Gun'ko, J. J. Boland, P. Niraj, G. Duesberg, S. Krishnamurthy, R. Goodhue, J. Hutchison, V. Scardaci, A. C. Ferrari, J. N. Coleman, *Nat. Nanotechnol.* **2008**, *3*, 563.
- [24] U. Khan, A. O'Neill, M. Lotya, S. De, J. N. Coleman, *Small* **2010**, *6*, 864.
- [25] J. H. Lee, D. W. Shin, V. G. Makotchenko, A. S. Nazarov, V. E. Fedorov, Y. H. Kim, J. Y. Choi, J. M. Kim, J. B. Yoo, *Adv. Mater.* **2009**, *21*, 4383.
- [26] W. W. Liu, J. N. Wang, *Chem. Commun.* **2011**, *47*, 6888.
- [27] M. Lotya, Y. Hernandez, P. J. King, R. J. Smith, V. Nicolosi, L. S. Karlsson, F. M. Blighe, S. De, W. Zhiming, I. T. McGovern, G. S. Duesberg, J. N. Coleman, *J. Am. Chem. Soc.* **2009**, *131*, 3611.
- [28] C. Vallés, C. Drummond, H. Saadaoui, C. A. Furtado, M. He, O. Roubeau, L. Ortolani, M. Monthieux, A. Pénicaud, *J. Am. Chem. Soc.* **2008**, *130*, 15802.

- [29] X. Wang, P. F. Fulvio, G. A. Baker, G. M. Veith, R. R. Unocic, S. M. Mahurin, M. Chi, S. Dai, *Chem. Commun.* **2010**, 46, 4487.
- [30] Y. Wang, Z. Shi, J. Fang, H. Xu, X. Ma, J. Yin, *J. Mater. Chem.* **2011**, 21, 505.
- [31] S. Bae, H. Kim, Y. Lee, X. Xu, J. S. Park, Y. Zheng, J. Balakrishnan, T. Lei, H. Ri Kim, Y. I. Song, Y. J. Kim, K. S. Kim, B. Özyilmaz, J. H. Ahn, B. H. Hong, S. Iijima, *Nat. Nanotechnol.* **2010**, 5, 574.
- [32] X. Li, W. Cai, J. An, S. Kim, J. Nah, D. Yang, R. Piner, A. Velamakanni, I. Jung, E. Tutuc, S. K. Banerjee, L. Colombo, R. S. Ruoff, *Science* **2009**, 324, 1312.
- [33] A. Gupta, G. Chen, P. Joshi, S. Tadigadapa, P. C. Eklund, *Nano Lett.* **2006**, 6, 2667.
- [34] J. C. Meyer, C. Kisielowski, R. Erni, M. D. Rossell, M. F. Crommie, A. Zettl, *Nano Lett.* **2008**, 8, 3582.
- [35] D. Li, M. B. Müller, S. Gilje, R. B. Kaner, G. G. Wallace, *Nat. Nanotechnol.* **2008**, 3, 101.
- [36] M. J. McAllister, J. L. Li, D. H. Adamson, H. C. Schniepp, A. A. Abdala, J. Liu, M. Herrera-Alonso, D. L. Milius, R. Car, R. K. Prud'homme, I. A. Aksay, *Chem. Mater.* **2007**, 19, 4396.
- [37] J. I. Parades, S. Villar-Rodil, A. Martínez-Alonso, J. M. D. Tascón, *Langmuir* **2008**, 24, 10560.
- [38] S. Park, J. An, I. Jung, R. D. Piner, S. J. An, X. Li, A. Velamakanni, R. S. Ruoff, *Nano Lett.* **2009**, 9, 1593.
- [39] H. C. Schniepp, J. L. Li, M. J. McAllister, H. Sai, M. Herrera-Alonso, D. H. Adamson, R. K. Prud'homme, R. Car, D. A. Seville, I. A. Aksay, *J. Phys. Chem. B* **2006**, 110, 8535.
- [40] V. C. Tung, M. J. Allen, Y. Yang, R. B. Kaner, *Nat. Nanotechnol.* **2009**, 4, 25.
- [41] K. V. Emtsev, A. Bostwick, K. Horn, J. Jobst, G. L. Kellogg, L. Ley, J. L. McChesney, T. Ohta, S. A. Reshanov, J. Röhrl, E. Rotenberg, A. K. Schmid, D. Waldmann, H. B. Weber, T. Seyller, *Nat. Mater.* **2009**, 8, 203.
- [42] K. J. Kim, H. Lee, J. H. Choi, H. K. Lee, T. H. Kang, B. Kim, S. Kim, *J. Phys.: Condens. Matter* **2008**, 20.
- [43] E. Rollings, G. H. Gweon, S. Y. Zhou, B. S. Mun, J. L. McChesney, B. S. Hussain, A. V. Fedorov, P. N. First, W. A. de Heer, A. Lanzara, *J. Phys. Chem. Solids* **2006**, 67, 2172.
- [44] C. Virojanadara, M. Syväjarvi, R. Yakimova, L. I. Johansson, A. A. Zakharov, T. Balasubramanian, *Physical Review B - Condensed Matter and Materials Physics* **2008**, 78.
- [45] V. Nicolosi, M. Chhowalla, M. G. Kanatzidis, M. S. Strano, J. N. Coleman, *Science* **2013**, 340.
- [46] U. Halim, C. R. Zheng, Y. Chen, Z. Lin, S. Jiang, R. Cheng, Y. Huang, X. Duan, *Nat. Commun.* **2013**, 4, 2213.
- [47] Y.-H. Lee, X.-Q. Zhang, W. Zhang, M.-T. Chang, C.-T. Lin, K.-D. Chang, Y.-C. Yu, J. T.-W. Wang, C.-S. Chang, L.-J. Li, T.-W. Lin, *Adv. Mater.* **2012**, 24, 2320.
- [48] J. C. Shaw, H. Zhou, Y. Chen, N. O. Weiss, Y. Liu, Y. Huang, X. Duan, *Nano Res.* **2014**, 7, 511.
- [49] K. Kang, S. Xie, L. Huang, Y. Han, P. Y. Huang, K. F. Mak, C.-J. Kim, D. Muller, J. Park, *Nature* **2015**, 520, 656.
- [50] A. S. Mayorov, R. V. Gorbachev, S. V. Morozov, L. Britnell, R. Jalil, L. A. Ponomarenko, P. Blake, K. S. Novoselov, K. Watanabe, T. Taniguchi, A. K. Geim, *Nano Lett.* **2011**, 11, 2396.
- [51] C. Lee, X. Wei, J. W. Kysar, J. Hone, *Science* **2008**, 321, 385.
- [52] A. A. Balandin, *Nat. Mater.* **2011**, 10, 569.
- [53] R. R. Nair, P. Blake, A. N. Grigorenko, K. S. Novoselov, T. J. Booth, T. Stauber, N. M. R. Peres, A. K. Geim, *Science* **2008**, 320, 1308.
- [54] J. S. Bunch, S. S. Verbridge, J. S. Alden, A. M. Van Der Zande, J. M. Parpia, H. G. Craighead, P. L. McEuen, *Nano Lett.* **2008**, 8, 2458.
- [55] J. Moser, A. Barreiro, A. Bachtold, *Appl. Phys. Lett.* **2007**, 91.
- [56] D. Kong, Y. Cui, *Nat Chem* **2011**, 3, 845.
- [57] A. K. Geim, K. S. Novoselov, *Nat. Mater.* **2007**, 6, 183.
- [58] K. F. Mak, K. L. McGill, J. Park, P. L. McEuen, *Science* **2014**, 344, 1489.
- [59] H. Zeng, J. Dai, W. Yao, D. Xiao, X. Cui, *Nat Nano* **2012**, 7, 490.
- [60] J. Kido, T. Matsumoto, *Appl. Phys. Lett.* **1998**, 73, 2866.
- [61] J. Huang, M. Pfeiffer, A. Werner, J. Blochwitz, K. Leo, S. Liu, *Appl. Phys. Lett.* **2002**, 80, 139.
- [62] Lu, amp, x, H. th, *Solid Surfaces, Interfaces and Thin Films* **2001**.
- [63] Y. Guo, G. Yu, Y. Liu, *Adv. Mater.* **2010**, 22, 4427.

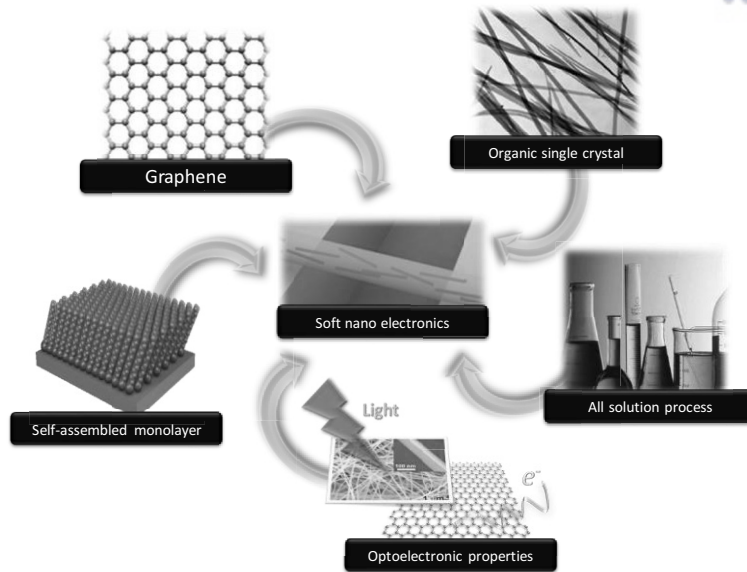


Figure 1.1. Schematic illustration of strategies to achieve soft nano electronics.

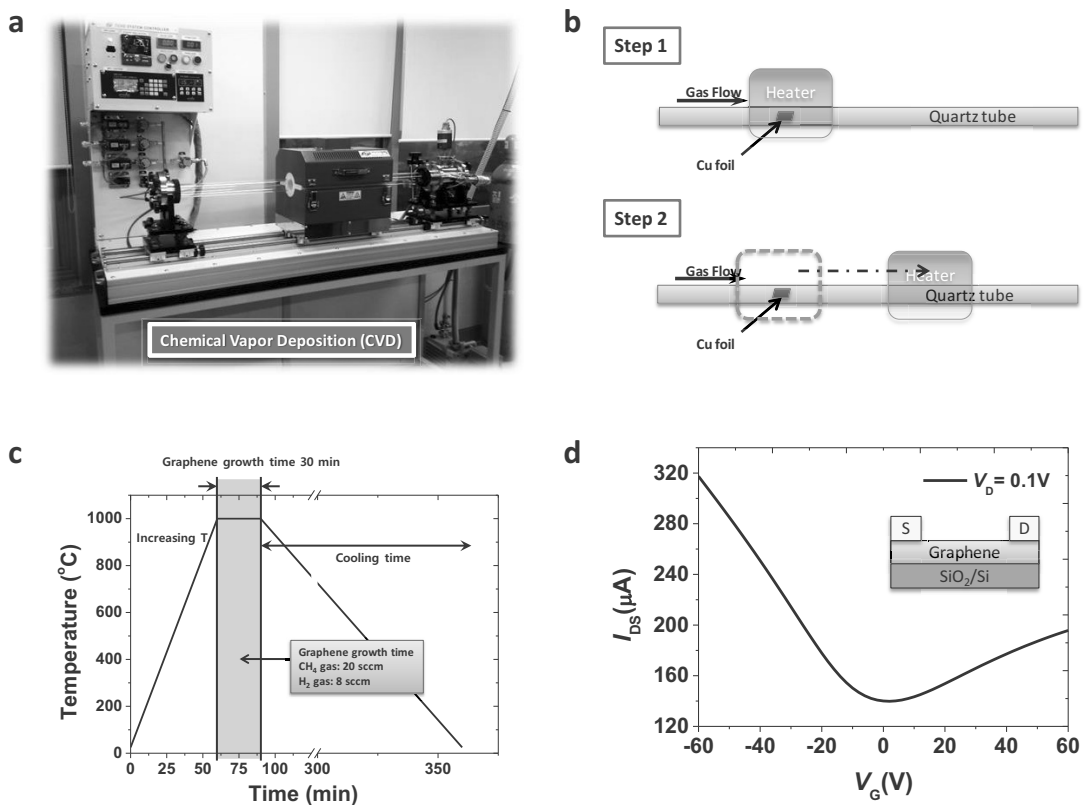


Figure 1.2. Graphene growth using CVD. (a) Photograph of CVD. (b) Detailed illustration of CVD process for the growth of graphene. CVD heater is placed on the position of Cu foil for the growth of graphene (Step 1). Heater is moved away from the Cu foil to cool down quickly (Step 2). (c) Temperature gradient versus time in CVD process and gas (CH₄, H₂) flow condition (d) Transfer curve of CVD grown graphene measured in vacuum condition (1×10^{-6} torr).

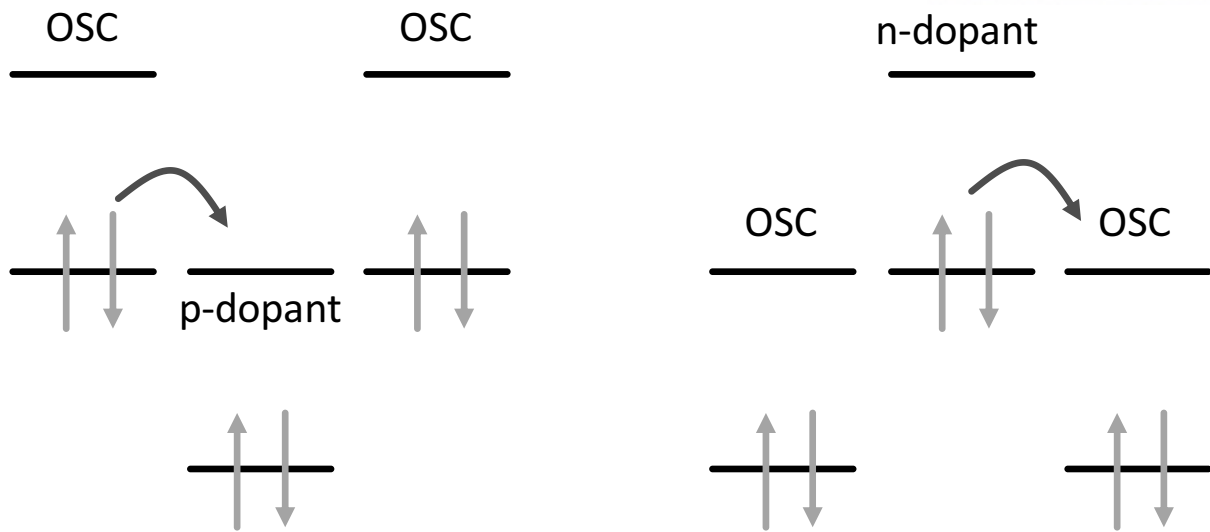


Figure 1.3. Scheme of the doping process for molecular p-type (left) and n-type doping (right).

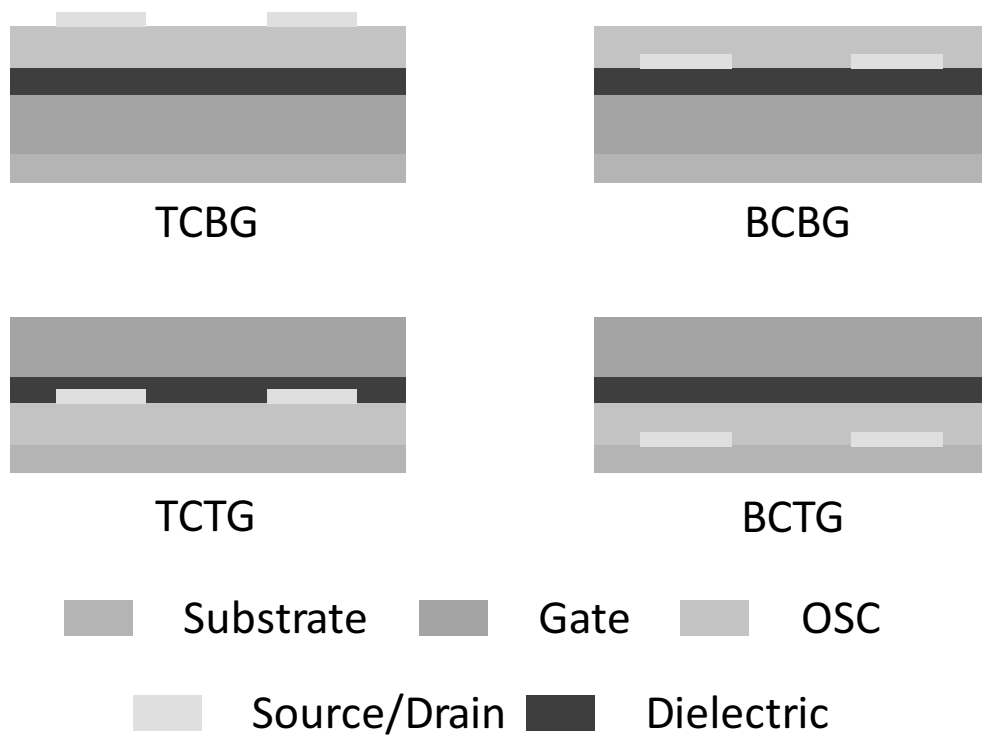


Figure 1.4. The configurations of organic field effect transistor.

Chapter 2. Graphene-ruthenium Complex Hybrid Photodetectors With Ultrahigh Photoresponsivity

2.1. Introduction

Graphene, a single layer of two-dimensional carbon atoms in a honeycomb lattice, has attracted enormous attention due to its unique electronic, optical, thermal, and mechanical properties.^[1–8] It has an extremely high charge carrier mobility ($\sim 200,000 \text{ cm}^2\text{V}^{-1}\text{s}^{-1}$),^[9] an optical transmittance of 97.7%,^[10] a theoretical sheet resistance of $30 \text{ }\Omega/\text{sq}$,^[11] a high fracture strain resistance greater than 20%, and chemical stability.^[12] These features make it highly promising for applications in flexible electronics and energy conversion devices, including touch screens, field-effect transistors (FETs), capacitors, batteries, solar cells, and light-emitting diodes (LEDs).^[13–17] However, the zero band gap, small optical absorption, and chemical inertness have limited its practical application in switching and optoelectronic devices. Several methods including doping, dual-gated bilayer structures, nanoribbon and nanomesh structures,^[18–23] have been developed to open up and control an electronic band gap. Furthermore, chemical modification via covalent or non-covalent functionalization has been utilized to enhance the optical absorption and chemical reactivity of graphene. Covalent functionalization has been performed by the reaction of graphene with reactive intermediates of free radicals, nitrenes, carbenes and arynes, which has resulted in a non-zero band gap and a change in the electrical conductivity.^[24] However, it is difficult to control the composition of the graphene surface due to the side reactions caused by high reactivity of the intermediates. On the other hand, most non-covalent functionalization has been carried out via π - π stacking of pyrene-functionalized derivatives.^[25]

Although graphene is a promising material for photodetection applications due to the broad spectral bandwidth and high charge carrier mobility,^[26–41] the photoresponsivity of pure monolayer graphene-based photodetectors has not exceeded 10 mA W^{-1} , which is attributed to the small optical absorption and the short recombination lifetime (of a few picoseconds).^[42] Recently, PbS quantum dots (QDs) have been utilized as a photosensitizing layer on the graphene surface.^[43,44] The responsivity of PbS QDs/graphene hybrid photodetectors reached up to 10^7 A W^{-1} at an ultralow incident light intensity ranging from picowatts (pW) to femtowatts (fW). This ultrahigh responsivity was attributed to the increased optical absorption of the QD-functionalized graphene, as well as to the long lifetime of photoexcited charge carriers. In energy conversion applications such as solar cells and water splitting, ruthenium polypyridyl complexes have been used as photoactive components for graphene or carbon nanotube (CNT)-based nanocomposites.^[45–48] These hybrid materials are known to facilitate the separation and transport of electron-hole pairs, and reduce the recombination of charge carriers. However, there has been little effort for exploiting transition metal complexes as charge transfer materials in photodetectors. Although transition metal complexes based on porphyrins and

phthalocyanines have been utilized as the active materials of FETs,^[49-53] these FETs did not function as photodetectors.

Here, we report a graphene hybrid photodetector modified with a photoactive ruthenium complex. The photoactive ruthenium complex **1** was synthesized by the condensation reaction of acyl chloride ruthenium complex **3** with the amino group of a pyrene derivative **2** (see **Scheme 2.1**). Complex **1** was attached to the graphene surface using a pyrene functional group via non-covalent π - π interactions. **Figure 2.1** shows a simplified schematic depiction of the photoactive ruthenium complex **1**/graphene hybrid photodetector, and illustrates the electron transfer pathway from complex **1** to the graphene under illumination. The hybrid photodetector exhibited a responsivity of $\sim 1 \times 10^5$ AW⁻¹ and a gain of $\sim 3 \times 10^6$ with an incident light intensity on the order of milliwatts. It is noteworthy that this excellent performance was achieved by the functionalization of graphene with an ultrathin layer (4-nm-thick) of the transition metal complex. This substantiates the high efficiency of ruthenium complex **1** as charge transfer agent for graphene-based photodetectors.

2.2. Experimental Section

All starting materials were purchased either from Aldrich or Acros and used without further purification. All solvents are ACS grade unless otherwise noted. ¹H-NMR and ¹³C-NMR spectra were recorded on a VNMRS 600 (Varian, USA) spectrophotometer using CDCl₃ and CD₃CN as solvent and tetramethylsilane (TMS) as the internal standard. ESI-MS spectra were obtained from Ultraflex III (Bruker, Germany).

Compound **2** and **3** were synthesized according to previously reported methods (**Scheme 2.1**).^[62, 63] Ruthenium complex **1** was synthesized by following the reported procedure.^[64] In a 10 mL round bottom flask, compound **3** (308 mg, 0.33 mmol) was dissolved in dry CH₃CN (5 mL) under N₂. Compound **2** (91 mg, 0.33 mmol) and triethylamine (0.5 mL) were dissolved in dry CH₃CN (1 mL), which was added to the above compound **3** solution using a syringe and kept at 0 °C for 1 h under N₂. After another 4 h at room temperature, the solvent was evaporated in vacuum, and the resulted red-orange crude product was purified on a column of silica gel (CH₃CN/H₂O/KNO₃ = 100:15:4). After chromatography, the eluent was evaporated to give red-orange solid. The product was dissolved in small scale water and added the excess NH₄PF₆. The CH₂Cl₂ (3 × 20 mL) was added to the above water solution to extract the product from water to CH₂Cl₂, followed by the drying with NaSO₄ and filtered by celite. The resulted CH₂Cl₂ solution of product was evaporated to give 77 mg (20%) of the desired ruthenium compound **1**. The CVD growth graphene was transferred to SiO₂/n-doped Si substrate. The thickness of SiO₂ was 300 nm. Then the Au source and drain electrodes were deposited on top of the graphene film through a shadow mask by thermal evaporation and formed a channel of $W/L = 1$. The graphene transistor was characterized with a semiconductor parameter analyzer (Keithley 4200-SCS) under vacuum ($\sim 10^{-6}$ Torr). Monochromatic light measurements were recorded using a LS 150 xenon arc lamp source

monochromated by a Mmac-200 monochromator. The laser spot is 4 mm in radius. Raman spectra were taken with a He-Ne laser (532 nm) as the excitation source by using confocal Raman microscopy (Alpha 300S, WITec, Germany). AFM images were recorded in high-resolution tapping mode under ambient conditions. Agilent 5500 scanning probe microscope running with a Nanoscope V controller was used to obtain AFM images.

2.3. Results and Discussion

Single-layer graphene was synthesized on a copper foil via chemical vapor deposition (CVD), and then transferred onto a SiO₂/Si substrate.^[54,55] The graphene/SiO₂/Si samples were immersed in an acetonitrile solution of ruthenium complex **1** (6.5 mg mL⁻¹) for 12 h, followed by rinsing with acetonitrile to remove any unbound complex **1** and drying at room temperature in a nitrogen atmosphere for 24 h. Raman spectra of the pristine graphene and ruthenium complex **1**/graphene are shown in **Figure 2.2**. The pristine graphene exhibited a typical 2D band (2673 cm⁻¹) and a G band (1585 cm⁻¹). The intensity ratio of 2D/G was approximately 2, which indicates that a graphene monolayer was successfully grown and transferred onto the SiO₂/Si substrate.^[56] The high quality of the graphene monolayer was confirmed by the negligible D band in the Raman spectra and the relatively few defects in the atomic force microscopy (AFM) images of pristine graphene/SiO₂/Si (**Figure 2.3a**). The G and 2D bands of the ruthenium complex **1**/graphene exhibited an upshift from 1585 to 1595 cm⁻¹ and a downshift from 2673 to 2669 cm⁻¹ compared with those of pristine graphene/SiO₂/Si. The downshift of the Raman 2D band is indicative of *n*-type doping,^[57] which is consistent with the current–voltage (*I*–*V*) characteristics, where the Dirac point (i.e., the charge neutrality point), *V*_{Dirac}, was shifted to more negative values after functionalization with ruthenium complex **1** (vide infra). Raman spectra of ruthenium complex **1**/graphene exhibited a broad baseline with a 2D/G intensity ratio of ~1/2, which is also indicative of doping. AFM images were collected over ten different locations to investigate the morphology of the ruthenium complex **1** film, indicating that the film was coated on the graphene with an average thickness of 4 nm and a surface coverage of 80%. A typical AFM image is shown in **Figure 2.3b**. X-ray photoelectron spectroscopy (XPS) analysis exhibited characteristic peaks of O1s (533.2 eV, 535.2 eV), N1s (398.8 eV), Ru3p (461.5eV, 485.1eV) and Ru3d (281.5 eV), which supports the successful functionalization of ruthenium complex **1** on the surface of the graphene (see **Figure 2.4**).

Figure 2.5a shows the source–drain current (*I*_{DS}) as a function of the gate voltage (*V*_G) of pristine graphene and the ruthenium complex **1**/graphene devices. The *V*_{Dirac} of graphene devices was shifted from +3 V to –20 V upon functionalization with ruthenium complex **1**, indicating that the ruthenium complex **1** acts as an *n*-type dopant. The charge carrier mobility (*μ*_{FE}) was calculated by using the following equation (1):

$$\mu_{FE} = \frac{g_m L}{V_{DS} W C_g} \quad (1)$$

where g_m is the transconductance, V_{DS} is the source–drain voltage, L is the channel length, W is the channel width, and C_g is the capacitance of the dielectric layer.^[26] Here, the typical device performance was measured under the following parameters: $W = L = 25 \mu\text{m}$, $C_g = 1.08 \times 10^{-8} \text{ F cm}^{-2}$, $V_{DS} = 1 \text{ V}$. Under dark condition, the functionalized graphene device with ruthenium complex **1** showed higher average charge carrier mobilities for both holes and electrons ($\mu_{FE,h} = 3198 \pm 81 \text{ cm}^2\text{V}^{-1}\text{s}^{-1}$, $\mu_{FE,e} = 1130 \pm 46 \text{ cm}^2\text{V}^{-1}\text{s}^{-1}$), compared with those of pristine graphene device ($\mu_{FE,h} = 1632 \pm 31 \text{ cm}^2\text{V}^{-1}\text{s}^{-1}$, $\mu_{FE,e} = 742 \pm 30 \text{ cm}^2\text{V}^{-1}\text{s}^{-1}$). The maximum charge carrier mobility increased from 2200 to 4040 $\text{cm}^2\text{V}^{-1}\text{s}^{-1}$ for holes, and from 1040 to 1600 $\text{cm}^2\text{V}^{-1}\text{s}^{-1}$ for electrons. The I_{DS} at the Dirac point was slightly increased from 0.64 mA to 0.68 mA (see Figure 2.5a), which can be attributed to the unintentional doping by the trapped impurities and/or the local dipole moments in the ruthenium functionalized graphene. It has been known that such doping effects tend to increase mobility and off current in field-effect transistors.^[58,59] In addition, the ruthenium complex **1**/graphene device exhibited hysteresis behavior to some degree (see **Figure 2.6**). The hysteresis in ruthenium complex **1**/graphene device can be ascribed to the trapped impurities engendered from device fabrication and the ketone group in ruthenium complex **1** that might act as charge trapping sites in the active channel. Compared to forward gate voltage sweep (from -80 V to $+80 \text{ V}$), the backward gate sweep (from $+80 \text{ V}$ to -80 V) showed the broadened Dirac point that could not be determined exactly. The change of the Dirac point in the forward and backward sweeps induces the change of the transconductance, leading to a certain degree of variations in the determined mobility.

The I – V characteristics of ruthenium complex **1**/graphene devices coupled with light irradiations were measured with different incident light intensities under vacuum (**Figure 2.5b**). The V_{Dirac} was shifted to more negative voltages as the incident light intensity increased. The n -type doping effect is attributed to electron injection via the metal–ligand charge transfer (MLCT) from ruthenium complex **1** to graphene. In the electron-enhancement regions ($V_G > V_{Dirac}$), the I_{DS} increased with increasing optical intensity owing to the transfer of photogenerated electrons from ruthenium complex **1** to the graphene via MLCT. In the hole-enhancement regions ($V_G < V_{Dirac}$), the I_{DS} decreased with increasing optical intensity due to the injection of photogenerated electrons from ruthenium complex **1** to graphene that reduces the density of hole carriers induced by the back gate.

The output characteristics were measured under different optical intensities. Under the hole-enhancement condition of $V_G = -80 \text{ V}$, the output current decreased with increasing optical intensity, as shown in **Figure 2.5c**. The I_{DS} increased with increasing optical intensity in the electron-dominated region ($V_G = 0 \text{ V}$), as shown in **Figure 2.5d**, which is consistent with the result of the transfer characteristics. On the other hand, the output characteristics of pristine graphene devices exhibited negligible changes under different optical intensity (see **Figure 2.7**). **Figure 2.5e** shows the change in the energy level of pristine graphene when it is functionalized with ruthenium complex **1** and optically

illuminated sequentially. To investigate the optical absorption of the ruthenium-modified graphene, we fabricated pristine graphene/glass and ruthenium complex **1**/graphene/glass specimens using the same methods. The transmittance of the pristine graphene/glass was above 95% in visible light region, while that of the ruthenium complex **1**/graphene/glass was still greater than 85% in visible light region (**Figure 2.8a**). The change of I_{DS} was negligible with regard to the wavelengths under the incident light with a similar intensity (**Figure 2.8b**).

Figure 2.9a shows the photoresponse of the ruthenium complex **1**/graphene devices at $V_G = 0$ V. A pronounced change in the current was observed under the on/off switching of illumination. In addition, I_{DS} in pure pyrene-functionalized graphene FET devices did not exhibit any noticeable change under optical illumination,^[26] indicating that the ruthenium moiety in complex **1** plays a key role in the photoresponse. The ruthenium complex **1**/graphene device exhibited *n*-type characteristics at $V_G = 0$ V. The density of charge carriers (electrons) in the channel increased as more electrons were injected from ruthenium complex **1** to the graphene under optical illumination, leading to the increase in I_{DS} .

When the ruthenium complex **1** is illuminated, ground-state electrons are promoted to an excited state via the MLCT, which is termed an MLCT excited state. These electrons are then injected into the graphene. It is noteworthy that such charge transfer was highly efficient even with the ultrathin (approximately 4-nm-thick) film of ruthenium complex **1**. The Ru^{2+} is oxidized to Ru^{3+} upon absorption of light, and the resulting holes are trapped in the ruthenium complex **1** on the surface of the graphene. The photogenerated electrons are injected into the graphene, and drift to the drain electrode due to the applied bias V_{DS} over the drift time, $\tau_{transit}$. Electrons from the source electrode fill the vacancies formed by the electron drift. If the lifetime of the photo-excited charge separation state ($Ru^{3+} - e^-$) is sufficiently long, the drift electrons will recirculate in the circuit to provide multiple electrons per single incident photon.

The photoconductive gain is given by $G = \eta\tau_{lifetime}/\tau_{transit}$, where η is the quantum efficiency and $\tau_{lifetime}$ is the lifetime of photo-excited charge separation state (indicating the importance of long lifetime and high carrier mobility). The power of the laser was 0.3 mW cm^{-2} , and the wavelength was 450 nm, which gives a photon flux of $\Phi_{photon} = 6.6 \times 10^{14} \text{ cm}^{-2}\text{s}^{-1}$, and led to a shift of V_{Dirac} by 4 V (see **Figure 2.5b**). For 300-nm-thick SiO_2 , the captured photoinduced charge density was $1.36 \times 10^{11} \text{ cm}^{-2}\text{s}^{-1}$, which gives $\eta \approx 0.021\%$. The responsivity can be calculated from

$$R = \frac{\Delta I_{DS}}{WLE} \quad (2)$$

where E is the intensity of the incident light and ΔI_{DS} is the difference between the current under optical illumination and the dark current.⁴⁴ The responsivity as a function of the gate voltage is shown in **Figure 2.9b**, and the maximum responsivity of $\sim 1 \times 10^5 \text{ A/W}$ was obtained at $V_G = -65 \text{ V}$.

Figure 2.10a and **b** show the time response of the photocurrent for the ruthenium complex **1**/graphene photodetectors as the polychromatic illumination is turned on and off. The dynamic response of the device under illumination can be described by

$$I(t) = I_{\text{dark}} + A[\exp(t/\tau_1)] \quad (3)$$

$$I(t) = I_{\text{dark}} + A[\exp(-t/\tau_1)] + B[\exp(-t/\tau_2)] \quad (4)$$

where t is time, τ_1 and τ_2 are time constants, I_{dark} is the dark current, and A and B are scaling constants.²⁸ In **Figure 2.10a** and **b**, the black squares correspond to the experimental results and the red curve represents a fit to equations (3) and (4). The time constants for growth and decay of the photocurrent can be estimated from fits to these expressions. The time constant for the growth of the photocurrent was $\tau_1 = 2.8$ s, which is related to the diffusion time of photogenerated electrons from the interface of the graphene into the channel. Electron injection from ruthenium polypyridyl complexes into TiO_2 is very fast (on a sub-picosecond timescale).^[60] Karousis *et al.* reported an electron injection rate of $1.95 \times 10^{10} \text{ s}^{-1}$ from ZnPc to graphene in a zinc phthalocyanine–graphene hybrid material.^[61] We can therefore deduce that the electron injection rate from ruthenium complex **1** to graphene is faster than the time resolution of the experiment. The ruthenium complex **1**/graphene photodetectors showed a fast initial decay, where the photocurrent dropped in the first 2.0 s ($\tau_1 = 2.0$ s) after the illumination was turned off, and a further photocurrent decay process that lasted for 20 s ($\tau_2 = 20$ s), during which the current decreased to the dark current level. The drift time of carriers (τ_{transit}) in the channel is inversely proportional to the carrier mobility, i.e.,

$$\tau_{\text{transit}} = \frac{L^2}{\mu_{\text{FE}} V_{\text{DS}}} \quad (5)$$

where μ_{FE} is the charge carrier mobility and L is the channel length.^[37] the τ_{transit} was approximately 1.5×10^{-9} s. Thus, the photoconductive gain is estimated to be $\sim 3 \times 10^6$.

To the best of our knowledge, a gain of the order of 10^6 and a responsivity of the order of 10^5 are the highest reported for graphene-based photodetectors with an optical intensity of the order of sub-milliwatts. The responsivity of the PbS QD/graphene device described in Ref. 44 was approximately 10^3 AW^{-1} at a similar incident light intensity (\sim sub-milliwatts).

Photodetectors based on graphene functionalized with a photoactive layer can achieve ultrahigh responsivities. The largest reported responsivities ($\sim 10^7 \text{ AW}^{-1}$) for hybrid graphene–QD photodetectors were achieved by coating PbS QDs films with a thickness of 80 nm^[43] or 150 nm^[44] on the surface of graphene under an ultralow incident light intensity (pW \sim fW). The responsivity of the PbS QD/graphene device was approximately 10^3 AW^{-1} at an incident light intensity of the order of sub-milliwatts. In our work, graphene hybrid photodetector functionalized with ruthenium complex **1** exhibited an ultrahigh responsivity of $\sim 1 \times 10^5 \text{ AW}^{-1}$ and a photoconductive gain of $\sim 3 \times 10^6$ under incident optical intensity of the order of sub-milliwatts. We attribute the ultrahigh photoresponsivity of our devices to the long lifetime of photoexcited charge carriers, which are effectively separated at the interface between the ruthenium complex **1** and graphene ($\text{Ru}^{3+} - \text{e}^-$) and thus charge transport effectively takes place until recombination occurs, as well as to the high carrier mobility of the active layer. Furthermore, the responsivity of our devices was dependent only on the intensity of the incident

light, and its dependence on the wavelength of the incident light could be negligible because a higher transmittance was remained after graphene was functionalized with 4-nm-thick ruthenium complex. The non-covalent functionalization of graphene with the ruthenium complex **1** is found to improve the electrical properties of graphene owing to the strong n-type doping effect via MLCT. In addition, our devices exhibit an ultrahigh responsivity over a broad range of wavelengths, from ultraviolet to visible ranges.

2.4. Conclusion

We have demonstrated monolayer graphene-based FET-type photodetectors with an ultrahigh responsivity of $\sim 1 \times 10^5 \text{ AW}^{-1}$ and a photoconductive gain of $\sim 3 \times 10^6$ at milliwatt optical intensities. Graphene-based photodetectors were functionalized using a 4-nm-thick photoactive ruthenium complex, which resulted in the generation of electron-hole pairs with long lifetime. Our approach does not destroy the favorable electrical and optical properties of monolayer graphene, i.e., both the electron and hole mobilities further increased by functionalization with the photoactive compound, while maintaining the high optical transparency of monolayer graphene. Under illumination, the graphene-ruthenium complex hybrid phototransistors exhibited substantially enhanced electron current owing to the pronounced n-type doping effect engendered by electron transfer via MLCT from the ruthenium complex to graphene. The developed methodology opens a viable way for enhancing the photoresponsivity of graphene-based FET-type photodetectors, and can be extended to various state-of-the-art photodetector platforms that are based on π -conjugated photoactive materials including organic small molecules, polymers, and carbon nanotubes.

2.5. References

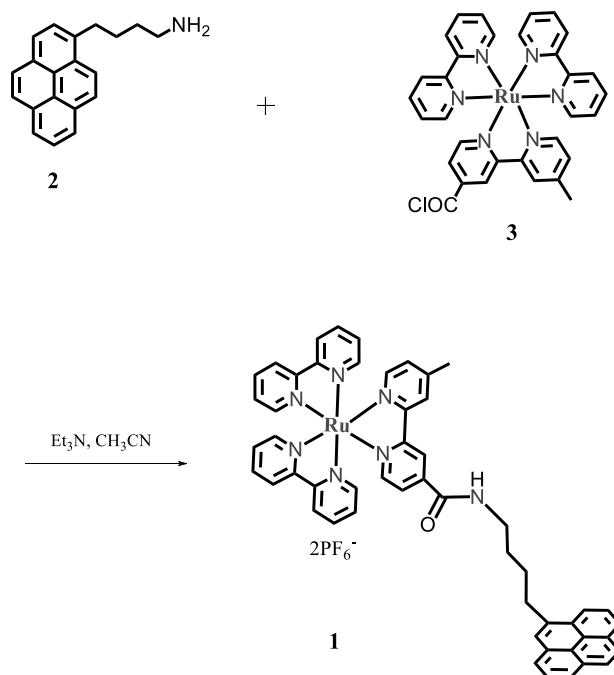
- [1] K. S. Novoselov, A. K. Geim, S. V. Morozov, D. Jiang, Y. Zhang, S. V. Dubonos, I. V. Grigorieva, A. A. Firsov, *Science* **2004**, *306*, 666.
- [2] K. S. Novoselov, A. K. Geim, S. V. Morozov, D. Jiang, M. I. Katsnelson, I. V. Grigorieva, S. V. Dubonos, A. A. Firsov, *Nature* **2005**, *438*, 197.
- [3] Y. B. Zhang, Y. W. Tan, H. L. Stormer, P. Kim, *Nature* **2005**, *438*, 201.
- [4] A. K. Geim, *Science* **2009**, *324*, 1530.
- [5] A. N. Grigorenko, M. Polini, K. S. Novoselov, *Nat. Photon.* **2012**, *6*, 749.
- [6] C. Lee, X. Wei, J. Kysar, J. Hone, *Science* **2008**, *321*, 385.
- [7] A. A. Balandin, S. Ghosh, W. Z. Bao, I. Calizo, D. Teweldebrhan, F. Miao, C. N. Lau, *Nano Lett.* **2008**, *8*, 902.
- [8] S. J. Park, R. S. Ruoff, *Nat. Nanotech.* **2009**, *4*, 217.
- [9] K. I. Bolotin, K. J. Sikes, Z. Jiang, M. Klima, G. Fudenberg, J. Hone, P. Kim, and H. L. Stormer, *Solid State Commun.* **2008**, *146*, 351.
- [10] R. R. Nair, P. Blake, A. N. Grigorenko, K. S. Novoselov, T. J. Booth, T. Stauber, N. M. R. Peres, A. K. Geim, *Science* **2008**, *320*, 1308.
- [11] J. H. Chen, C. Jang, S. D. Xiao, M. Ishigami, M. S. Fuhrer, *Nature Nanotech.* **2008**, *3*, 206.
- [12] K. S. Kim, Y. Zhao, H. Jang, S. Y. Lee, J. M. Kim, K. S. Kim, J. H. Ahn, P. Kim, J. Y. Choi, B. Hee. Hong, *Nature* **2009**, *457*, 706.

- [13] J. B. Wu, M. Agrawal, H. A. Becerril, Z. A. Bao, Z. F. Liu, Y. S. Chen, P. Peumans, *ACS Nano* **2010**, *4*, 43.
- [14] X. Wang, L. Zhi, K. Müllen, *Nano Lett.* **2008**, *8*, 323.
- [15] H. L. Wang, L. F. Cui, Y. Yang, H. S. Casalongue, J. T. Robinson, Y. Y. Liang, Y. Cui, H. J. Dai, *J. Am. Chem. Soc.* **2010**, *132*, 13978.
- [16] G. H. Yu, L. B. Hu, N. Liu, H. L. Wang, M. Vosgueritchian, Y. Yang, Y. Cui, Z. A. Bao, *Nano Lett.* **2011**, *11*, 4438.
- [17] S. H. Chae, W. J. Yu, J. J. Bae, D. L. Duong, D. Perello, H. Y. Jeong, Q. H. Ta, T. H. Ly, Q. A. Vu, M. Yun, X. F. Duan, Y. H. Lee, *Nature Mater.* **2013**, *12*, 403.
- [18] O. S. Kwon, S. J. Park, J. Y. Hong, A. R. Han, J. S. Lee, J. S. Lee, J. H. Oh, J. Jang, *ACS Nano* **2012**, *6*, 1486.
- [19] X. R. Wang, X. L. Li, L. Zhang, Y. K. Yoon, P. K. Weber, H. L. Wang, J. Guo, H. J. Dai, *Science* **2009**, *324*, 768.
- [20] W. J. Yu, L. Liao, S. H. Chae, Y. H. Lee, X. F. Duan, *Nano Lett.* **2011**, *11*, 4759.
- [21] D. V. Kosynkin, A. L. Higginbotham, A. Sinitskii, J. R. Lomeda, A. Dimiev, B. K. Price, J. M. Tour, *Nature* **2009**, *458*, 872.
- [22] J. W. Bai, X. Zhong, S. Jiang, Y. Huang, X. F. Duan, *Nature Nanotech.* **2010**, *5*, 190.
- [23] Y. B. Zhang, T. T. Tang, C. Girit, Z. Hao, M. C. Martin, A. Zettl, M. F. Crommie, Y. R. Shen, F. Wang, *Nature* **2009**, *459*, 820.
- [24] J. Park, M. Yan, *Acc. Chem. Res.* **2013**, *46*, 181.
- [25] V. Georgakilas, M. Otyepka, A. B. Bourlinos, V. Chandra, N. D. Kim, K. C. Kemp, P. Hobza, R. Zboril, K. S. Kim, *Chem. Rev.* **2012**, *112*, 6156.
- [26] M. Kim, N. S. Safron, C. S. Huang, M. S. Arnold, P. Gopalan, *Nano Lett.* **2012**, *12*, 182.
- [27] A. R. Jang, E. K. Jeon, D. W. Kang, G. W. Kim, B. S. Kim, D. J. Kang, H. S. Shin, *ACS Nano* **2012**, *6*, 9207.
- [28] B. Chitara, L. S. Panchakarla, S. B. Krupanidhi, C. N. R. Rao, *Adv. Mater.* **2011**, *23*, 5419.
- [29] M. Freitag, T. Low, P. Avouris, *Nano Lett.* **2013**, *13*, 1644.
- [30] Manga, K. K. *et al.* High-Performance Broadband Photodetector Using Solution-Processible PbSe–TiO₂–Graphene Hybrids. *Adv. Mater.* **24**, 1697–1702 (2012).
- [31] L. Vicarelli, M. S. Vitiello, D. Coquillat, A. Lombardo, A. C. Ferrari, W. Knap, M. Polini, V. Pellegrini, A. Tredicucci, *Nature Mater.* **2012**, *11*, 865.
- [32] A. Urich, K. Unterrainer, T. Mueller, *Nano Lett.* **2011**, *11*, 2804.
- [33] Y. Liu, R. Cheng, L. Liao, H. L. Zhou, J. W. Bai, G. Liu, L. X. Liu, Y. Huang, X. F. Duan, *Nature Commun.* **2011**, *2*, 579.
- [34] M. Furchi, A. Urich, A. Pospischil, G. Lilley, K. Unterrainer, H. Detz, P. Klang, A. M. Andrews, W. Schrenk, G. Strasser, T. Mueller, *Nano Lett.* **2012**, *12*, 2773.
- [35] F. N. Xia, T. Mueller, Y. M. Lin, A. V. Garcia, P. Avouris, *Nature Nanotech.* **2009**, *4*, 839.
- [36] K. K. Manga, S. Wang, M. Jaiswal, Q. L. Bao, K. P. Loh, *Adv. Mater.* **2010**, *22*, 5265.
- [37] Y. Z. Zhang, T. Liu, B. Meng, X. H. Li, G. Z. Liang, X. N. Hu, Q. J. Wang, *Nature Commun.* doi:10.1038/ncomms2830.
- [38] H. Chang, H. Wu, *Adv. Funct. Mater.* **2013**, *23*, 1984.
- [39] Q. Bao, K. Loh, *ACS Nano* **2012**, *6*, 3677.
- [40] F. Bonaccorso, Z. Sun, T. Hasan, A. Ferrari, *Nature Photon.* **2010**, *4*, 611.
- [41] F. Schwierz, *Nature Nanotech.* **2010**, *5*, 487.
- [42] T. Mueller, F. Xia, P. Avouris, *Nature Photon.* **2010**, *4*, 297.
- [43] G. Konstantatos, M. Badioli, L. Gaudreau, J. Osmond, M. Bernechea, F. P. Garcia de Arquer, F. Gatti, F. H. L. Koppens, *Nature Nanotech.* **2012**, *7*, 363.
- [44] Z. H. Sun, Z. K. Liu, J. H. Li, G. A. Tai, S. P. Lau, F. Yan, *Adv. Mater.* **2012**, *24*, 5878.
- [45] F. Li, B. B. Zhang, X. N. Li, Y. Jiang, L. Chen, Y. Q. Li, L. C. Sun, *Angew. Chem. Int. Ed.* **2011**, *50*, 12276.
- [46] A. Mukherji, B. Seger, G. Lu, L. Wang, *ACS Nano* **2011**, *5*, 3483.
- [47] J. Zhang, J. Yu, M. Jaroniec, J. Gong, *Nano Lett.* **2012**, *12*, 4584.
- [48] Z. K. Liu, J. H. Li, Z. H. Sun, G. A. Tai, S. P. Lau, F. Yan, *ACS Nano* **2012**, *6*, 810.

- [49] A. R. Jang, E. K. Jeon, D. W. Kang, G. W. Kim, B. S. Kim, D. J. Kang, H. S. Shin, *ACS Nano* **2012**, *6*, 9207.
- [50] J. L. Kan, Y. L. Chen, D. D. Qi, Y. Q. Liu, J. Z. Jiang, *Adv. Mater.* **2012**, *24*, 1755.
- [51] Y. N. Gao, P. Ma, Y. L. Chen, Y. Zhang, Y. Z. Bian, X. Y. Li, J. Z. Jiang, C. Q. Ma, *Inorg. Chem.* **2009**, *48*, 45.
- [52] W. Liu, B. Y. L. Jackson, J. Zhu, C. Q. Miao, C. H. Chung, Y. J. Park, K. Sun, J. Woo, Y. H. Xie, *ACS Nano* **2010**, *4*, 3927.
- [53] T. B. Singh, R. Koeppel, N. S. Sariciftci, M. Morana, C. J. Brabec, *Adv. Funct. Mater.* **2009**, *19*, 789.
- [54] X. S. Li, W. W. Cai, J. H. An, S. Y. Kim, J. H. Nah, D. X. Yang, R. Piner, A. Velamakanni, I. Jung, E. Tutuc, S. K. Banerjee, L. Colombo, R. S. Ruoff, *Science* **2009**, *324*, 1312.
- [55] C. Mattevi, H. Kim, M. Chhowalla, *J. Mater. Chem.* **2011**, *21*, 3324.
- [56] A. C. Ferrari, J. C. Meyer, V. Scardaci, C. Casiraghi, M. Lazzeri, F. Mauri, S. Piscanec, D. Jiang, K. S. Novoselov, S. Roth, and A. K. Geim, *Phys. Rev. Lett.* **97**, 187401 (2006).
- [57] A. Das, S. Pisana, B. Chakraborty, S. Piscanec, S. K. Saha, U. V. Waghmare, K. S. Novoselov, H. R. Krishnamurthy, A. K. Geim, A. C. Ferrari, A. K. Sood, *Nature Nanotech.* **2008**, *3*, 210.
- [58] P. Wei, J. H. Oh, G. Dong, Z. Bao, *J. Am. Chem. Soc.* **2010**, *132*, 8852.
- [59] J. H. Oh, P. Wei, Z. Bao, *Appl. Phys. Lett.* **2010**, *97*, 243305.
- [60] C. A. Kelly, G. J. Meyer, *Coord. Chem. Rev.* **2001**, *211*, 295.
- [61] N. Karousis, J. Ortiz, K. Ohkubo, T. Hasobe, S. Fukuzumi, A. S. Santos, N. Tagmatarchis, *J. Phys. Chem. C* **2012**, *116*, 20564.
- [62] T. J. Dale, J. R. Jr, *J. Am. Chem. Soc.* **2006**, *128*, 4500.
- [63] B. M. Peck, G. T. Ross, S. W. Edwards, G. J. Meyer, B. W. Erickson, *Int. J. Pept. Protein. Res.* **1991**, *38*, 114.
- [64] A. Johansson, M. Abrahamsson, A. Magnuson, P. Huang, J. Mårtensson, S. Styring, L. Hammarström, L. C. Sun, B. Åkermark, *Inorg. Chem.* **2003**, *42*, 7502.

Reprinted in part with permission from E. K. Lee, *et al.*, *Small* **2014, *10*, 3700-3706 Copyright ©

2014 WILEY-VCH Verlag GmbH & Co. KGaA, Weinheim



Scheme 2.1. Synthetic procedure for ruthenium complex **1**.

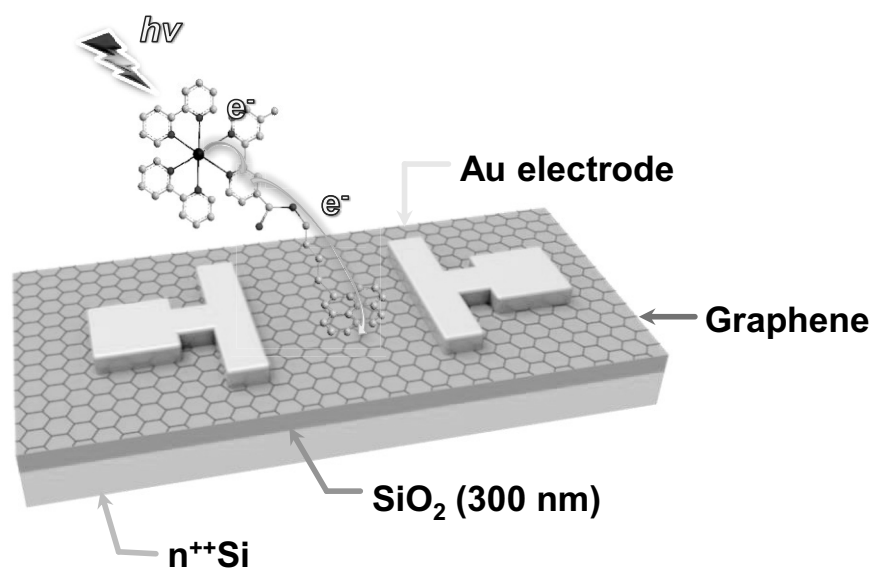


Figure 2.1. Chemical structure of ruthenium complex **1** and schematic depiction of graphene-ruthenium complex hybrid FET-type photodetector. In the chemical structure of complex **1**: H atoms were omitted and C, N, O, Ru atoms were represented by gray, blue, light-red and dark-red balls. For clarity, the scale of complex **1** is enlarged compared to graphene.

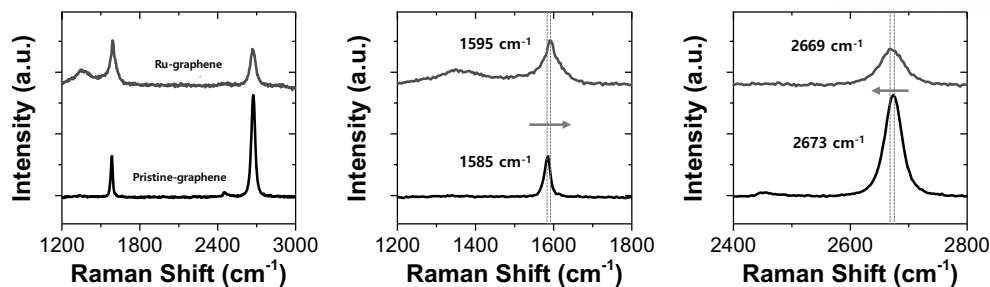


Figure 2.2. Raman spectra of graphene/SiO₂/Si (Bottom) and ruthenium compound **1**/graphene/SiO₂/Si (Top). The Raman spectra were excited at 532 nm with an incident power < 1 mW (Laser spot diameter was 500 nm).

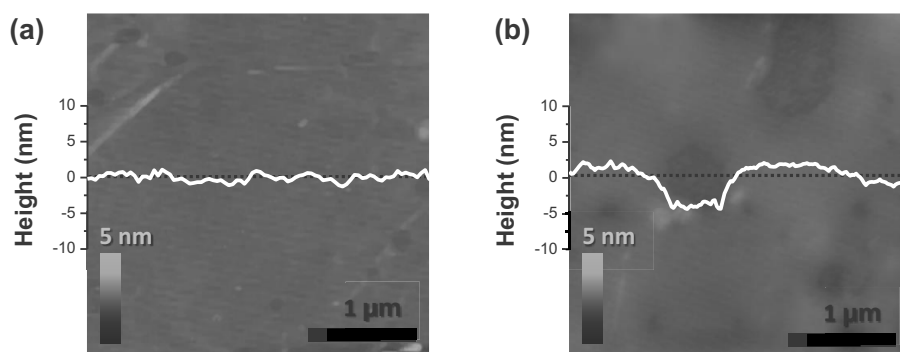


Figure 2.3. AFM height and surface profile (white line) along the black dotted line: (a) pristine graphene/SiO₂/Si. (b) ruthenium complex **1**/graphene/SiO₂/Si.

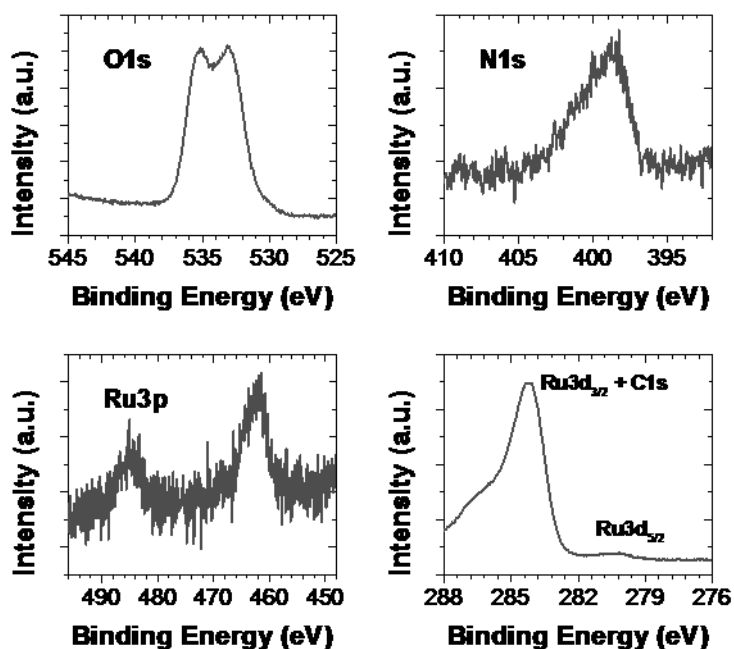


Figure 2.4. XPS spectra of ruthenium compound **1**/graphene/SiO₂/Si ($h\nu = 1486.6$ eV). Some of the characteristic peaks are marked (O1s, N1s, C1s, Ru3p and Ru3d). The Ru3d_{3/2} peak is merged with the C1s emission.

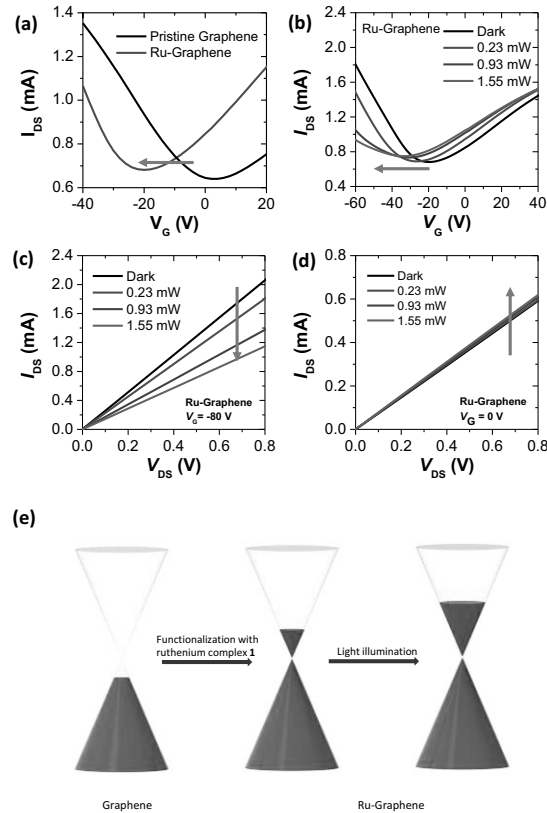


Figure 2.5. Current-voltage characteristics and energy level change of ruthenium complex 1/graphene FET device. (a) Transfer characteristics of pristine graphene and ruthenium complex 1/graphene devices ($V_{DS} = 1$ V) under dark condition. (b) Transfer characteristics under dark and polychromatic incident light with different intensities ($V_{DS} = 1$ V). (c) Output characteristics coupled with light illumination under hole-enhancement mode ($V_G = -80$ V). (d) Output characteristics coupled with light illumination without applying gate field ($V_G = 0$ V). (e) Energy level changes of pristine graphene upon functionalization with ruthenium complex 1 and optical illumination.

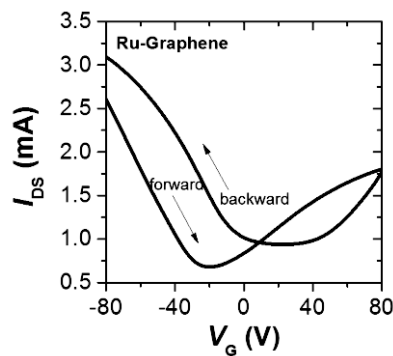


Figure 2.6. Hysteresis of ruthenium complex 1/graphene device under vacuum ($\sim 10^{-5}$ torr).

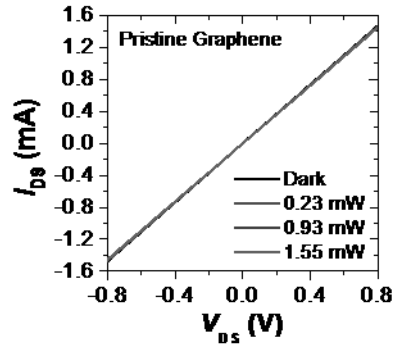


Figure 2.7. Current–voltage characteristics. I_{DS} - V_{DS} characteristics of pristine graphene device using incident light with different intensities under vacuum ($\sim 10^{-5}$ Torr) ($V_G = -80$ V).

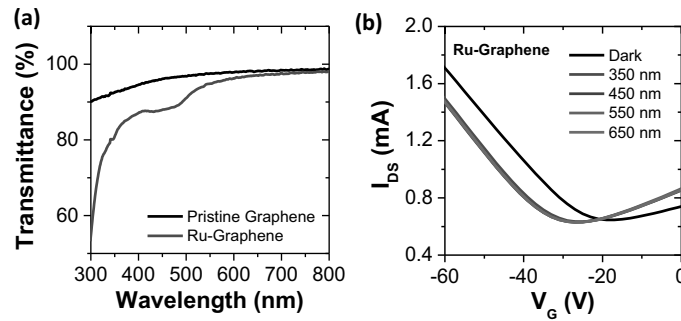


Figure 2.8. (a) UV-vis spectra of pristine graphene/glass and ruthenium 1/graphene/glass. (b) Transfer characteristics (I_{DS} - V_G) ($V_{DS} = 1$ V) under dark and monochromatic light illumination with different wavelengths (0.15 ~ 0.16 mW).

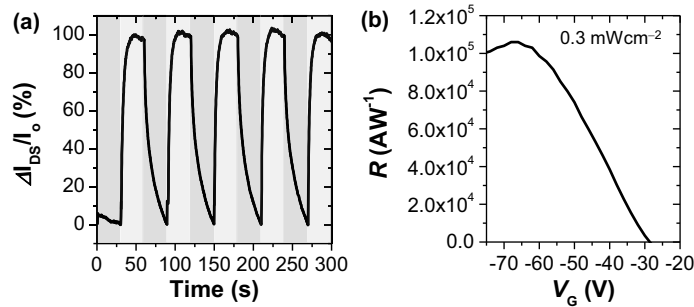


Figure 2.9. Photoresponse. (a) Normalized current response of graphene-ruthenium complex hybrid photodetectors upon on/off switching of illumination ($V_{DS} = 1$ V; $V_G = 0$ V; Irradiation: polychromatic light of 0.93 mW). (b) Responsivity as a function of gate voltage (the wavelength of incident light: $\lambda = 450$ nm).

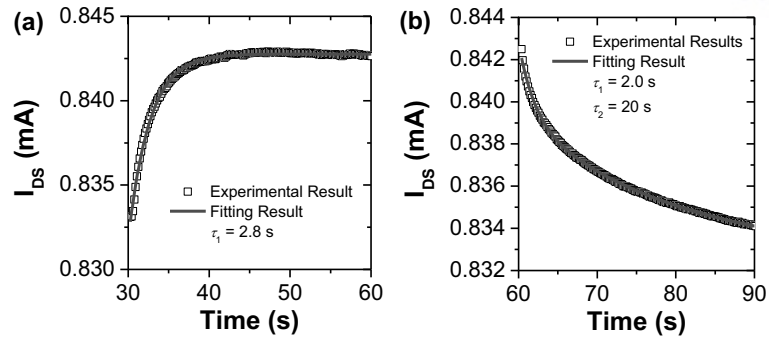


Figure 2.10. Time response of photocurrent growth and decay for graphene-ruthenium complex hybrid photodetectors. (a) Photocurrent growth upon illumination. (b) Photocurrent decay after turning off the light. $V_{DS} = 1$ V; $V_G = 0$ V.

Chapter 3. Flexible Organic Phototransistor Array with Enhanced Responsivity via Metal-Ligand Charge Transfer

3.1. Introduction

Organic semiconductors are of great interest as active materials for electronic and photonic devices because of their ease of synthesis and property tunability through molecular design and engineering. In particular, their ability to selectively absorb a variety of light wavelengths from the ultraviolet to near-infrared has inspired the development of organic light detecting electronic devices, such as photodiodes and phototransistors as alternatives to inorganic systems.^[1-11] Phototransistors have three terminal configurations, i.e., source, drain and gate, while photodiodes have two terminal configurations, i.e., anode and cathode. Phototransistors typically exhibit higher responsivity than photodiodes because the current generated by photons is amplified by gate voltage modulation without increasing noise.^[7, 12] Mass production, simple fabrication, and ease of functional modification of organic semiconductors and long-term stability in ambient condition must be achieved in order to further the applications of optoelectronic devices.^[8, 10, 13]

Ruthenium complexes have received great attention as a photosensitizer in dye-sensitized solar cells (DSSCs).^[14-18] Their photoelectrochemical properties and high stability in the oxidized state have led to power conversion efficiency over 12 % in DSSCs.^[19] In spite of their high photoelectrochemical properties, there is few report that utilized ruthenium complexes for phototransistors.^[20] On the other hand, we recently investigated photogenerated charge carrier dynamics of organic phototransistors based on single-crystalline nanowires self-assembled from *N,N'*-bis(2-phenylethyl)-perylene-3,4:9,10-tetracarboxylic diimide (BPE-PTCDI), which is an air-stable *n*-type semiconductor.^[12, 21] Single BPE-PTCDI nanowire phototransistors exhibited much higher external quantum efficiency (EQE), compared with a thermally evaporated BPE-PTCDI film. This behavior was attributed to the intrinsically defect-free, single-crystalline feature of the nanowires.^[12, 22] However, preformed organic nanowires cannot be easily integrated into a desired circuitary because of the difficulty in the alignment control of individual wires. On the other hand, an evaporated BPE-PTCDI film had a relatively poor EQE compared with single-crystalline nanowires. Thus, single component system using either BPE-PTCDI nanowires or evaporated BPE-PTCDI films could not fully satisfy practical, large-scale device applications.

Although organic phototransistors based on organic small molecules have often been reported, their photoresponsivity was not enough for commercialization, in comparison with inorganic counterparts.^[7, 8, 23-25] Therefore, widely available materials for the fabrication of high-performance phototransistors are acutely needed in order to further the practical applications of organic optoelectronic devices. Possible routes include the fabrication of donor-acceptor bulk heterojunction systems^[26] and the

incorporation of secondary materials such as quantum dots,^[27] graphene,^[28] and organic dye molecules^[29] in the base films as light absorbers or charge transport media.

We report herein the fabrication of high-performance phototransistors using a BPE-PTCDI thin-film and a solution-processable transition metal complex, i.e., ruthenium complex **1** (Ru-complex **1**, see Figure 3.1 for its chemical structure). The BPE-PTCDI thin film was thermally evaporated over a large area (up to $2.5 \times 2.5 \text{ cm}^2$) on a silicon wafer and a transparent polyimide (PI) substrate and the Ru-complex **1** was simply drop-cast from an environmentally benign aqueous solution onto the thin film. The Ru-complex **1** is attached to the BPE-PTCDI film via non-covalent functionalization of the pyrene moieties that promote interaction between BPE-PTCDI and Ru-complex **1**. This approach significantly enhanced the air-stability and the photoresponsivity of the phototransistor via metal-ligand charge transfer (MLCT). In addition, we fabricated a large 10×10 phototransistor array on a transparent PI substrate, which showed well-defined distinct light mapping. The fabricated phototransistor array was highly flexible, twistable and worked well under tensile and compressive strains. Our findings suggest that application of solution-processable charge transfer complexes in film-based optoelectronics could provide an effective and economical route to the large-area manufacturing of wearable organic optoelectronic devices.

3.2. Experimental Section

All starting materials were purchased either from Sigma-Aldrich or Acros and used without further purification. All solvents were ACS grade unless otherwise noted. The thickness of SiO_2 was 300 nm. A Tunable Light Source Model TLS-300X (Newport) was used to generate the monochromatic incident light. The spot size was 800 μm . AFM images were recorded in high-resolution tapping mode under ambient conditions. An Agilent 5500 scanning probe microscope running with a Nanoscope-V controller was used to obtain AFM images. All of the I - V characteristics were measured with a Keithley 4200-SCS in ambient condition. Bending stage was run with a programmable motion controller, PMC-1HS from Autonics.

Fabrication of Ru-complex 1-modified BPE-PTCDI phototransistor on SiO_2/Si wafer: Ru-complex **1** was synthesized by following the reported procedure.¹⁹ Heavily n -doped Si wafers ($<0.004 \Omega \text{ cm}$) with a thermally grown 300 nm-thick oxide layer (SiO_2 , $C_g = 10 \text{ nF cm}^{-2}$) were cleaned with Piranha (H_2SO_4 and H_2O_2 with volume ratio of 7:3) solution. The SiO_2/Si substrates were sequentially modified by UV-ozone treatment. The SiO_2 surface was treated with OTS as self-assembled monolayer. The OTS solution (3 mM) prepared in trichloroethylene was spin-coated onto the wafers at 3000 rpm for 30 s, and then the wafers were placed overnight in a vacuum desiccator with ammonia vapor. The wafers were sequentially washed with toluene, acetone, and isopropyl alcohol, followed by drying under the gentle flow of nitrogen gas. The contact angle of DI water on the OTS-treated wafer was approximately 110° . 30-nm-thick BPE-PTCDI thin film was thermally deposited on the SiO_2/Si substrate at a substrate

temperature of 110 °C. The prepared Ru-complex solution (0.1 mg mL⁻¹ in water) was coated on the fabricated device, and dried at room temperature in nitrogen atmosphere for 1 day. Finally, source and drain electrodes (Au/Cr, 40/4 nm) were thermally deposited through a shadow mask.

Fabrication of Ru-complex 1-modified BPE-PTCDI phototransistor on a transparent PI substrate: A transparent PI precursor vanish was purchased from FAFNIE in Korea. The PI vanish was drop-coated on a pre-cleaned glass substrate and annealed up to 300 °C with a ramping speed of temperature, 20 °C h⁻¹ in nitrogen atmosphere. Au/Cr gate electrode (40/4 nm) was thermally evaporated through a shadow mask. SU-8 2000 dielectric solution diluted with γ -butylactone (20 wt%) was spin-coated on the substrate, and then annealed at 65 °C for 2 min and at 95 °C for 2 min, sequentially. UV light (25 mWcm⁻²) was exposed to the substrate for 10 s. 30-nm-thick BPE-PTCDI thin film was thermally deposited on the SU-8 dielectric at a substrate temperature of 95 °C. The prepared Ru-complex solution was coated on the fabricated device, and dried at room temperature in nitrogen atmosphere for 1 day. Finally, source and drain electrodes (Au/Cr, 40/4 nm) were thermally deposited through a shadow mask.

3.3. Results and Discussion

Fabrication of Ru-complex 1-modified BPE-PTCDI film phototransistors

Ru-complex **1** was obtained by transforming the PF₆⁻ ligand of its precursor to Cl⁻. This made complex **1** water-soluble.^[20] The ruthenium precursor was prepared according to the reported method.^[20] Figure 3.1 presents a schematic diagram of the Ru-complex **1**-modified BPE-PTCDI film phototransistor having a bottom-gate/top-contact configuration. A 30-nm-thick film of BPE-PTCDI was vacuum-deposited at a rate of ca. 0.1–0.2 Å s⁻¹ under a pressure of ca. 1 × 10⁻⁶ Torr onto an *n*-octadecyltriethoxysilane (OTS)-treated SiO₂/Si substrate held at 125 °C. The Ru-complex **1** (0.1 mg mL⁻¹ in water) was added dropwise onto the surface of the BPE-PTCDI film and kept overnight to form a uniform film using non-covalent functionalization between pyrene moieties and BPE-PTCDI basal planes. After drying at room temperature in a nitrogen atmosphere for 24 h, gold electrodes (40-nm-thick) were thermally evaporated onto the Ru-complex **1**-modified BPE-PTCDI film using a shadow mask to form the source and drain electrodes. The width-to-length ratio (*W/L*) of the shadow mask's channel was 20 (*W* = 1000 μm, *L* = 50 μm). Figure 3.2a shows the ultraviolet–visible (UV-Vis) spectra of Ru-complex **1**, the pristine BPE-PTCDI film, and the Ru-complex **1**-modified BPE-PTCDI film. Absorption maxima were observed at 617 and 627 nm for the pristine BPE-PTCDI and Ru-complex **1**-modified BPE-PTCDI films, respectively. The maximum absorption band of the Ru-complex **1**-modified BPE-PTCDI film was red-shifted compared with that of the pristine BPE-PTCDI film. This shift was attributed to π – π stacking between perylene group in BPE-PTCDI and pyrene group in the Ru-complex **1**.^[30–32] Such stacking is similar to that observed between graphene and carbon nanotubes containing polyaromatic rings.^[33–36] The absorption spectrum of the Ru-complex **1**-modified BPE-

PTCDI film was a combination of those of Ru-complex **1** and pristine BPE-PTCDI. The metal-to-ligand charge transfer (MLCT) absorption band of the Ru-complex **1** film appeared at 466 nm, which nearly overlapped the 463-nm absorption band of the pristine BPE-PTCDI film and the Ru-complex **1**-modified BPE-PTCDI film. The absorption bands of the Ru-complex **1**-modified BPE-PTCDI film between 300 and 400 nm were similar to those of the Ru-complex **1** film and were thus assigned to ligand–center (LC) π - π transitions of Ru-complex **1**.

Analysis of Ru-complex **1 thin film**

Atomic force microscopy (AFM) images were collected at ten different locations to investigate the morphology of the photoactive channel. The pristine BPE-PTCDI film consisted of packed, large nanoflakes (Figure 3.2b). After drop-casting the Ru-complex **1**, the large nanoflakes became indistinct and the Ru-complex **1**-modified BPE-PTCDI film tended to be relatively uniform (Figure 3.2c). The thickness of the Ru-complex **1** film was ca. 10 nm, which was deduced from the average height (ca. 40 nm) of the cross-section of the Ru-complex **1**-modified BPE-PTCDI film/SiO₂/Si entity (Figure 3.3). In addition, the Ru-complex **1** partially formed nanogranular aggregates from their self-assemblies on the BPE-PTCDI film. Scanning electron microscopy (SEM) images of the pristine BPE-PTCDI (Figure 3.2d) and Ru-complex **1**-modified BPE-PTCDI films (Figure 3.2e) confirmed the large area coating of Ru-complex **1** on the BPE-PTCDI film. X-ray photoelectron spectroscopy (XPS) analyses yielded characteristic peaks for O (1s) (531.6 eV), N (1s) (400.0 eV), Ru (3d_{5/2}) (281.1 eV), and Ru (3d_{3/2}) + C (1s) (284.8 eV), which support the successful functionalization of Ru-complex **1** on the surface of the BPE-PTCDI film (Figure 3.4).

Electrical and optoelectrical properties of Ru-complex **1-modified BPE-PTCDI film devices**

Figure 3.5a and 3c show the transfer and output characteristics of the pristine BPE-PTCDI film devices, respectively. The field-effect transistor (FET) characteristics were measured at room temperature in air. In a typical *n*-channel operating mode, a positive gate bias induced the accumulation of electron carriers at the interface between active and dielectric layer. The field-effect mobility (μ) and threshold voltage (V_{th}) were determined from the slope and intercept of the linear plot of the square root of the drain-to-source current ($I_{DS}^{1/2}$) as a function of the gate voltage (V_{GS}) in the saturation regime using Equation (1) as follows

$$I_{DS} = \frac{WC_g\mu}{2L} (V_{GS} - V_{th})^2 \quad (1)$$

where C_g is the capacitance per unit area of the total dielectric layer and V_{th} is the threshold voltage. The maximum electron mobility of the pristine BPE-PTCDI film devices was $3.58 \times 10^{-2} \text{ cm}^2\text{V}^{-1}\text{s}^{-1}$ with a V_{th} of 5.2 V. From Figure 3.5b and 3d, we deduced that the maximum electron mobility of the Ru-complex **1**-modified BPE-PTCDI devices was $1.36 \times 10^{-2} \text{ cm}^2\text{V}^{-1}\text{s}^{-1}$ with a V_{th} of -12.65 V. The slightly

reduced electron mobility might originate from the solvent residues generated during the functionalization process of BPE-PTCDI film using Ru-complex **1** solution, which could act as charge traps. The Ru-complex **1**-modified BPE-PTCDI film devices showed a minimal hysteresis at the turn-on state, but exhibited a relatively larger hysteresis at the turn-off state which might come from impurities generated during the fabrication process (Figure 3.6). Because clear photocurrent behavior at ca. 450 nm originated from Ru-complex **1** (refer to UV-vis spectra in Figure 3.2a), photobehaviors of devices were characterized using 450 nm wavelength laser. The transfer I - V characteristics of pristine BPE-PTCDI and the Ru-complex **1**-modified BPE-PTCDI film devices were measured in the dark and at a wavelength of 450 nm with an incident light intensity of $1.5 \mu\text{Wcm}^{-2}$ (Figure 3.5e and 3f). For the Ru-complex **1**-modified BPE-PTCDI device, I_{DS} increased with increasing optical intensity because of the transfer of photo-generated electrons from Ru-complex **1** to BPE-PTCDI via MLCT. The device made from pristine BPE-PTCDI also exhibited a slightly increased I_{DS} that was attributed to the photo-exciton of BPE-PTCDI itself, for which the extent of the photoresponse was much lower than that of the Ru-complex **1**-modified BPE-PTCDI device.

Figure 3.7a shows the photoresponse of the Ru-complex **1**-modified BPE-PTCDI film devices as a function of time using different incident light intensities of 1.5, 30 and $100 \mu\text{Wcm}^{-2}$ at 450 nm ($V_{\text{GS}} = 0 \text{ V}$, $V_{\text{DS}} = 100 \text{ V}$). A pronounced change in the current was observed under on/off switching of the light. Furthermore, the photocurrent increased with increasing incident light intensity. When the Ru-complex **1** is illuminated, ground-state electrons are promoted to the MLCT excited state. These electrons are then injected into the BPE-PTCDI channel. The Ru^{2+} is oxidized to Ru^{3+} upon absorption of light and the resulting holes are trapped in the Ru-complex **1** on the surface of BPE-PTCDI. If the lifetime of the photo-excited charge separation state ($\text{Ru}^{3+} - \text{e}^-$) is sufficiently long, it will recirculate in the circuit to provide multiple electrons per single incident photon. The photoresponsivity (R) can be calculated from Equation (2) as follows^[37]

$$R = \frac{I_{\text{ph}}}{P_{\text{inc}}A} = \frac{I_{\text{light}} - I_{\text{dark}}}{P_{\text{inc}}A} \quad (2)$$

where I_{ph} is the photocurrent, P_{inc} is the incident light intensity on the channel of the device, I_{light} is the drain current under illumination, and I_{dark} is the drain current in the dark. A is the area of the transistor channel. The responsivity of pristine BPE-PTDCI and Ru-complex **1**-modified BPE-PTDCI as a function of the gate voltage is shown in Figure 3.7b. Photoresponsivities of 345, 3725 and 7230 AW^{-1} were obtained at $V_{\text{GS}} = -12.1$ (which is the threshold voltage of the device), 10 and 80 V for the Ru-complex **1**-modified BPE-PTDCI, respectively. The responsivity was raised by a factor of ca. 1000 times after coating of Ru-complex **1**. The EQE (η) is defined as the number of carriers circulating through a phototransistor per absorbed photon per unit area and is expressed by Equation (3) as follows^[37]

$$\eta = \frac{(I_{light} - I_{dark}) \hbar c}{e P_{inc} A \lambda} \quad (3)$$

where h is Planck's constant, c is the speed of light, e is the fundamental unit of charge, A is the area of the transistor channel, and λ is the wavelength of the incident light. Figure 3.8 shows the EQE of the Ru-complex **1**-modified BPE-PTCDI and pristine BPE-PTCDI devices as a function of V_{GS} . The EQE values of the Ru-complex **1**-modified BPE-PTCDI device were ca. 50000- and 3500-times higher than those of pristine BPE-PTCDI at $V_{GS} = 20$ and 80 V, respectively. This ultrahigh EQE was attributed to the long lifetime of the photo-induced excited-state ($\text{Ru}^{3+} - e^-$).

If the dark current is a major source of shot noise, then the detectivity (D^*) is expressed by Equation (4) as follows^[38]

$$D^* = \frac{J_{light}/P_{inc}}{\sqrt{2qJ_{dark}}} \quad (4)$$

where q is the electronic charge, P_{inc} is the incident light intensity, and J_{light} and J_{dark} are the corresponding light and dark current intensities. For the Ru-complex **1**-BPE-PTCDI device, the calculated detectivity was ca. 1.9×10^{13} Jones (1 Jone = $1 \text{ cm H}^{1/2}\text{W}^{-1}$) at a wavelength of 450 nm under $1.5 \mu\text{Wcm}^{-2}$ ($V_{GS} = 20$ V), which is comparable to the high detectivities obtained from other organic phototransistors.^[39-42]

Figure 3.7c and 4d show the time response of a photocurrent for the Ru-complex **1**/BPE-PTCDI phototransistor when a polychromatic illumination is turned on and off. The dynamic response of the phototransistor under the illumination can be described by Equation (5) and (6) for growth and decay, respectively:

$$I(t) = I_{dark} + Ae^{\left(\frac{t}{\tau_1}\right)} \quad (5)$$

$$I(t) = I_{dark} + Ae^{\left(-\frac{t}{\tau_1}\right)} + Be^{\left(-\frac{t}{\tau_2}\right)} \quad (6)$$

where t is time, τ_1 and τ_2 are time constants, I_{dark} is the dark current, and A and B are scaling constants.^[20, 21] The time constants for growth and decay of the photocurrent can be estimated from fits to these expressions. The time constant for the growth of the photocurrent was $\tau_1 = 0.12$ s, which is related to the diffusion time of photogenerated electrons from the interface of the BPE-PTCDI film into the channel. The Ru-complex **1**/graphene photodetectors showed a fast initial decay, where the photocurrent dropped in the first 0.17 s ($\tau_1 = 0.17$ s) after the illumination was turned off, and a further photocurrent decay process that lasted for 57 s ($\tau_2 = 57$ s), during which the current decreased to the dark current level.

Fabrication and characterization of 10×10 Ru-complex **1-modified BPE-PTCDI phototransistor array on a flexible substrate**

A 10×10 Ru-complex **1**-modified BPE-PTCDI phototransistor array was fabricated to establish the feasibility of creating Ru-complex **1** phototransistors using a polymer dielectric on a plastic substrate for flexible multi-array devices. Figure 3.9a shows a schematic illustration of the 10×10 Ru-complex **1** phototransistor array. Figure 3.9b is a detailed structure of a single phototransistor of the 10×10 device array. A transparent polyimide (PI) precursor was prepared on a glass substrate. The prepared PI thickness was 50 μm . Gate electrodes (Au/Cr, 40/4 nm) were defined by conventional photolithography on the transparent PI. SU-8 20 negative epoxy photoresist was diluted with γ -butyrolactone to 20 wt% and the solution was spin-coated onto the substrate. The sample was annealed at 65 $^{\circ}\text{C}$ for 2 min and at 95 $^{\circ}\text{C}$ for 2 min, consecutively. The substrate was then exposed to ultraviolet light (25 mWcm^{-2}) for 10 s and annealed at 95 $^{\circ}\text{C}$ for 5 min. This resulted in a SU-8 dielectric that was 35-nm-thick (Figure 3.10a) having a capacitance of 5 nFcm^{-2} (Figure 3.10b). A coating of BPE-PTCDI and the Ru-complex **1** (40 nm) was deposited as described previously. Finally, the source and drain (Au/Cr, 40/4 nm) were thermally deposited through a shadow mask ($W/L = 750/50 \mu\text{m}$). Figure 3.9c shows a photograph of the 10×10 phototransistor array on the PI substrate and optical image of single device layout (inset of Figure 3.9c). The size of the device including PI substrate was $2.5 \times 2.5 \text{ cm}^2$. A white background was visible through the fabricated transparent device except for small areas corresponding to the source, drain, and gate electrodes and interconnect lines (gold, 0.8% of the total device area).

A pristine BPE-PTCDI device was fabricated without Ru-complex **1** for comparison (Figure 3.11a). The devices showed clear field-effect behavior (Figure 3.11b). The calculated average electron mobilities across all 100 phototransistors in the dark and under illumination were $2.98 (\pm 0.30)$ and $3.01 (\pm 0.31) \times 10^{-2} \text{ cm}^2\text{V}^{-1}\text{s}^{-1}$. Additionally, the photocurrent was negligible under $1.5 \mu\text{Wcm}^{-2}$ of illumination (Figure 3.12b).

Figure 3.9d is typical 10 selected transfer curves of BPE-PTCDI functionalized with Ru-complex **1** on the above transparent PI substrate under illumination ($1.5 \mu\text{Wcm}^{-2}$) and in the dark. The average electron mobilities across all 100 phototransistors were $2.61 (\pm 0.31)$ and $1.49 (\pm 0.35) \times 10^{-2} \text{ cm}^2\text{V}^{-1}\text{s}^{-1}$, respectively. The drain currents were 8.12 and $3.21 \times 10^{-8} \text{ A}$ under illumination and in the dark, respectively, with an amplifying ratio of 2.53.

In order to characterize air stability of the Ru-complex **1**/BPE-PTCDI phototransistors on the PI substrate, the variation of electron mobility in ambient laboratory environment was observed (Figure 3.9e). The electron mobility was barely changed during 7 days. Statistically, all the 100 phototransistors remained the electron mobility by 90 % (± 4.2 %) after 7 days compared to the initial values. Although the device performance was slightly reduced, all the 100 devices survived in ambient condition. Because both BPE-PTCDI and Ru-complex **1** are stable in air,^[43-46] the synergistic combination of BPE-PTCDI and Ru-complex **1** might result in excellent ambient stability.

Figure 3.9f shows the drain current mapping at $V_{DS} = 3$ V, when a small light source (diameter, 2 mm) was incident to the center (column : row = 5 : 5) of the 10×10 Ru-complex **1**-modified BPE-PTCDI phototransistor array. The mapping demonstrated that the areas of the device receiving illumination were clearly discernible compared with the unexposed areas, which indicates that the environmentally benign, water-processable Ru-complex **1** is highly appropriate for use in large-area devices and transparent component systems using PI and SU-8 dielectric.^[47-51]

The flexibility is important for various applications, e.g., wearable, medical and military devices. The flexibility of the fabricated phototransistor devices modified with Ru-complex **1** was examined with respect to its bending cycles, bending radius, and twistability. Figure 3.13a shows photographs for the cases of tensile (top) and compressive (bottom) strain. A fabricated device was initially placed on the surface of the PI substrate. When it was bent upward, the device was under tensile strain, while when bent downward, it was under compressive strain (Inset of Figure 3.13b). Changes in electron mobility were noted after upward and downward bending for 6000 cycles over a 10-mm bending radius. No device performance degradation was found (Figure 3.13b). Additionally, the devices were twisted by up to 40° (Figure 3.13c), which demonstrated that our device was stable to twisting. Figure 3.13d shows the electron mobility change as a function of bending radius from 16 to 2 mm under illuminated and dark conditions. Tensile strain can be calculated by Equation (7) as follows

$$\varepsilon_{tensile} = \frac{t}{2R_0} \quad (7)$$

where $\varepsilon_{tensile}$ is the tensile strain, t is the thickness of the basal film, and R_0 is the radius from the center of the bending to the neutral line of the film. (See the detail in Figure 3.12). Our devices exhibited no significant change in mobility until 1.01% of the tensile strain ($2R_0 = 5$ mm). At higher tensile strain, i.e., 2.15 % ($2R_0 = 2$ mm), the mobility started to decrease under both illuminated and dark conditions. This was attributed to the increased strain experienced by the device components, i.e., the BPE-PTCDI, dielectric, and Ru-complex **1**.

3.4. Conclusion

A Ru-complex **1**-modified BPE-PTCDI phototransistor was fabricated by simple drop-casting of the transition metal complex. The resultant phototransistor exhibited a high photoresponsivity of ca. 3725 and 7230 AW^{-1} under an incident light intensity of $1.5 \mu\text{Wcm}^{-2}$ at $V_{GS} = 10$ and 80 V, respectively. Under illumination, the electrons were populated to the MLCT excited state from the ground state of Ru-complex **1** and were continually injected into the channel of the n -type BPE-PTCDI, which made the phototransistor highly photoresponsive. The EQE values of the Ru-complex **1**-modified BPE-PTCDI device were ca. 50000- and 3500-times higher than those of pristine BPE-PTCDI at $V_{GS} = 20$ and 80 V, respectively. This behavior stemmed from the long lifetime of electron-hole pairs ($\text{Ru}^{3+} - e^-$). The phototransistor had a high detectivity of 1.9×10^{13} Jones. Furthermore, functionalization of Ru-

complex **1** on the BPE-PTCDI phototransistor array is feasible for the fabrication of large-area (10×10 phototransistor components), transparent optoelectronic devices with high flexibility and twistability. We believe that our study provides a simple method to enhance the photoresponsivity of organic phototransistors for wearable organic optoelectronic devices, such as flexible image scanners, optical communications, and biomedical sensing gadgets.

3.5 References

- [1] M. S. Arnold, J. D. Zimmerman, C. K. Renshaw, X. Xu, R. R. Lunt, C. M. Austin, S. R. Forrest, *Nano Lett.* **2009**, *9*, 3354.
- [2] P. Reiss, E. Couderc, J. De Girolamo, A. Pron, *Nanoscale* **2011**, *3*, 446.
- [3] S. F. Tedde, J. Kern, T. Sterzl, J. Fürst, P. Lugli, O. Hayden, *Nano Lett.* **2009**, *9*, 980.
- [4] H. W. Lin, S. Y. Ku, H. C. Su, C. W. Huang, Y. T. Lin, K. T. Wong, C. C. Wu, *Adv. Mater.* **2005**, *17*, 2489.
- [5] Y. Zhou, L. Wang, J. Wang, J. Pei, Y. Cao, *Adv. Mater.* **2008**, *20*, 3745.
- [6] Z. Sun, Q. Ye, C. Chi, J. Wu, *Chem. Soc. Rev.* **2012**, *41*, 7857.
- [7] K. J. Baeg, M. Binda, D. Natali, M. Caironi, Y. Y. Noh, *Adv. Mater.* **2013**, *25*, 4267.
- [8] H. Dong, H. Zhu, Q. Meng, X. Gong, W. Hu, *Chem. Soc. Rev.* **2012**, *41*, 1754.
- [9] Y. Yao, Y. Liang, V. Shrotriya, S. Xiao, L. Yu, Y. Yang, *Adv. Mater.* **2007**, *19*, 3979.
- [10] P. Peumans, A. Yakimov, S. R. Forrest, *J. Appl. Phys.* **2003**, *93*, 3693.
- [11] H. Tanaka, T. Yasuda, K. Fujita, T. Tsutsui, *Adv. Mater.* **2006**, *18*, 2230.
- [12] H. Yu, Z. Bao, J. H. Oh, *Adv. Funct. Mater.* **2013**, *23*, 629.
- [13] L. Zhang, Y. Cao, N. S. Colella, Y. Liang, J. L. Bredas, K. N. Houk, A. L. Briseno, *Acc. Chem. Res.* **2015**, *48*, 500.
- [14] G. C. Vougioukalakis, A. I. Philippopoulos, T. Stergiopoulos, P. Falaras, *Coord. Chem. Rev.* **2011**, *255*, 2602.
- [15] M. Grätzel, *J. Photochem. Photobiol., C* **2003**, *4*, 145.
- [16] Y. Tachibana, S. A. Haque, I. P. Mercer, J. R. Durrant, D. R. Klug, *J. Phys. Chem. B* **2000**, *104*, 1198.
- [17] A. S. Polo, M. K. Itokazu, N. Y. Murakami Iha, *Coord. Chem. Rev.* **2004**, *248*, 1343.
- [18] Y. Qin, Q. Peng, *Int. J. Photoenergy* **2012**, *2012*, 21.
- [19] T. Kinoshita, J. T. Dy, S. Uchida, T. Kubo, H. Segawa, *Nat. Photonics* **2013**, *7*, 535.
- [20] X. Liu, E. K. Lee, J. H. Oh, *Small* **2014**, *10*, 3700.
- [21] H. Yu, P. Joo, D. Lee, B. S. Kim, J. H. Oh, *Adv. Opt. Mater.* **2015**, *3*, 241.
- [22] J. H. Oh, H. W. Lee, S. Mannsfeld, R. M. Stoltenberg, E. Jung, Y. W. Jin, J. M. Kim, J.-B. Yoo, Z. Bao, *Proc. Natl. Acad. Sci.* **2009**, *106*, 6065.
- [23] Y.-Y. Noh, D.-Y. Kim, Y. Yoshida, K. Yase, B.-J. Jung, E. Lim, H.-K. Shim, *Appl. Phys. Lett.* **2005**, *86*, 043501.
- [24] C. K. Renshaw, X. Xu, S. R. Forrest, *Org. Electron.* **2010**, *11*, 175.
- [25] X. Zhang, J. Jie, W. Zhang, C. Zhang, L. Luo, Z. He, X. Zhang, W. Zhang, C. Lee, S. Lee, *Adv. Mater.* **2008**, *20*, 2427.
- [26] T. Zukawa, S. Naka, H. Okada, H. Onnagawa, *J. Appl. Phys.* **2002**, *91*, 1171.
- [27] Z. Sun, J. Li, F. Yan, *J. Mater. Chem.* **2012**, *22*, 21673.
- [28] C.-H. Liu, Y.-C. Chang, T. B. Norris, Z. Zhong, *Nat. Nanotechnol.* **2014**, *9*, 273.
- [29] P. Pattanasattayavong, S. Rossbauer, S. Thomas, J. G. Labram, H. J. Snaith, T. D. Anthopoulos, *J. Appl. Phys.* **2012**, *112*, 074507.
- [30] K. Kawaoka, D. R. Kearns, *J. Chem. Phys.* **1966**, *45*, 147.
- [31] H. M. Colquhoun, Z. Zhu, D. J. Williams, M. G. B. Drew, C. J. Cardin, Y. Gan, A. G. Crawford, T. B. Marder, *Chem. Eur. J.* **2010**, *16*, 907.
- [32] N. V. Anh, F. Schlosser, M. M. Groeneveld, I. H. M. Van Stokkum, F. Würthner, R. M. Williams, *J. Phys. Chem. C* **2009**, *113*, 18358.

- [33]Q. Su, S. Pang, V. Alijani, C. Li, X. Feng, K. Müllen, *Adv. Mater.* **2009**, *21*, 3191.
- [34]B. Xing, C.-W. Yu, K.-H. Chow, P.-L. Ho, D. Fu, B. Xu, *J. Am. Chem. Soc.* **2002**, *124*, 14846.
- [35]D. M. Guldi, G. M. A. Rahman, N. Jux, N. Tagmatarchis, M. Prato, *Angew. Chem. Int. Ed.* **2004**, *43*, 5526.
- [36]C. Ehli, G. M. A. Rahman, N. Jux, D. Balbinot, D. M. Guldi, F. Paolucci, M. Marcaccio, D. Paolucci, M. Melle-Franco, F. Zerbetto, S. Campidelli, M. Prato, *J. Am. Chem. Soc.* **2006**, *128*, 11222.
- [37]L. Li, P. S. Lee, C. Y. Yan, T. Y. Zhai, X. S. Fang, M. Y. Liao, Y. Koide, Y. Bando, D. Golberg, *Adv. Mater.* **2010**, *22*, 5145.
- [38]X. L. Liu, H. X. Wang, T. B. Yang, W. Zhang, X. Gong, *ACS Appl. Mater. Inter.* **2012**, *4*, 3701.
- [39]J. Lee, A. R. Han, H. Yu, T. J. Shin, C. Yang, J. H. Oh, *J. Am. Chem. Soc.* **2013**, *135*, 9540.
- [40]R. Nie, Y. Wang, X. Deng, *ACS Appl. Mater. Inter.* **2014**, *6*, 7032.
- [41]D. Yang, X. Zhou, D. Ma, *Org. Electron.* **2013**, *14*, 3019.
- [42]H. Zhang, S. Jenatsch, J. De Jonghe, F. Nüesch, R. Steim, A. C. Véron, R. Hany, *Sci. Rep.* **2015**, *5*, 9439.
- [43]M. M. Ling, P. Erk, M. Gomez, M. Koenemann, J. Locklin, Z. Bao, *Adv. Mater.* **2007**, *19*, 1123.
- [44]T. Taniguchi, Y. Fukasawa, T. Miyashita, *J. Phys. Chem. B* **1999**, *103*, 1920.
- [45]M. Chandrasekharam, G. Rajkumar, C. S. Rao, T. Suresh, P. Y. Reddy, Y. Soujanya, *J. Chem. Sci.* **2011**, *123*, 555.
- [46]P. Wang, S. M. Zakeeruddin, J. E. Moser, M. K. Nazeeruddin, T. Sekiguchi, M. Grätzel, *Nat. Mater.* **2003**, *2*, 402.
- [47]T. N. Ng, J. H. Daniel, S. Sambandan, A.-C. Arias, M. L. Chabinyc, R. A. Street, *J. Appl. Phys.* **2008**, *103*, 044506.
- [48]Y. J. Park, S. K. Lee, M. S. Kim, H. Kim, J. H. Ahn, *ACS Nano* **2014**, *8*, 7655.
- [49]S. J. Kwon, A. R. Jang, J. Bae, Y. S. Kim, S. W. Lee, *J. Nanoelectron. Optoe.* **2013**, *8*, 588.
- [50]D. S. Wu, T. N. Chen, E. Lay, C. H. Liu, C. H. Chang, H. F. Wei, L. Y. Jiang, H. U. Lee, Y. Y. Chang, *J. Electrochem. Soc.* **2010**, *157*, C47.
- [51]H. J. Park, J. W. Park, S. Y. Jeong, C. S. Ha, *Proc. IEEE* **2005**, *93*, 1447.

Reprinted with permission from X. Liu, E. K. Lee, *et al.*, *ACS Appl. Mater. Interfaces* **2016, *8*, 7291–7299. Copyright © 2016 American Chemical Society

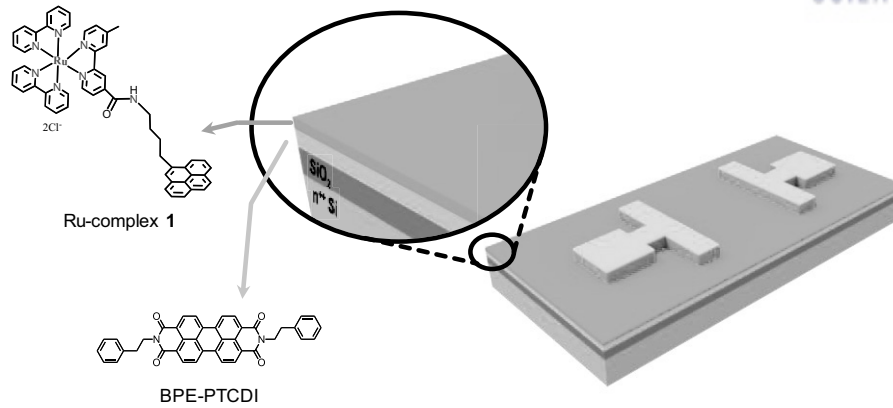


Figure 3.1. Schematic depiction of Ru-complex 1/BPE-PTCDI/Si/SiO₂ phototransistor and chemical structures of Ru-complex 1, BPE-PTCDI.

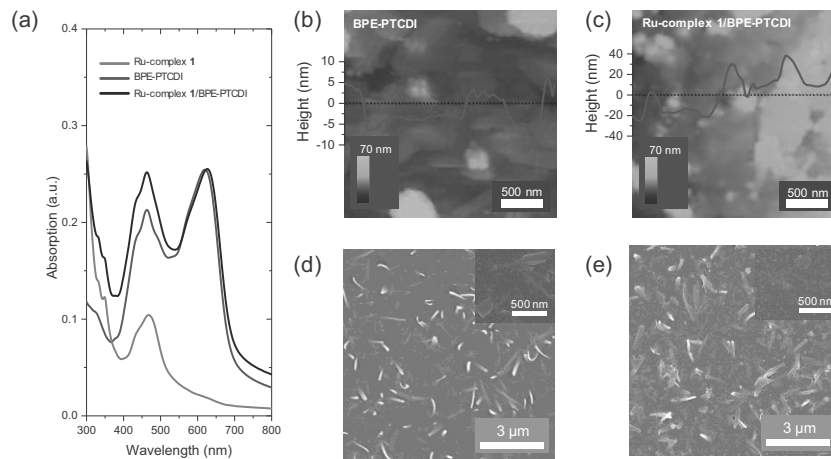


Figure 3.2. (a) UV-vis spectra of Ru-complex 1/glass, BPE-PTCDI/glass and Ru-complex 1/BPE-PTCDI/glass. AFM height and surface roughness: (b) BPE-PTCDI/SiO₂/Si. (c) Ru-complex 1/BPE-PTCDI/SiO₂/Si. SEM images of (d) BPE-PTCDI/SiO₂/Si. (e) Ru-complex 1/BPE-PTCDI/SiO₂/Si.

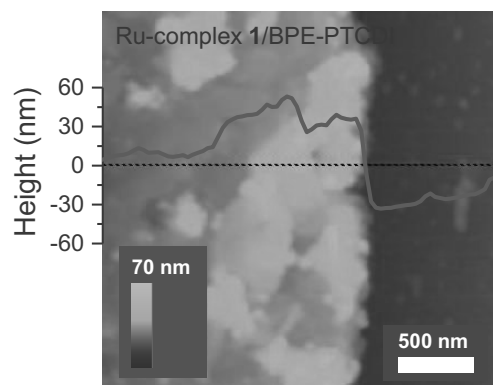


Figure 3.3. AFM height images and cross-sectional profiles with the surface roughness: Ru-complex 1/BPE-PTCDI/SiO₂/Si (The dark red part is the surface of SiO₂/Si wafer obtained by scraping off the Ru-complex 1/BPE-PTCDI part).

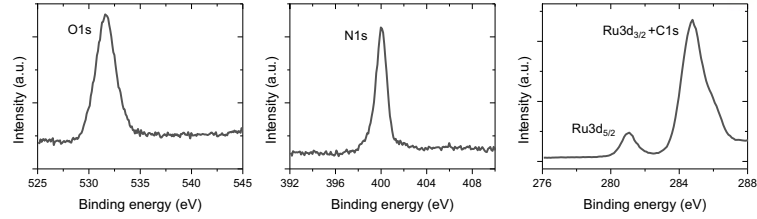


Figure 3.4. XPS spectra of Ru-complex **1**-modified BPE-PTCDI/SiO₂/Si ($h\nu = 1486.6$ eV). Some of the characteristic peaks are marked (O1s, N1s, C1s and Ru3d). The Ru3d_{3/2} peak is merged with the C1s emission.

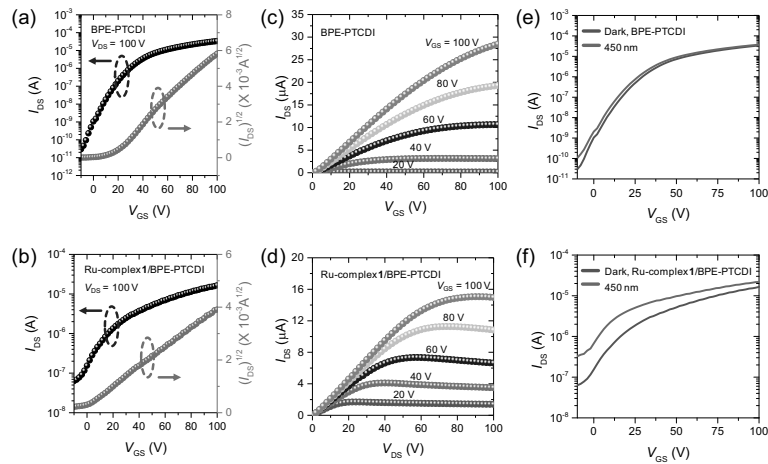


Figure 3.5. Current-voltage characteristics of BPE-PTCDI and Ru-complex **1**/BPE-PTCDI FET devices. Transfer characteristics ($V_{DS} = 100$ V) of (a) BPE-PTCDI and (b) Ru-complex **1**/BPE-PTCDI FET devices. Output characteristics of (c) BPE-PTCDI and (d) Ru-complex **1**/BPE-PTCDI FET devices. ($V_{GS} = 20, 40, 60, 80, 100$ V). Transfer characteristics of (e) BPE-PTCDI/SiO₂/Si and (f) Ru-complex **1**/BPE-PTCDI/SiO₂/Si devices under dark and monochromatic light ($\lambda = 450$ nm, $1.5 \mu\text{Wcm}^{-2}$, $V_{DS} = 100$ V).

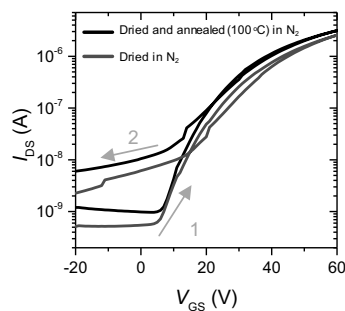


Figure 3.6. Hysteresis of Ru-complex **1**-modified BPE-PTCDI phototransistors. The red line shows the result of a device dried in N₂ condition for 1 day, while the black line exhibits the result of a device dried at room temperature for 1 day in N₂ and annealed at 100 °C in N₂ consecutively.

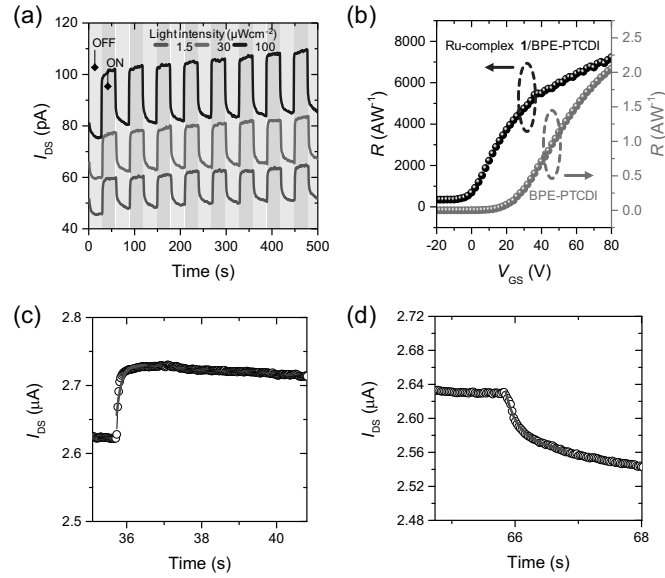


Figure 3.7. (a) Normalized current response of Ru-complex 1/BPE-PTCDI/SiO₂/Si phototransistor upon on (yellow area)/off (blue area) switching of illumination ($V_{DS} = 100$ V; $V_{GS} = 0$ V; Irradiation: 1.5, 30, 100 μWcm^{-2}). (b) Photoresponsivity of Ru-complex 1/BPE-PTCDI/SiO₂/Si and BPE-PTCDI/SiO₂/Si devices as a function of gate voltage ($\lambda = 450$ nm, 1.5 μWcm^{-2}). Time response of (c) photocurrent growth and (d) decay for Ru-complex 1/BPE-PTCDI phototransistors and its exponential fitted results (red solid lines) using Equation (5) and (6), respectively, $V_{DS} = 100$ V; $V_{GS} = 100$ V.

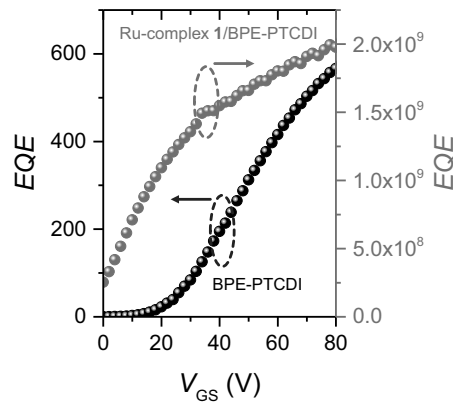


Figure 3.8. External quantum efficiency (EQE) (η) of Ru-complex 1/BPE-PTCDI and BPE-PTCDI devices as a function of V_{GS} ($\lambda = 450$ nm, 1.5 $\mu\text{W cm}^{-2}$).

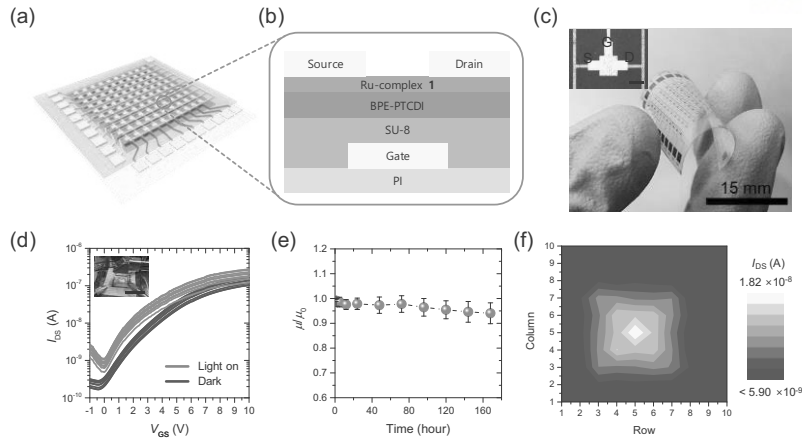


Figure 3.9. (a) Schematic illustration of 10×10 Ru-complex 1/BPE-PTCDI/SU-8 phototransistor device fabricated on a flexible transparent PI. (b) Detailed schematic structure of a single phototransistor. (c) Photograph of the 10×10 phototransistor array prepared on a PI substrate. (Inset: optical image of single device layout, S, D and G indicate source, drain and gate respectively, scale bar, $200 \mu\text{m}$) (d) Typical 10 selected transfer curves ($V_{DS} = 3 \text{ V}$) among phototransistor array under dark (pink) and illumination condition (purple). (Inset: photograph when light is incident to the device, scale bar, 1 cm) (e) Electron mobility change and its distribution (black error bars) with time for 7 days in ambient laboratory condition. (f) Photocurrent mapping of the 10×10 phototransistor array for the light spot (illumination position: column, row = 5, 5). Light wavelength and intensity were $\lambda = 450 \text{ nm}$ and $1.5 \mu\text{Wcm}^{-2}$, respectively.

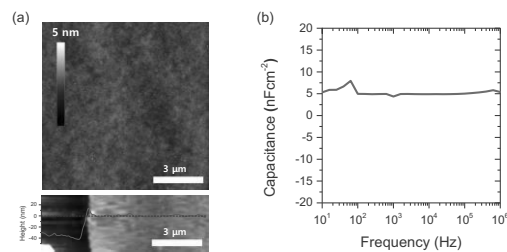


Figure 3.10. (a) AFM height image of SU-8 dielectric layer. (Top) Surface morphology and (Bottom) the cross-sectional profile showing the thickness of 35 nm . (b) Capacitance vs. frequency of SU-8 dielectric layer.

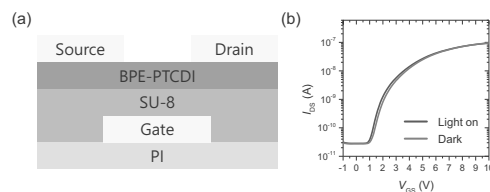


Figure 3.11. (a) Schematic cross-sectional diagram of BPE-PTCDI on SU-8 and PI as dielectric and substrate, respectively. (b) The transfer curves ($V_{DS} = 3 \text{ V}$) of the device when the light was on (purple) and off (pink). Light intensity was $1.5 \mu\text{Wcm}^{-2}$.

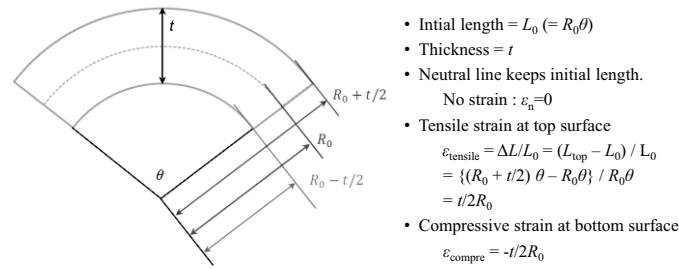


Figure 3.12. Calculation of tensile and compressive strains with respect to the bending radius.

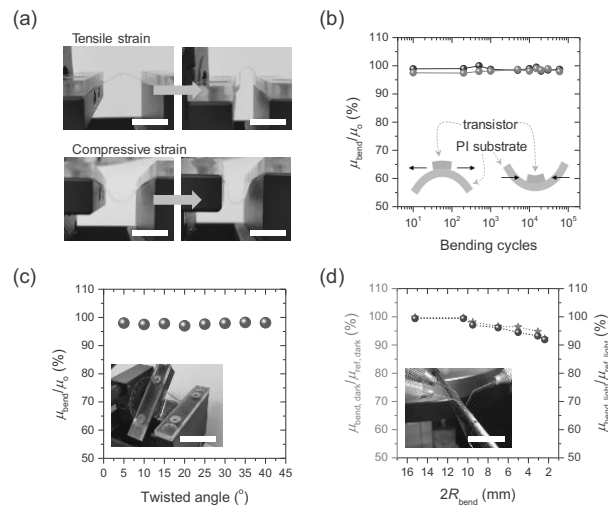


Figure 3.13. Flexibility test of the phototransistor array prepared on a PI substrate. (a) The phototransistor array was placed on the top surface of PI substrate. A tensile strain was applied during upward bending (top), in contrast, a compressive strain was applied during downward bending (bottom), scale bar = 20 mm. (b) Normalized electron mobility change after tensile strain bending (black) and compressive bending (red) cycles. (Inset: schematic figures of devices during tensile (left) and compressive strain (right)) (c) Normalized electron mobility change with respect to various twisted angles from 5° to 40° (Inset: photograph of twisted device, scale bar = 35 mm). (d) Normalized mobility change with respect to $2R_{\text{bend}}$ under dark (red) and light (blue) where R_{bend} is bending radius (Inset: photograph of device measurement for investigating the effect of bending radius on the performance, scale bar = 5 mm).

Chapter 4. Chemically Robust Ambipolar Organic Transistor Array Directly Patterned by Photolithography

4.1. Introduction

With the continuing development of soft electronics, organic semiconductors have increasingly been in the spotlight because of their solution processability, mechanical flexibility, and tunable electrical properties via rational molecular design.^[1-3] In recent years, a large number of studies on the applications of organic field-effect transistors (OFETs), such as sensors,^[4-9] logic circuits,^[10-13] and light-emitting transistors,^[14-16] have been reported. However, there are critical drawbacks to overcome before they can be commercialized, such as low solvent resistance, the difficulty of directly patterning organic semiconductors, and the unbalanced charge transport of electrons and holes.

Conventional photolithography is a necessary process for the large-scale production of electronic devices; however, a major problem for organic electronics is the severe degradation of organic semiconductors during the patterning process. Inkjet printing and spray coating with shadow masks are alternative reliable techniques for patterning solution-processable polymer semiconductors, but pattern sizes are often limited compared to conventional photolithography. One strategy to pattern organic semiconductors using conventional photolithography is to use parylene layer as intermediary between organic semiconductor and photoresist.^[17, 18] Parylene layer is chemically stable to tolerate chemicals related to photolithographical process. On the other hand, the vast majority of organic materials are either oleophilic or hydrophilic which are orthogonal to highly fluorinated chemicals.^[19] Organic semiconductors were patterned by conventional photolithography using highly fluorinate chemicals to pattern organic electronic materials without chemical damages.^[19-21] In addition, directly photo-patternable organic semiconductor materials mixed with a small amount of photo-initiator were demonstrated.^[22-24] However, considering the high impact of photolithographically patternable organic semiconductors on practical applications, there is still a strong demand for the development of organic semiconductors with outstanding chemical robustness, yet solution-processability. Ideally, photolithography requires chemically robust organic semiconductor to pattern it. The chemical robustness of organic semiconductors is also essential for sensor applications, which are required to endure harsh environments.^[5, 8, 9]

The geometry of transistor devices greatly affects the performance of OFETs. OFETs are frequently tested in a top-contact geometry, in which the top contacts offer a larger effective contact area and a lower contact resistance because of metal penetration into the film and intermixing between the two components during deposition.^[25] However, the integration of thin film-based transistors into circuits is often based on a bottom-gate bottom-contact (BGBC) geometry, because damages to the deposited organic semiconductors can be minimized by reducing the following processing steps.^[26-31]

Ambipolar polymer semiconductors, in which both holes and electrons act as charge carriers, are ideal candidates for the easy and low-cost fabrication of organic complementary circuits and light-emitting field-effect transistors.^[32, 33] There is an increasing demand for balanced hole and electron charge transport for their practical applications. One sophisticated method for achieving balanced charge transport is to employ electrodes that have a work function matched with the highest occupied molecular orbital (HOMO) and the lowest unoccupied molecular orbital (LUMO) of the organic semiconductor, to minimize the charge injection barrier for both holes and electrons.^[34-39]

We recently reported high performance ambipolar OFETs based on diketopyrrolopyrrole (DPP)-selenophene copolymers with siloxane-terminated side chains (**PTDPPSe-Si**) in bottom-gate top-contact (BGTC) geometry.^[40, 41] The alkyl spacer length of the hybrid side chains was systematically tuned from butyl to hexyl units to optimize the ambipolar performance. It is noteworthy that the solubility of DPP-based copolymers was remarkably reduced as the spacers became shorter, indicating the enhanced chemical resistance for **PTDPPSe-SiC4** with butyl spacers with the maximum mobilities of 6.16 and 3.07 cm²V⁻¹s⁻¹ for hole and electron transport, respectively. In addition, the **PDPPTT-SiC4** exhibited enhanced ambient stability compared to the alkyl-terminated analogues.^[42] Although the BGTC geometry is widely adopted to investigate the intrinsic charge transport of organic semiconductor, the BGBC structure of OFETs should also be developed for their use in practical applications.

In this study, we investigate the possibility of directly patterning the DPP-based ambipolar polymer semiconductor **PTDPPSe-SiC4** in a BGBC OFET geometry via conventional photolithography, and report the construction of a 10 × 10 OFET array using **PTDPPSe-SiC4** with electrically balanced ambipolar properties in a BGBC geometry on a flexible and transparent plastic substrate. Using graphene electrodes with a lower work function,^[43-45] the OFETs exhibited much higher electron mobilities and balanced ambipolar operation, compared with gold electrodes-based devices. Hole and electron mobilities of the **PTDPPSe-SiC4** transistors with graphene electrodes increased by a factor of 3 and 50, respectively, compared with those of gold electrodes. In addition, due to the high insolubility of **PTDPPSe-SiC4** film after annealing, the OFETs showed superior chemical robustness and operated after soaking in various organic solvents for 24 h, and could therefore be applied as a sensor platform for detecting acetone vapor. Our results provide a viable method for improving charge transport balance in ambipolar transistors and represents a significant step towards the practical application of organic electronics.

4.2. Experimental Section

Materials and Instrumentation: All starting materials were purchased either from Aldrich or Acros and used without further purification. All solvents were ACS grade unless otherwise noted. An Agilent 5500 scanning probe microscope running with a Nanoscope V controller was used to obtain AFM images. AFM images were recorded in a high-resolution tapping mode under ambient conditions.

Raman spectroscopy was conducted at a wavelength of 532 nm (WITec, Micro Raman). Grazing incidence X-ray diffraction (GIXD) measurements were performed at the PLS-II 9A U-SAXS beamline of Pohang Accelerator Laboratory (PAL) in Korea. The X-ray beam was monochromated at 11.05 keV (wavelength = 1.12199 Å) and the incidence angle of X-ray beam was set in the range of 0.07–0.14°, which was analogous with the critical angle of samples. The recorded patterns were calibrated by using a precalibrated sucrose (monoclinic, P21) and the sample-to-detector distance was ~223.7 mm.

Device fabrication based on SiO₂/n⁺Si wafer: The CVD-grown graphene was transferred on a SiO₂ (300 nm, the specific capacitance is 10 nFcm⁻²)/Si wafer. Graphene electrodes were patterned by conventional photolithography. Graphene film was grown on a copper foil (0.025 mm thickness, Alfa Aesar) by conventional chemical vapor deposition (CVD) method using H₂ and CH₄ gas. After growth of graphene, PMMA was coated on graphene surface in order to support graphene for further process. Copper foil was etched by ammonium persulfate ((NH₄)₂S₂O₈) aqueous solution (0.1 M). After copper foil was etched away, PMMA/graphene had been transferred on the substrate and annealed at 130 °C for 30 min. Then PMMA was removed using acetone. To pattern the transferred graphene film, photolithography technique was used. A positive PR (DSAM-3037, Dongjin Semichem) was spin-coated on the graphene film (4000 rpm for 30s), and annealed at 100 °C for 60 s. UV light was illuminated on the PR with a photomask, and the pattern was developed using 2.15 % TMAH solution. The graphene area without patterned PR was etched away using RIE plasma (100 W for 5 s). Channel width and length of graphene electrodes were 100 μm and 30 μm, respectively. The wafers with patterned graphene electrodes were modified with *n*-octadecyltrimethoxysilane (OTS) self-assembled monolayer (SAM). A small bottle with few drops of OTS was placed in a desiccator with graphene-patterned wafers, and then heated at 140 °C for 12 h under vacuum. After heating, the wafers were sequentially washed with toluene, acetone, and isopropyl alcohol, and dried under nitrogen gas. The semiconductor layer was formed from a 3 mg mL⁻¹ solution of **PTDPPSe-SiC4** in anhydrous chlorobenzene using spin-coating, drop-casting, and solution-shearing methods. For spin-coating, the film was coated at 3000 rpm for 30 s. The pre-heating temperature and the shearing rate were 80 °C and 0.12 mms⁻¹ for solution-shearing. After deposition of the polymer films, substrates were annealed on a hot plate at 220 °C for 30 min. Polymeric semiconductor deposition and annealing processes were conducted under N₂ atmosphere.

Device fabrication based on a transparent PI: A transparent PI was purchased from FAFNIE (Guri-Si, Gyunggi-do, Korea), and used as a plastic substrate for transparent and flexible array devices. The transparent PI resin was coated on a cleaned glass substrate (3 cm × 3 cm), and annealed for 8 h at a gradually increasing temperature from 50 °C to 300 °C, to form a solid PI film. After PI film was prepared, gate electrodes array was patterned by photolithography, followed by thermal evaporation of

Cr (4 nm)/ Au (40 nm) and the lift-off of the residual PR. For a transparent dielectric layer, SU-8 10 mixed with γ -butyrolactone (7:3 = γ -butyrolactone:SU-10 8, volume ratio) was prepared on a substrate by spin-coating at 7000 rpm for 120 s and films were annealed at 95 °C for 1 min. Then films were exposed to UV radiation for UV-induced cross-linking, and annealed at 150 °C for 30 min. The resultant capacitance of SU-8 10 film (150 nm thickness) was 1 nF cm⁻² as shown in Figure 4.1. Graphene electrodes were patterned as mentioned previously. The channel width and length of patterned graphene source and drain electrodes were 65 and 50 μ m, respectively. The **PTDPPSe-SiC4** solution was coated on the substrate using solution-shearing methods and annealed on a hot plate at 220 °C for 30 min. All the films were coated under N₂ atmosphere. Then, PR was spin-coated on **PTDPPSe-SiC4** film. After annealing at 100 °C, the substrate was exposed to the UV light ($\lambda = 380$ nm, 20 mW cm⁻² of intensity) with a photomask and developed in 2.15 % TMAH solution. The exposed **PTDPPSe-SiC4** film was etched away using a dry etcher under CF₄ atmosphere. The residual PRs were stripped away in acetone. After patterning of polymer film, the devices were peeled off from the glass substrate.

Electrical Measurement: The electrical performance of Si wafer based FETs was measured under N₂ condition using a Keithley 4200-SCS semiconductor parametric analyzer. The transistors were operated in the saturation regime ($V_D = -100$ V for p-channel, $V_D = 100$ V for n-channel), and the field-effect mobility (μ) was calculated in the saturation regime using the following equation:

$$I_{DS} = \frac{W}{2L} \mu C_g (V_{GS} - V_T)^2$$

where I_{DS} is the drain current, W is the channel width, L is the channel length, μ is the mobility, C_g is the specific capacitance of the gate dielectric, V_{GS} is the gate voltage, and V_T is the threshold voltage, respectively.

Width-normalized channel resistance of the devices with graphene electrodes and Cr/Au electrodes were measured using a TLM method. The electrical properties of 10 \times 10 FET array device on a transparent PI were measured in ambient conditions. Acetone vapor sensing experiment was conducted under ambient condition. For vaporization of acetone, N₂ gas was flowed into a flask filled with liquid-phase acetone. Then the surface of the device was exposed to the acetone vapor flowed through a tube connected to the sensor device. Nitrogen gas flow was maintained at 4 SLM during sensing. Capacitance of SU-8 10 gate dielectric was measured using a high power electrochemical analyzer (Ivium Stat).

Chemical resistance experiment using UV-visible spectroscopy: UV-vis spectral analysis was performed to check the solvent resistance of **PTDPPSe-SiC4** film, using a UV-vis spectrometer (Cary 500, Agilent). **PTDPPSe-SiC4** FETs prepared on OTS-modified SiO₂ (300 nm)/Si wafer were placed into various solvents, i.e., DI water, ethyl alcohol, acetone, and chlorobenzene. Then the substrates with the polymer film were soaked in each solvent for 24 h. A small amount of each solvent was then taken

out and the UV-vis spectra were measured once again. Then the two spectra before and after soaking were compared. For comparison of solvent resistance with other commercial polymer semiconductor film, poly(3-hexylthiophene) (P3HT, EM Index) was used. P3HT solution in chlorobenzene (3 mg mL⁻¹) was spin-coated on an OTS-modified substrate, then annealed on a hot plate at 140 °C for 30 min. The following steps were exactly same as described above. UV-vis spectra were also measured to investigate the transparency of PI based FET array. By following the aforementioned preparation process, the transparency of PI/glass, graphene/PI/glass, and **PTDPPSe-SiC4**/graphene/PI/glass were measured using a glass substrate as the reference.

4.3. Results and Discussion

The **PTDPPSe-SiC4** film (molecular structure depicted in Figure 4.2b) was deposited using solution-shearing on an octadecyltrichlorosilane (OTS)-modified SiO₂/n⁺⁺Si wafer substrate with graphene electrodes (See details in Figure 4.3). The optical image in inset of **Figure 4.2a** clearly shows patterned graphene electrodes on SiO₂/n⁺⁺Si wafer via photolithography. Raman spectroscopy was performed on different positions of the graphene electrode (Figure 4.2a), as shown in different colors in inset of Figure 4.2a. The Raman spectrum of the position marked with grey dots showed no remarkable peaks, indicating that no residual graphene remained at this position, suggesting that the graphene was well etched during the patterning process. The pink-dot position showed a strong G band (~1580 cm⁻¹) and 2D band (~2700 cm⁻¹), which indicates formation of the monolayer graphene. The purple-dot position showed a 2D band with a weaker intensity than that of the pink dot position, indicating that few-layer graphene was grown,^[46] and the Raman spectrum of the blue-dot position, which was the edge of the patterned graphene electrode, showed a D band (~1350 cm⁻¹), indicating a defect caused by the patterning process that resulted in discontinuity of the lattice structure of the graphene electrode.

Atomic force microscope (AFM) images of the **PTDPPSe-SiC4** film deposited on the graphene-patterned substrate by the solution-shearing method were examined to analyze the surface morphology (Figure 4.2c and Figure 4.4 for high-resolution AFM images) The images showed different morphologies depending on the presence of graphene under the polymer film. The alignment of the polymer chains induced by shear stress applied during the solution-shearing process was observed on the SiO₂ surface. In contrast, the film morphology on the graphene film showed randomly oriented polymer chains as shown in Figure 4.4. This was presumably due to the strong π - π interaction between the honeycomb lattice of graphene and the conjugated polymer chain, which was strong enough to resist alignment of the polymer chains against the applied shear stress.^[47-55] For comparison, AFM images of **PTDPPSe-SiC4** film deposited by spin coating were obtained, as shown in Figure 4.5. The spin-coated films on graphene and SiO₂ showed similar morphologies of the granular domains.

2D grazing incidence X-ray diffraction (GIXD) analysis was performed to identify the crystallinity and molecular orientation of the **PTDPPSe-SiC4** on both SiO₂ and graphene. Figure 4.2d and 1e present

2D GIXD profiles of **PTDPPSe-SiC4** on SiO₂ and graphene, respectively. The solution-processed films on SiO₂ and graphene exhibited high-order (*h00*) peaks up to the fourth order along the out-of-plane direction. The coherence length (L_c) on SiO₂ was ~ 133 Å in the out-of-plane direction, whereas that on graphene was ~ 240 Å along the in-plane direction. The (*010*) peaks observed at $q = \sim 1.7$ Å⁻¹ in both the in-plane and out-of-plane directions corresponded to π - π stacking, indicating the formation of 3D charge conduction channels in **PTDPPSe-SiC4** films on SiO₂ (Figure 4.2d). On the other hand, the films on graphene exhibited an intense π - π stacking peak ($q_z = 1.687$ Å⁻¹) only in the out-of-plane direction (Figure 4.2e). For quantitative comparison of π - π stacking in polymer films fabricated on SiO₂ and graphene, we performed pole figure analysis for (*010*) diffraction (Figure 4.2f). It is worth noting that **PTDPPSe-SiC4** on SiO₂ featured advanced bimodal distributions in π -systems with an edge-on portion of 16.5% and a face-on portion of 83.5%, whereas that on graphene showed a face-on portion of 98% with an edge-on portion of only 2%. In addition, the π - π stacking between the conjugated backbones was not affected by the changes in X-ray penetrating depth generated by tuning the X-ray incident angle (Figure 4.6a and S4b), which indicated the existence of strong π - π interactions between **PTDPPSe-SiC4** and graphene in the out-of-plane direction (Figure 4.6c).

The electrical properties of **PTDPPSe-SiC4** based FETs were measured in an N₂ atmosphere. The ambipolar transistors were operated in saturation regime and hole and electron mobilities were calculated from the mobility equation in saturation mode. **Figure 4.7a** and **2b** are the p-channel and n-channel transfer characteristics of **PTDPPSe-SiC4** transistors with graphene electrodes, respectively. The corresponding output curves are shown in Figure 4.8, demonstrating the ambipolar characteristics of **PTDPPSe-SiC4** FETs using graphene electrodes. The maximum hole and electron mobilities were 1.43 and 0.37 cm² V⁻¹ s⁻¹, respectively. Although the hole and electron mobilities in the BGBC geometry were slightly lower than those of the previously reported top-contact devices^[40, 41] due to the difference in device structure, these mobilities are comparable to those of amorphous silicon. The hole and electron mobilities estimated from the transfer curves for FETs based on spin-coated (Figure 4.9a and S6c), drop-cast (Figure 4.9b and S6d), and solution-sheared **PTDPPSe-SiC4** films are tabulated as shown in Table 4.1. Solution-sheared devices show the highest mobility among the fabricated devices, due to the higher degree of molecular orientation after solution shearing.^[56-64]

The electrical performances of the OFETs with graphene electrodes were compared to those of Cr/Au electrodes in BGBC configuration. The charge carrier mobilities with the Cr/Au electrodes were lower than the mobilities of graphene electrode devices. The maximum hole mobilities of the device with Cr/Au electrodes were 0.33, 0.43, and 0.54 cm² V⁻¹ s⁻¹ for spin coating, drop-casting, and solution shearing, respectively, which were less than half of those of OFET devices with graphene electrodes. The spin-coated devices showed the maximum electron mobility of 7×10^{-3} cm² V⁻¹ s⁻¹, whereas the drop-cast and solution sheared devices showed the same maximum electron mobility of 9×10^{-3} cm² V⁻¹ s⁻¹. The electron mobilities of devices with Cr/Au electrodes were $\sim 5\%$ of the graphene electrode

devices. The HOMO and LUMO levels of **PTDPPSe-SiC4** were -5.17 and -3.56 eV, respectively.^[40] The work functions of graphene and gold are -4.5 and -5.1 eV, respectively.^[65-67] Hence, a lower energy barrier can be achieved for electron transport using graphene electrodes instead of gold (Figure 4.7c). The lower energetic barrier for n-type operation can be beneficial to electron transport when graphene electrodes are used. Contrarily, this tends to negatively impact hole mobility due to the higher energetic barrier to hole transport, compared with Au electrodes. However, both hole and electron mobilities were improved for graphene electrodes as shown in Table 4.1. This result indicates that the morphological factor was more influential in the electrical performance than the energetic factor.

We have performed the stability test of **PTDPPSe-SiC4 FET** in ambient condition for 72 hours as shown in Figure 4.10. The devices were stored in ambient condition and measured in vacuum condition (~10⁻⁶ torr). The hole and electron mobilities were maintained up to 83.2 % and 80.6 %, respectively, after 72 hours.

OFET-based inverter characteristics with graphene electrodes were tested using a single-layer **PTDPPSe-SiC4** film, which exhibited a higher gain of 20.3 (Figure 4.7d) compared to that (7.9) with gold electrodes (Figure 4.11). The high gain of graphene electrode devices can be attributed to the more balanced, higher charge carrier mobilities.

We further investigated the width-normalized channel resistance of the devices with graphene and Cr/Au electrodes using a transfer line method (TLM), as shown in Figure 4.12.^[68, 69] The measured contact resistances for the graphene electrode were only 1.2% and 1.1% of the Cr/Au electrodes with respect to hole and electron transports, respectively. Strong π - π interactions between **PTDPPSe-SiC4** and graphene induced a face-on portion of 98% with an edge-on portion of 2% on graphene electrode from GIXD results. Judging from our device structure and contact resistance analysis in comparison with gold electrode, this molecular packing would be more beneficial for efficient charge injection and collection in the contact region. On the other hand, in the channel region, **PTDPPSe-SiC4** on SiO₂ featured advanced bimodal distributions in π -systems with an edge-on portion of 16.5% and a face-on portion of 83.5% from GIXD results. The bimodal crystalline nature in the channel region can provide 3D charge conduction channel that facilitates charge transport along the source-drain direction, as reported by previous studies.^[40, 70, 71] The strong π - π interactions with dominant face-on orientations between graphene and **PTDPPSe-SiC4** as observed from the AFM and GIXD analyses led to the lower contact resistance and higher hole mobilities.

Figure 4.13a illustrates the schematic device structure using graphene electrodes and a **PTDPPSe-SiC4** polymeric semiconductor on transparent polyimide (PI). Briefly, the patterned graphene electrode was prepared on top of SU-8 dielectric/gate electrode/transparent PI substrate (Figure 4.13b). The **PTDPPSe-SiC4** semiconductor layer was deposited on top of the sample using solution-shearing method (Figure 4.13c). The formed **PTDPPSe-SiC4** semiconductor layer was patterned via conventional photolithography process including photoresist (PR) coating, development, etching, and

stripping, sequentially (Detailed device construction steps are described in Experimental Section and Figure 4.14).

PTDPPSe-SiC4 film was robust enough to tolerate harsh photolithography procedures due to the high insolubility induced by the hybrid siloxane side chain group,^[42] and thus, could be directly patterned by photolithography. PR was spin-coated on top of the **PTDPPSe-SiC4** film. After annealing at 100°C, the substrate was exposed to UV light and developed in 2.15% tetramethylammonium hydroxide (TMAH). The exposed **PTDPPSe-SiC4** film was etched away using a dry-etcher under a CF₄ atmosphere. The remaining part of the PR was removed in acetone (Figure 4.13d). Thus, OFET devices in a BGBC configuration were successfully constructed. In addition, the **PTDPPSe-SiC4** film was patterned on Si wafer to verify the reliability of the photolithographic patterning with various feature length ranging from 2 to 20 μm (Figure 4.15). The optical images show that the deposited film is compatible with conventional photolithography.

Figure 4.13e is a photograph of a 10 × 10 FET array on a transparent PI (the array size is 2.5 × 2.5 cm²). The transmittance at a wavelength of 550 nm was 91% for the fully processed array structure without a gold gate electrode (Figure 4.16). An optical image of the single transistor device of the 10 × 10 FET array is shown in Figure 4.13f. Well-patterned graphene electrodes were observed underneath the **PTDPPSe-SiC4** film. The **PTDPPSe-SiC4** film showed a well-defined patterned structure on graphene electrodes and a SU-8 dielectric layer. The average hole and electron mobilities of the 10 × 10 FET array were 0.37 (±0.02) and 0.05 (±0.02) cm²V⁻¹s⁻¹ measured in an N₂ atmosphere, respectively (Figure 4.17). Although the average hole and electron mobilities of the FETs on the PI film were slightly lower than those of the FETs on the Si wafer, the ambipolarity of the **PTDPPSe-SiC4** FETs was well maintained after the photolithography process on the PI substrate. The relatively lower mobility on the plastic substrate is mainly due to the different interfacial condition between dielectric and polymer semiconductor. Charge trap sites could be efficiently removed by treating the OTS on the Si wafer. However, SU-8 dielectric material contains oxygen-containing functional groups, for example, ether and epoxy groups which act as trap sites for charge transport. In addition, the relatively higher surface roughness of PI film compared to OTS-treated Si wafer might give detrimental effects on the electrical performance.

The hole mobilities of the flexible 10 × 10 FETs array measured in ambient conditions were mapped as shown in Figure 4.13g. The electron transport of the **PTDPPSe-SiC4** was not observable under ambient conditions, due to the trapping of electrons by ambient oxidants such as oxygen and water molecules. The representative p-type transfer curves measured in N₂ and ambient condition are shown in Figure 4.18. The threshold voltage was slightly shifted from -16 to -24 V. All of the 100 OFET devices prepared using the solution shearing method showed well-defined p-channel behaviors with a maximum hole mobility of 0.35 cm² V⁻¹ s⁻¹ and an average hole mobility of 0.17 (± 0.05) cm² V⁻¹ s⁻¹, comparable to those of amorphous Si transistors. It is noteworthy that the fabricated devices exhibited

ambipolar behaviors under vacuum or N₂ condition, while they showed only p-type behaviors in the ambient condition due to the trapping caused by ambient oxidants such as oxygen and water molecules. The devices recovered the ambipolar characteristics when measured again under vacuum or N₂ condition after exposure to ambient condition.

The flexible OFET devices fabricated on a transparent PI substrate were also characterized with a bending test. Figure 4.13h shows the hole mobility changes as a function of bending radius from 10 to 3 mm in parallel and perpendicular direction with respect to shearing direction. The tensile strain can be calculated using the following equation (1)

$$\varepsilon_{tensile} = \frac{t}{2R_{bend}} \quad (1)$$

where $\varepsilon_{tensile}$ is the tensile strain, t is the thickness of the basal film, 0.1 mm, and R_{bend} is the radius from the centre of bending to the neutral line of the film (See details in Figure 4.19). Our devices exhibited isotropic trends with regard to the bending direction and a gradual decrease in mobility by up to 50% compared to the initial mobility from 1.01% of the tensile strain ($2R_{bend} = 10$ mm) to a higher tensile strain, i.e., 3.23% ($2R_{bend} = 3$ mm). The bending test on the fabricated FET array showed that the hole mobility decreased to 95.5, 68.2, and 50.0% of the initial value under bending radii of 10, 8, and 3 mm, respectively. After releasing the strain on the device, the mobility recovered to its original value. The reversible mobility change may be attributed to the flexible characteristics of the device components (i.e., the **PTDPPSe-SiC4**, SU-8 dielectric layer).

It has been proposed that the siloxane group containing polymers may be more chemically robust.^[42, 72] The solvent resistivity of **PTDPPSe-SiC4** film against various organic solvents was investigated (see Experimental Section). An OTS-modified SiO₂/n⁺⁺Si wafer substrate was chosen to avoid detrimental effects arising from a polymeric substrate, such as volumetric swelling in the presence of organic solvents.^[73] UV-vis spectra of four solvents (i.e., DI water, ethyl alcohol, acetone, and chlorobenzene) were measured as control solvents. Then, each substrate was put into four bottles filled with each of the different organic solvents for 24 h (**Figure 4.20a**). Poly(3-hexylthiophene) (P3HT) films as a control film were deposited on a SiO₂/Si wafer and put into four different bottles filled with the same solvents. The color of chlorobenzene containing the P3HT film changed to yellow, whereas that of chlorobenzene containing the **PTDPPSe-SiC4** film was unchanged, which demonstrates the strong solvent resistance of **PTDPPSe-SiC4** film (**Figure 4.20b**). The UV-vis spectra (**Figure 4.21**) before and after soaking of the **PTDPPSe-SiC4** films were almost identical, whereas the spectra of solvents used to soak the P3HT films showed clear P3HT absorption peaks for acetone (**Figure 4.19c**) and chlorobenzene solvents (**Figure 4.21d**). These results indicate that **PTDPPSe-SiC4** film shows much higher chemical resistance to organic solvents than the P3HT film. In addition, UV-vis spectra of **PTDPPSe-SiC4** and **PTDPPSe-alkyl** (the molecular structures are shown in **Figure 4.22a**) in solution and films were obtained to further investigate the insolubility of **PTDPPSe-SiC4**, as shown in **Figure 4.22**. In the case of **PTDPPSe-alkyl**, the absorption spectra in solution and films were almost same. On the other hand, the 0-1 transition

peak of **PTDPPSe-SiC4** was more discernible and the spectral edge in the longer wavelength was slightly red-shifted (Figure 4.22b), suggesting that the molecular packing conformation of **PTDPPSe-SiC4** film was distinctly changed. This phenomenon often takes place when the conjugated backbone of polymers becomes more planar in the film. This result may imply that hybrid siloxane side chains in **PTDPPSe-SiC4** render the film more rigid and insoluble, compared to the alkyl side chains in **PTDPPSe-alkyl**.

The hole (Figure 4.20c) and electron (Figure 4.20d) mobilities of fabricated FET devices in an N₂ atmosphere were measured before and after soaking in the four solvents. Briefly, the fabricated devices were soaked in the four solvents for 24 h, and dried under a flow of N₂ gas, and annealed at 220°C for 30 min under an N₂ atmosphere. Although both the hole and electron mobilities of the devices were reduced compared to those of the as-prepared properties, all of the devices operated well after soaking (see Table 4.2). These results substantiate the superior chemical robustness of **PTDPPSe-SiC4** arising from high insolubility of the polymer.^[42]

To briefly explore the feasibility of **PTDPPSe-SiC4** OFETs as a platform for chemical sensors, the **PTDPPSe-SiC4** FET were exposed to an acetone vapor flow (4 SLM) with on/off switching (Figure 4.20e). Acetone is a widely used chemical polar solvent in lab and industry. The mixture of its vapor and the air will explode when the volume concentration of acetone is in the range of 2.6–12.8%. The acetone vapor sensing response is shown in Figure 4.20f. Acetone vapor exposure resulted in a decreased drain current, which indicates destructive (negative) sensing behavior. Exposure to polar analyte vapors typically decreases hole currents because of dipole-induced charge trapping at the grain boundary of the organic semiconductor layer.^[4, 74] Acetone is a polar and electron-donating analyte^[75] and shows destructive sensing signals as expected. The OFET-based acetone sensor showed stable operation in acetone gas OFF region and slight sensing deviation in acetone gas ON region over 20 cycles. The deviation in ON region might originate from the deviation in the input gas amount in our manual sensing system. The average value of I_D/I_{Base} on ON region was ~0.75. The sensitivity of the device ($S = I_{acetone-off}/I_{acetone-on}$, defined as the ratio of drain-source current between acetone gas-off and gas-on) was 1.3. After exposure to acetone-gas flow, the source-drain current decreased immediately, resulting in a response time of 0.88 s. Switching-off of the acetone-gas flow, the current was recovered to its saturation current level in 2.63 s (recovery time) as shown in Figure 4.23. The recovery time was longer than the response time, because the adsorbed acetone molecules require some time to be naturally desorbed from the device. Stable and repeatable sensing signals could be obtained, indicating the potential of the developed OFET devices to be used as a chemical sensing platform.

4.4. Conclusion

In summary, we fabricated ambipolar OFET arrays with well-balanced hole and electron mobilities via conventional photolithography using a chemically robust organic semiconductor **PTDPPSe-SiC4**

and graphene electrodes. To the best of our knowledge, this is the first demonstration of fabrication of ambipolar OFET arrays with graphene electrodes using conventional photolithography to pattern a solution-processable organic semiconductor in a BGBC configuration on a flexible substrate. Owing to the high insolubility of **PTDPPSe-SiC4**, the organic semiconductor could be directly patterned by conventional photolithography. Graphene electrode devices showed higher carrier mobilities for both p-channel ($1.43 \text{ cm}^2 \text{ V}^{-1} \text{ s}^{-1}$) and n-channel operations ($0.37 \text{ cm}^2 \text{ V}^{-1} \text{ s}^{-1}$), compared to p-channel ($0.54 \text{ cm}^2 \text{ V}^{-1} \text{ s}^{-1}$) and n-channel mobilities ($0.009 \text{ cm}^2 \text{ V}^{-1} \text{ s}^{-1}$) of Cr/Au based devices on OTS-treated $\text{SiO}_2/\text{n}^{++}\text{Si}$ wafer. Because of the lower energetic barriers and favorable intermolecular interactions between graphene and **PTDPPSe-SiC4**, the contact resistance of the graphene device was much lower than that of the Cr/Au device. The **PTDPPSe-SiC4** OFETs operated normally after soaking in various solvents, and proved the chemical robustness of **PTDPPSe-SiC4**. As a further application, **PTDPPSe-SiC4** OFETs were used as a sensor platform for detecting acetone vapors. Our results represent a significant step forward in improving balanced charge transport in ambipolar OFETs and substantiate the applicability of polymer semiconductors in conventional microelectronic infrastructures, which will lead to progress in the realization of plastic electronics.

4.5. References

- [1] T. Sekitani, U. Zschieschang, H. Klauk, T. Someya, *Nat. Mater.* **2010**, *9*, 1015.
- [2] H. Yan, Z. Chen, Y. Zheng, C. Newman, J. R. Quinn, F. Dotz, M. Kastler, A. Facchetti, *Nature* **2009**, *457*, 679.
- [3] Q. Cao, Z.-T. Zhu, M. G. Lemaitre, M.-G. Xia, M. Shim, J. A. Rogers, *Appl. Phys. Lett.* **2006**, *88*, 113511.
- [4] B. Kang, M. Jang, Y. Chung, H. Kim, S. K. Kwak, J. H. Oh, K. Cho, *Nat. Commun.* **2014**, *5*, 4752.
- [5] M. Y. Lee, H. J. Kim, G. Y. Jung, A. R. Han, S. K. Kwak, B. J. Kim, J. H. Oh, *Adv. Mater.* **2015**, *27*, 1540.
- [6] O. Knopfmacher, M. L. Hammock, A. L. Appleton, G. Schwartz, J. Mei, T. Lei, J. Pei, Z. Bao, *Nat. Commun.* **2014**, *5*, 2954.
- [7] P. Lin, F. Yan, *Adv. Mater.* **2012**, *24*, 34.
- [8] M. Yun, A. Sharma, C. Fuentes-Hernandez, K. Hwang do, A. Dindar, S. Singh, S. Choi, B. Kippelen, *ACS Appl. Mater. Interfaces* **2014**, *6*, 1616.
- [9] M. E. Roberts, S. C. Mannsfeld, N. Queralto, C. Reese, J. Locklin, W. Knoll, Z. Bao, *Proc. Natl. Acad. Sci. U. S. A.* **2008**, *105*, 12134.
- [10] D. Gentili, P. Sonar, F. Liscio, T. Cramer, L. Ferlauto, F. Leonardi, S. Milita, A. Dodabalapur, M. Cavallini, *Nano Lett.* **2013**, *13*, 3643.
- [11] L. Zhang, C.-a. Di, G. Yu, Y. Liu, *J. Mater. Chem.* **2010**, *20*, 7059.
- [12] E. J. Meijer, D. M. de Leeuw, S. Setayesh, E. van Veenendaal, B. H. Huisman, P. W. Blom, J. C. Hummelen, U. Scherf, J. Kadam, T. M. Klapwijk, *Nat. Mater.* **2003**, *2*, 678.
- [13] H. Klauk, U. Zschieschang, J. Pflaum, M. Halik, *Nature* **2007**, *445*, 745.
- [14] K. Kudo, *Curr. Appl. Phys.* **2005**, *5*, 337.
- [15] M. A. McCarthy, B. Liu, E. P. Donoghue, I. Kravchenko, D. Y. Kim, F. So, A. G. Rinzler, *Science* **2011**, *332*, 570.
- [16] R. Capelli, S. Toffanin, G. Generali, H. Usta, A. Facchetti, M. Muccini, *Nat. Mater.* **2010**, *9*, 496.
- [17] I. Kymissis, C. D. Dimitrakopoulos, S. Purushothaman, *J. Vac. Sci. Technol., B* **2002**, *20*, 956.
- [18] J. A. Defranco, B. S. Schmidt, M. Lipson, G. G. Malliaras, *Org. Electron.* **2006**, *7*, 22.

- [19] A. A. Zakhidov, J. K. Lee, J. A. Defranco, H. H. Fong, P. G. Taylor, M. Chatzichristidi, C. K. Ober, G. G. Malliaras, *Chem. Sci.* **2011**, *2*, 1178.
- [20] A. A. Zakhidov, H. H. Fong, J. A. Defranco, J. K. Lee, P. G. Taylor, C. K. Ober, G. G. Malliaras, M. He, M. G. Kane, *Appl. Phys. Lett.* **2011**, *99*.
- [21] H. H. Fong, J. K. Lee, Y. F. Lim, A. A. Zakhidov, W. W. H. Wong, A. B. Holmes, C. K. Ober, G. G. Malliaras, *Adv. Mater.* **2011**, *23*, 735.
- [22] P. S. Rudati, D. C. Mueller, K. Meerholz, "The characteristic of organic hole-only devices based on crosslinked hole-transport layer", presented at *Proceedings - 2014 International Symposium on Computer, Consumer and Control, IS3C 2014*, 2014.
- [23] A. Köhnen, N. Riegel, J. H. W. M. Kremer, H. Lademann, D. C. Müller, K. Meerholz, *Adv. Mater.* **2009**, *21*, 879.
- [24] M. C. Gather, A. Köhnen, A. Falcou, H. Becker, K. Meerholz, *Adv. Funct. Mater.* **2007**, *17*, 191.
- [25] D. Braga, G. Horowitz, *Adv. Mater.* **2009**, *21*, 1473.
- [26] H. E. A. Huitema, G. H. Gelinck, J. van der Putten, K. E. Kuijk, K. M. Hart, E. Cantatore, D. M. de Leeuw, *Adv. Mater.* **2002**, *14*, 1201.
- [27] C. Bartic, B. Palan, A. Campitelli, G. Borghs, *Sens. Actuators, B* **2002**, *83*, 115.
- [28] C. D. Sheraw, L. Zhou, J. R. Huang, D. J. Gundlach, T. N. Jackson, M. G. Kane, I. G. Hill, M. S. Hammond, J. Campi, B. K. Greening, J. Francl, J. West, *Appl. Phys. Lett.* **2002**, *80*, 1088.
- [29] J. A. Rogers, Z. Bao, K. Baldwin, A. Dodabalapur, B. Crone, V. R. Raju, V. Kuck, H. Katz, K. Amundson, J. Ewing, P. Drzaic, *Proc. Natl. Acad. Sci. U. S. A.* **2001**, *98*, 4835.
- [30] B. Crone, A. Dodabalapur, A. Gelperin, L. Torsi, H. E. Katz, A. J. Lovinger, Z. Bao, *Appl. Phys. Lett.* **2001**, *78*, 2229.
- [31] G. H. Gelinck, T. C. T. Geuns, D. M. de Leeuw, *Appl. Phys. Lett.* **2000**, *77*, 1487.
- [32] E. J. Meijer, D. M. De Leeuw, S. Setayesh, E. Van Veenendaal, B. H. Huisman, P. W. M. Blom, J. C. Hummelen, U. Scherf, T. M. Klapwijk, *Nat. Mater.* **2003**, *2*, 678.
- [33] J. Zaumseil, H. Sirringhaus, *Chem. Rev.* **2007**, *107*, 1296.
- [34] J.-P. Hong, A.-Y. Park, S. Lee, J. Kang, N. Shin, D. Y. Yoon, *Appl. Phys. Lett.* **2008**, *92*, 143311.
- [35] Y. Shi, K. K. Kim, A. Reina, M. Hofmann, L.-J. Li, J. Kong, *ACS Nano* **2010**, *4*, 2689.
- [36] J. Park, W. H. Lee, S. Huh, S. H. Sim, S. B. Kim, K. Cho, B. H. Hong, K. S. Kim, *J. Phys. Chem. Lett.* **2011**, *2*, 841.
- [37] J. O. Hwang, J. S. Park, D. S. Choi, J. Y. Kim, S. H. Lee, K. E. Lee, Y.-H. Kim, M. H. Song, S. Yoo, S. O. Kim, *ACS Nano* **2012**, *6*, 159.
- [38] T. Yasuda, T. Goto, K. Fujita, T. Tsutsui, *Appl. Phys. Lett.* **2004**, *85*, 2098.
- [39] D. Natali, M. Caironi, *Adv. Mater.* **2012**, *24*, 1357.
- [40] J. Lee, A. R. Han, H. Yu, T. J. Shin, C. Yang, J. H. Oh, *J. Am. Chem. Soc.* **2013**, *135*, 9540.
- [41] J. Lee, A. R. Han, J. Kim, Y. Kim, J. H. Oh, C. Yang, *J. Am. Chem. Soc.* **2012**, *134*, 20713.
- [42] A. R. Han, J. Lee, H. R. Lee, J. Lee, S. H. Kang, H. Ahn, T. J. Shin, J. H. Oh, C. Yang, *Macromolecules* **2016**, *49*, 3739.
- [43] S. Bae, H. Kim, Y. Lee, X. Xu, J. S. Park, Y. Zheng, J. Balakrishnan, T. Lei, H. R. Kim, Y. I. Song, Y. J. Kim, K. S. Kim, B. Ozyilmaz, J. H. Ahn, B. H. Hong, S. Iijima, *Nat. Nanotechnol.* **2010**, *5*, 574.
- [44] Y. Zhou, C. Fuentes-Hernandez, J. Shim, J. Meyer, A. J. Giordano, H. Li, P. Winget, T. Papadopoulos, H. Cheun, J. Kim, M. Fenoll, A. Dindar, W. Haske, E. Najafabadi, T. M. Khan, H. Sojoudi, S. Barlow, S. Graham, J. L. Brédas, S. R. Marder, A. Kahn, B. Kippelen, *Science* **2012**, *336*, 327.
- [45] W. H. Lee, J. Park, S. H. Sim, S. B. Jo, K. S. Kim, B. H. Hong, K. Cho, *Adv. Mater.* **2011**, *23*, 1752.
- [46] D. B. Farmer, G. M. Roksana, V. Perebeinos, Y. M. Lin, G. S. Tuievski, J. C. Tsang, P. Avouris, *Nano Lett.* **2009**, *9*, 388.
- [47] J. Cho, J. Smerdon, L. Gao, O. Sützer, J. R. Guest, N. P. Guisinger, *Nano Lett.* **2012**, *12*, 3018.
- [48] F. Faglioni, C. L. Claypool, N. S. Lewis, W. A. Goddard Iii, *J. Phys. Chem. B* **1997**, *101*, 5996.
- [49] R. G. S. Goh, N. Motta, J. M. Bell, E. R. Waclawik, *Appl. Phys. Lett.* **2006**, *88*, 1.
- [50] H. Huang, S. Chen, X. Gao, W. Chen, A. T. S. Wee, *ACS Nano* **2009**, *3*, 3431.

- [51] A. J. Pollard, E. W. Perkins, N. A. Smith, A. Saywell, G. Goretzki, A. G. Phillips, S. P. Argent, H. Sachdev, F. Müller, S. Hüfner, S. Gsell, M. Fischer, M. Schreck, J. Osterwalder, T. Greber, S. Berner, N. R. Champness, P. H. Beton, *Angew. Chem., Int. Ed.* **2010**, *49*, 1794.
- [52] X. Sun, J. Zhang, X. Wang, C. Zhang, P. Hu, Y. Mu, X. Wan, Z. Guo, S. Lei, *Chem. Commun.* **2013**, *49*, 10317.
- [53] H. Zhou, L. Zhang, J. Mao, G. Li, Y. Zhang, Y. Wang, S. Du, W. A. Hofer, H. J. Gao, *Nano Res.* **2013**, *6*, 131.
- [54] Y. Jiang, L. Yang, Z. Guo, S. Lei, *Sci. Rep.* **2015**, *5*, 17720.
- [55] D. H. Kim, H. S. Lee, H.-J. Shin, Y.-S. Bae, K.-H. Lee, S.-W. Kim, D. Choi, J.-Y. Choi, *Soft Matter* **2013**, *9*, 5355.
- [56] H. Yu, H. H. Cho, C. H. Cho, K. H. Kim, D. Y. Kim, B. J. Kim, J. H. Oh, *ACS Appl. Mater. Interfaces* **2013**, *5*, 4865.
- [57] J. Lee, A. R. Han, J. Hong, J. H. Seo, J. H. Oh, C. Yang, *Adv. Funct. Mater.* **2012**, *22*, 4128.
- [58] W. Y. Lee, G. Giri, Y. Diao, C. J. Tassone, J. R. Matthews, M. L. Sorensen, S. C. B. Mannsfeld, W. C. Chen, H. H. Fong, J. B. H. Tok, M. F. Toney, M. He, Z. Bao, *Adv. Funct. Mater.* **2014**, *24*, 3524.
- [59] W. Y. Lee, J. H. Oh, S. L. Suraru, W. C. Chen, F. Würthner, Z. Bao, *Adv. Funct. Mater.* **2011**, *21*, 4173.
- [60] H. A. Becerril, M. E. Roberts, Z. Liu, J. Locklin, Z. Bao, *Adv. Mater.* **2008**, *20*, 2588.
- [61] J. Shin, T. R. Hong, T. W. Lee, A. Kim, Y. H. Kim, M. J. Cho, D. H. Choi, *Adv. Mater.* **2014**, *26*, 6031.
- [62] Z. Liu, J. H. Oh, M. E. Roberts, P. Wei, B. C. Paul, M. Okajima, Y. Nishi, Z. Bao, *Appl. Phys. Lett.* **2009**, *94*, 203301.
- [63] Q. Meng, F. Zhang, Y. Zang, D. Huang, Y. Zou, J. Liu, G. Zhao, Z. Wang, D. Ji, C. A. Di, W. Hu, D. Zhu, *J. Mater. Chem. C* **2014**, *2*, 1264.
- [64] G. Giri, E. Miller, Z. Bao, *J. Mater. Res.* **2014**, *29*, 2615.
- [65] Y.-J. Yu, Y. Zhao, S. Ryu, L. E. Brus, K. S. Kim, P. Kim, *Nano Lett.* **2009**, *9*, 3430.
- [66] R. Garg, K. N. Dutta, R. N. Choudhury, *Nanomaterials* **2014**, *4*, 267.
- [67] S. M. Song, J. K. Park, O. J. Sul, B. J. Cho, *Nano Lett.* **2012**, *12*, 3887.
- [68] G. B. Blanchet, C. R. Fincher, M. Lefenfeld, J. A. Rogers, *Appl. Phys. Lett.* **2004**, *84*, 296.
- [69] C. Reese, Z. Bao, *Adv. Funct. Mater.* **2009**, *19*, 763.
- [70] S. Park, M. H. Lee, K. S. Ahn, H. H. Choi, J. Shin, J. Xu, J. Mei, K. Cho, Z. Bao, D. R. Lee, M. S. Kang, D. H. Kim, *Adv. Funct. Mater.* **2016**.
- [71] G. Kim, S. J. Kang, G. K. Dutta, Y. K. Han, T. J. Shin, Y. Y. Noh, C. Yang, *J. Am. Chem. Soc.* **2014**, *136*, 9477.
- [72] J. Mei, H. Kim do, A. L. Ayzner, M. F. Toney, Z. Bao, *J. Am. Chem. Soc.* **2011**, *133*, 20130.
- [73] M. K. Ghosh, K. L. Mittal, *Polyimides: Fundamentals and applications*, Marcel Dekker 1996.
- [74] T. Someya, A. Dodabalapur, J. Huang, K. C. See, H. E. Katz, *Adv. Mater.* **2010**, *22*, 3799.
- [75] J. Li, P. Tang, J. Zhang, Y. Feng, R. Luo, A. Chen, D. Li, *Ind. Eng. Chem. Res.* **2016**, *55*, 3588.

Reprinted in part with permission from E. K. Lee, *et al.*, *Adv. Mater.* **2017, DOI: 10.1002/adma.201605282 Copyright © 2017 WILEY-VCH Verlag GmbH & Co. KGaA, Weinheim

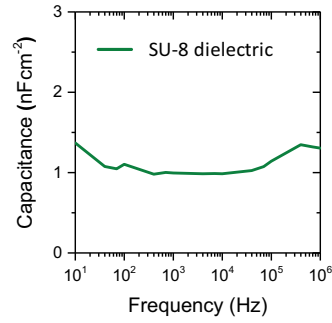


Figure 4.1. The specific capacitance of SU-8 dielectric (150 nm). The 1 nFcm⁻² of capacitance was obtained from the stable region (10³~10⁵ Hz).

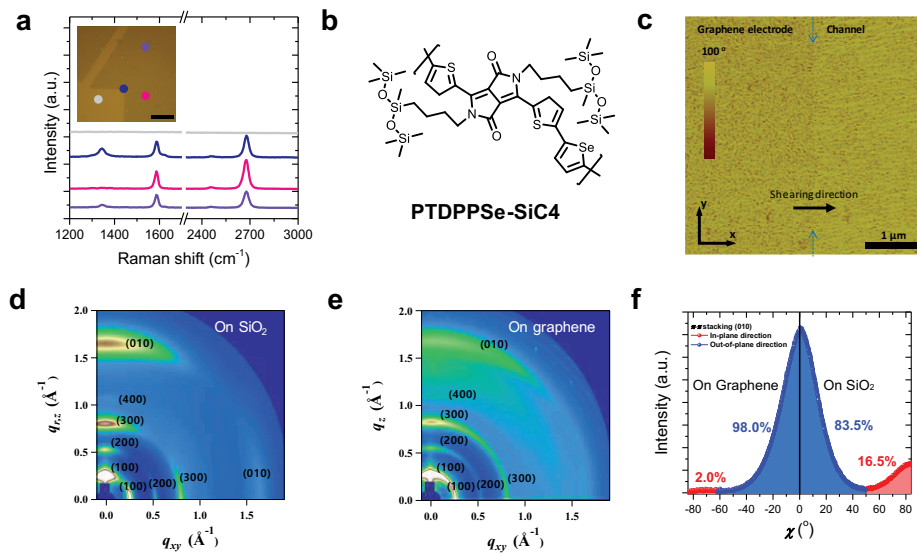


Figure 4.2. (a) Raman spectra of graphene electrode at different positions. The color of solid line corresponds to the same color position of inset. Inset: Optical image of patterned graphene using conventional photolithography and RIE on 300 nm SiO₂/n⁺Si wafer. Scale bar is 40 μ m. (b) The chemical structure of **PTDPPSe-SiC4**. (c) AFM image of **PTDPPSe-SiC4** solution-sheared film on graphene electrode (left) and Si wafer (right). Dashed blue arrows indicate the transition. 2D GIXD profiles of **PTDPPSe-SiC4** on (d) SiO₂ 300 nm wafer and (e) graphene. (f) Pole figure for (010) diffraction of **PTDPPSe-SiC4** on graphene and SiO₂ (where χ is defined as the semicircular angle between the crystallite orientation and the surface normal).

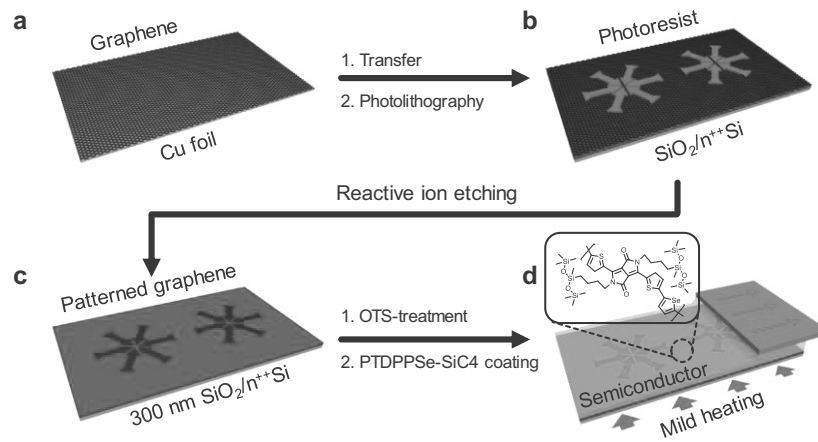


Figure 4.3. (a) Graphene was grown on Cu foil using chemical vapor deposition (CVD). CVD-grown graphene was transferred on the Si wafer and patterned (c) and etched away using reactive ion etching. The sample was treated with octadecyltrichlorosilane self-assembled monolayer. (OTS-SAM) (d) The polymer semiconductor, **PTDPPSe-SiC₄**, was deposited on the substrate by solution-shearing method.

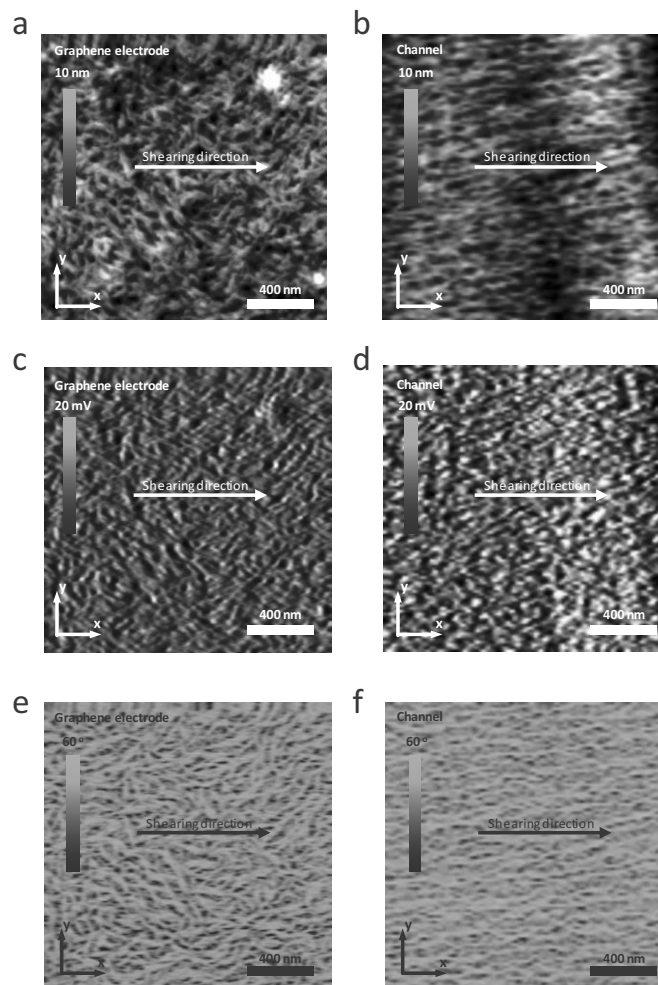


Figure 4.4. High-resolution AFM images of **PTDPPSe-SiC4** on graphene (a, c, e) and the SiO₂ wafer (b, d, f) after shearing coating. The height (a, b), amplitude (c, d) and phase (e, f) images of AFM. The shearing direction corresponds x axis.

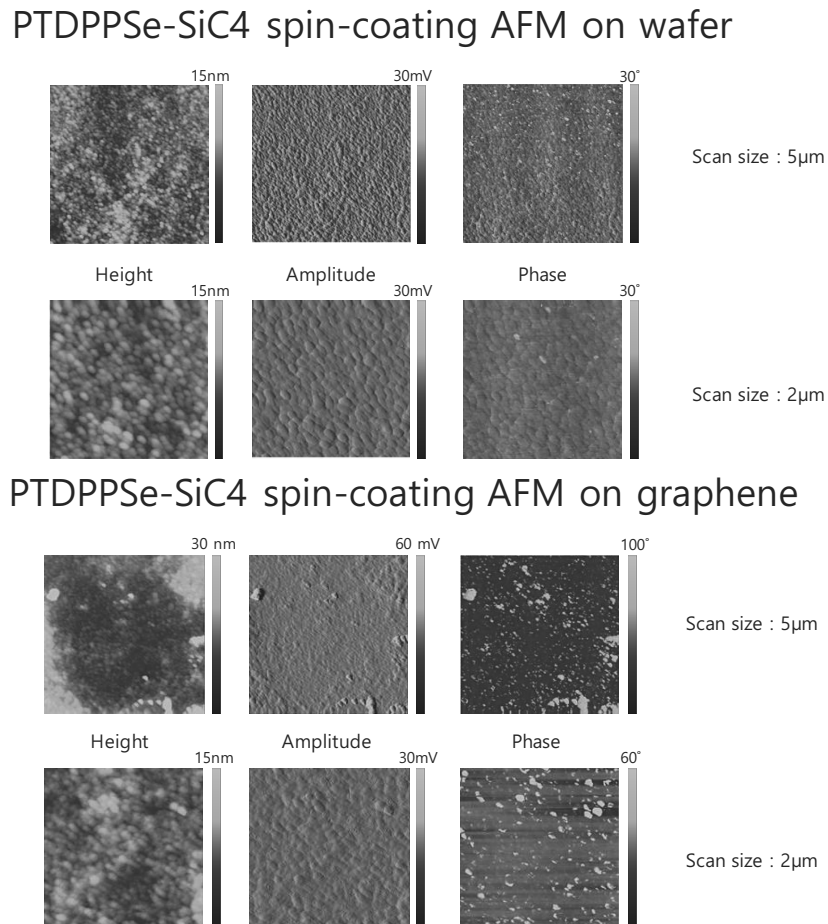


Figure 4.5. AFM images of the spin-coated **PTDPPSe-SiC4**. The **PTDPPSe-SiC4** film was coated on Si wafer (top) and graphene (bottom).

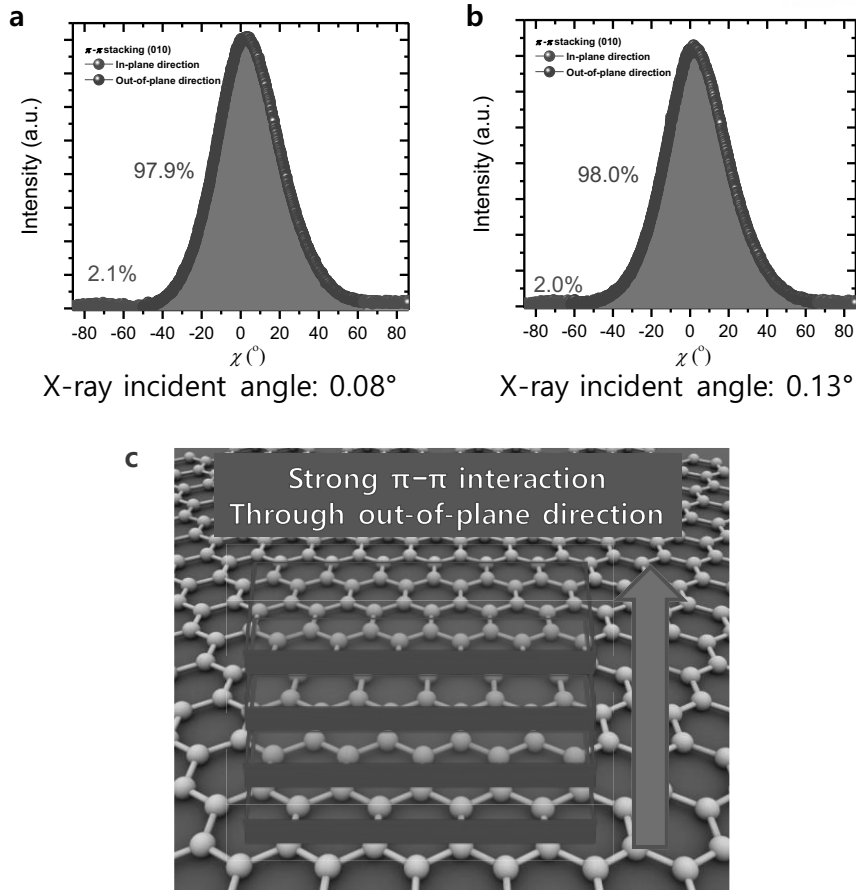


Figure 4.6. Pole figure for (010) diffraction of PTDPPSe-SiC4 on graphene. (a) 0.08° and (b) 0.13° as X-ray incidence angles. χ is defined as the semicircular angle between the crystallite orientation and the surface normal. (c) Proposed stacking illustration of PTDPPSe-SiC4 on graphene electrode.

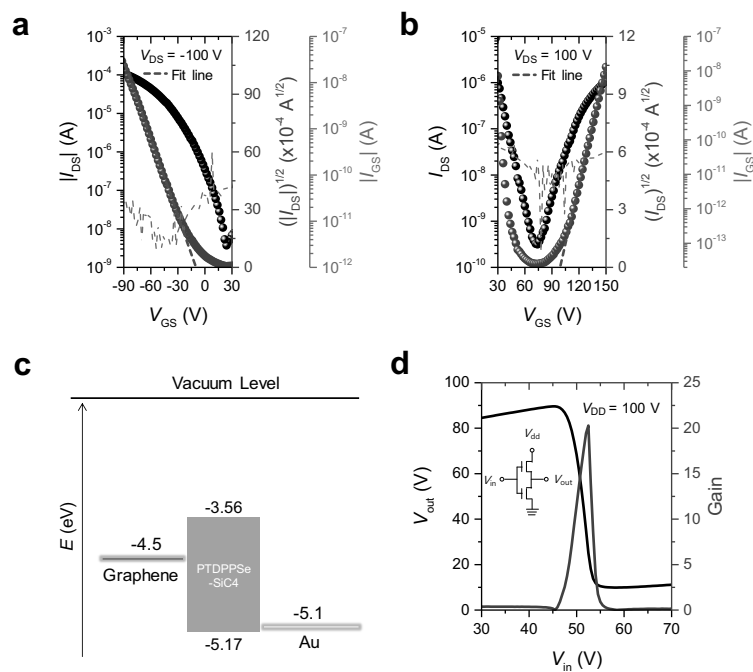


Figure 4.7. (a) The p-channel (under $V_{DS} = -100V$) and (b) n-channel (under $V_{DS} = 100V$) transfer characteristics of solution-sheared **PTDPPSe-SiC4** FETs with graphene electrodes on the OTS-treated 300 nm $SiO_2/n^{++}Si$ wafer. (c) Energy diagram of graphene, **PTDPPSe-SiC4** and gold. (d) OFET-based inverter characteristics of **PTDPPSe-SiC4** under $V_{DD} = 100 V$ (inset: schematic diagram of the complementary inverter structure).

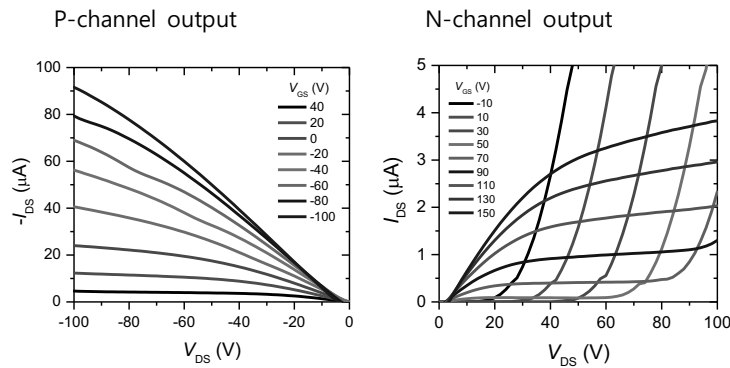


Figure 4.8. Output curves of **PTDPPSe-SiC4** on Si wafer. The p-channel (left) and n-channel (right) output curves ($I_{DS}-V_{DS}$) were obtained from transistors with graphene electrodes based on **PTDPPSe-SiC4** film prepared by solution shearing method.

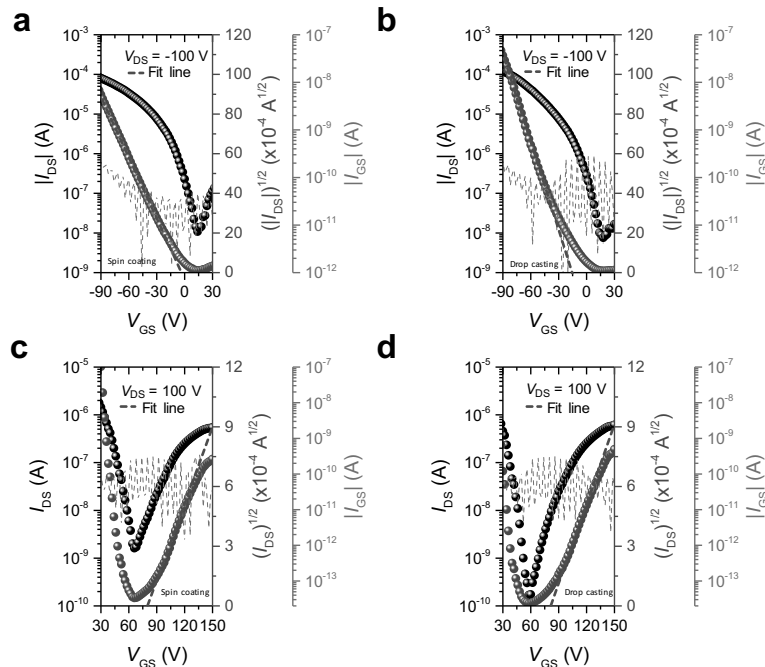


Figure 4.9. Transfer ($I_{DS}-V_{GS}$) characteristics of **PTDPPSe-SiC4** FETs with graphene electrodes. The **PTDPPSe-SiC4** FETs were made by spin coating for (a) p-channel and (c) n-channel, drop casting for (b) p-channel and (d) n-channel on OTS-treated 300 nm $SiO_2/n^{++}Si$ wafer.

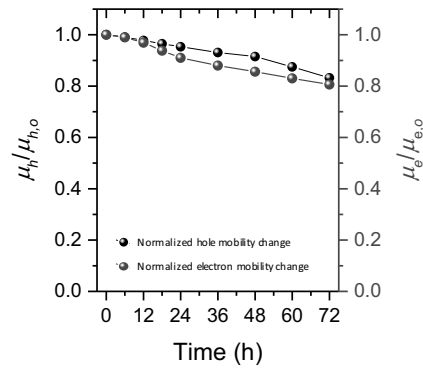


Figure 4.10. The stability test of the **PTDPPSe-SiC4** FET. The devices were stored in ambient condition and measured in vacuum condition ($\sim 10^{-6}$ torr).

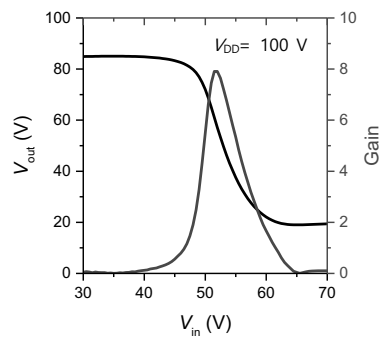


Figure 4.11. OFET-based inverter characteristics of **PTDPPSe-SiC4** FETs using Au electrodes.

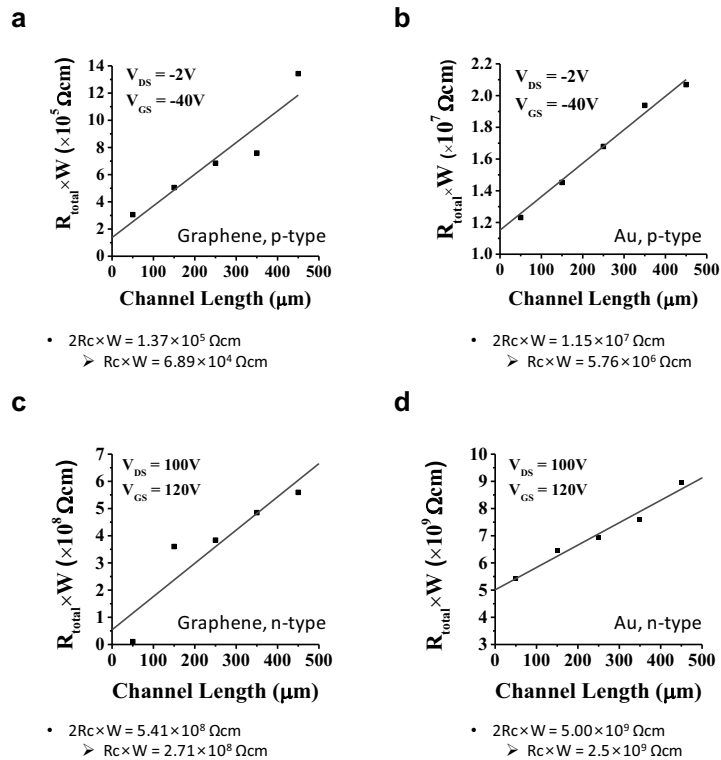


Figure 4.12. Width-normalized channel resistance measured using transfer line method (TLM). When channel length goes to 0, R_{total} becomes R_C which means contact resistance. The width of channel was 1000 μm . Width-normalized channel resistances of the OFET with graphene electrodes for (a) p-type and (c) n-type operations. Width-normalized channel resistances of the OFET with Au electrodes for (b) p-type and (d) n-type operations.

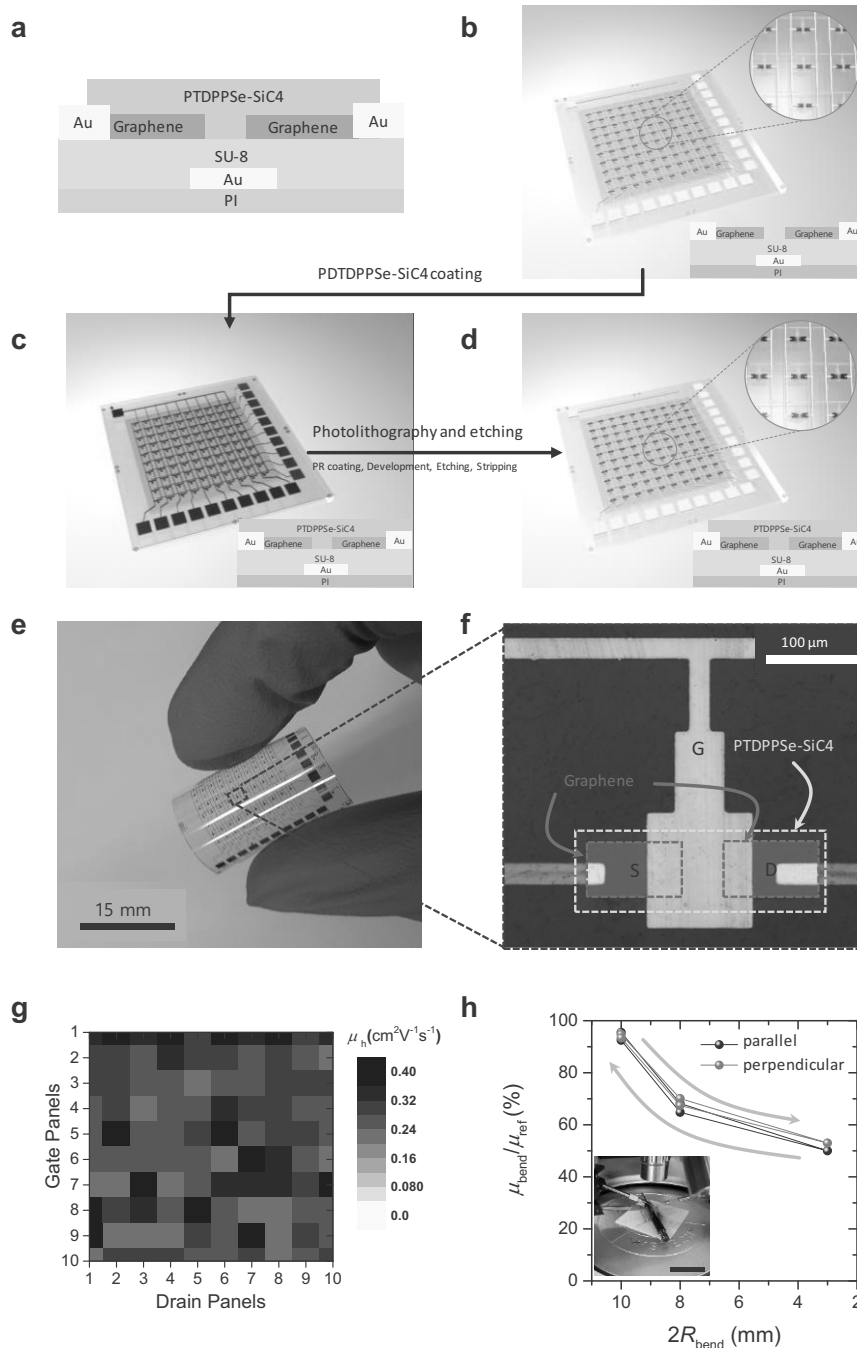


Figure 4.13. (a) Schematic BGBC transistor structure. (b) Graphene electrodes patterned on SU-8 dielectric layer. (c) PTDPPSe-SiC4 film was coated on the whole area of plastic substrate using solution-shearing. (d) PTDPPSe-SiC4 film was patterned by conventional photolithography. Insets are

schematic 3D illustration (top right) and structure (bottom right) of unit device from (b) to (d). Full device fabrication procedures can be found in Figure 4.11. (e) A photograph of 10 x 10 transistor on PI film. (f) An optical image of single transistor device from the blue rectangular area of Figure 4.13e. Channel width and length were 65 μm and 50 μm , respectively. (g) Hole mobility mapping on the 10 \times 10 flexible transistor arrays in ambient condition. (h) Normalized hole mobility changes with respect to the bending radius (R_{bend}) in parallel (black symbol) and perpendicular (red symbol) bending with respect to shearing direction. (Inset: a photograph of device measurement for investigating the effect of bending radius, scale bar = 30 mm).

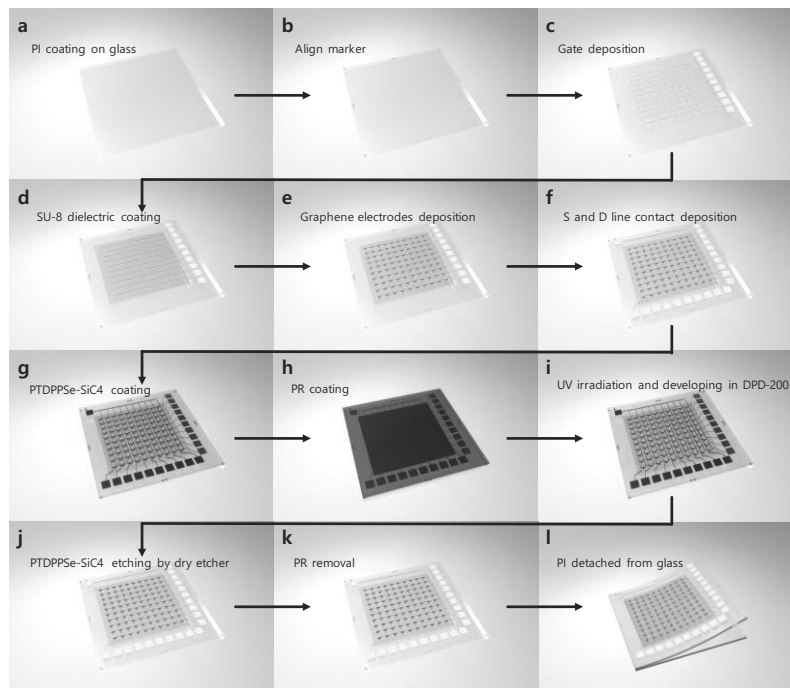


Figure 4.14. Schematic fabrication steps of transparent 10 x 10 transistor array on PI film. (a) Transparent polyimide was coated on a glass substrate. (b) Align marker (Cr/Au, 40 nm) were formed using photolithography. (c) Gate electrodes were formed using photolithography. (d) A diluted SU-8 solution in gamma-butyrolactone was patterned for the dielectric layer. (e) CVD-grown graphene electrodes as source and drain were transferred onto the substrate and patterned by photolithography and reactive ion etching to form channel gap. (f) Gold lines was deposited to connect graphene electrodes with contacts. (g) **PTDPPSe-SiC4** as a semiconductor layer was deposited by solution shearing. (h) Photoresist (DSAM-3000) was spin-coated. (i) The substrate was irradiated with UV through photomask and developed in DPD-200 developer, forming photoresist mask. (j) Unnecessary part of **PTDPPSe-SiC4** was etched away using dry etcher under the atmosphere of CF_4 . (k) Photoresist mask was removed in acetone. The substrate was washed away with DI water and nitrogen gas. (l) The device was detached from the glass substrate.

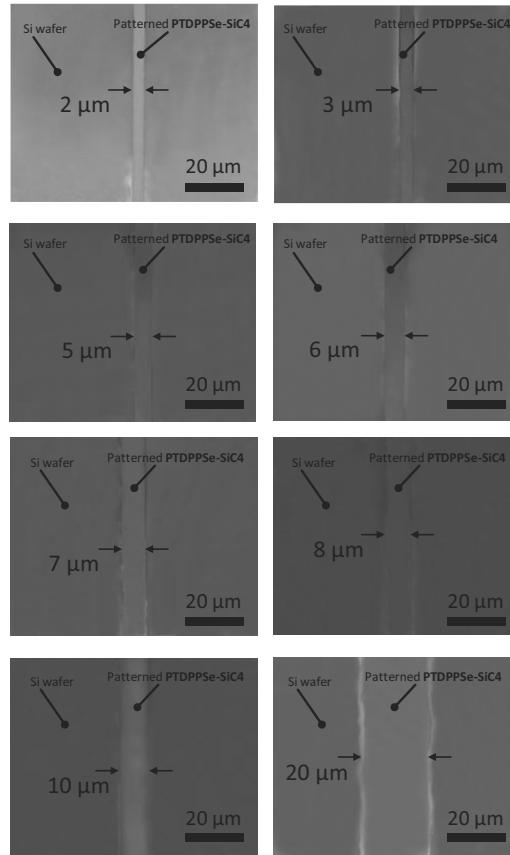


Figure 4.15. Optical images of line-patterned **PTDPPSe-SiC4** on Si wafer using conventional photolithography. The feature sizes of line pattern were varied from 2 to 20 μm .

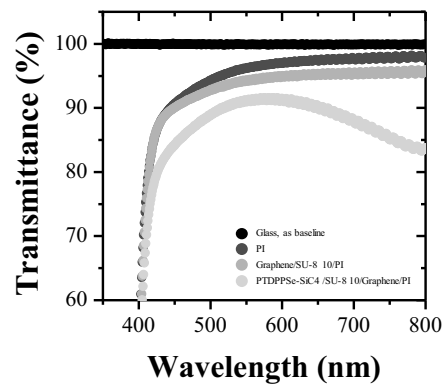


Figure 4.16. Transmittance of transparent devices with PI/Graphene/SU-8/ **PTDPPSe-SiC4**

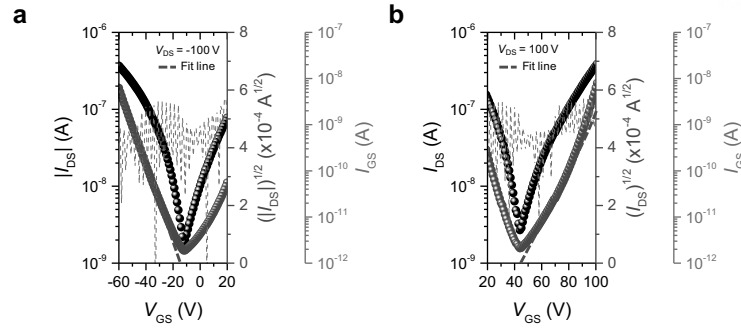


Figure 4.17. Transfer curves of PTDPPSe-SiC4 FETs prepared on flexible PI film. The transfer curve under (a) p-channel and (b) n-channel operation, respectively, was measured in an N₂ atmosphere.

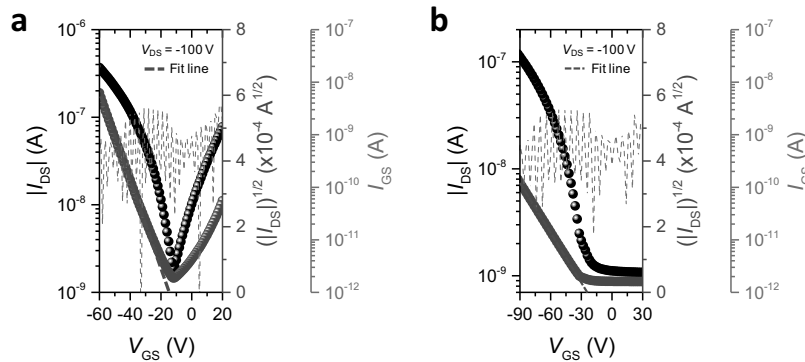


Figure 4.18. P-type transfer curves of PTDPPSe-SiC4 FET based on the flexible PI substrate measured in (a) N₂ condition and (b) ambient condition. $W/L = 65/50 \mu\text{m}$.

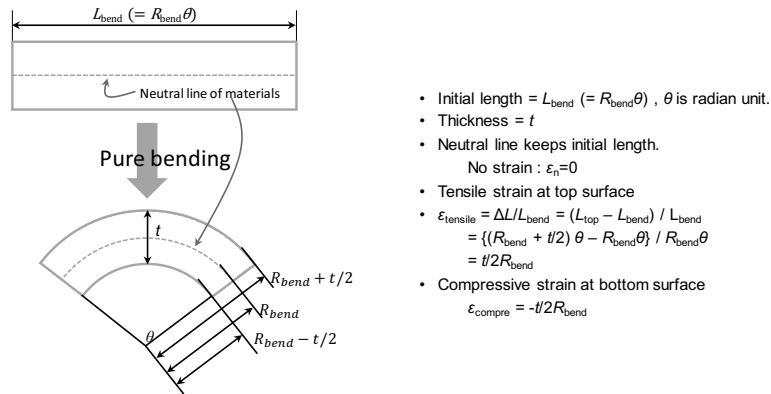


Figure 4.19. Calculation of tensile strain with respect to bending radius (R_{bend}).

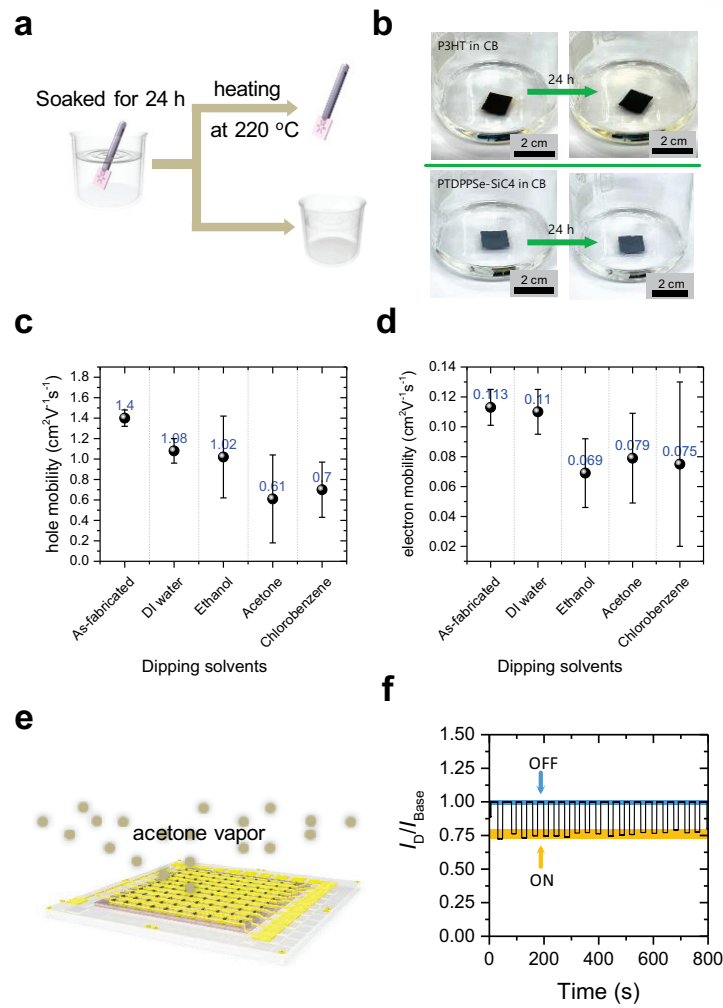


Figure 4.20. (a) Schematic illustration for demonstration of the solvent resistance. PTDPPSe-SiC4 transistors using graphene electrode were soaked in various solvents for 24 h. Then the solvents were removed by blowing N_2 gas and heating at $220\text{ }^\circ\text{C}$ in N_2 condition. (b) Photographs of **P3HT** and **PTDPPSe-SiC4** FETs after soaking in chlorobenzene (CB) for 24 h. (c) Hole and (d) electron mobility distributions of 10 measured devices after soaking in solvents for 24 h. (e) Schematic illustration for acetone sensing using a **PTDPPSe-SiC4** FET array. (f) I_D/I_{Base} changes upon on/off switching (20 cycles) of acetone vapors exposed to the device. Purple areas in the graph indicate the response upon exposing to 4 SLM of acetone vapor ($V_{\text{DS}} = V_{\text{GS}} = -100\text{ V}$).

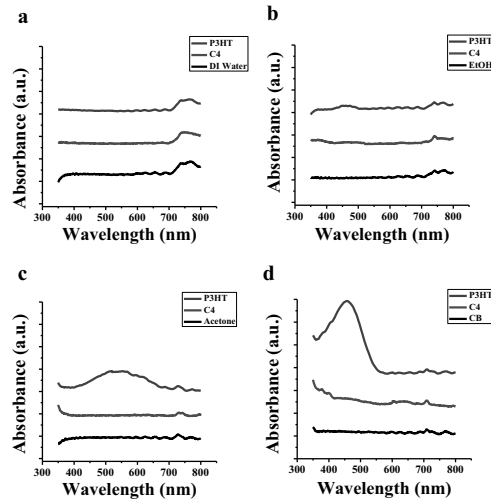


Figure 4.21. UV-Vis spectra to test the solvent-resistance of the deposited films before and after the polymer film coated wafers were soaked into various solvents. (a) DI water, (b) ethanol, (c) acetone and (d) chlorobenzene. The devices were soaked for 24 hours.

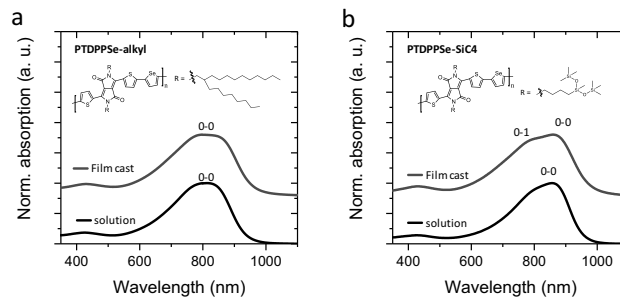


Figure 4.22. UV-vis absorption spectra of (a) **PTDPPSe-alkyl** and (b) **PTDPPSe-SiC4** in 1 mg mL^{-1} in chlorobenzene solution (black line) and film (red line). Insets in (a) and (b) are molecular structures of **PTDPPSe-alkyl** and **PTDPPSe-SiC4**, respectively.

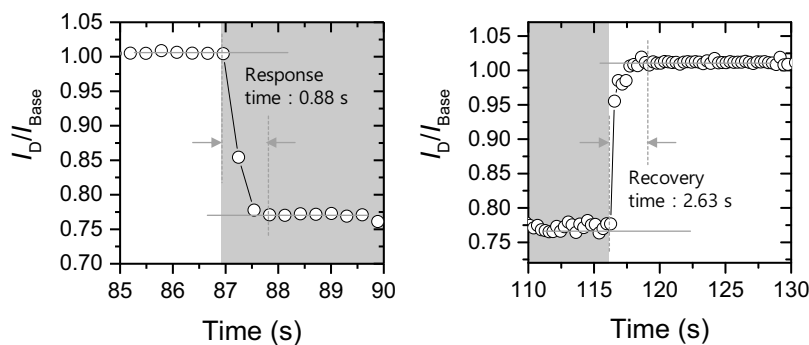


Figure 4.23. The evaluation of response time (left) and recovery time (right) of the **PTDPPSe-SiC4** based acetone sensor.

Table 4.1. OFETs performance of the devices with different electrodes. The p-channel and n-channel characteristics of FETs on OTS-treated SiO₂ (300 nm)/n⁺⁺Si wafer were measured with $V_{DS} = -100$ and 100 V, respectively. The electrical measurement was performed in nitrogen atmosphere. In the case of spin-coating and solution-shearing method, device yield was 100%. In the case of drop-casting, device yield was 71% due to the film thickness issue (5 fabricated out of 7 devices).

	Film Condition ^a	$\mu_{h,avg}$ [cm ² V ⁻¹ s ⁻¹]	$\mu_{h,max}$ [cm ² V ⁻¹ s ⁻¹]	$I_{on}/I_{off,h}$	$\mu_{e,avg}$ [cm ² V ⁻¹ s ⁻¹]	$\mu_{e,max}$ [cm ² V ⁻¹ s ⁻¹]	$I_{on}/I_{off,e}$
Graphene electrodes	Spin-coated	0.56 (±0.22) ^b	0.86	> 10 ⁴	0.06 (±0.05)	0.11	> 10 ³
	Drop-casted	0.79 (±0.27)	1.17	> 10 ⁴	0.09 (±0.08)	0.22	> 10 ³
	Solution-sheared	1.00 (±0.26)	1.43	> 10 ⁵	0.20 (±0.10)	0.37	> 10 ²
Gold electrodes	Spin-coated	0.29 (±0.03)	0.33	> 10 ⁵	0.004 (±0.002)	0.007	> 10 ³
	Drop-casted	0.31 (±0.09)	0.43	> 10 ⁴	0.004 (±0.002)	0.009	> 10 ²
	Solution-sheared	0.33 (±0.08)	0.54	> 10 ⁵	0.004 (±0.002)	0.009	> 10 ²

^aFor each condition, 7 devices were calculated for statistical information.

^bThe standard deviation

Table 4.2. Comparison of electrical properties before and after soaked in various solvents for 24 hours. Properties of as-fabricated devices were measured before soaked in solvents. Then the devices properties were measured again after soaking in various solvents (DI water, ethyl alcohol, acetone and chlorobenzene) for 24 h and heating the devices at 220 °C under N₂ condition.

	$\mu_{h,max}$ [cm ² V ⁻¹ s ⁻¹]	I_{on}/I_{off}	$\mu_{e,max}$ [cm ² V ⁻¹ s ⁻¹]	I_{on}/I_{off}
As-fabricated	1.40	> 10 ⁵	0.113	> 10 ⁴
DI water	1.08	> 10 ⁵	0.110	> 10 ³
Ethyl alcohol	1.02	> 10 ⁵	0.069	> 10 ³
Acetone	0.61	> 10 ⁶	0.079	> 10 ²
Chlorobenzene	0.70	> 10 ⁴	0.075	> 10 ³

Chapter 5. Reduced Pyronin B Doping on Graphene and Organic Semiconductor

5.1. Introduction

2-dimensional (2D) nanomaterials and organic semiconductors are highly promising materials as a semiconductor component for flexible electronics. Particularly, high potential of organic semiconductors for low-cost flexible electronics has driven extensive investigation in organic field-effect transistors (OFETs). The realization of integrated logic circuits requires the development of both p-channel and n-channel semiconductors. Doping process is an essential step for the fabrication of high performance complementary metal oxide semiconductor (CMOS) devices as well as the enhancement of the conductivity. Organic integrated logic circuits require the development of both organic p-type and organic n-type dopants to improve the device performance and tune the electrical properties while minimizing damages on the semiconductor during the deposition of dopants. Thus, surface transfer doping which is a nondestructive doping technique has been applied instead of interstitial doping in organic electronics.^[1, 2]

Organic n-type dopants have rarely been developed compared with p-type organic dopants. Organic n-type dopants with energetically highly lying highest occupied molecular orbital (HOMO) level are necessary for electrons to be easily transferred to the lowest unoccupied molecular orbital (LUMO) of organic semiconductor. Organic n-type dopants with high HOMO levels generally show instability in ambient condition due to the characteristic of easy degradation by oxygen and water molecules in air.^[3] Such air instability in organic n-type dopants significantly delayed the development of n-type organic dopants in organic electronics.

To facilitate electron transport of n-type organic semiconductors, solution-processable organic n-type dopants are widely employed as a surface transfer dopant. A reduced benzyl viologen by NaBH₄ which is a strong reducing agent was utilized in carbon nanotube,^[3] graphene^[4] and transition metal dichalcogenides (TMDCs).^[5] A charged state of viologen was reduced by NaBH₄ in water to a neutral state of benzyl viologen which was transferred separately to toluene, resulting in a toluene solution containing the reduced benzyl viologen.^[3] Surface transfer n-type doping effect was observed when the reduced benzyl viologen was coated on semiconductors. However, the instability of the dopant hampers the utilization in electronics without high concentration.

For air-stable organic n-type dopants, the application of air-stable precursor molecules releasing the n-type dopant compound in blend with a matrix material has been proposed. The air-stable thin film transistors n-type doped by 1H-benzoimidazole derivatives have been reported.^[6-8] (4-(1,3-dimethyl-2,3-dihydro-1H-benzoimidazol-2-yl)phenyl)dimethylamine (N-DMBI) improved air-stability of N-DMBI-doped n-channel OTFTs by solution processing. However, for low concentration, the doping

effect is not efficient compared to air-unstable n-type dopants at low concentration. On the other hand, remaining chemical reaction products contained in thin film hamper the charge transport at high doping concentration.

Polyethylene imine (PEI) containing simple aliphatic amine groups electron-donating functional group in polymer branch has been widely utilized to n-type doped graphene^[9-11] and carbon nanotube.^[12] PEI behaves as long-range scatterers on graphene which create homogeneous potentials to cause conductance suppression of hole carrier type.^[13] New strategy for PEI as n-type dopant in graphene electronics should be applied to circumvent the conductance suppression of hole carriers.

Pyronin B (PyB), an organic cationic dye, can be transformed into its leuco form upon a heating under vacuum.^[14-17] The leuco form of PyB can behave as an effective n-type dopant in organic electronics. However, leuco form of PyB turns back to the original state under ambient condition.

Herein, we have developed a solution-based organic n-type dopant using PyB. A charged state of PyB was reduced by NaBH₄ in water to a neutral state of PyB which was transferred to toluene, resulting in a toluene solution containing a reduced PyB (rPyB) in a bisolvent system. The rPyB shows an effective n-type doping effect on graphene as active layer and electrodes in FET and a commercially available n-type organic semiconductor, N2200. The doping effect with respect to the rPyB was characterized via UV-vis spectroscopy, Kelvin probe spectroscopy and Ultraviolet photoemission spectroscopy (UPS). Upon the doping of rPyB on graphene, reduced contact resistance between graphene and Au electrodes was observed. With an advantage of solution-processability, simple selective stamping doping using rPyB solution and polydimethylsiloxane (PDMS) mold was performed on 16 × 16 graphene FET array in ambient condition. The stamping-doped graphene FET array show highly stable electrical performance in ambient condition for 90 days.

5.2. Experimental Section

Materials and Instrumentation. All starting materials were purchased either from Aldrich or Alfa Aesar and used without further purification. All solvents were ACS grade unless otherwise noted. An Agilent 5500 scanning probe microscope running with a Nanoscope V controller was used to obtain AFM images. AFM images were recorded in a high-resolution tapping mode under ambient conditions. Raman spectroscopy was conducted at a wavelength of 532 nm (WITec, Micro Raman). KP mapping was obtained from the Kelvin probe and air photoemission system (APS02-5050, KP Technology Ltd). ESCALAB 250XI of Thermo Fisher Scientific was utilized to measure UPS data under vacuum, $\sim 1 \times 10^{-10}$ torr.

The synthesis of rPyB. 0.01 mg of PyB was dissolved in 10 mL of deionized water, followed by an addition of 10 mL of toluene to form biphasic solution. NaBH₄ in water (200 mM) was added to the biphasic solution. The resulting biphasic solution was left for a day. The dark purple color of PyB in deionized water turned transparent after reaction. The toluene phase was carefully separated using pipet.

The fabrication of graphene electrodes. Graphene film was grown on a copper foil (0.025 mm thickness) by conventional chemical vapor deposition (CVD) method using H₂ and CH₄ gas. After growth of graphene, PMMA was coated on graphene surface to support graphene for further process. Copper foil was etched by ammonium persulfate ((NH₄)₂S₂O₈) aqueous solution (0.1 M). After copper foil was etched away, PMMA/graphene had been transferred on the substrate and annealed at 130 °C for 30 min. Then PMMA was removed using acetone. To pattern the transferred graphene film, photolithography technique was used. A positive PR (DSAM-3037, Dongjin Semichem) was spin-coated on the graphene film (4000 rpm for 30s), and annealed at 100 °C for 60 s. UV light was illuminated on the PR with a photomask and the pattern was developed using 2.15 % TMAH solution. The graphene area without patterned PR was etched away using RIE plasma (100 W for 5 s). The stripper of PR removed the remained PR. The channel width and length were 200 and 50 μm, respectively.

The fabrication of graphene and N2200 FETs. For the fabrication of graphene FETs, CVD-grown graphene was transferred onto a SiO₂/n⁺⁺Si wafer. PMMA to support graphene was removed by acetone. Au electrodes were thermally deposited via shadow masks. The channel width and length were 200 and 50 μm, respectively. For the fabrication of N2200 FETs, commercially available polymer semiconductor, N2200 (Polyera Corporation), was dissolved in chlorobenzene (3 mg mL⁻¹). The solution was spin-coated at 3000 rpm in N₂ atmosphere. The N2200 film was placed in vacuum oven at 130 °C for 1 day.

Electrical Measurement. The electrical performance of rPyB doped graphene FETs and N2200 FETs was measured under ambient condition using a Keithley 4200-SCS semiconductor parametric analyzer. The transistors were operated in the linear regime ($V_{DS} = 1$ V), and the field-effect mobility (μ) was calculated using the following equation:

$$I_{DS} = \frac{W}{L} \mu C_g V_{DS} (V_{GS} - V_T)$$

where I_{DS} is the drain current, W is the channel width, L is the channel length, μ is the mobility, C_g is the capacitance of the gate dielectric, V_{DS} is the source-drain voltage, V_{GS} is the gate voltage, and V_T is the threshold voltage, respectively.

Width-normalized channel resistance of the devices with graphene electrodes and Cr/Au electrodes were measured using a TLM method. The electrical properties of 10 × 10 FET array device on a transparent PI were measured in ambient conditions. Acetone vapor sensing experiment was conducted under ambient condition. For vaporization of acetone, N₂ gas was flowed into a flask filled with liquid-phase acetone. Then the surface of the device was exposed to the acetone vapor flowed through a tube connected to the sensor device. Nitrogen gas flow was maintained at 4 SLM during sensing. Capacitance of SU-8 10 gate dielectric was measured using a high power electrochemical analyzer (Ivium Stat).

5.3. Results and Discussion

Figure 5.1a-1c are synthesis schemes of rPyB. A chemical structure of PyB is shown in Figure 5.1d. As purchased, PyB molecules are cationic dyes with FeCl_4^- . PyB solution in water was prepared in water (concentration: 0.01 mg/mL, volume: 10 mL). Then an addition of 10mL toluene was followed on top of PyB solution, resulting in biphasic solution as shown in Figure 5.1a (top layer: toluene solution, bottom layer: PyB solution). 2 mg of NaBH_4 was added into the resulting biphasic solution (Figure 5.1b). After the reaction for 24 h, transparent toluene solution containing rPyB was separated from the biphasic solution as shown in Figure 5.1c. The rPyB solution was kept in ambient condition for 1 week in order to check the stability of the rPyB solution. No color change in the rPyB solution was observed, indicating that rPyB was stable in ambient condition for a long time (Figure 5.2). A drop of the synthesized rPyB solution ($\sim 5 \mu\text{L}$) was spin-coated on the chemical vapor deposition (CVD)-grown graphene film supported on 300 nm $\text{SiO}_2/\text{n}^+\text{Si}$ wafer. Toluene solvent was removed by annealing at 120 °C for 10 min in air

The black and red lines in Figure 5.3a are the ultraviolet-visible (UV-vis) spectra of PyB in water and rPyB in toluene. Each line is base-lined by the water and toluene solvent, respectively. The absorption band shapes were changed after the reduction of PyB for 24 h. Before the treatment of reduction of PyB using sodium borohydride (NaBH_4), the maximum absorption intensity appeared at the 553 nm. After the reduction of the PyB using NaBH_4 , the peak at the 553 nm disappeared, a new absorption peak at 366 nm was observed. These results indicated a new optical energy state was formed after the reduction treatment. The transmittance of pure graphene film and the graphene films coated with rPyB dopant (Figure 5.3b). The transmittance of CVD grown graphene was 96.6 % at 550 nm. On the other hand, the transmittance of 1 time rPyB-coated graphene film was 93.2 % at 550 nm. Increasing the number of rPyB coating on the graphene, optical transmittance was decreased from 93.2 % for 1 time rPyB coating to 79.3 % for 4 time rPyB coating on graphene.

Raman spectroscopy was utilized to characterize the effect of rPyB doping on graphene (Figure 5.3c). Our pristine graphene film exhibited 2D peak ($\sim 2683 \text{ cm}^{-1}$) and G peak ($\sim 1592 \text{ cm}^{-1}$). After doping of rPyB on graphene, 2D peak was down-shifted to $\sim 2677 \text{ cm}^{-1}$. On the other hand, G peak was up-shifted to 1602 cm^{-1} . Those Raman shifts are consistent with previous n-type doping results on graphene.^[18-20] Upon the increasing the number of rPyB coating, Raman signal was enhanced shown in Figure 5.4, which is similar to surface enhanced Raman scattering (SERS). This phenomenon would be attributed to graphene-enhanced Raman scattering (GERS).^[21-25] rPyB molecules were chemically enhanced through a charge transfer between rPyB and graphene substrate for the GERS.^[21-25] It is noteworthy that D peak ($\sim 1340 \text{ cm}^{-1}$) intensity was barely changed after the doping, indicating defects was not formed on the graphene surface.

The investigation of the electrostatic properties was performed using Kelvin probe force microscopy (KPFM) in ambient condition. To estimate work function (WF) of samples, a direct current is applied

to the sample to nullify the contact potential difference between the KPFM tip and the sample surface, thus the sample should be prepared on a conductive substrate.^[26-29] Gold film (WF = 5.1 eV) was measured as a reference. Figure 5.3d and Figure 5.3e illustrate the work function mapping scanned KPFM before and after doping of rPyB on graphene film in ambient condition, respectively. Pristine graphene film shows 4.62 eV of average WF over 100 positions. rPyB-coated graphene exhibits 4.48 eV of average WF over 100 positions. After coating of rPyB, uniform n-type doping effect have been observed over the graphene film. We further investigated the effect of the number of coating of rPyB on graphene as shown in Figure 5.5. We found the WF was reduced up to 4.39 eV at 4 coating of rPyB in ambient condition.

Figure 5.6a and b show the transfer characteristics of the pristine graphene film and rPyB doped graphene film devices, respectively. The Dirac point (V_{Dirac}) where charges are neutralized was shifted from +39 V to -20 V upon coating with rPyB, indicating that rPyB effectively acts as an n-type dopant. The charge carrier mobility (μ_{FE}) was calculated by using the following Equation 1:

$$\mu_{FE} = \frac{g_m L}{V_{DS} W C_g}$$

where g_m is the transconductance, V_{DS} is the source-drain voltage, L is the channel length, W is the channel width, and C_g is the capacitance per unit area of the total gate dielectric layer. The typical device performance was measured under the following parameters: $W = L = 50 \mu\text{m}$, $C_g = 1.08 \times 10^{-8} \text{ Fcm}^{-2}$, $V_{DS} = 1 \text{ V}$. The hole and electron mobilities were 810 and 264 $\text{cm}^2\text{V}^{-1}\text{s}^{-1}$ for the pristine graphene in air condition, respectively (Figure 5.6a). After the coating of rPyB on graphene FET, the hole and electron mobilities were both increased to 2,387 and 602 $\text{cm}^2\text{V}^{-1}\text{s}^{-1}$, respectively.

In addition, we fabricated organic field effect transistors (OFETs) using pristine graphene (Figure 5.6c) and rPyB doped graphene (Figure 5.6d) as electrodes. Polymeric semiconductor film was prepared by spin coating a commercially available n-type semiconductor, N2200 (Polyera Corporation), in chlorobenzene (5 mg/mL) at spin rate of 3000 rpm on a OTS treated 300 nm $\text{SiO}_2/\text{n}^+\text{Si}$ wafer where graphene electrodes were patterned. The coated N2200 film was annealed at 150 °C for 2 h under vacuum. The electron mobility was 6.2×10^{-3} and $1.3 \times 10^{-2} \text{ cm}^2\text{V}^{-1}\text{s}^{-1}$ for graphene electrodes and rPyB doped graphene electrodes, respectively. The notable difference of those two devices are the huge increase on/off ratio and the increase of the transconductance (g_m). In addition, fast saturation was observed in the rPyB-doped case. This is attributed to the lowering of the work function of graphene electrodes using rPyB matched with lowest unoccupied molecular orbital (LUMO).

The OFETs were fabricated with Au electrodes and rPyB-doped Au. However, electrical performances were barely changed before and after coating of rPyB as shown in Figure 5.7. From the results, it is noteworthy that rPyB molecules has an interaction with conjugated system. rPyB solution was mixed with N2200 solution in order to investigate the rPyB doping effect on N2200 FETs, changing the weight percent of rPyB in N2200 solution from 1 to 50 %. Increasing the rPyB percent in N2200

solution, the electrical performance was degraded shown in Figure 5.8. Atomic Force Microscopy (AFM) images of the N2200 films mixed with rPyB revealed that the increased rPyB molecules hindered the formation of fibril structure on N2200 (Figure 5.9).

rPyB was applied to the interface between N2200 and parylene dielectric layers (500 nm) in bottom contact top gate (BCTG) configuration. Transfer curve of N2200 FET in BCTG (Figure 5.6e) shows electron mobility and on/off ratio are $1.2 \times 10^{-3} \text{ cm}^2\text{V}^{-1}\text{s}^{-1}$ and 1.4×10^7 , respectively. In the case of rPyB doped at the interface between N2200 and parylene dielectric layers (Figure 5.6f), electron mobility and on/off ratio are $6.4 \times 10^{-2} \text{ cm}^2\text{V}^{-1}\text{s}^{-1}$ and 4.9×10^4 , respectively. The increased mobility and reduced on/off ratio clearly demonstrated the effect of rPyB as an n-type dopant.

To investigate the energy level alignment and interfacial electronic structure of rPyB film on graphene, Ultraviolet photoelectron spectroscopy (UPS) was performed at a base pressure of 10^{-10} torr using He I excitation lines (21.22 eV) from a Helium discharge lamp for a close examination of the interfacial contact between rPyB and the graphene film. The work functions of the pristine graphene and rPyB doped graphene films were estimated to be 4.50 and 3.98 eV, respectively, as shown in Figure 5.10a. The results indicated an interfacial charge transfer from the n-type dopant to the underlying graphene.^[30, 31] This difference between the ionization potential of graphene and the electron affinity of the rPyB film can lead to charge transfer and carrier doping effects at the interface. Figure 5.10b is illustration of energy level of graphene and rPyB on graphene. As shown in Figure 5.10b, the potential difference (0.54 eV) at the interface causes the electrons from the rPyB to diffuse into the graphene film. The vacuum level was shifted after doping of rPyB due to the interfacial dipole formation resulting electron transfer from rPyB to graphene. It is noteworthy that KP and UPS data were obtained at ambient and high vacuum condition, respectively. Thus, the discrepancies between the KP and UPS experiments are caused by the different atmosphere and experimental condition. The highest occupied molecular orbital (HOMO) and lowest unoccupied molecular orbital (LUMO) of N2200 were -5.36 and -3.91 eV, respectively.^[32, 33] Electrons are transported from the source to drain electrodes through LUMO in n-type transistors. The injection barrier between LUMO level and WF of electrodes should be reduced to promote an effective charge transport. The injection barrier was reduced from 0.59 to 0.07 eV when rPyB-doped graphene was used. The reduce injection barrier resulted in a fast saturation and enhanced electrical properties of N2200 FETs.

The air stability of organic n-type dopant is very crucial for commercialization of organic electronics. The electron mobility of graphene FETs with various rPyB-coating from one to four times were monitored for 90 days (Figure 5.10d). In the case of 1 coating of rPyB, the electron mobility was maintained up to 75 % after 90 days. The electron mobility was maintained up to 97 % after 90 days in the case of 4 coatings of rPyB, demonstrating the air stability of rPyB.

To demonstrate the simple and effective graphene doping on large-area array system, stamping doping using polydimethylsiloxane (PDMS, Dow Chemical) was applied. 16×16 graphene FET array

was fabricated on the 300 nm SiO₂/n⁺⁺Si wafer. SU-8 mold, commercially available epoxy photoresist (PR), was prepared via conventional photolithography. The detailed size of the bump in PDMS stamp is 500 μm of diameter and 20 μm of height as shown in Figure 5.11. The fabricated PDMS stamp was soaked in the rPyB dopant solution for 1 min. After annealing the PDMS stamp to remove toluene solvent, the stamp was placed on top of the 16 × 16 graphene FET array (Figure 5.12a and b). After detaching the PDMS stamp from the 16 × 16 graphene FET array, transfer curves of graphene FET were obtained shown in Figure 5.13. As-fabricated device shows p-doped behavior due to the fabrication process of 16 × 16 graphene FET array which contains photolithography PR to result p-doping. Dirac point could not be observed with the gate swipe range of -60 to +60 V (Figure 5.13a). After rPyB doping using the PDMS stamp, Dirac point was placed at +9 V, showing that n-type doping using stamping was successful (Figure 5.13b). To exploit the advantage of the stamping doping, spare PDMS pieces were placed at the corner of the array to give enough space between the PDMS stamp and the 16 × 16 graphene FET array. The center part of the PDMS stamp had been touched with a fingertip to induce the stamping doping on the area of center of the 16 × 16 graphene FET array as shown in Figure 5.12c. Before the stamping doping, V_{Dirac} was not observed with the gate swipe range of -60 to +60 V (Figure 5.12d). After the stamping doping, V_{Dirac} was observed around ~9 V of gate voltage (Figure 5.12e). This demonstrated successful selective stamping doping with the fingertip using rPyB.

5.4. Conclusion

In conclusion, a solution-processable organic n-type dopant was synthesized via a simple chemical reaction using PyB as an organic cation dye and NaBH₄ as a reducing agent. The synthesized organic cationic dye, rPyB, was applied to graphene FETs and OFETs with the N2200 polymeric n-type semiconductor. The rPyB dopant is highly effective to graphene due to the infinite conjugated system. Raman spectroscopy, KPFM and UPS confirmed that surface transfer rPyB doping on graphene and N2200 could be used to tune the WF of graphene and the charge transport of N2200 in the transistors. The electron mobility of graphene FETs with 4 times coating of rPyB were maintained up to 97.8 % for 90 days, resulting rPyB are highly stable. Finally, 16 × 16 graphene FET array was rPyB-doped using PDMS stamp. By touch the center of the PDMS stamp with a fingertip, only center area of 16 × 16 graphene FET array was selectively rPyB-doped. This work demonstrates a significant advance in the field of the organic doping synthesis for next generation high-performance graphene and organic electronics by providing a significant step forward in materialization of the low-cost n-type doping synthesis.

5.5. References

- [1] K. Takei, R. Kapadia, Y. Li, E. Plis, S. Krishna, A. Javey, *J. Phys. Chem. C* **2013**, *117*, 17845.
- [2] W. Chen, D. Qi, X. Gao, A. T. S. Wee, *Prog. Surf. Sci.* **2009**, *84*, 279.

- [3] S. M. Kim, J. H. Jang, K. K. Kim, H. K. Park, J. J. Bae, W. J. Yu, H. Lee Ii, G. Kim, D. D. Loc, U. J. Kim, E. H. Lee, H. J. Shin, J. Y. Choi, Y. H. Lee, *J. Am. Chem. Soc.* **2009**, *131*, 327.
- [4] W. J. Yu, L. Liao, S. H. Chae, Y. H. Lee, X. Duan, *Nano Lett.* **2011**, *11*, 4759.
- [5] D. Kiriya, M. Tosun, P. Zhao, J. S. Kang, A. Javey, *J. Am. Chem. Soc.* **2014**, *136*, 7853.
- [6] P. Wei, J. H. Oh, G. Dong, Z. Bao, *J. Am. Chem. Soc.* **2010**, *132*, 8852.
- [7] B. D. Naab, S. Himmelberger, Y. Diao, K. Vandewal, P. Wei, B. Lussem, A. Salleo, Z. Bao, *Adv Mater* **2013**, *25*, 4663.
- [8] S. Zhang, B. D. Naab, E. V. Jucov, S. Parkin, E. G. B. Evans, G. L. Millhauser, T. V. Timofeeva, C. Risko, J. L. Brédas, Z. Bao, S. Barlow, S. R. Marder, *Chemistry - A European Journal* **2015**, *21*, 10878.
- [9] Y. Zhang, Y. Liang, J. Zhou, *Acta Chim. Sinica* **2014**, 367.
- [10] Y. Zhou, C. Fuentes-Hernandez, J. Shim, J. Meyer, A. J. Giordano, H. Li, P. Winget, T. Papadopoulos, H. Cheun, J. Kim, M. Fenoll, A. Dindar, W. Haske, E. Najafabadi, T. M. Khan, H. Sojoudi, S. Barlow, S. Graham, J. L. Brédas, S. R. Marder, A. Kahn, B. Kippelen, *Science* **2012**, *336*, 327.
- [11] Y. Choi, Q. Sun, E. Hwang, Y. Lee, S. Lee, J. H. Cho, *ACS Nano* **2015**, *9*, 4354.
- [12] M. Shim, A. Javey, N. W. S. Kam, H. Dai, *J. Am. Chem. Soc.* **2001**, *123*, 11512.
- [13] D. B. Farmer, G. M. Roksana, V. Perebeinos, Y. M. Lin, G. S. Tuievski, J. C. Tsang, P. Avouris, *Nano Lett.* **2009**, *9*, 388.
- [14] J. H. Oh, P. Wei, Z. Bao, *Appl. Phys. Lett.* **2010**, *97*, 243305.
- [15] C. K. Chan, E. G. Kim, J. L. Brédas, A. Kahn, *Adv. Funct. Mater.* **2006**, *16*, 831.
- [16] A. Werner, F. Li, K. Harada, M. Pfeiffer, T. Fritz, K. Leo, S. Machill, *Adv. Funct. Mater.* **2004**, *14*, 255.
- [17] A. G. Werner, F. Li, K. Harada, M. Pfeiffer, T. Fritz, K. Leo, *Appl. Phys. Lett.* **2003**, *82*, 4495.
- [18] P. Wei, N. Liu, H. R. Lee, E. Adijanto, L. Ci, B. D. Naab, J. Q. Zhong, J. Park, W. Chen, Y. Cui, Z. Bao, *Nano Lett.* **2013**, *13*, 1890.
- [19] A. Das, S. Pisana, B. Chakraborty, S. Piscanec, S. K. Saha, U. V. Waghmare, K. S. Novoselov, H. R. Krishnamurthy, A. K. Geim, A. C. Ferrari, A. K. Sood, *Nat. Nanotechnol.* **2008**, *3*, 210.
- [20] S. Pisana, M. Lazzeri, C. Casiraghi, K. S. Novoselov, A. K. Geim, A. C. Ferrari, F. Mauri, *Nat. Mater.* **2007**, *6*, 198.
- [21] L. M. Malard, M. A. Pimenta, G. Dresselhaus, M. S. Dresselhaus, *Physics Reports* **2009**, *473*, 51.
- [22] F. Schedin, E. Lidorikis, A. Lombardo, V. G. Kravets, A. K. Geim, A. N. Grigorenko, K. S. Novoselov, A. C. Ferrari, *ACS Nano* **2010**, *4*, 5617.
- [23] N. Jung, A. C. Crowther, N. Kim, P. Kim, L. Brus, *ACS Nano* **2010**, *4*, 7005.
- [24] S. Feng, M. C. dos Santos, B. R. Carvalho, R. Lv, Q. Li, K. Fujisawa, A. L. Elías, Y. Lei, N. Perea-López, M. Endo, M. Pan, M. A. Pimenta, M. Terrones, *Science Advances* **2016**, *2*.
- [25] A. C. Ferrari, *Solid State Commun.* **2007**, *143*, 47.
- [26] V. Panchal, R. Pearce, R. Yakimova, A. Tzalenchuk, O. Kazakova, *Sci. Rep.* **2013**, *3*.
- [27] R. Wang, S. Wang, D. Zhang, Z. Li, Y. Fang, X. Qiu, *ACS Nano* **2011**, *5*, 408.
- [28] L. Yan, C. Punckt, I. A. Aksay, W. Mertin, G. Bacher, *Nano Lett.* **2011**, *11*, 3543.
- [29] H. Yuan, S. Chang, I. Bargatin, N. C. Wang, D. C. Riley, H. Wang, J. W. Schwede, J. Provine, E. Pop, Z. X. Shen, P. A. Pianetta, N. A. Melosh, R. T. Howe, *Nano Lett.* **2015**, *15*, 6475.
- [30] K. C. Kwon, K. S. Choi, B. J. Kim, J. L. Lee, S. Y. Kim, *J. Phys. Chem. C* **2012**, *116*, 26586.
- [31] S. S. Naghavi, T. Gruhn, V. Alijani, G. H. Fecher, C. Felser, K. Medjanik, D. Kutnyakhov, S. A. Nepijko, G. Schönhense, R. Rieger, M. Baumgarten, K. Müllen, *J. Mol. Spectrosc.* **2011**, *265*, 95.
- [32] H. Yan, Z. Chen, Y. Zheng, C. Newman, J. R. Quinn, F. Dotz, M. Kastler, A. Facchetti, *Nature* **2009**, *457*, 679.
- [33] Z. Chen, Y. Zheng, H. Yan, A. Facchetti, *J. Am. Chem. Soc.* **2009**, *131*, 8.

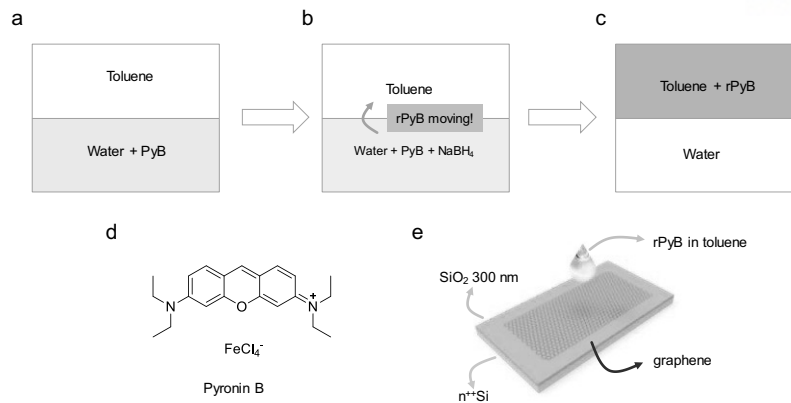


Figure 5.1. From a to c: Synthesis of reduced pyronin B (rPyB). (a) Toluene was layered on top of the pyronin b (PyB) solution dissolved in water. (b) NaBH_4 was added to the PyB solution to synthesize rPyB. The rPyB is not charged, thus rPyB molecules were moving to toluene spontaneously. (c) After 24 hour, rPyB molecules moved to toluene completely. (d) Chemical structure of PyB. (e) Schematic illustration of rPyB solution doping on a graphene field-effect transistor (FET)

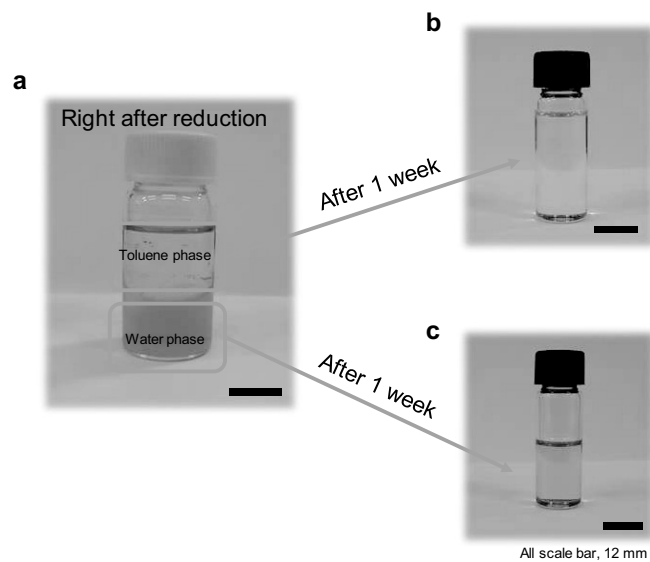


Figure 5.2. Photographs of the biphasic solution reaction to synthesize rPyB. (a) right after reduction of PyB with NaBH_4 . after 1day, toluene and water part were separated. after 1 week of (b) toluene part, containing rPyBs and (c) water part.

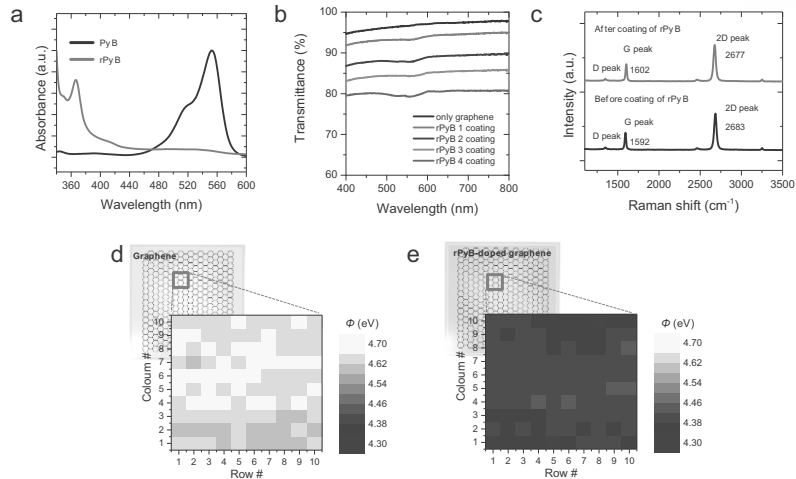


Figure 5.3. (a) Absorption spectra of PyB (black) and rPyB (red) (b) Transmittance of graphene and graphene after coating of rPyB (c) Raman spectra of graphene before and after coating of rPyB Kelvin probe (KP) mapping before (d) and after (e) coating of rPyB on graphene. Work function of reference electrode was gold which is 5.1 eV. KP mapping area = (10 x 100 x 635 nm) x (10 x 100 x 635 nm) = 0.40 mm². Φ , work function.

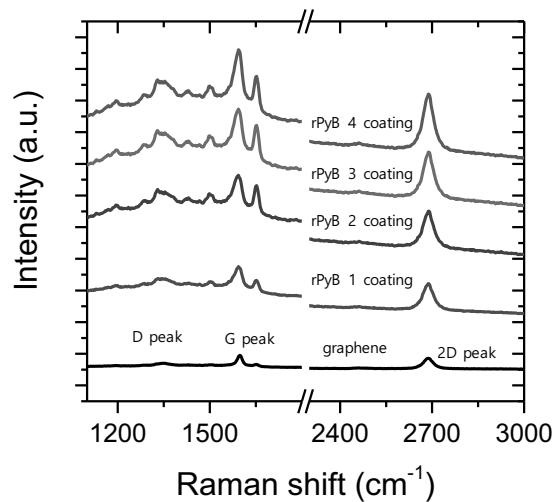


Figure 5.4. Raman spectra of graphene with respect to the number of rPyB coating

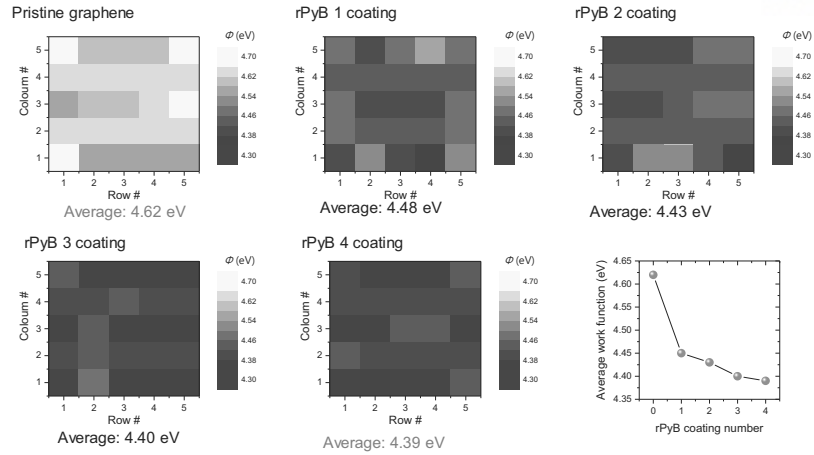


Figure 5.5. Kelvin probe mapping of graphene with respect to the number of rPyB.

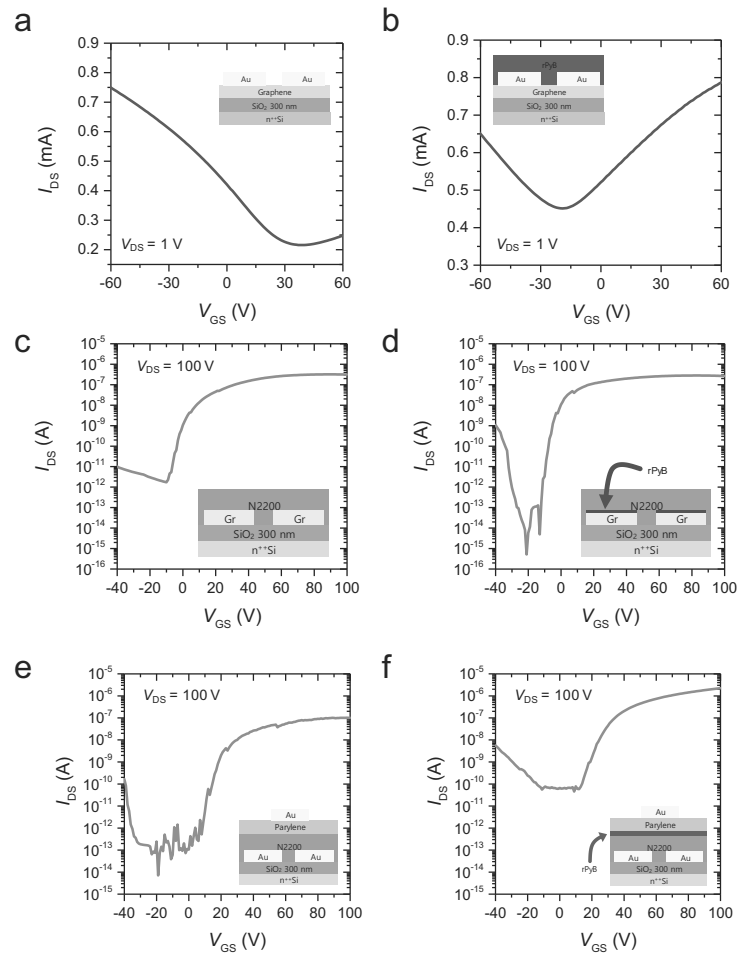


Figure 5.6. Transfer curves of graphene before (a) and after (b) rPyB coating. Transfer curves of N2200 FETs with (c) pure graphene electrodes and (d) graphene electrodes coated rPyB. Transfer curves of N2200 FET with bottom contact top gate (BCTG) configuration (e) without and (f) with rPyB coating (insets: schematic device structure)

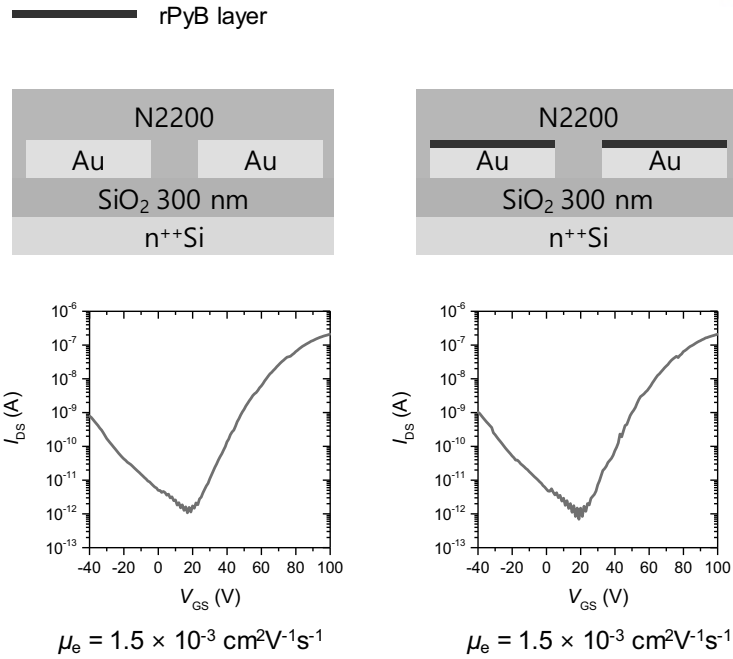


Figure 5.7. Transfer curves of N2200 before (left) and after (right) coating of rPyB at the interface between Au electrodes and N2200.

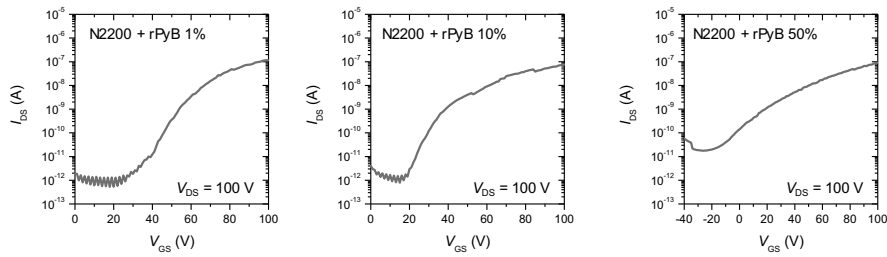


Figure 5.8. Transfer curves of N2200 FETs. N2200 solution (3 mg/mL in chlorobenzene) was mixed with rPyB from 1 wt % to 50 wt %.

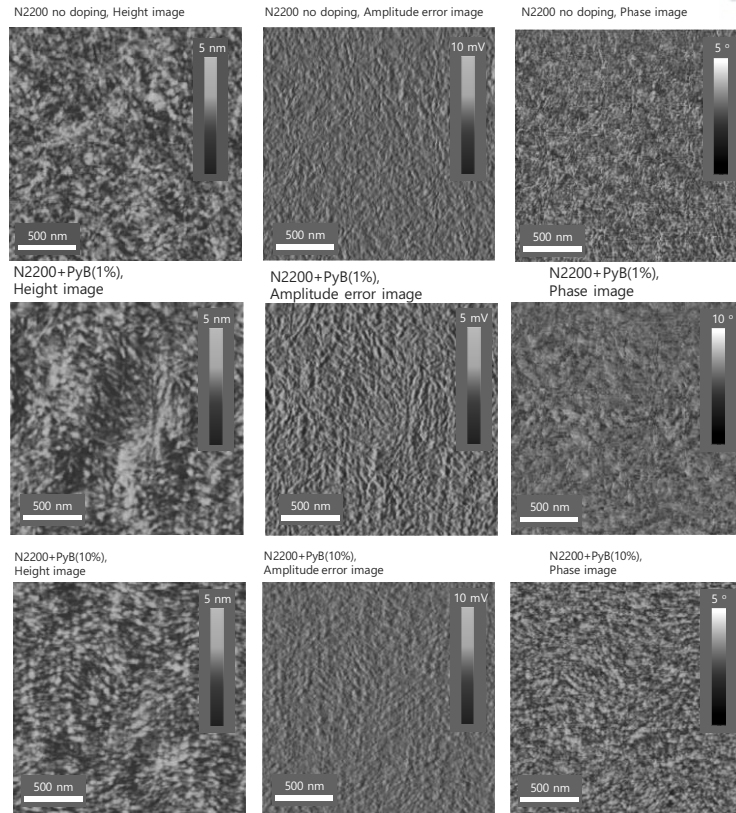


Figure 5.9. Atomic force microscopy images on N2200 film mixing with rPyB (1 ~ 10 wt %).

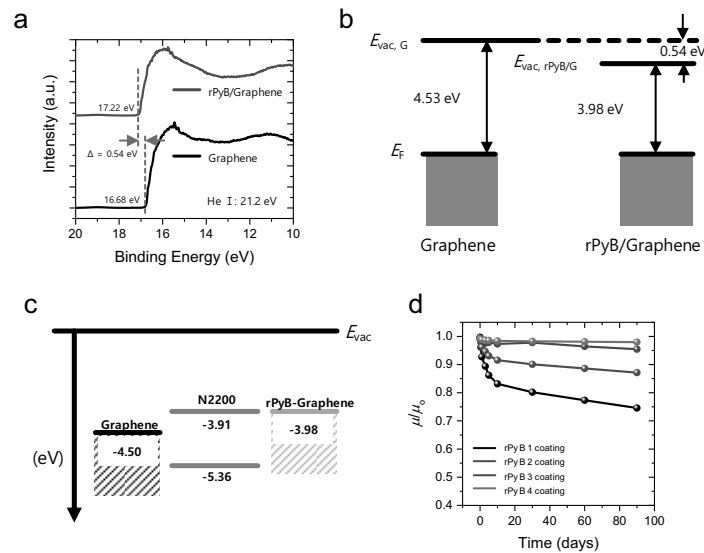


Figure 5.10. (a) Ultraviolet photoemission spectroscopy (UPS) of graphene electrode (black) and rPyB-doped graphene electrode (red). (b) Energy diagram of graphene electrode and rPyB-doped graphene electrode derived from UPS. (c) Comparison of energy levels of graphene, N2200, Au and rPyB-doped graphene. (d) electron mobility changes of graphene FETs in ambient condition for 90 days with respect to the number of rPyB coating (from 1 to 4 rPyB coating).

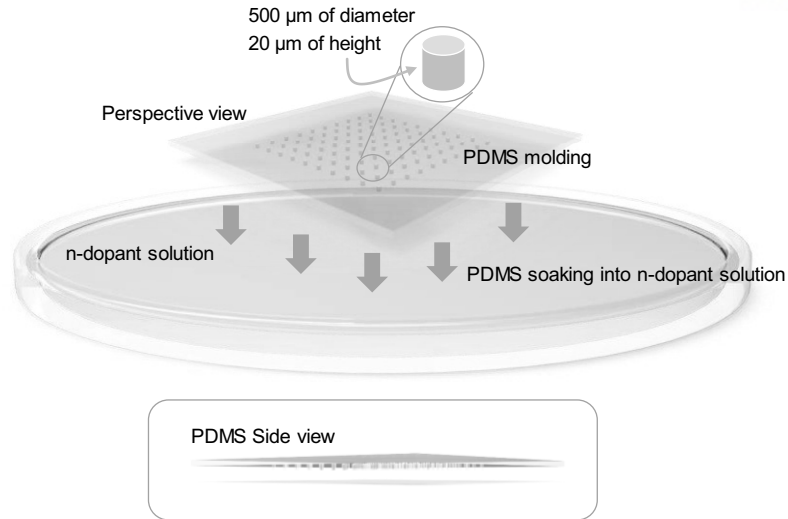


Figure 5.11. Schematic image of PDMS stamp and the detail for the preparation of stamping doping. PDMS stamp was fabricated by photolithography with SU-8 photoresist. The fabricated PDMS stamp was soaked into rPyB solution for 1 min. After drying toluene at 120 oC, PDMS stamp was placed on a position of destination.

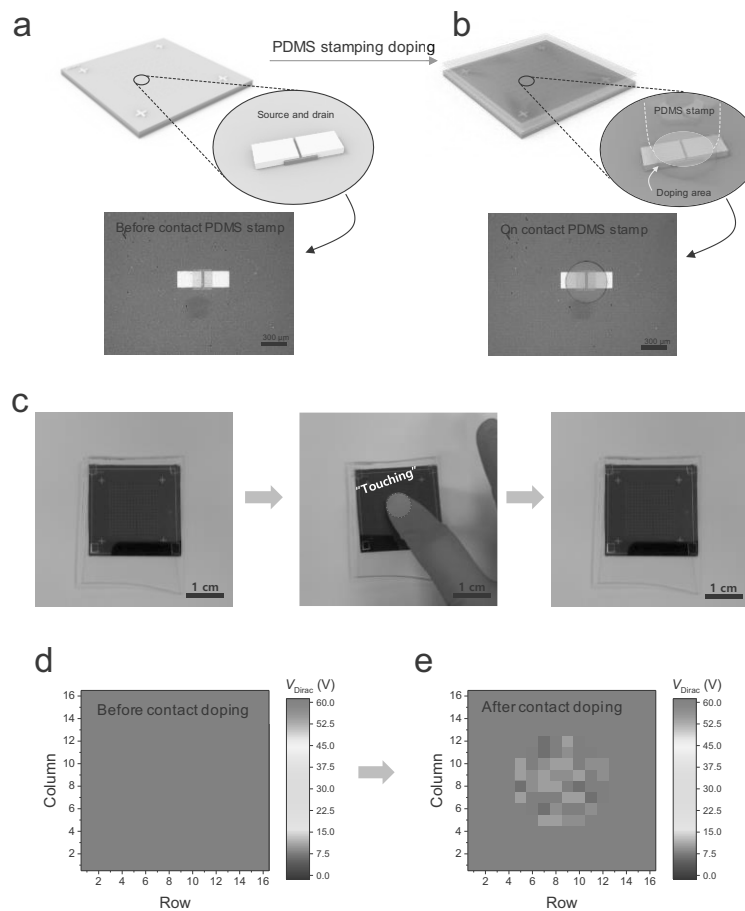


Figure 5.12. Solution processable, selective on-demand contact doping using PDMS stamp. (a) 16×16 graphene FET array was fabricated on 300 nm $\text{SiO}_2/\text{n}^+\text{Si}$ wafer using a conventional

photolithography. (b) The fabricated PDMS stamp was soaked in rPyB solution. The PDMS stamp was placed on top of the graphene FET array. On-demand selective n-type doping using PDMS stamp with fingertip. (c) PDMS stamp was placed on top of the graphene FET. Fingertip touched at the center of PDMS for the on-demand contact doping. Fingertip was detached. V_{Dirac} mapping before (d) and after (f) selective stamping doping at the center of PDMS stamp.

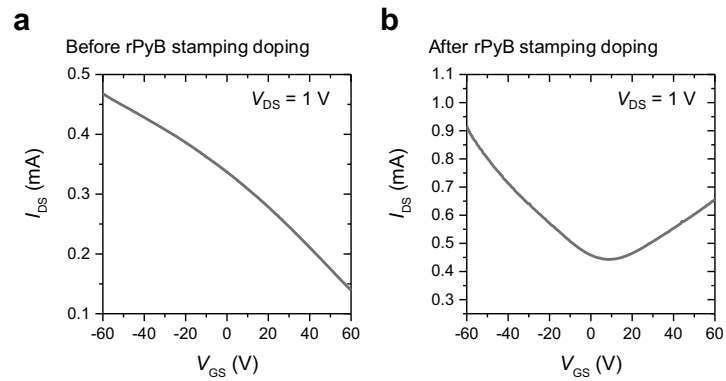


Figure 5.13. Transfer curves of graphene FET before (left) and after (right) rPyB stamping doping.

Chapter 6. Highly Enhanced Optoelectronic Properties in MoSe₂ with Reduced Organic Cationic Dye as Molecular N-Dopant

6.1. Introduction

Atomically thin 2-dimensional materials are gaining immense interests recently, especially on a specific group known as transition metal dichalcogenides (TMDCs) for its possible vast applications in electronics and optoelectronics.^[1-6] This is due to their properties such as tunable band gap, an appropriate carrier mobility and large on-off ratio up to 10⁸.^[7-10] TMDCs also have high mechanical strength and flexibility at atomically thin thickness, which can be achieved by bulk materials isolation or single to few layer growth via chemical vapor deposition (CVD).^[11] Molybdenum disulfide, MoS₂ is the most comprehensively studied out of all TMDCs so far. However, the lesser-studied selenide analogue, molybdenum diselenide (MoSe₂) also have its own attractive properties such as narrower band gap as well as its nearly degenerate direct and indirect bandgap.^[12] Semiconducting MoSe₂ has a tunable band gap ranging from 1.1 to 1.5 eV which shifted from being indirect to direct band gap moving from bulk to monolayer.^[12-14] Direct band gap of 1.5 eV in monolayer MoSe₂ is ideal for solar energy conversion applications such as solar cell compared to other TMDCs. Owing to its narrow band gap, MoSe₂ has shown substantial potentials as phototransistor with photoresponsivity as high as 93.7 AW⁻¹ in its thin film form.^[15] This value is much higher than other reported thin film of 2D materials such as in MoS₂ (9 × 10⁻² AW⁻¹),^[16] GaS (64.43 AW⁻¹),^[17] and InSe (12.3 AW⁻¹).^[18]

Monolayer MoSe₂ similar like other monolayer TMDCs, can have a trigonal prismatic phase or an octahedral phase that commonly referred as 2H and 1T phase, respectively.^[19] The 2H and 1T phase offer different electrical properties as the 2H phase behaves as a semiconductor, while the 1T phase possesses metallic properties. In nature, MoSe₂ exists in 2H phase as it is thermodynamically stable and the 1T phase is a metastable phase which can be reversibly converted to 2H phase.^[20]

Study on 2D TMDC-organic interface is very important and beneficial for the improvement of future electronics. Organic doping is one of the common method to create such interface. In order to realize high-performance flexible 2D TMDC electronic devices for smart devices, their doping properties is a prerequisite that should be extensively studied. Ion implantation is the most common doping method in Si based device, however, such serial system method is not proper for monolayer 2D materials due to its very thin in thickness and large area application, as well as inducing lattice defects on the doped materials.^[21, 22] However, this issue is avoidable with surface charge transfer doping which is an appropriate doping technique for such thin materials. With this doping technique, its rather easy doping method, usually by dip-coating, drop-casting and spin-coating is highly beneficial for industrial applications in term of cost and time efficient.

In this paper, we demonstrate the surface charge transfer in CVD grown MoSe₂ by a reduced Pyronin B (rPyB). rPyB is an organic dye molecules reduced by sodium borohydride in water. Herein, we study

the mechanism that occurs in the interfacial between monolayer TMDC and organic dopant by utilizing various means, which include optical analyses and electrical characterization of field effect transistor (FET) device.

We also for the first time, analyze the photobehavior of doped MoSe₂ as a phototransistor which is to our best knowledge, hitherto never been studied in any monolayer TMDCs. Our doped MoSe₂ phototransistor exhibits an ultrahigh photoresponsivity of 5700 AW⁻¹ and external quantum efficiency, EQE of 1.3x10⁶ % under light wavelength of 532 nm. These superior values are the highest reported so far for MoSe₂ and TMDCs-based phototransistor, which attributed to improved mobility and good electrical contact of our device. Another important merit of our work is we successfully incorporate our device into a flexible device and measure its performance and mechanical flexibility. This work further extends the range of possible applications as ultrathin, lightweight and flexible device applications.

6.2. Experimental Section

CVD growth of MoSe₂

MoO₃ powder (Alfa Aesar, 99.998%) and Se pellets (Sigma Aldrich, 99.99%) were used as precursors to grow monolayer MoSe₂. Monolayer MoSe₂ was grown on Si wafer with 300 nm SiO₂ which was cleaned with toluene, acetone and IPA prior to grow. Se pellets and MoO₃ were put on the same quartz boat with Si substrate (SiO₂ facing down) on top of MoO₃ before being loaded into center of the CVD furnace. Vacuum and Ar purging was carried out for at least 20 minutes to remove most of the ambient gases. After that, Ar was purge until ambient pressure was reached before the growth process was carried out. Furnace was heated to 850 °C at a rate of 50 °Cmin⁻¹ and kept at that temperature for 10 minutes. 20 sccm of Ar and 5 sccm of H₂ was used as carrier and reducing gases during the growth process. After completion, furnace was left to cool to room temperature under Ar flows.

Transfer to new substrate

As grown MoSe₂ on Si wafer was spin coated with polystyrene, PS of concentration 40 g/L. Edge of the wafer was cleaned with toluene to removed PS coated on the edge side of the substrate. The underlying SiO₂ was etched with hot KOH solution (20% w/w). The delaminated PS/MoSe₂ film was rinse multiple times in DI water before being fished out by target substrate (Si/SiO₂ or PET for flexible device). The stack (PS/MoSe₂/substrate) was baked at 150 °C to improve the surface interaction between substrate and MoSe₂. PS film was removed by putting the stack on toluene bath for overnight at room temperature followed by toluene bath at 109 °C for 2 hours.

1T phase conversion

Phase conversion was carried out by exposing monolayer MoSe₂ to 5 mL of 1.5M n-buLi in hexane for 2 hours inside a glove box. After 2 hours, the sample was cleaned with hexane for at least 3 times and dried before taking out from glove box to further wash with IPA and DI water.

6.3. Results and Discussion

MoSe₂ was grown following the single step CVD technique with Se pellets and MoO₃ powder as the precursors as in other previous works.^[3, 15, 23, 24] The growth was carried out in a quartz tube with single zone furnace and the pressure was maintained at atmospheric pressure throughout the growth process. Growth temperature was set to 850 °C and kept at the temperature for 10 minutes before being cooled down to room temperature unassisted. Details of the growth procedure and conditions can be found on the Method section of this paper. By manipulating the growth parameters such as temperature and growth time, isolated domain (Figure 6.1a) as well as large-area monolayer MoSe₂ can be grown. Increasing growth temperature will increase the crystal size, and if the growth was carried out for extended time, isolated domains will grow large enough before merged together and formed large – area monolayer film as in Figure 6.1b.

Figure 6.2 depicts the device fabrication steps of MoSe₂ device. In Figure 6.2a, the monolayer MoSe₂ grown with CVD was transferred onto new substrate as the CVD growth was carried out at high temperature (850 °C), which distorted the dielectric properties of the underlying SiO₂ on growth substrate.^[25] Photoresist coating and photolithography patterning was used to define the electrode areas as in Figure 6.2b. After development process of the photolithography, (Figure 6.2c) the exposed MoSe₂ for electrode deposition was treated to n-butyllithium for 2 hours to convert it into metallic 1T phase, while keeping the covered MoSe₂ channel area as semiconducting 2H phase.^[26] This was done to reduce the contact resistance between the monolayer MoSe₂ and the deposited metal electrode. Next, as illustrated in Figure 6.2c and Figure 6.2d, Cr/Au (4, 40 nm) was deposited as electrode followed by lift-off process. Finally, rPyB solution was spin coated (3000 rpm, 40s) on the device and annealed at 110 °C to remove the residual solvent. Figure 6.2f shows the device schematic structure of the fabricated device before doped with rPyB.

Quality of the CVD grown MoSe₂ was confirmed with various analysis tools such as Raman, AFM and TEM as shown in **Figure 6.3**. Figure 6.3a shows the optical image of the MoSe₂ isolated domain. To estimate the thickness of the synthesized MoSe₂, atomic force microscopy (AFM) was utilized to get the height profile which confirmed to be monolayer with thickness of about 0.72 nm as shown in Figure 6.3b.^[23, 27, 28] AFM was also used to check and compare the change in morphology of monolayer MoSe₂ upon doping (Figure 6.4). It was found that not only the thickness of monolayer MoSe₂ increases as in Figure 6.4b, but the dopant was coated conformally and uniformly throughout MoSe₂ surface, while formed ring-like morphology on SiO₂ surface. This is probably due to benzene rings in rPyB which conform favorably to hexagonal lattices present in MoSe₂ while absent in SiO₂. To prove this statement, rPyB was coated onto graphene, which also possessed the hexagonal lattice structure. Figure 6.5a and Figure 6.5b show the thickness differences in pristine graphene and rPyB – coated graphene.

The doped graphene is thicker in thickness and exhibits uniform morphology which confirms the conformity of rPyB to materials with hexagonal lattice.

The doped samples were also characterized by Raman spectroscopy (Figure 6.3c). The original Raman spectrum (before doping with rPyB) shows vertical (A_{1g}) and lateral (E_{2g}^1) vibration modes of $MoSe_2$ around 240 and 284 cm^{-1} , respectively. After doping with rPyB, the A_{1g} peak shifted to a lower wavenumber as a result of the softening of A_{1g} vibrations at high electron concentrations.^[29, 30] On the other hand, the E_{2g}^1 peak remained unchanged. These spectroscopic observations are comparable to those in a previous report of electrostatic doping of MoS_2 by a back-gate potential, where the electron–phonon coupling of the A_{1g} mode was suggested to be stronger than that of the E_{2g} mode.^[30]

Figure 6.3d shows high-resolution transmission electron microscopy (TEM) image of $MoSe_2$. Here, the atoms appear bright in a dark background. It appears that CVD-grown $MoSe_2$ possess hexagonally symmetry.

Further study on the $MoSe_2$ structure was carried out with optical characterization. X-ray photoemission spectroscopy (XPS) results on binding energies of Mo and Se for 2H, 1T as well as rPyB doped sample were analyzed. For 2H (as-grown) $MoSe_2$, Figure 6.3e shows two peaks corresponded to Mo $3d_{5/2}$ and Mo $3d_{3/2}$ located at 229.3 eV and 232.4 eV respectively. Two other peaks originating from Se $3d_{5/2}$ and Se $3d_{3/2}$ are located at 54.8 eV and 55.6 eV as shown in Figure 6.3f. All of the peaks from our CVD grown $MoSe_2$ are in agreement with the other literature values.^[23, 28, 31] These peaks reveal the existence of Mo^{4+} and Se^{2-} with atomic composition ratio for Mo and Se of 1:2. Figure 6.3e and Figure 6.3f also reveals the Mo and Se peaks correspond to 1T phase $MoSe_2$. All of the peaks for 1T phase show broader peaks and down – shifted by about 0.6 to 0.8 eV relative to the 2H phase which similar to the case of chemically exfoliated TMDCs.^[32] The XPS characterization of rPyB doped $MoSe_2$ as well as further analysis on each contributing peaks in 2H and 1T phase of $MoSe_2$ can be found on in Figure 6.6, Figure 6.7, Figure 6.8).

In order to assess and compare the effect of $MoSe_2$ phase transition as well as doped $MoSe_2$ on the performance of $MoSe_2$ transistor, three configuration of devices were fabricated as shown in **Figure 6.9a**. Device 2H consists of 2H phase of $MoSe_2$ as the channel and under the electrode region. For 1T device, phase conversion was carried out before electrode deposition to convert the $MoSe_2$ under the electrode pad into metallic 1T phase, while maintaining the semiconducting 2H phase in the channel region. Meanwhile, the rPyB device have the same configuration as in 1T device, but with additional rPyB layer on top of the active channel to acts as dopant to $MoSe_2$ channel.

The transfer characteristics of all three devices operating at drain voltage, V_{DS} of 10 V are shown in Figure 6.9b. All of the devices display n–type behavior which agrees with literature. Device enhancement can be seen with five orders of magnitude larger in on–current for device with 1T phase as contact, compared to 2H phase as contact. This improvement is due to more effective charge carrier injection between the metal electrodes and $MoSe_2$ channel which was achieved by 1T phase $MoSe_2$ as

intermediate.^[26] The metallic nature of the 1T phase greatly reduced the contact resistance of the device. 1T MoSe₂ has work function (eV) lies very close to 2H MoSe₂ conduction band (4.27 eV). This energy level is very near to Cr (4.5 eV) and Au (5.1 eV) work function, thus contribute to easier charge carrier injection across the small energy offset. Once charge carrier injected onto 1T MoSe₂, it can be easily transferred to the 2H phase of the channel due to edge contact configuration as well as the fact that the two phases are covalently bonded together which create a seamless contact.^[33]

Upon doped with rPyB, the transfer characteristic drastically change. Both, on and off–state shifted to higher current, while the threshold voltage, V_{TH} shifted negatively. The transfer curve also shows minimal dependence on gate voltage, V_{GS} , which pertaining to doping effect of rPyB. These doping behaviors agreed with previous works on n-type doping of TMDCs.^[22, 29] The extracted average mobility in linear regime for 2H, 1T, and rPyB doped devices were 0.016, 10.60 and 154.30 cm² V⁻¹s⁻¹, respectively. **Table 6.1** shows the tabulated data related to the FET performances of the three different devices. Output curves, shown in Figure 6.10a, b and c which represent 2H, 1T, and rPyB doped MoSe₂ transistors indicate the enhanced charge injection after n – butyllithium treatment which led to phase transion from 2H to 1T as previously discussed.

The optoelectronic properties of rPyB doped MoSe₂ phototransistor was studied. Due to its band gap of 1.5 eV , two different wavelengths of 532 and 650 nm which lie on the visible range of light were chosen. **Figure 6.11a** presents the transfer characteristics of the device operating in dark as well as under various light wavelengths. Under illumination of 300 μW of 532 and 650 nm wavelength, the off–current increases to more than three orders or magnitude. The photocurrent to dark current ratio, P and photoresponsivity, R which are the key parameters in phototransistor, were calculated for both wavelengths using Equation (1) and (2),

$$P = \frac{I_{light} - I_{dark}}{I_{dark}} \quad (1)$$

$$R = \frac{I_{light} - I_{dark}}{P_{inc}} \quad (2)$$

where I_{light} and I_{dark} are the drain current under illumination and in dark, while P_{inc} is the power of the incident light. As expected, device operating under illumination of 532 nm shows higher P and R , reaching to 1200 and 5700 AW⁻¹, while the one under illumination of 650 nm have P and R of 900 and 3700 AW⁻¹ respectively. Such values were contributed by higher photon energy at $\lambda = 532$ nm which results in higher photocurrent generated in the phototransistor upon illumination. Figure 6.11b shows the photoresponsivity, R as a function of gate voltage, V_{GS} for both wavelengths of light, 532 and 650 nm. Figure 6.11c and d show the photoswitching behavior for wavelength of 532 and 650 nm while operating at $V_{GS} = -20$ V. It is worth noted that larger photocurrent can be achieved by operating at much larger negative V_{GS} .

In order to compare the effect of doping on optoelectronic properties of MoSe₂, the photobehavior of 1T device was conducted under similar V_{GS} and wavelengths of 532 and 650 nm (Figure 6.12). Our undoped MoSe₂ phototransistor shows very poor performance as compared to the doped MoSe₂. As can be seen from Figure 6.12a, the transfer curves show abysmal changes when operated in the dark and under the light. Thus, the undoped device demonstrates a poor photoswitching behavior with on – current only in the range of pico-ampere (Figure 6.12b and c). **Table 6.2** shows the summarized photobehavior parameters for both; undoped and doped MoSe₂ phototransistors. Tremendous improvement can be seen on the doped MoSe₂ phototransistor which covers enhanced photocurrent, photoresponsivity, R as well as external quantum efficiency, EQE values.

At $\lambda = 532$ nm, the photocurrent to dark current ratio, P was increased to more than 20 times after doping to 1200, while only 53 for undoped MoSe₂. Maximum photoresponsivity, R was enhanced to almost 7 orders of magnitude after doped to value of 5700 AW⁻¹ as opposed to only 2.36x10⁻⁴ AW⁻¹ in undoped MoSe₂. Other than P and R , external quantum efficiency, EQE is also another important parameter in evaluating the practicality of a phototransistor. EQE can be calculated using the equation in (3)

$$EQE, \eta = \frac{R}{e\lambda} hc \quad (3)$$

where h is the Plank constant, c is the speed of light, e is the elementary electron charge, and λ is the wavelength of the illuminated light. The doped MoSe₂ exhibits EQE value of 1.3x10⁶ %. This value is exorbitantly large compared to the undoped MoSe₂ with EQE value of only 0.055 %.

The mechanism to explain the great improvement on rPyB doped MoSe₂ system involved the understanding of the exciton and trion formation in 2D TMDCs. Upon illumination ($h\nu > \text{MoSe}_2$ bandgap), hole created in valence band and excited electron in conduction band will bound together into exciton. But this excited electron is unstable and usually relaxed to valence band while radiating photoluminescence, in other word, not all of the excited electron give rise to photocurrent. However, in the case of doped system, trion, a quasi – particle with two electron bound to a hole, or two hole bound to an electron is formed due to excess charge carrier (electron or hole).^[34] These emerging trions effectively reduced photoluminescence which indicating the reduced radiative relaxation / recombination and thus, ultimately results in higher photocurrent.^[35]

The flexibility is important for various applications, e.g., wearable, medical and military devices. The flexibility of the rPyB doped MoSe₂ phototransistor was examined with respect to its bending radius. Figure 6.13a shows photographs of rPyB doped MoSe₂ phototransistor and schematic illustration of device structure (inset). Briefly, the SiO₂ layer in the established rPyB doped MoSe₂ phototransistor on SiO₂/n⁺⁺Si wafer was etched using 2% HF solution. Then the floating layer was wet-transferred to parylene (500 nm)/PEDOT/PET substrate. After annealing the device in vacuum oven for 1 day at 100 °C, the flexible device was measured. Figure 6.13b is optical image of the fabricated devie on the flexible PET substrate. A triangular shape of rPyB doped MoSe₂ can be found. Transfer curves of rPyB

doped MoSe₂ phototransistor on the PET substrate were obtained shown in Figure 6.13c. Figure 6.13d shows the electron mobility change as a function of bending radius from 16 to 2 mm under illuminated and dark conditions. Tensile strain can be calculated by Equation as follows

$$\varepsilon_{tensile} = \frac{t}{2R_{bend}}$$

where $\varepsilon_{tensile}$ is the tensile strain, t is the thickness of the basal film, and R_{bend} is the radius from the center of the bending to the neutral line of the film. Our devices exhibited no significant change in mobility until 1.01% of the tensile strain ($2R_{bend} = 5$ mm).

6.4. Conclusion

In conclusion, we have studied the organic – inorganic interface between organic rPyB molecular dye with monolayer molybdenum diselenide. Also for the first time, we analyzed the photobehavior of doped monolayer TMDC by incorporating into phototransistor. Our rPyB doped MoSe₂ phototransistor showed enormous enhancement compared to undoped MoSe₂ due to trion formation in doped system, coupled with the conformity of the dopant to MoSe₂ surface which facilitate smoother electron transfer across the interface.

6.5. References

- [1] O. Lopez-Sanchez, D. Lembke, M. Kayci, A. Radenovic, A. Kis, *Nat. Nanotechnol.* **2013**, *8*, 497.
- [2] L. Britnell, R. M. Ribeiro, A. Eckmann, R. Jalil, B. D. Belle, A. Mishchenko, Y.-J. Kim, R. V. Gorbachev, T. Georgiou, S. V. Morozov, A. N. Grigorenko, A. K. Geim, C. Casiraghi, A. H. C. Neto, K. S. Novoselov, *Science* **2013**, *340*, 1311.
- [3] H.-Y. Chang, M. N. Yogeesh, R. Ghosh, A. Rai, A. Sanne, S. Yang, N. Lu, S. K. Banerjee, D. Akinwande, *Adv. Mater.* **2016**, *28*, 1818.
- [4] K. F. Mak, K. L. McGill, J. Park, P. L. McEuen, *Science* **2014**, *344*, 1489.
- [5] M. Park, Y. J. Park, X. Chen, Y.-K. Park, M.-S. Kim, J.-H. Ahn, *Adv. Mater.* **2016**, *28*, 2556.
- [6] K. Roy, M. Padmanabhan, S. Goswami, T. P. Sai, G. Ramalingam, S. Raghavan, A. Ghosh, *Nat Nano* **2013**, *8*, 826.
- [7] H. Zhou, C. Wang, J. C. Shaw, R. Cheng, Y. Chen, X. Huang, Y. Liu, N. O. Weiss, Z. Lin, Y. Huang, X. Duan, *Nano Lett.* **2015**, *15*, 709.
- [8] Y. Yoon, K. Ganapathi, S. Salahuddin, *Nano Lett.* **2011**, *11*, 3768.
- [9] B. Radisavljevic, A. Radenovic, J. Brivio, V. Giacometti, A. Kis, *Nature Nanotechnology* **2011**, *6*, 147.
- [10] S. Larentis, B. Fallahzad, E. Tutuc, *Appl. Phys. Lett.* **2012**, *101*.
- [11] S. Bertolazzi, J. Brivio, A. Kis, *ACS Nano* **2011**, *5*, 9703.
- [12] S. Tongay, J. Zhou, C. Ataca, K. Lo, T. S. Matthews, J. Li, J. C. Grossman, J. Wu, *Nano Lett.* **2012**, *12*, 5576.
- [13] L. Liu, S. B. Kumar, Y. Ouyang, J. Guo, *IEEE Transactions on Electron Devices* **2011**, *58*, 3042.
- [14] K. K. Kam, B. A. Parkinson, *J. Phys. Chem.* **1982**, *86*, 463.
- [15] C. Jung, S. M. Kim, H. Moon, G. Han, J. Kwon, Y. K. Hong, I. Omkaram, Y. Yoon, S. Kim, J. Park, *Sci. Rep.* **2015**, *5*.
- [16] W. Choi, M. Y. Cho, A. Konar, J. H. Lee, G. B. Cha, S. C. Hong, S. Kim, J. Kim, D. Jena, J. Joo, S. Kim, *Adv. Mater.* **2012**, *24*, 5832.
- [17] S. Yang, Y. Li, X. Wang, N. Huo, J. B. Xia, S. S. Li, J. Li, *Nanoscale* **2014**, *6*, 2582.

- [18] S. R. Tamalampudi, Y. Y. Lu, R. Kumar U, R. Sankar, C. D. Liao, K. Moorthy B, C. H. Cheng, F. C. Chou, Y. T. Chen, *Nano Lett.* **2014**, *14*, 2800.
- [19] D. Voiry, A. Mohite, M. Chhowalla, *Chem. Soc. Rev.* **2015**, *44*, 2702.
- [20] Q. Tang, D. E. Jiang, *Chem. Mater.* **2015**, *27*, 3743.
- [21] A. Nipane, D. Karmakar, N. Kaushik, S. Karande, S. Lodha, *ACS Nano* **2016**, *10*, 2128.
- [22] H. Y. Park, M. H. Lim, J. Jeon, G. Yoo, D. H. Kang, S. K. Jang, M. H. Jeon, Y. Lee, J. H. Cho, G. Y. Yeom, W. S. Jung, J. Lee, S. Park, S. Lee, J. H. Park, *ACS Nano* **2015**, *9*, 2368.
- [23] X. Wang, Y. Gong, G. Shi, W. L. Chow, K. Keyshar, G. Ye, R. Vajtai, J. Lou, Z. Liu, E. Ringe, B. K. Tay, P. M. Ajayan, *ACS Nano* **2014**, *8*, 5125.
- [24] S. Najmaei, Z. Liu, W. Zhou, X. Zou, G. Shi, S. Lei, B. I. Yakobson, J. C. Idrobo, P. M. Ajayan, J. Lou, *Nat. Mater.* **2013**, *12*, 754.
- [25] R. Forbes, S. Zukotynski, *J. Electrochem. Soc.* **1989**, *136*, 736.
- [26] R. Kappera, D. Voiry, S. E. Yalcin, B. Branch, G. Gupta, A. D. Mohite, M. Chhowalla, *Nat. Mater.* **2014**, *13*, 1128.
- [27] J. Xia, X. Huang, L. Z. Liu, M. Wang, L. Wang, B. Huang, D. D. Zhu, J. J. Li, C. Z. Gu, X. M. Meng, *Nanoscale* **2014**, *6*, 8949.
- [28] Y. H. Chang, W. Zhang, Y. Zhu, Y. Han, J. Pu, J. K. Chang, W. T. Hsu, J. K. Huang, C. L. Hsu, M. H. Chiu, T. Takenobu, H. Li, C. I. Wu, W. H. Chang, A. T. S. Wee, L. J. Li, *ACS Nano* **2014**, *8*, 8582.
- [29] D. Kiriya, M. Tosun, P. Zhao, J. S. Kang, A. Javey, *J. Am. Chem. Soc.* **2014**, *136*, 7853.
- [30] B. Chakraborty, A. Bera, D. V. S. Muthu, S. Bhowmick, U. V. Waghmare, A. K. Sood, *Phys. Rev. B* **2012**, *85*, 161403.
- [31] W. e. A. Abdallah, A. E. Nelson, *Journal of Materials Science* **2005**, *40*, 2679.
- [32] C. A. Papageorgopoulos, W. Jaegermann, *Surf. Sci.* **1995**, *338*, 83.
- [33] A. Allain, J. Kang, K. Banerjee, A. Kis, *Nat. Mater.* **2015**, *14*, 1195.
- [34] J. S. Ross, S. Wu, H. Yu, N. J. Ghimire, A. M. Jones, G. Aivazian, J. Yan, D. G. Mandrus, D. Xiao, W. Yao, X. Xu, *Nat. Commun.* **2013**, *4*, 1474.
- [35] K. F. Mak, K. He, C. Lee, G. H. Lee, J. Hone, T. F. Heinz, J. Shan, *Nat Mater* **2013**, *12*, 207.

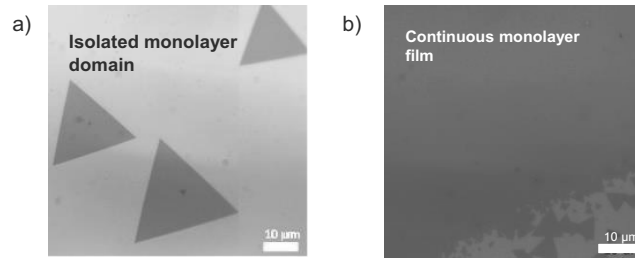


Figure 6.1. MoSe₂ growth. By controlling growth parameters such as temperature, amount of precursors as well as growth time, MoSe₂ can be grown into (a) isolated domain with the common triangular shape or (b) continuous monolayer film.

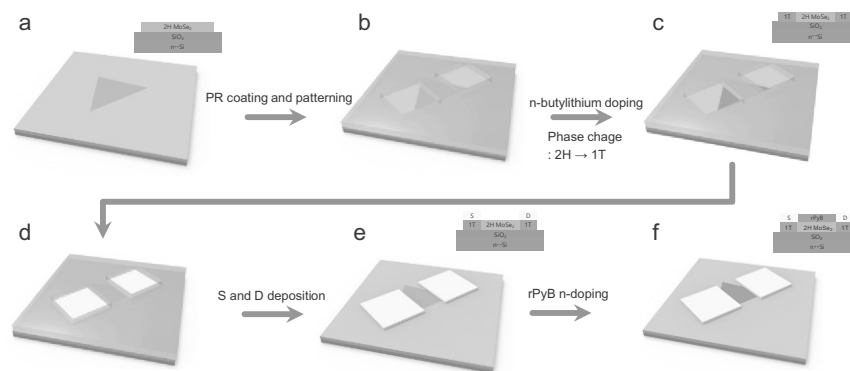


Figure 6.2. Device fabrication. (a) Monolayer MoSe₂ was grown with CVD technique. (b) Photolithography was used to define the source and drain electrode. (c) Exposed areas for S/D electrode were treated to n-buLi for phase transition from 2H to 1T. (d – e) S/D electrodes were deposited by thermal evaporation of Cr and Au. (f) The device was doped by spin – coating with rPyB solution

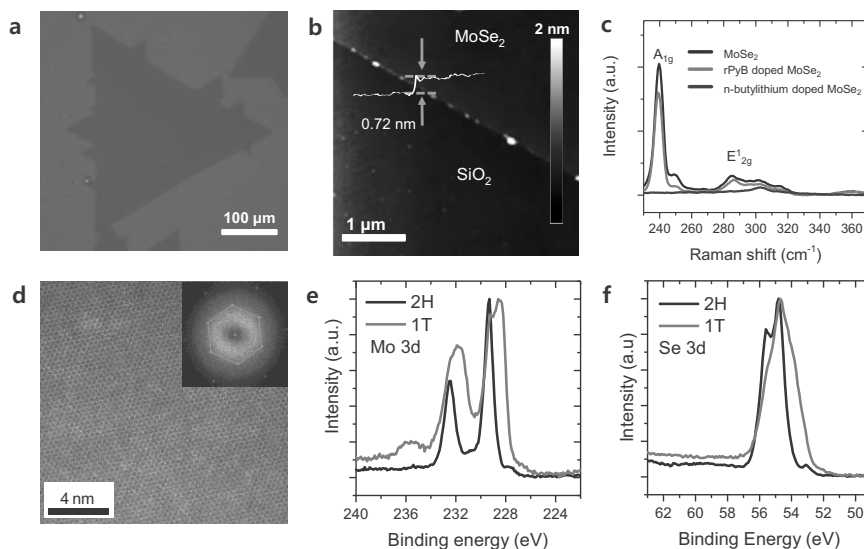


Figure 6.3. Material characterization. (a) Optical microscope image of the CVD grown MoSe₂. (b) AFM image of monolayer MoSe₂ with thickness of 0.72 nm. (d) Raman spectra of as grown (2H), 1T phase and rPyB doped MoSe₂. (d) TEM image of monolayer MoSe₂. (e – f) XPS spectra of Mo 3d and Se 3d for 2H and 1T phases of MoSe₂.

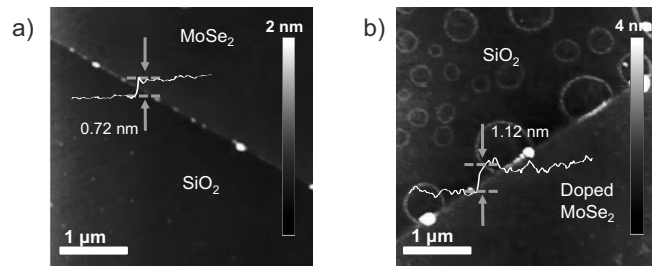


Figure 6.4. AFM analysis on before and after doped MoSe₂. (a) The morphology of as grown monolayer MoSe₂ on Si/SiO₂ substrate. (b) The change in thickness of monolayer MoSe₂ to about 0.4 nm than actual thickness of monolayer MoSe₂ after being doped with rPyB

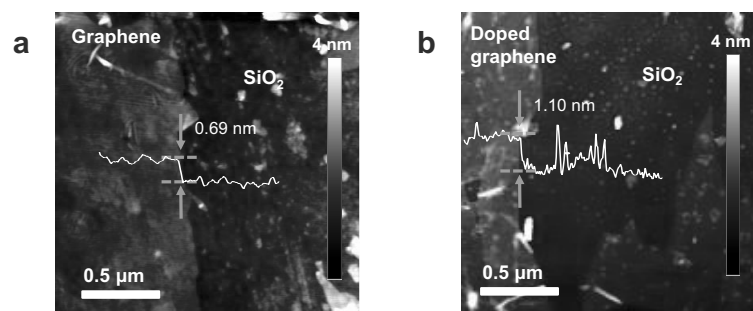


Figure 6.5. AFM analysis on before and after doped graphene. (a) The morphology of pristine graphene on Si/SiO₂ substrate with thickness of 0.69 nm. (b) The change in thickness of graphene to about 0.41 nm thicker than actual thickness of pristine graphene after being doped with rPyB.

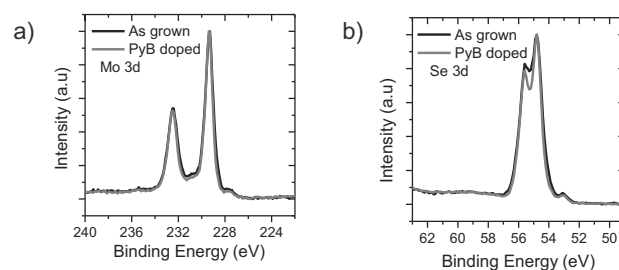


Figure 6.6. XPS analysis. (a) and (b) show the Mo and Se peaks of rPyB doped MoSe₂. The conformity of the rPyB doped MoSe₂ to as grown MoSe₂ shows that there are no lattice defects on MoSe₂ induced by the doping.

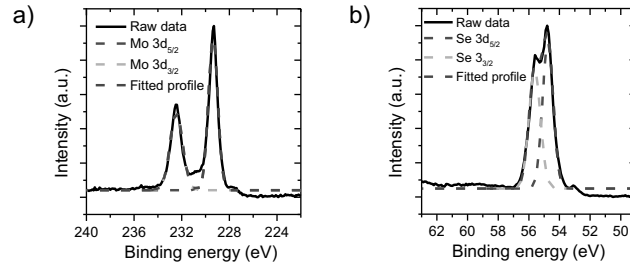


Figure 6.7. a) and b) show the individual peaks with respect to Mo 3d_{5/2}, Mo 3d_{3/2} and Se 3d_{5/2}, Se 3d_{3/2} of as grown sample.

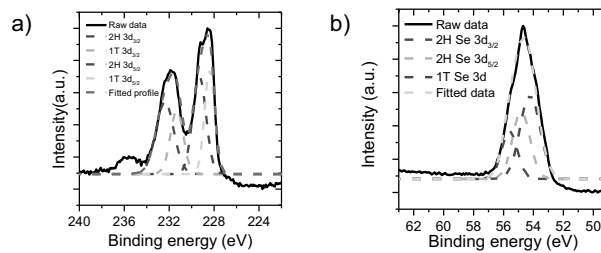


Figure 6.8. a) and b) show the individual peaks with respect to 2H and 1T phases in 1T sample.

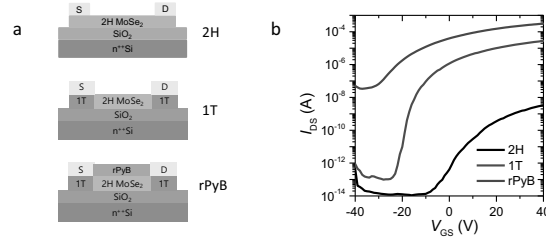


Figure 6.9. Electrical performance. (a) Device configuration of 2H, 1T and rPyB devices. (b) Transfer characteristics of corresponding devices operating at $V_{DS} = 10$ V.

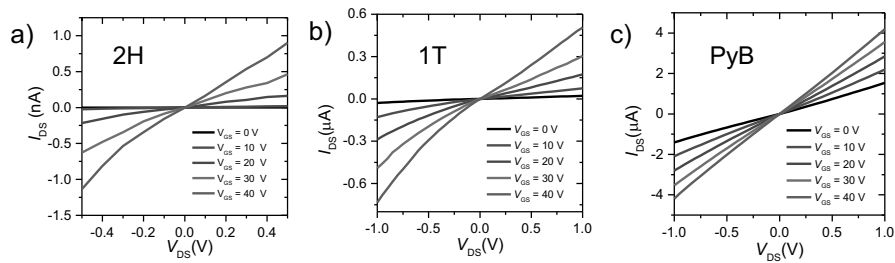


Figure 6.10. Output characteristics of corresponding (a) 2H, (b) 1T and (c) rPyB devices.

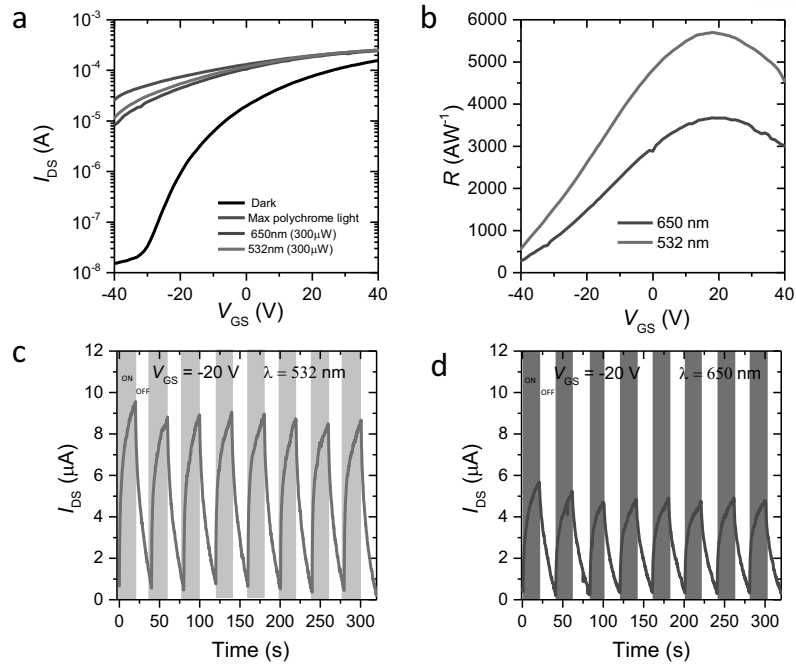


Figure 6.11. Wavelength dependent photoresponse of rPyB doped MoSe₂ photodetector. (a) Transfer characteristic in dark and various light conditions operating at $V_{DS} = 10$ V. (b) Photoresponsivity for wavelength of 650 and 532 nm as function of gate voltage. Photoswitching behavior at wavelength of (c) 532nm and (d) 650nm with light intensity of 300 μ W

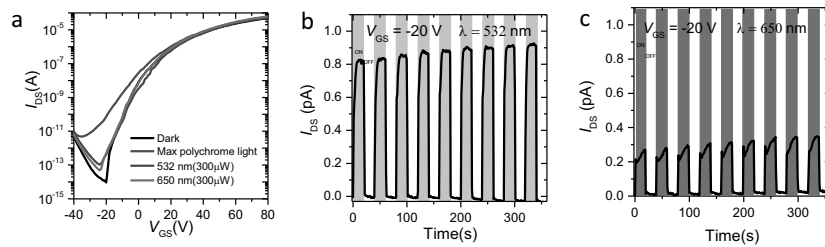


Figure 6.12. Optoelectronic properties of undoped (1T) device. (a) The transfer characteristics of 1T device in dark as well as under various light illumination. The photoswitching behavior of the phototransistor under illumination of $\lambda = 532$ nm (b) and $\lambda = 650$ nm (c) at $V_{GS} = -20$ V.

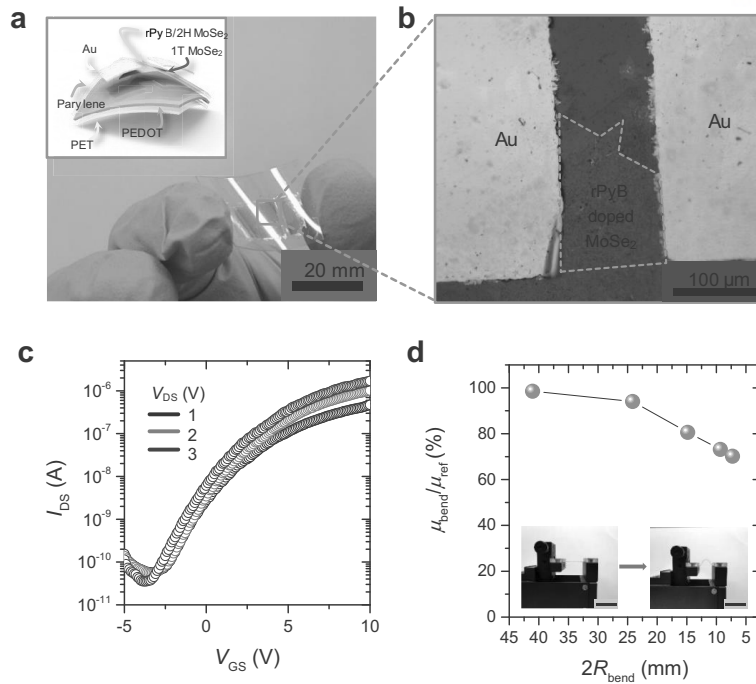


Figure 6.13. rPyB doped MoSe₂ photodetector on a flexible substrate and its electrical characteristic. (a) Schematic depiction of the rPyB doped MoSe₂ photodetector on flexible PET film. PEDOT was coated on PET film as a flexible gate electrode. 500 nm of parylene dielectric was deposited. (b) A photograph of the flexible MoSe₂ photodetector on flexible PET film and (c) a magnified optical image from the green rectangle of Figure 6.13a. (d) Transfer curves of the rPyB doped MoSe₂ photodetector on flexible PET film. (e) Normalized electron mobility change with respect to various bending radii (R_{bend}) (Inset: photograph of bent devices, scale bar = 20 mm).

Table 6.1. Tabulated data of FET performances of 2H, 1T and rPyB doped devices.

Device	μ_{Avg} ($\text{cm}^2 \text{V}^{-1} \text{s}^{-1}$)	μ_{Max} ($\text{cm}^2 \text{V}^{-1} \text{s}^{-1}$)	V_{TH} (V)	On – off ratio
2H	0.016	0.018	5	10^3
1T	10.60	11.21	-7	10^7
rPyB	154.3	162.3	-29	10^4

Table 6.2. Summary of optoelectronic performance of undoped (1T) and doped (rPyB) MoSe₂ based devices.

Parameter	Wavelength, λ			
	532 nm		650 nm	
	Undoped	Doped	Undoped	Doped
P	53	1.2×10^3	44	9.0×10^2
R (AW^{-1})	2.36×10^{-4}	5.70×10^3	9.07×10^{-5}	3.7×10^3
EQE, η (%)	0.055	1.3×10^6	0.010	7.1×10^5

Chapter 7. Nitrogen-Doped Graphene Nanoplatelets from Simple Solution Edge-Functionalization for n-Type Field-Effect Transistors

7.1. Introduction

Graphene, composed of carbon atoms densely packed into a 2D honeycomb crystal lattice, has attracted tremendous interest for various applications due to its fascinating properties such as large surface area, high thermal/electrical conductivity, and high mechanical strength.^[1-3] Although several methods, including mechanical exfoliation,^[3] epitaxial growth,^[4] structural restoration from graphene oxide (GO),^[1] and bottom-up synthesis from small organic molecules,^[5] have been developed to prepare various graphene structures, graphitization of graphene oxide (GO) has been most widely investigated due to its good processability and capability of mass production.^[6, 7]

On the other hand, it is known that graphene is a zero band-gap semiconductor with a carrier mobility as high as $2 \times 10^5 \text{ cm}^2\text{V}^{-1}\text{s}^{-1}$, which is an order of magnitude higher than that of silicon wafer.^[8] Therefore, the modulation of their electrical properties (e.g., the band-gap opening and tuning) is of great importance to performance optimization for the graphene-based optoelectronic devices.^[9-13] One of the most feasible approaches to control the electronic properties of graphene is chemical doping by incorporation of heteroatoms (e.g., boron, nitrogen) into graphitic framework, which can not only alter the band structure but also generate specific charge carriers (holes and electrons).^[9, 11, 14] In particular, nitrogen-doped graphene has attracted great attention due to its superior performance in various devices, such as fuel cells,^[15-18] batteries^[19] and field-effect transistors (FETs).^[9, 11, 13, 20, 21]

In general, graphene-based FETs show p-type behaviors due to the adsorption of oxygen or water in air.^[11] Therefore, it is more challenging to develop n-type graphene compared with the easily obtainable p-type graphene. Hitherto, several methods, including chemical vapor deposition (CVD),^[13, 22] annealing with NH_3 after N^+ ion irradiation^[9] of mechanically exfoliated graphene,^[9] supercritical reaction^[21] and post-treatment of GO,^[20, 23] have been developed to produce nitrogen-doped graphene, which shows unique n-type behaviors in FETs. Although nitrogen-doped graphene prepared from GO is desirable for mass production with good reproducibility, it shows relatively poorer performances in FETs than its counterparts from other synthetic methods due to a relatively low nitrogen doping level and an inefficient structural restoration intrinsically associated with the reduced GO.^[20, 23]

Recently, we developed a facile and scalable synthetic method of nitrogen-doped graphene nanoplatelets and their large-area high-quality films using Friedel-Crafts acylation reaction between pristine graphite and 4-aminobenzoic acid.^[15] Although outstanding electrocatalytic activity for oxygen reduction reaction (ORR) was obtained, they showed the relatively low nitrogen-doping level of around 1.63 wt% after heat treatment. In addition, several nitrogen-doped graphene nanoplatelets with high nitrogen-doping levels have also been prepared by hydrothermal reaction^[24-27] and wet-chemical

reactions^[28] between GO and nitrogen-containing small molecules. However, they showed relatively poorer device performances, probably due to the larger structural defects originated from less controlled reaction mechanisms and existing oxygenated groups in graphitic structure. In order to enhance the performance of graphene-based devices such as FETs and fuel cells, therefore, the development of facile and controlled preparation methods for post-treatment of GO to produce nitrogen-doped graphene nanoplatelets with high doping levels and lower structural defects is highly desirable.

7.2. Experimental Section

Materials and preparation of nitrogen-doped graphene. Graphite nanopowders (450 nm APS, 99.9% purity) from Nanostructured & Amorphous Materials Inc. were used in this study. GO was prepared by the modified Hummers' method using the graphite nanopowders.^[54] For the preparation of iGO, GO (1 g) was dispersed in an acetic acid (140 ml)/toluene (30 ml) mixture and applied sonication for 1 h. Then, 4-fluoroaniline (1 g) was added in the reaction mixture, which was heated under reflux with stirring overnight. Water formed during the dehydration reaction was completely removed by using Dean-Stark trap. After cooling to room temperature, the mixture was filtered using a PTFE membrane (0.45 μm) and washed with plenty of THF and methanol. The product was further purified by Soxhlet extraction with methanol and THF. Finally, iGO was obtained as black powders after drying under reduced pressure (0.05 mmHg) at 50 °C overnight. For the preparation of pGO, 1,2-diamino-4-fluorobenzene (1 g) was added in the same amount GO containing solution and carried out using similar reaction and work-up procedures for iGO. The heat-treatment of iGO and pGO to produce hiGO and hpGO was conducted at 900 °C under nitrogen atmosphere for 2 h.

Instrumentations. Elemental analysis (EA) was conducted with a Thermo Scientific Flash 2000. Solid-state ¹³C magic-angle spinning (MAS) NMR spectra were recorded on a Varian UnityNova 600 (600 MHz) spectrometer, using a 5-mm probe spinning at 9 kHz. Fourier transform infrared (FT-IR) spectra were recorded on a Perkin-Elmer Spectrum 100 using KBr disks. Thermogravimetric analysis (TGA) was conducted with a TA Q200 (TA Instrument) under oxygen atmosphere at a heating rate of 10 °C min⁻¹. X-Ray diffraction (XRD) patterns were recorded with a Rigaku D/MAZX 2500V/PC with Cu-K α radiation (35 kV, 20 mA, $\lambda = 1.5418 \text{ \AA}$). Raman spectra were taken with a He-Ne laser (532 nm) as the excitation source by using confocal Raman microscopy (Alpha 300S, WITec, Germany), in conjunction with atomic force microscopy (AFM). X-ray photoelectron spectra (XPS) were recorded on a Thermo Fisher K-alpha XPS spectrometer. The field emission scanning electron microscopy (FE-SEM) was performed with a FEI Nanonova 230, while the high-resolution transmission electron microscope (HR-TEM) employed in this work is a JEOL JEM-2100F (Cs) microscope operating at 200 kV. The TEM specimens were prepared by dipping carbon micro-grids (Ted Pella Inc., 200 Mesh Copper Grid) into well-dispersed samples in NMP.

DFT Calculations. For computations, we used the Vienna Ab initio Simulation Package (VASP) to calculate the ground state of many electrons system in the frame work of density functional theory.^{S1-S4} The plane-wave basis set with an energy cut-off of 400 eV and the PBE-type gradient-corrected exchange-correlation potential was employed.^{S5}

Fabrication and measurement of FETs. Heavily n-doped Si wafers with 300-nm-thick thermally grown SiO₂ (capacitance per unit area (C_i) = 10 nFcm⁻²) (SiO₂/Si wafers) were utilized as the substrates for FETs. In the typical procedure, GO derivatives (GO, hGO, iGO, pGO, hiGO and hpGO) were dispersed in N-methyl-2-pyrrolidone (NMP) and water (only for GO) at a concentration of 0.03 mg mL⁻¹. NMP was chosen as the solvent because it has a high boiling point (202 °C) that can avoid the formation of GO agglomerates by rapid evaporation and it is a polar aprotic solvent that can dissolve GO derivatives. A small amount of the solution was drop-cast onto a SiO₂/Si wafer and placed at 120 °C (60 °C for GO solution in water) for 30 min in ambient condition. The film thickness of samples could be tuned by controlling the concentration and the volume of the solution. For instance, drop casting of 10 μL of the solution with a concentration of 0.03 mg/mL yielded 4 to 5 nm-thick-films. The sample films were thermally treated at 750 °C for 2 h (optimized condition for the formation of a large-area uniform film of hpGO, while the heat-treatment of bulk samples was 900 °C for 2 h). Then, PMMA was spin-coated onto the film. The SiO₂ layer was etched off by floating on aqueous 1M hydrofluoric acid (HF) solution and the PMMA-coated sample film was peeled off. The resulting PMMA-coated sample film was wet-transferred onto the desired device substrate. The PMMA support layer was removed by dipping into acetone for 2 min, followed by rinsing the substrate with freshly distilled acetone and drying at room temperature for 1 day. Then, the gold electrodes were prepared with either conventional photolithography for microscale channel dimensions ($L = 3 \mu\text{m}$) or e-beam lithography for nanoscale channel dimensions ($L = 500 \text{ nm}$). Finally, the fabricated devices were characterized in N₂ atmosphere.

7.3. Results and Discussion

Herein, we, for the first time, report a highly efficient synthetic protocol for producing nitrogen-doped graphene *via* simple acid-catalyzed dehydration reactions between aromatic ketone (C=O) and primary amine (NH₂) groups. Figure 7.1a shows the condensation reaction between the mono-ketone (C=O) in GO and single amine to form imine (-C=N-, Schiff base) linkage. The double-condensation reaction between α -diketone (O=C-C=O) and 1,2-diamine (or *ortho*-diamine) produces stable aromatic pyrazine rings (Figure 7.1b). In GO, the single ketone is most likely observed at zigzag edges, while the α -diketone should exclusively exist at armchair edges. Since the driving force for the reaction between α -diketone and *ortho*-diamine is aromatization, the formation of aromatic pyrazine rings is

expected to be much more favorable than the imine formation. Indeed, density functional theory (DFT) calculations revealed that the formation energies of imine and pyrazine are +11.9 and -20.4 kcal/mol, respectively (Figure 7.2). On this basis, two types of aromatic amine compounds containing fluorine atoms as an indicator (e.g., 4-fluoroaniline, 1,2-diamino-4-fluorobenzene) for example, for X-ray photoelectron spectroscopic (XPS) measurements, have been reacted with GO (Figure 7.1c) to yield nitrogen-containing GO in the forms of imine (iGO) and pyrazine (pGO). Imine linkage is known to be less stable against hydrolysis and thermolysis than aromatic pyrazine rings. As shown in Figure 7.1c, the subsequent heat treatment (900 °C for 2h) of iGO and pGO under nitrogen atmosphere produced heat-treated iGO (hiGO) and pGO (hpGO), respectively. In addition, chemical reduction process (e.g., using hydrazine) was not applied to our system, since it can cause additional doping effect on the GO plate.^[29-31] Field-effect transistors (FETs) fabricated from hiGO and hpGO exhibited high hole and electron mobilities of up to 11.5 and 12.4 cm²V⁻¹s⁻¹, respectively. The Dirac point was negatively shifted to -16 V, indicating the successful n-type doping. Our doping method allowed for a high-quality and powerful nitrogen-doping of graphene, and thus it will pave a viable way toward the tuning of electronic properties of graphene.

The chemical compositions of all samples (e.g., graphite, GO, iGO, hiGO, pGO and hpGO) were characterized by elemental analyses (EA) and the results are summarized in Table 7.1. The starting graphite is mostly composed of carbon atom (98.81 wt%), while GO contains high oxygen content (45.45 wt%). However, iGO and pGO have dramatically decreased oxygen contents of 19.41 and 9.85 wt%, respectively, while the corresponding nitrogen contents have increased to 2.75 and 9.05 wt%. It is noteworthy that pGO has more significant compositional change than iGO, supporting that the formation of pyrazine ring is much more favorable than the imine formation. As a result, the ratio of nitrogen (N)/carbon (C) is about 1/10, which is, so far, the highest nitrogen content among all nitrogen-doped graphene materials produced by solution processes.^[15, 32] Hence, the scalable production of nitrogen-doped graphene nanoplatelets with such a high nitrogen content should be one of the notable achievements for many applications. Although similar nitrogen-doping levels have been obtained through chemical vapor deposition (CVD)^[11, 19] and heat-treatment of GO with nitrogen containing molecules,^[17, 20, 33, 34] the former has a significant drawback due to the scalability and the latter often shows that the quality of nitrogen-doped graphene was poor for device applications.^[11, 20, 33] However, the formation of stable pyrazine rings between α -diketone functionalities at the armchair edges of GO and *ortho*-diamine derivatives can spontaneously take place during acid catalyzed dehydration reaction, because of the large thermodynamic gain by aromatization (-20.4 kcal/mol). Further heat-treatment of iGO and pGO at elevated temperature under nitrogen atmosphere not only removed remnant oxygenated groups but also restored graphitic structure (Figure 7.1c). The resultant heat-treated samples, hiGO and hpGO, showed the ratios of oxygen (O)/carbon (C) approaching to zero (Table 7.1), which is the lowest value ever reported so far.^[35] Furthermore, hiGO and hpGO have maintained high nitrogen

contents of 3.12 and 7.73 %, respectively (Table 7.1). Note that the higher N/C ratio of hpGO than that of hiGO indicates that pyrazine ring is much more stable than imine, which is weaker against thermolysis.

The solid state ^{13}C magic-angle spinning (MAS) NMR spectra of GO, iGO and pGO indicate significant structural changes have been induced by the acid-catalyzed reactions between GO and amine containing molecules (Figure 7.3a). The NMR spectrum of GO shows that the peaks at 60.73 and 70.44 ppm correspond to ^{13}C nuclei near epoxide and hydroxyl groups, respectively.^[7, 36] The resonance peak at 131.68 ppm is assignable to un-oxidized sp^2 carbons in graphitic structure. The peak at 193.95 ppm presumably attributes to carbonyl carbons.^[7, 36] However, the peak intensities of oxygenated (60.73 and 70.44 ppm) and carbonyl (193.95 ppm) carbons have been greatly reduced for the spectra from iGO and pGO in respect to the graphitic sp^2 carbon peak, which also shifted from 131.68 ppm to around 120 ppm. After conversion of all ketone ($\text{C}=\text{O}$) groups by acid-catalyzed imine ($\text{C}=\text{N}$) formation (see Figure 7.1), the carbonyl peak around 193.95 ppm was shifted to 171.65 ppm for iGO.^[36] Interestingly, pGO displays major sp^2 carbon peak near 120.42 ppm with traces of minor peaks around 48.43 and 186.48 ppm correspond to ^{13}C nuclei near epoxide and carbonyl groups, respectively. Furthermore, the sharp decrease of ^{13}C nuclei near hydroxyl groups at 70.44 ppm was observed due to the acid-catalyzed dehydration reactions at high temperature between hydroxyl groups and adjacent hydrogen atoms.^[32, 37, 38] The result indicates that graphitic structure has already been significantly restored by the formation of aromatic pyrazine rings at the edges (Figure 7.1c) as well as the transformation of sp^3 C-C bonds into sp^2 C-C bonds. Like heat-treated GO,^[35] the formation of aromatic pyrazine rings in pGO and subsequent heat treatment could also promote spontaneous reduction of GO at the same time.

FT-IR spectroscopic measurements using KBr pellets were also conducted to further understand the structural changes before and after reactions and subsequent heat-treatments. As shown in Figure 7.3b, the pristine graphite shows only a weak characteristic band of the vibration mode of adsorbed water molecules at 1632 cm^{-1} .^[39] The spectrum from GO displays several oxygenated bands at 1730 ($\nu_{\text{C}=\text{O}}$), 1624 ($\nu_{\text{C}=\text{C}}$), 1377 ($\nu_{\text{O-H}}$), 1230 (ν_{phenolic}) and 1066 cm^{-1} ($\nu_{\text{C-O}}$), along with hydroxyl bands (3400 cm^{-1}), and it agrees well with literatures.^[11, 36, 40] However, iGO and pGO show the two characteristic peaks, in-plane vibrations of aromatic $\text{C}=\text{C}$ sp^2 hybridized carbon in graphitic network^[41, 42] at around 1590 cm^{-1} and notable $\text{C}=\text{N}$ stretching mode^[43] near 1240 cm^{-1} , in conjunction with concomitant decrease of oxygenated peaks including carbonyl peak at 1730 cm^{-1} . In addition, both characteristic peaks of $\nu_{\text{O-H}}$ (1377 cm^{-1}) and $\nu_{\text{C-O}}$ (1066 cm^{-1}) were disappeared due to the acid-catalyzed dehydration reaction between hydroxyl groups and adjacent hydrogen atoms in GO. Furthermore, the complete removal of carbonyl group was obtained after post-annealing process at an elevated temperature in hiGO and hpGO. These spectroscopic results are in accordance with the structures proposed in Figure 7.1c.

Thermogravimetric analysis (TGA) of all samples was conducted in air and the results are presented in Figure 7.3c. As expected, GO shows a weight loss starting from around $100\text{ }^\circ\text{C}$, which is attributed

to the elimination of bound water between layers and hygroscopic functional groups. The catastrophic weight loss near 200 °C is related to the loss of oxygenated functional groups before the complete oxidative decomposition of the graphitic substrate over 200 – 500 °C. On the other hand, the acid-catalyzed reactions have induced a significant reduction and elimination of edge-functionalized groups *via* the formation of iGO and pGO, which display much improved thermal stability. Furthermore, heat-treated samples, hiGO and hpGO, show the highest thermal stability, compared favorable or even better than the pristine graphite. The great enhancement in thermal stability is presumably due to the high degree of structural restoration in hiGO and hpGO.

The powder X-ray diffraction (XRD) patterns of all samples are shown in Figure 7.3d. The pristine graphite shows a sharp strong peak at $2\theta = 26.4^\circ$ (d -spacing ~ 3.37 Å), while GO displays a broad weak peak at $\text{ca. } 11.7^\circ$ (d -spacing ~ 7.68 Å). The increase in d -spacing of GO is due to a lattice expansion by oxygenated functional groups and bound small molecules between layers. However, the broad peak for iGO is significantly shifted to 24.4° (d -spacing ~ 3.63 Å) and the sharper and narrower peak for hiGO is further shifted to 26.5° (d -spacing ~ 3.36 Å). The peak location (d -spacing) is almost the same as that of the pristine graphite (d -spacing ~ 3.36 Å). Interestingly, compared with iGO, pGO shows relatively much narrower peak at 26.1° (d -spacing ~ 3.40 Å), which is already comparable to that of the pristine graphite, indicating that spontaneous reduction and the formation of aromatic pyrazine rings have occurred. After heat-treatment, the peak from hpGO was slightly shifted to 26.4° (d -spacing ~ 3.37 Å). These results, once again, indicate that the acid-catalyzed reactions and post heat-treatments are feasible approaches for the preparation of well-ordered graphene nanoplatelets with high nitrogen contents.

Raman spectra obtained from the powder samples are shown in Figure 7.3e. The pristine graphite shows the G and 2D bands at 1564 and 2679 cm^{-1} , respectively. Due to the large grain size, its D band at 1335 cm^{-1} associated with the edge distortion is negligible, and thus the ratio of the D to G-band intensities (I_D/I_G) is ~ 0.05 . In contrast, GO showed a broad and strong D band at 1355 cm^{-1} with a high I_D/I_G ratio of 0.93, indicating the reduction in size of the in-plane- sp^2 domains and increase in structural distortions. Furthermore, the G band at 1588 cm^{-1} was slightly up-shifted with respect to that of graphite (1564 cm^{-1}) due to the presence of isolated double bonds, which shows the higher resonance frequencies than that of G band in graphite.^[44] iGO also showed similar D and G bands at 1347 and 1563 cm^{-1} , respectively, but it has a higher I_D/I_G ratio of 1.07 than that of GO ($I_D/I_G = 0.93$), indicating the presence of large amounts of topological defects during acid-catalyzed nitrogen-doping process.^[13] After heat-treatment, hiGO shows D and G bands at 1347 and 1576 cm^{-1} , respectively, with a similar I_D/I_G ratio (1.05) to iGO (1.07). Interestingly, the significant decrease in I_D/I_G ratio of hpGO (0.88) from pGO (1.06) was observed, which can be also closely related to the efficient structural restoration of graphitic framework during the post-annealing process to yield high quality hpGO.

The chemical composition changes during the acid-catalyzed reactions and post annealing process were further monitored by X-ray photoelectron spectroscopy (XPS) (Figure 7.3f). The N 1s and F 1s

peaks in iGO and pGO were clearly detected at around 400 and 687 eV, respectively, to assure incorporation of nitrogen and fluorine. After heat-treatment at 900 °C, both N 1s and F 1s peaks in hiGO were largely disappeared, while hpGO still maintained N 1s peak without F 1s peak. These results indicated that aromatic pyrazine ring is thermally stable compared with imine and C-fluorine linkages (see Figure 7.1). As shown in Figure 7.4, the high-resolution C 1s peak from GO can be deconvoluted into several peaks corresponding to sp^2 carbon at 284.8 eV and other oxygenated carbons such as C-O, C=O and O-C=O, respectively (Figure 7.4b).^[7, 35, 37] Although the high resolution C 1s spectra of iGO (Figure 7.4c) and pGO (Figure 7.4e) also show minor peaks higher than 284.8 eV, their intensities are much lower compared with those of GO. Furthermore, a new peak at 285.8 eV, which is reflecting different bonding nature of carbon such as C=N,^[13] was observed in iGO and pGO. After heat-treatment, the C 1s spectra of hiGO and hpGO became similar to that of the pristine graphite with a major peak at 284.4 eV and a minor peak at 285.8 eV, corresponding to sp^2 carbon and C=N, respectively. As shown in Figure 7.5, the high-resolution N 1s spectra also show the significant compositional changes after acid-catalyzed nitrogen-doping reactions for iGO and pGO and subsequent heat-treatments for hiGO and hpGO. While the pristine graphite and GO have no detectable nitrogen peaks (Figure 7.5a and 5b), iGO exhibits a prominent N 1s peak at 399.7 eV, which is attributable to imine-N (C=N).^[45] Interestingly, pGO displays three peaks at 398.5, 399.7 and 400.5 eV, corresponding to pyrazine-N,^[46] imine-N and amine-N,^[45] respectively. Although characteristic peak of imine (-C=N-) and amine (-NH₂) bonds from the reaction between mono-ketone in GO and *ortho*-diamine, are still observed in pGO, the existence of nitrogen in different environment like pyrazine was confirmed by XPS analysis. Upon the post annealing, the graphitic nitrogen peak at 400.7 eV for hiGO and hpGO was greatly enhanced, which is accompanied by the appearance of an additional peak at around 397.9 eV attributable to pyridinic-N and its resonance form in graphitic structure (Figure 7.1c).^[1, 15, 47] Therefore, it can be deduced that the characteristic nature of nitrogen atoms was changed before and after the heat-treatment. In addition to carbon and nitrogen atoms, the F atom in 4-fluoroaniline and 1,2-diamino-4-fluorobenzene moieties of iGO and pGO can serve as an XPS probe for elucidating the structural changes during the post-annealing. As expected, Figure 7.6a and 6b show no F 1s peak for the pristine graphite and GO, whereas a strong F 1s peak was observed at around 686.8 eV for both iGO and pGO. For hiGO and hpGO, however, the F 1s peak was completely disappeared (Figure 7.6d and 6f), indicating that all fluorine atoms were stripped off from the iGO and pGO by the heat-treatment.^[48] The above spectroscopic and diffraction measurements, therefore, are consistent well with the structural changes during the acid-catalyzed reactions and subsequent heat-treatment to produce nitrogen-doped graphene, as proposed in Figure 7.1c.

Comparing with GO, the iGO and pGO displayed a significantly enhanced flat UV-vis absorbance up to 900 nm (Figure 7.7), indicating that the electronic conjugation within the graphitic structure was largely retained during the acid-catalyzed reactions.^[35] The flat absorbance was further enhanced for

the heat-treated hiGO and hpGO Due to the effective structural restoration of graphitic framework during the subsequent heat-treatments.

The morphological and microstructural changes were investigated by transmission electron microscopy (TEM). TEM images obtained from the pGO and hpGO at low magnification also exhibit wrinkled paper-like morphology (Figure 7.8a and 8d). The edge-on views at a high magnification show highly crystalline interior (Figure 7.8b and 8e), indicating high degree of structural restoration had occurred during the acid-catalyzed reactions and subsequent heat-treatments. Corresponding the selected area electron diffraction (SAED) patterns further support the high crystallinity of pGO and hpGO (Figure 7.8c and 8f). The SAED pattern of pGO given in Figure 7.8c shows a ring-like diffraction spots, which indicates the regional disruption of crystal lattice in pGO. After the heat-treatment, however, hpGO shows a symmetric hexagonal diffraction pattern, which is ascribed to a typical diffraction pattern of graphite,^[49, 50] suggesting that graphitic structure had been well restored in hpGO.

To shed light on the electrical properties of the nitrogen-doped graphene nanoplatelets, we fabricated field-effect transistors (FETs) using the GO derivatives as the active layers. The schematic illustration of a typical FET device is presented in Figure 7.9a, while the details on the film preparation are described in the Experimental Section. Atomic force microscope (AFM) analysis on the hpGO film revealed that the average (mean) thickness of the sample (out of 19 samples) was 4.5 ± 0.6 nm (Figure 7.9b), which corresponds to the stacking of 3 to 5 layers of hpGO sheets. The films of other GO derivatives also exhibited a similar thickness of 4 – 5 nm. The inset of Figure 7.9c displays the optical image of representative hpGO FET placed on a SiO₂/Si wafer with photolithographically patterned gold electrodes (the channel width-to-length ratio (W/L) = 40, $L = 3$ μm). Figure 7.9c exhibits a typical transfer curve of the hpGO FETs. The hole and electron mobilities were extracted from the linear regime of the transfer characteristics using the following equation:

$$I_D = \mu \frac{W}{L} C_i V_D (V_G - V_{th})$$

where I_D is drain current, μ is field-effect mobility, C_i is the specific capacitance of the dielectric, V_D is drain voltage, V_G is gate voltage, V_{th} is threshold voltage, W and L are channel width and length, respectively. Calculated hole and electron mobilities from the transfer curve in Figure 7.9c were 9.0 and 7.9 cm²V⁻¹s⁻¹, respectively. Dirac point, in which charges are neutralized, was found to be -10 V, indicating that nitrogen-doping was performed successfully. The small On/Off current ratio indicates the band-gap of hpGO was not opened. The artificial and regular lattice defects limit electron/hole mobilities and introduce a significant bandgap into monolayer graphene crystal.^[29-31] The hpGO film was multilayer with its thickness of around 4–5 nm. The electrical performances of all the samples, i.e. GO, heat-treated GO (hGO), iGO, hiGO, pGO, and hpGO were statistically compared by characterizing the I - V characteristics of 64 FET devices for each sample, and the results are summarized in Table 7.2.

As can be seen, the pristine GO did not show any field-effect behavior because of its insulating nature, whereas hGO exhibited hole and electron mobilities of 8.5 ± 0.4 and 6.3 ± 0.9 $\text{cm}^2\text{V}^{-1}\text{s}^{-1}$, respectively. The Dirac point was 28 ± 1.0 V, which clearly indicates p-doped nature by ambient adsorbates.^[11, 51, 52] In contrast, iGO and pGO could exhibit field-effect characteristics without heat treatment because of the reduced content of oxygen induced by the dehydration reactions to form imines and aromatic pyrazine rings (see Figure 7.1c). The hiGO FETs exhibited hole and electron mobilities of 1.1 ± 0.02 and 0.5 ± 0.03 $\text{cm}^2\text{V}^{-1}\text{s}^{-1}$, respectively. The hpGO FETs showed hole and electron mobilities of 8.4 ± 0.9 and 7.1 ± 1.1 $\text{cm}^2\text{V}^{-1}\text{s}^{-1}$, respectively. The hpGO FETs have resulted higher mobilities and n-doping effect than those of hiGO FETs due to the higher nitrogen content and more structural restoration. The negative shift of the Dirac point in both hiGO and hpGO FETs clearly indicates that nitrogen-doping on graphene nanoplatelets was successfully performed.

In order to elucidate more intrinsic electrical properties of hpGO by minimizing the grain boundary effects, we fabricated hpGO FETs with a short channel length of 500 nm using e-beam lithography. The optical and AFM images of the top-contact FETs are displayed in Figure 7.10a and the inset of Figure 7.10b. The typical transfer curve is presented in Figure 7.10b, where the maximum hole and electron mobilities were as high as 11.5 and 12.4 $\text{cm}^2\text{V}^{-1}\text{s}^{-1}$, respectively, with the Dirac point of -16 V. The average (mean) hole and electron mobilities obtained from 8 devices were 11.0 ± 0.5 , 12.2 ± 0.3 $\text{cm}^2\text{V}^{-1}\text{s}^{-1}$, respectively, with the Dirac point of -15 ± 1.2 V. The discrepancy in the mobility of the FETs patterning with gold electrodes by photolithography and e-beam lithography could be attributed to the difference in the channel length, which is closely related to the charge scattering induced by the grain boundaries. Short channel devices tend to hold less grain boundaries in the active channel, leading to the enhanced charge transport,^[50, 53] which was also confirmed by our supplementary experiments using a long channel length of 50 μm by thermally depositing the gold electrodes through the shadow mask (Figure 7.11). The difference in the Dirac point values of the FETs prepared from photolithography and e-beam lithography might originate from the different process conditions that can produce different trap densities. In addition, the Dirac point shift and the device hysteresis were also tested by applying gate voltages with different sweep ranges in N_2 atmosphere. The hpGO FETs showed a little hysteresis (Figure 7.12 and Table 7.3). In the forward sweep (from negative to positive gate voltage), Dirac point was shifted to a more negative value, compared with the reverse sweep. The hysteresis is presumably due to the small portion of remaining oxygen-containing groups in hpGO that may act as charge trapping sites in the active channel. The hpGO FETs were also measured in ambient atmosphere (Figure 7.13 and Table 7.4). The Dirac point was still negative in ambient condition. This reveals that n-type doping of hpGO was successfully performed.

7.4. Conclusion

We have developed a simple, but efficient and reliable, nitrogen-doping method *via* the reaction between the most commonly studied GO and primary amine containing molecules in a solution phase. This newly-developed doping method offers a powerful means to produce high-quality nitrogen-doped graphene nanoplatelets with the neutral point (Dirac point) located at around -16 V. Furthermore, the graphene nanoplatelets have a high hole and electron mobilities as high as 11.5 and 12.4 cm²V⁻¹s⁻¹, respectively, in the short channel length (500 nm). The process developed in this study provides a simple solution method for large-scale production of high-quality nitrogen-doped graphene nanoplatelets for n-type FETs and new insights into the utilization of functional groups at the edges of GO to tune the electronic properties of graphene nanoplatelets.

7.5. References

- [1] Z. Sun, D. K. James, J. M. Tour, *J. Phys. Chem. Lett.* **2011**, *2*, 2425.
- [2] G. Eda, G. Fanchini, M. Chhowalla, *Nat. Nanotechnol.* **2008**, *3*, 270.
- [3] K. S. Novoselov, A. K. Geim, S. V. Morozov, D. Jiang, Y. Zhang, S. V. Dubonos, I. V. Grigorieva, A. A. Firsov, *Science* **2004**, *306*, 666.
- [4] J. Hass, W. A. De Heer, E. H. Conrad, *J. Phys.: Condens. Matter* **2008**, *20*.
- [5] K. S. Kim, Y. Zhao, H. Jang, S. Y. Lee, J. M. Kim, K. S. Kim, J. H. Ahn, P. Kim, J. Y. Choi, B. H. Hong, *Nature* **2009**, *457*, 706.
- [6] D. R. Dreyer, S. Park, C. W. Bielawski, R. S. Ruoff, *Chem. Soc. Rev.* **2010**, *39*, 228.
- [7] S. Stankovich, D. A. Dikin, R. D. Piner, K. A. Kohlhaas, A. Kleinhammes, Y. Jia, Y. Wu, S. T. Nguyen, R. S. Ruoff, *Carbon* **2007**, *45*, 1558.
- [8] X. Du, I. Skachko, A. Barker, E. Y. Andrei, *Nat. Nanotechnol.* **2008**, *3*, 491.
- [9] B. Guo, Q. Liu, E. Chen, H. Zhu, L. Fang, J. R. Gong, *Nano Lett.* **2010**, *10*, 4975.
- [10] T. B. Martins, R. H. Miwa, A. J. R. Da Silva, A. Fazzio, *Phys. Rev. Lett.* **2007**, *98*.
- [11] X. Wang, X. Li, L. Zhang, Y. Yoon, P. K. Weber, H. Wang, J. Guo, H. Dai, *Science* **2009**, *324*, 768.
- [12] T. O. Wehling, K. S. Novoselov, S. V. Morozov, E. E. Vdovin, M. I. Katsnelson, A. K. Geim, A. I. Lichtenstein, *Nano Lett.* **2008**, *8*, 173.
- [13] D. Wei, Y. Liu, Y. Wang, H. Zhang, L. Huang, G. Yu, *Nano Lett.* **2009**, *9*, 1752.
- [14] H. Wang, T. Maiyalagan, X. Wang, *ACS Catalysis* **2012**, *2*, 781.
- [15] I. Y. Jeon, D. Yu, S. Y. Bae, H. J. Choi, D. W. Chang, L. Dai, J. B. Baek, *Chem. Mater.* **2011**, *23*, 3987.
- [16] L. Qu, Y. Liu, J. B. Baek, L. Dai, *ACS Nano* **2010**, *4*, 1321.
- [17] Z. H. Sheng, L. Shao, J. J. Chen, W. J. Bao, F. B. Wang, X. H. Xia, *ACS Nano* **2011**, *5*, 4350.
- [18] S. Wang, D. Yu, L. Dai, D. W. Chang, J. B. Baek, *ACS Nano* **2011**, *5*, 6202.
- [19] A. L. M. Reddy, A. Srivastava, S. R. Gowda, H. Gullapalli, M. Dubey, P. M. Ajayan, *ACS Nano* **2010**, *4*, 6337.
- [20] X. Li, H. Wang, J. T. Robinson, H. Sanchez, G. Diankov, H. Dai, *J. Am. Chem. Soc.* **2009**, *131*, 15939.
- [21] W. Qian, X. Cui, R. Hao, Y. Hou, Z. Zhang, *ACS Appl. Mater. Interfaces* **2011**, *3*, 2259.
- [22] C. Zhang, L. Fu, N. Liu, M. Liu, Y. Wang, Z. Liu, *Adv. Mater.* **2011**, *23*, 1020.
- [23] M. A. Khaderbad, V. Tjoa, M. Rao, R. Phandripande, S. Madhu, J. Wei, M. Ravikanth, N. Mathews, S. G. Mhaisalkar, V. R. Rao, *ACS Appl. Mater. Interfaces* **2012**, *4*, 1434.
- [24] B. Zheng, J. Wang, F. B. Wang, X. H. Xia, *Electrochem. Commun.* **2013**, *28*, 24.
- [25] J. Wu, D. Zhang, Y. Wang, B. Hou, *J. Power Sources* **2013**, *227*, 185.
- [26] D. Long, W. Li, L. Ling, J. Miyawaki, I. Mochida, S. H. Yoon, *Langmuir* **2010**, *26*, 16096.
- [27] P. Chen, J. J. Yang, S. S. Li, Z. Wang, T. Y. Xiao, Y. H. Qian, S. H. Yu, *Nano Energy* **2013**, *2*, 249.
- [28] Y. Zhang, K. Fugane, T. Mori, L. Niu, J. Ye, *J. Mater. Chem.* **2012**, *22*, 6575.

- [29]V. Dua, S. P. Surwade, S. Ammu, S. R. Agnihotra, S. Jain, K. E. Roberts, S. Park, R. S. Ruoff, S. K. Manohar, *Angew. Chem., Int. Ed.* **2010**, *49*, 2154.
- [30]J. M. Englert, C. Dotzer, G. Yang, M. Schmid, C. Papp, J. M. Gottfried, H. P. Steinrück, E. Spiecker, F. Hauke, A. Hirsch, *Nat. Chem.* **2011**, *3*, 279.
- [31]B. Zhang, Y. U. Chen, X. Zhuang, G. Liu, B. Yu, E. T. Kang, J. Zhu, Y. Li, *J. Polym. Sci. A Polym. Chem.* **2010**, *48*, 2642.
- [32]D. Long, J. Y. Hong, W. Li, J. Miyawaki, L. Ling, I. Mochida, S. H. Yoon, J. Jang, *ACS Nano* **2011**, *5*, 6254.
- [33]L. S. Panchakarla, K. S. Subrahmanyam, S. K. Saha, A. Govindaraj, H. R. Krishnamurthy, U. V. Waghmare, C. N. R. Rao, *Adv. Mater.* **2009**, *21*, 4726.
- [34]L. S. Zhang, X. Q. Liang, W. G. Song, Z. Y. Wu, *Phys. Chem. Chem. Phys.* **2010**, *12*, 12055.
- [35]I. K. Moon, J. Lee, R. S. Ruoff, H. Lee, *Nat. Commun.* **2010**, *1*.
- [36]W. Gao, L. B. Alemany, L. Ci, P. M. Ajayan, *Nat. Chem.* **2009**, *1*, 403.
- [37]K. H. Liao, A. Mittal, S. Bose, C. Leighton, K. A. Mkhoyan, C. W. MacOsco, *ACS Nano* **2011**, *5*, 1253.
- [38]Y. Zhou, Q. Bao, L. A. L. Tang, Y. Zhong, K. P. Loh, *Chem. Mater.* **2009**, *21*, 2950.
- [39]D. W. Boukhvalov, M. I. Katsnelson, *J. Am. Chem. Soc.* **2008**, *130*, 10697.
- [40]T. Kim, H. Lee, J. Kim, K. S. Suh, *ACS Nano* **2010**, *4*, 1612.
- [41]I. Kaminska, M. R. Das, Y. Coffinier, J. Niedziolka-Jonsson, J. Sobczak, P. Woisel, J. Lyskawa, M. Opallo, R. Boukherroub, S. Szunerits, *ACS Appl. Mater. Interfaces* **2012**, *4*, 1016.
- [42]S. D. Perera, R. G. Mariano, K. Vu, N. Nour, O. Seitz, Y. Chabal, K. J. Balkus, *ACS Catalysis* **2012**, *2*, 949.
- [43]J. Zhang, X. S. Zhao, *J. Phys. Chem. C* **2012**, *116*, 5420.
- [44]A. C. Ferrari, J. Robertson, *Phys. Rev. B* **2000**, *61*, 14095.
- [45]P. Nowicki, R. Pietrzak, H. Wachowska, *Energy Fuels* **2010**, *24*, 1197.
- [46]A. Kira, Y. Matsubara, H. Iijima, T. Umeyama, Y. Matano, S. Ito, M. Niemi, N. V. Tkachenko, H. Lemmetyinen, H. Imahori, *J. Phys. Chem. C* **2010**, *114*, 11293.
- [47]J. Lahaye, G. Nansé, A. Bagreev, V. Strelko, *Carbon* **1999**, *37*, 585.
- [48]G. Nansé, E. Papirer, P. Fioux, F. Moguet, A. Tressaud, *Carbon* **1997**, *35*, 175.
- [49]A. C. Ferrari, J. C. Meyer, V. Scardaci, C. Casiraghi, M. Lazzeri, F. Mauri, S. Piscanec, D. Jiang, K. S. Novoselov, S. Roth, A. K. Geim, *Phys. Rev. Lett.* **2006**, *97*.
- [50]A. Reina, X. Jia, J. Ho, D. Nezich, H. Son, V. Bulovic, M. S. Dresselhaus, K. Jing, *Nano Lett.* **2009**, *9*, 30.
- [51]X. Li, X. Wang, L. Zhang, S. Lee, H. Dai, *Science* **2008**, *319*, 1229.
- [52]X. Wang, Y. Ouyang, X. Li, H. Wang, J. Guo, H. Dai, *Phys. Rev. Lett.* **2008**, *100*.
- [53]V. Coropceanu, J. Cornil, D. A. da Silva Filho, Y. Olivier, R. Silbey, J. L. Brédas, *Chem. Rev.* **2007**, *107*, 926.
- [54]W. S. Hummers Jr, R. E. Offeman, *J. Am. Chem. Soc.* **1958**, *80*, 1339.

Reprinted with permission from D. W. Chang, E. K. Lee, *et al.*, *J. Am. Chem. Soc.* **2013, *135*, 8981–

8988 Copyright © 2013, American Chemical Society

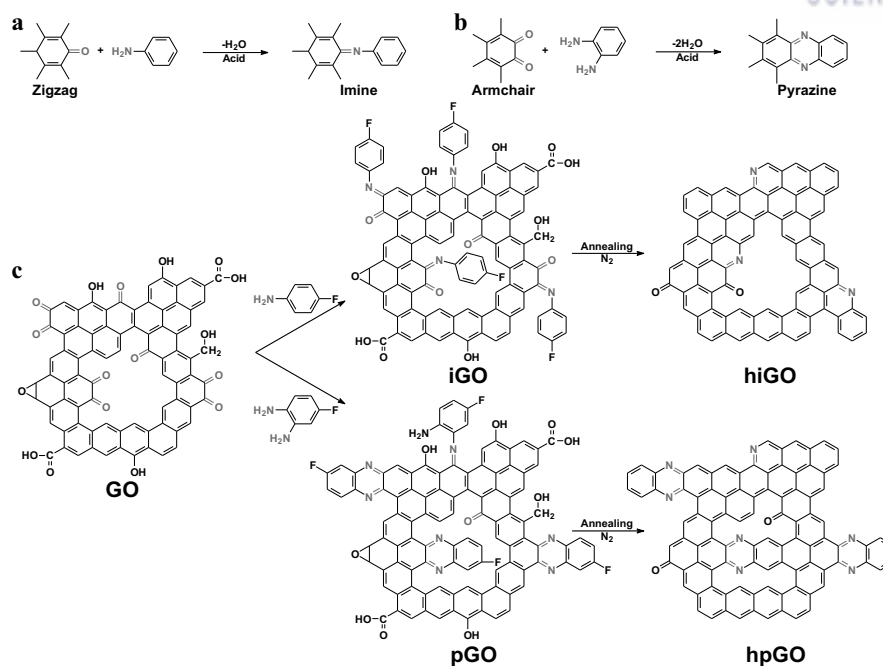


Figure 7.1. Schematic representations: (a) the formation of imine (Schiff base) from the condensation reaction between mono-ketone ($\text{C}=\text{O}$) and aniline (mono-amine); (b) the formation of aromatic pyrazine rings from the double-condensation reaction between α -diketone and 1,2-diaminobenzene (*ortho*-diamine); (c) the reaction between GO and 4-fluoroaniline or 1,2-diamino-4-fluorobenzene to yield iGO or pGO, respectively. Subsequent heat-treatment of iGO and pGO under nitrogen atmosphere produced hiGO and hpGO, respectively.

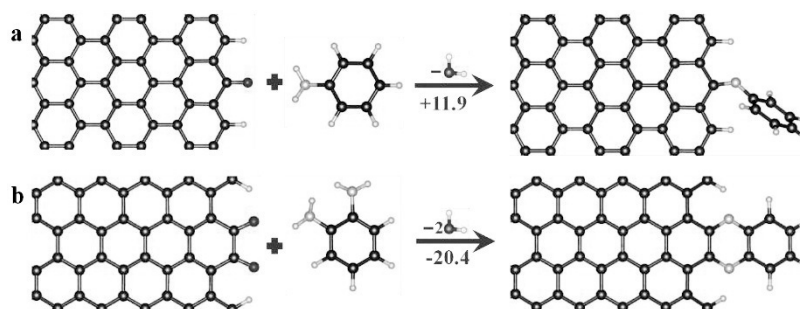


Figure 7.2. Schematic representations: (a) the formation of imine ($-\text{C}=\text{N}-$) bond after the reaction between the mono-ketone ($\text{C}=\text{O}$) group and mono-amine ($\text{H}_2\text{N}-$); (b) the formation 6-membered pyrazine ring after the reaction between the 1,2-diketone and *ortho*-diamine. The formation energies of imine and pyrazine are +11.9 and -20.4 kcal/mol, respectively, indicating the formation of pyrazine is spontaneous reaction.

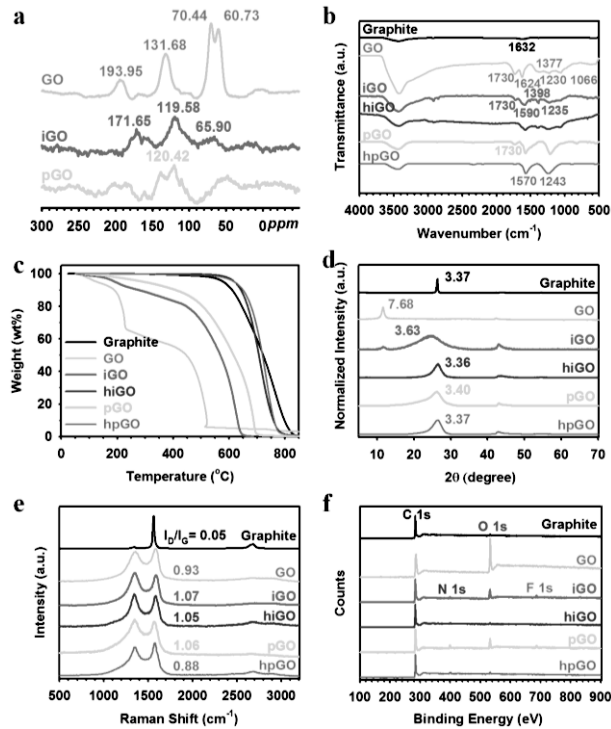


Figure 7.3. (a) Solid-state ^{13}C magic-angle spinning (MAS) NMR spectra of GO, iGO and pGO; (b) FT-IR spectra; (c) TGA thermograms obtained with a heating rate of $10\text{ }^\circ\text{C min}^{-1}$; (d) XRD diffraction patterns. The numbers are d -spacings in angstrom (\AA); (e) Raman spectra; (f) XPS survey spectra of graphite, GO, iGO, pGO, hiGO and hpGO.

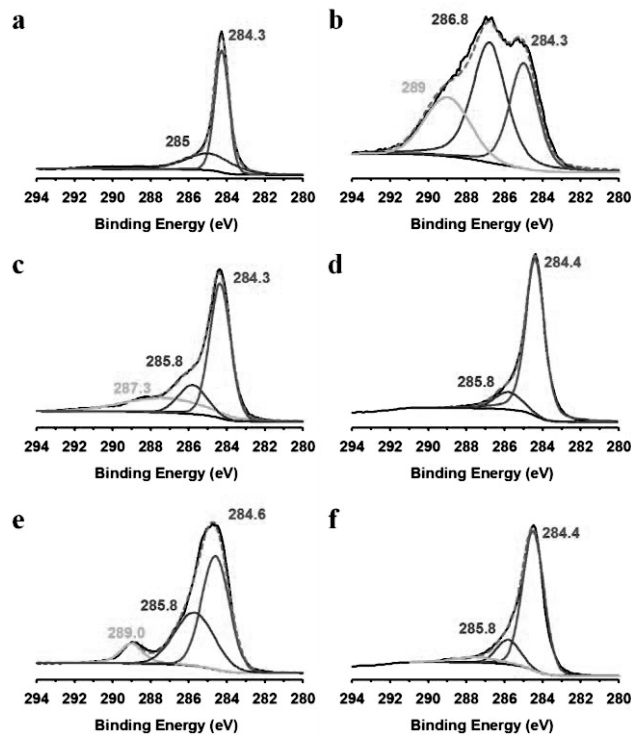


Figure 7.4. High-resolution XPS spectra of C 1s peaks: (a) graphite; (b) GO; (c) iGO; (d) hiGO; (e) pGO; (f) hpGO.

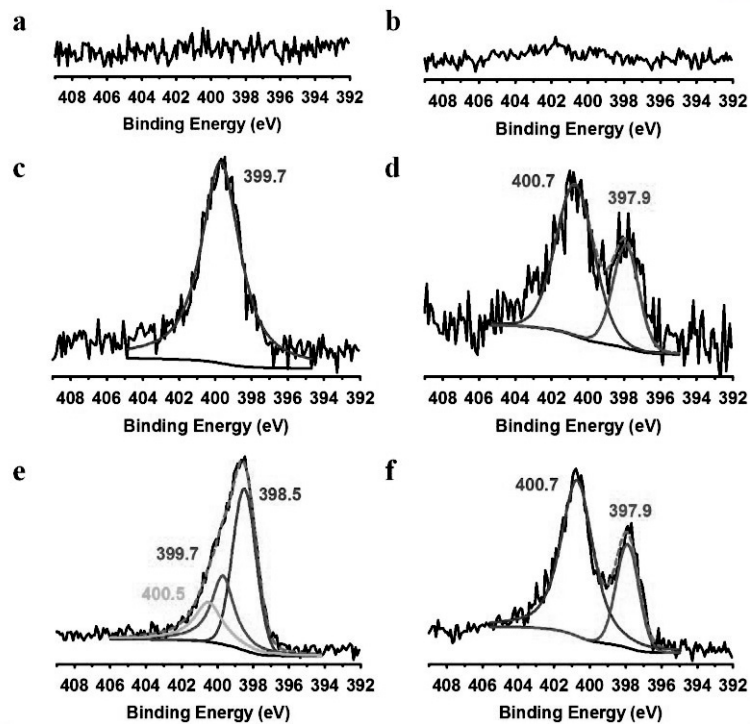


Figure 7.5. High-resolution XPS spectra of N 1s peaks: (a) graphite; (b) GO; (c) iGO; (d) hiGO; (e) pGO; (f) hpGO.

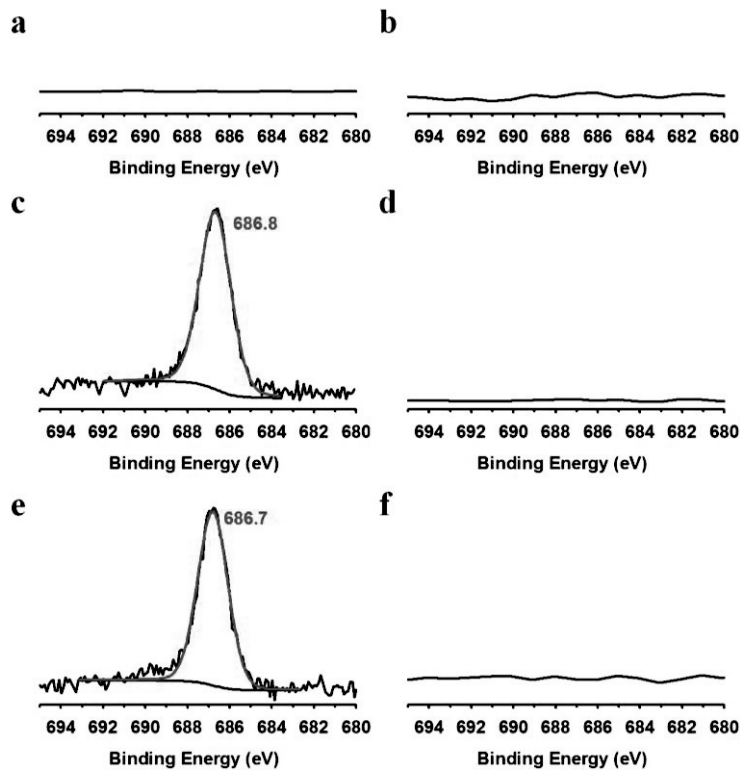


Figure 7.6. High-resolution XPS spectra of F 1s peaks: (a) graphite; (b) GO; (c) iGO; (d) hiGO; (e) pGO; (f) hpGO.

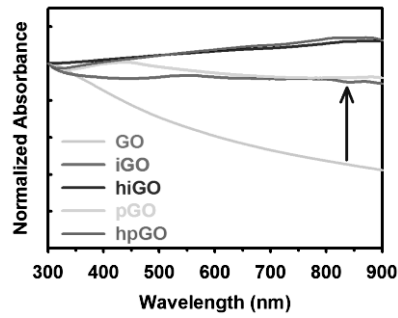


Figure 7.7. UV-vis spectra of GO, iGO, hiGO, pGO and hpGO in DMF solutions.

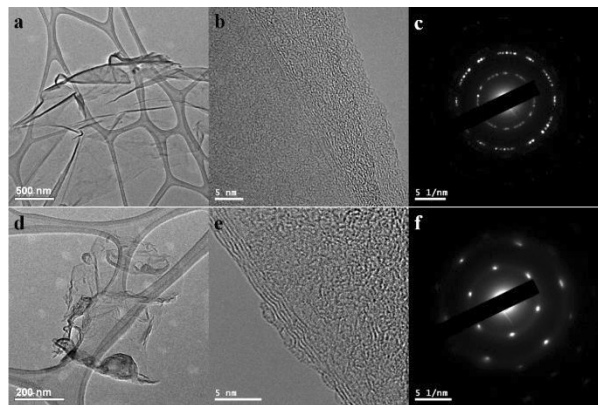


Figure 7.8. (a, b) TEM images of pGO at different magnifications; (c) corresponding selected-area electron diffraction (SAED) pattern taken at the relatively flat area. (d, e) TEM images of hpGO at different magnifications; (f) corresponding SAED pattern.

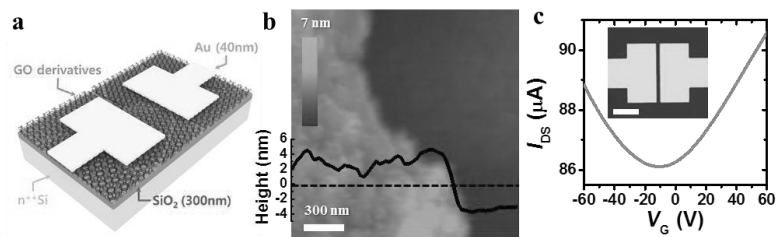


Figure 7.9. (a) Schematic illustration of FETs using GO derivatives as the active layers; (b) a tapping-mode AFM image of hpGO film on a SiO₂/Si wafer. The embedded graph is the thickness profile along the dashed line; (c) the typical transfer curve of hpGO FET at $V_D = 1$ V. The inset is an optical image of hpGO FET with photolithographically patterned gold electrodes ($W/L = 40, L = 3$ μm). Scale bar is 40 μm .

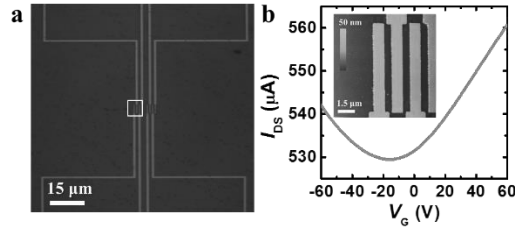


Figure 7.10. (a) Optical image of hpGO FETs with gold electrodes patterned using e-beam lithography ($W/L = 10$, $L = 500$ nm); (b) the typical transfer curve obtained at $V_D = 0.5$ V. Inset is AFM image of the active channel areas squared in (a).

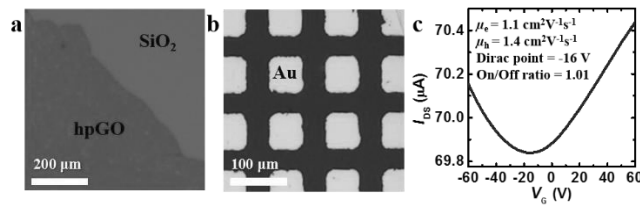


Figure 7.11. Optical microscope images of (a) large area of hpGO film on SiO_2 and (b) hpGO FET devices with top-contact gold electrodes ($W/L = 1.2$). (c) The typical transfer curve obtained at $V_D = 1$ V. Average electron and hole mobilities obtained from 82 FET devices with the long channel length were 1.0 ± 0.03 and 1.4 ± 0.04 $\text{cm}^2\text{V}^{-1}\text{s}^{-1}$, respectively, with the Dirac point of -16.2 ± 3.0 V. This strongly supports our proposition on the effects of grain boundaries.

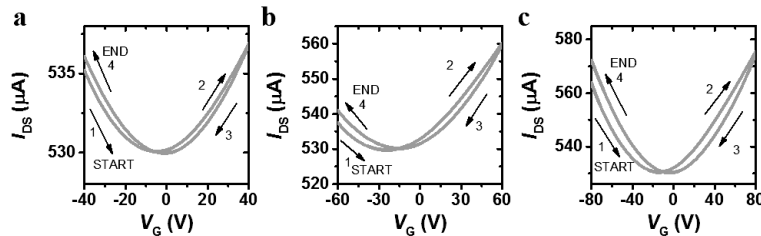


Figure 7.12. Transfer characteristics and hysteresis behaviors of hpGO FETs ($W/L = 10$, $L = 500$ nm). The sweep range of gate voltage varied with (a) -40 V \sim $+40$ V, (b) -60 V \sim $+60$ V and (c) -80 V \sim $+80$ V, respectively.

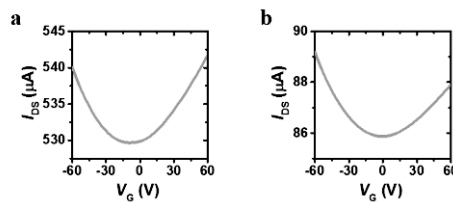


Figure 7.13. Transfer curves of hpGO FETs measured in ambient atmosphere environment: (a) $W/L = 10$, $L = 500$ nm and (b) $W/L = 40$, $L = 3$ μm .

Table 7.1. Elemental analyses of graphite, GO, iGO, hiGO, pGO and hpGO

Sample	C (%)	O (%)	H (%)	N (%)	Sum	O/C	N/C
Graphite	98.81	BDL ^a	0.13	BDL ^a	98.94	0	0
GO	48.92	45.45	2.13	0.05	96.55	1/1.43	1/1141
iGO	72.91	19.41	1.80	2.75	96.87	1/5.01	1/30.93
hiGO	94.29	BDL ^a	0.31	3.12	97.72	0	1/35.26
pGO	74.06	9.85	1.85	9.05	94.81	1/9.95	1/9.55
hpGO	91.80	BDL ^a	BDL ^a	7.73	99.75	0	1/13.86

^aBDL = Below detection limit.

Table 7.2. Average electrical properties of top-contact bottom-gate FET devices fabricated from various samples

Sample ^a	μ_e^b (cm ² V ⁻¹ s ⁻¹)	μ_h^c (cm ² V ⁻¹ s ⁻¹)	On/Off ratio	Dirac point (V)
GO	N/A ^d	N/A	N/A	N/A
hGO	6.3 (±0.9) ^e	8.5 (±0.4)	1.10 (±0.02)	28 (±1.0)
iGO	0.1 (±0.1)	0.1 (±0.1)	1.03 (±0.03)	10 (±3.0)
hiGO	0.5 (±0.03)	1.1 (±0.02)	1.10 (±0.01)	-1 (±0.4)
pGO	0.03 (±0.08)	0.03 (±0.07)	2.10 (±0.02)	16 (±3.0)
hpGO	7.1 (±1.1)	8.4 (±0.9)	1.01 (±0.01)	-7 (±0.7)

^a The average device performance was obtained from 64 devices for each sample. The source and drain electrodes with the channel width-to-length ratio (W/L) of 40 ($L = 3 \mu\text{m}$) were patterned with photolithography.

^b Electron mobility.

^c Hole mobility.

^d The electrical performance of GO FETs exhibited insulating behaviors.

^e The standard deviation.

Table 7.3. Summary of Dirac point shift according to forward and reverse sweeps with different gate voltage sweep ranges.

Gate sweep range (V)	Dirac Point (V)	
	Forward Sweep	Reverse Sweep
-40 ~ +40	-10	-1
-60 ~ +60	-22	-16

Table 7.4. Average (mean) electrical properties of the hpGO FETs measured in ambient atmosphere.

Sample ^a	$L = 500 \text{ nm}$	$L = 3 \mu\text{m}$
μ_h^b ($\text{cm}^2\text{V}^{-1}\text{s}^{-1}$)	8.5 (± 0.4) ^d	2.5 (± 0.5)
μ_e^c ($\text{cm}^2\text{V}^{-1}\text{s}^{-1}$)	6.1 (± 0.4)	1.1 (± 0.5)
Dirac point (V)	-10 (± 1)	-1 (± 1)
On/Off ratio	1.02 (± 0.02)	1.03 (± 0.02)

^a 24 devices were measured in ambient atmosphere.

^b Hole mobility.

^c Electron mobility.

^d The standard deviation.

Chapter 8. Two-dimensional Polyaniline From Carbonized Organic Single Crystals in Solid State

8.1. Introduction

Although one-dimensional (1D) linear polyaniline (PANI) has been discovered in 1834^[1], the word PANI was first coined in 1947^[2] and garnered immense attention from the scientific community due to its intrinsically conducting nature^[3]. During the last three decades, PANI has been one of the most extensively studied conducting polymers because of its simple synthesis, low-cost, high conductivity, environmental stability and doping chemistry^[4, 5]. Linear PANI has found broad applicability in rechargeable batteries^[6], electromagnetic shielding^[7], non-linear optics^[8], light emitting devices^[9], sensors^[10], field effect transistors^[11], erasable optical information storage^[12], membranes^[13], digital memory devices^[14], electrochemical capacitors^[15], electrochromic devices^[16], antistatic and anticorrosion coatings^[17], fuel cells^[18], solar cells^[19] and radar absorbing materials^[20]. Supramolecular PANI nanostructures such as zero-dimensional (0D, nanospheres)^[21], one-dimensional (1D, nanofibers^[22], nanowires^[23], nanorods^[24] and nanotubes^[25]), two-dimensional (2D, nanobelts^[26] and nanosheets^[27]), cyclic, spiral and complex nanostructures have also been reported^[28]. However, due to the mechanistic complexity of aniline polymerization, the atomic-scale control of PANI structure has not yet been realized^[28]. Together with the recent discovery of all carbon-based two-dimensional graphene and its promising potentials^[29], 2D network polymers galvanize a new wave of research in the scientific community^[30]. Here, we, for the first time, report the synthesis of real 2D PANI framework from ‘direct’ pyrolysis of organic single crystals, hexaaminobenzene trihydrochloride (HAB), at 500 °C. The new synthetic methodology could serve as a straightforward way for the design and synthesis of other new 2D layered materials with many potential applications from wet-chemistry to devices.

8.2. Experimental Section

All the chemicals and solvents were purchased from Sigma-Aldrich Chemical Inc. and used without further purification, unless otherwise specified.

Synthesis of hexaaminobenzene (HAB) trihydrochloride. 1,3,5-Triamino-2,4,6-trinitro-benzene (TATB, **2**) (3.0 g, 12 mmol) was placed in a high pressure hydrogenation vessel with 10% Pd/C (0.5 g) and anhydrous ethyl acetate (150 mL) as a solvent. The reaction mixture was agitated under hydrogen (H₂) atmosphere (4.2 bar) until the yellowish colored TATB suspension was completely disappeared. Then, concentrated hydrochloric acid (HCl, 100 mL) was added in to the reaction vessel and further agitated under H₂ (4.2 bar) for additional 5 h. The reaction mixture was then filtered under reduced pressure over Celite to remove the Pd/C catalyst. HAB trihydrochloride (**3**) crystallized out nicely in quantitative yield after washing the Celite with 2M HCl. The precipitates were collected by suction

filtration using polytetrafluoroethylene (PTFE) membrane (0.45 μm) and dried at 70 $^{\circ}\text{C}$ under reduced pressure overnight. To form high-quality single crystals, the white crystals (2.5 g) were dissolved again in deionized and degassed water (15 ml), filtered through PTFE membrane to remove solid impurities, if any, and added concentrated HCl (80 mL). The flask was tightly sealed and placed in the freezer until very large needle-type crystals developed (**Figure 8.1B**).

Synthesis of 2D PANI framework. Needle-type HAB crystals (white needles, 2.0 g) were taken in aluminum oxide crucible and put in the furnace and degassed the chamber five cycles of argon charge/discharge under reduced pressure (10^{-4} torr). Then, the furnace temperature was gradually increased to 500 $^{\circ}\text{C}$ (8 $^{\circ}\text{C}/\text{min.}$) under argon (10 cc/min) flow at reduced pressure for 2 h and maintained at 500 $^{\circ}\text{C}$ with continuous argon flow at reduced pressure (initial pressure: 4.5×10^{-4} ; under argon: 1.9×10^{-3} torr). Then, slowly cooled to room temperature and collected the sample to yield 770 mg (~quantitative) of black needles (**Figure 8.1E**).

STM experiments. The STM experiments were carried out in a ultra-high vacuum (UHV) low-temperature scanning tunneling microscope (SPECS JT-STM) at 77 K. The Cu(111) single crystal was cleaned by a few cycles of Ar^+ sputtering and annealing. After cleaning the Cu(111) substrate, HAB crystal was deposited on the pre-cleaned Cu(111) substrate by *in-situ* thermal evaporation under UHV condition. The sample evaporation temperature was about 600 K, and the temperature of the substrate was maintained at room temperature. To simulate the STM image, we integrated the Kohn-Sham charge density in the energy window of 0.7 eV below and above the Fermi level. The shown image in **Figure 8.2D** is the conduction bands part of the charge density in the plane 1 \AA about the atomic layer.

First-principle calculations. For computations, we used the Vienna *Ab initio* simulation package (VASP) to calculate the ground state of many electrons system in the framework of density functional theory^[35-38]. The plane-wave basis set with an energy cut-off of 400 eV and the PBE-type gradient-corrected exchange-correlation potential were employed^[39]. The ions were described by the projector augmented wave (PAW) potentials. In the self-consistent-field total energy calculations, the k-points are uniformly sampled over the reciprocal space of the two-dimensional triangular lattice with mesh 21 by 21. All the atomic positions were relaxed within residual forces smaller than 0.0 eV/ \AA .

Fabrication of 2D PANI FET devices. The 2D PANI crystalline films were fabricated by drop casting of the HAB crystals dissolved in trifluoromethanesulfonic acid (TFMSA) on the preheated (140 $^{\circ}\text{C}$) SiO_2 (300 nm)/Si substrate and subsequently heat-treated at 700 $^{\circ}\text{C}$ in argon atmosphere for 2 h. The thin flakes were transferred to fresh SiO_2 (300 nm)/Si substrate by polydimethylsiloxane (PDMS) stamping^[32]. Chromium (Cr, 4 nm) and gold (Au, 40 nm) were thermally evaporated. The source and drain electrodes were defined by e-beam lithography (channel length = 500 nm).

8.3. Results and Discussion

The key building block, HAB as a monomer with six functional groups (M6), was synthesized in a pure crystalline form (**Figure 8.1A and Figure 8.3**)^[31]. It was observed that the HAB single crystals pyrolyze prior to melting and maintain their well-defined, needle-like crystal morphologies even after pyrolysis at 500 °C. The pure HAB crystals have a well-defined hexagonal morphology (**Figure 8.1B, 1C, 1D; Figure 8.4 and Figure 8.5**), which is maintained even after annealing at 500 °C (**Figure 8.1E, 1F, 1G; Figure 8.6 and Figure 8.7**). These results suggest that HAB single crystals could be directly pyrolyzed into highly stable, rigid hexagonal rods. The pyrolyzed HAB crystals, which are up to a few millimetres long, have a rod-like hexagonal structure. High-resolution SEM images reveal a more layered graphitic structure and a highly wrinkled morphology (**Figure 8.1G; Figure 8.6**), which is attributed to the two-dimensional sheet-like appearance of the 2D PANI framework. Hence, we investigated the mechanism underlying the pyrolysis of HAB single crystals. The transformation of HAB crystals into a 2D layered PANI structure should involve releases of ammonium chloride (NH₄Cl) and ammonia (NH₃) *via* a concerted mechanism (**Figure 8.1A; Figure 8.8**).

To confirm the unusual chemistry of the 2D network-forming reaction and the stability of the resulting product, the pure HAB crystals were subjected to thermogravimetric analysis (TGA) (**Figure 8.9A**) under an argon atmosphere. At approximately 250 °C, the HAB single crystal (**left inset, Figure 8.9A**), which is considered to be a hexa-functional (M6) monomer, undergoes an endothermic weight loss of 15%. This weight loss is attributed to the partial evaporation of bound hydrochloric acid (HCl) and water. A highly exothermic weight loss of 42% is observed at approximately 325 °C, indicating that new covalent bonds and a stable network structure are formed (**right inset, Figure 8.9A**), as the remaining ammonium chloride (NH₄Cl) and ammonia (NH₃) molecules are released from the structure. The release of ammonium chloride and ammonia was confirmed using chemical methods (**Figure 8.10, the detailed test method and corresponding discussion are described**). The formation energy per repeating unit of the 2D PANI structure ($C_6N_6H_{15}Cl_3 \rightarrow C_6N_2 + 3NH_4Cl + NH_3$) was calculated to be -2.03 eV using first-principle density functional theory (DFT) calculations (**Figure 8.11**), demonstrating the driving force of reaction and stability of the formed product. Thus, the process is assumed to spontaneously produce a covalently bonded 2D PANI network structure. In addition, the product exhibits good thermal stability in both nitrogen (**Figure 8.9B**) and air (**Figure 8.12**), suggesting the formation of stable 2D PANI network structures.

The elemental composition determined using the different techniques is very close to the calculated value (**Table 8.1**). The empirical formula of the 2D PANI is C₃N for the core repeat unit (**structure 3, Figure 8.1A**). When bulk molecule with the edge amine functional groups is taken into account, the empirical formula is C₃NH (**structure 2, Figure 8.1A; structure 7, Figure 8.8**). This novel 2D PANI structure was further verified using solid-state carbon nuclear magnetic resonance (¹³C-NMR) measurements, showing only two peaks in the spectrum (**Figure 8.9C**). The peak at 150.80 ppm is attributed to the carbon atoms attached to tertiary nitrogen in the basal plane of 2D PANI framework

(dark-blue dot, inset in Figure 8.9C). The peak at 126.02 ppm is assigned to the carbon atoms covalently bonded to primary or secondary amine groups at the edges of 2D PANI framework (dark-yellow dot, inset in Figure 8.9C).

The chemical composition and bond nature of 2d PANI were probed using XPS. The XPS survey spectrum contains only C 1s, N 1s and O 1s peaks, and no other impurities are observed (Figure 8.9D). The high-resolution C 1s spectrum can be deconvoluted into three peaks at 284.6, 285.6 and 288.5 eV (Figure 8.13A). The peaks at 284.6 and 285.6 eV are assigned to sp^2 C-C and sp^2 C-N, respectively, in the 2D PANI framework, whereas the minor peak at 288.5 eV is attributed to C-NH₂ at the edges. The N 1s spectrum has two peaks at 398.6 and 400.6 eV due to sp^2 C₂-NH and sp^2 C₃-N, respectively (Figure 8.13B). The small oxygen content (O 1s) in the structure can be assigned to physically adsorbed molecular oxygen and water due to the polar nature of material (Figure 8.13C). The powder X-ray diffraction (PXRD) from the 2D PANI reveals three major peaks at at (2θ) 12.8, 26.12, 44.7 with corresponding d -spacing of 6.87, 3.40, 2.02 Å (Figure 8.14). The peak at 26.12° is related to interlayer d -spacing (3.40 Å) of the 2D PANI. The experimental XRD is well matching with the simulated XRD after Pawley refinement (Table 8.2).

To resolve the atomic-level structure of the 2D PANI framework, we performed scanning tunnelling microscopy (STM) (SPECS JT-STM). HAB molecules were deposited *in situ* on a clean Cu(111) single crystal by thermal evaporation at 600 K followed by annealing for 5 minutes. All of the STM experiments were performed under ultra-high vacuum (UHV) at a low temperature (77 K). The 2D PANI framework has a well-ordered triangular structure (Figure 8.2A) with the dot-to-dot distance of 442 ± 16 pm (Figure 8.2B). To examine the electronic structure of 2D PANI, scanning tunnelling spectroscopy (STS) was performed using the lock-in detection technique. Two prominent peaks were observed at -1.0 eV and 1.6 eV in the valence band and conduction band regions, respectively (Figure 8.2C), which is in good agreement with the electrochemically determined HOMO-LUMO gap of 2.67 eV (Figure 8.15A and B). The measurement of electrochemical HOMO-LUMO gap from the starting HAB molecules was not possible because of the instability of HAB in the measuring condition (Figure 8.15C), indicating that 2D PANI structures are distinctly different from those of self-assembled HAB molecular crystals without pyrolysis.

First-principles DFT calculations were performed to analyse the STM image and to determine the electronic structure. To produce the calculated STM image, the Kohn-Sham charge density was integrated from the Fermi level to 1.1 eV below the Fermi level. Theoretical lattice constant is 475 pm (Figure 8.2D), which is well matched with experimental observation (Figure 8.2A). The band structure along the symmetry lines in the Brillouin zone and the projected density of electronic states (PDOS) are shown in Figure 8.2E and 3F, respectively. Gradient-corrected DFT calculations show that 2D PANI framework has a non-zero finite density of states near the Fermi level, in agreement with the STS measurement (Figure 8.2C). The valence band maximum and conduction band minimum are both

derived from the carbon and nitrogen p_z orbitals. The detailed electronic structures are described in **Figure 8.16**. The conduction band minimum states closely resemble the electronic structures of benzene rings bridged by nitrogen atoms.

To elucidate the electrical properties, field-effect transistors (FETs) were fabricated using 2D PANI flakes as the active layer. 2D PANI flakes were isolated onto Si wafer with 300 nm-thick SiO_2 by using polydimethylsiloxane (PDMS) stamping from the prepared films ^[32]. **Figure 8.17A** is a typical optical image of the FET based on a 2D PANI flake. Source and drain electrodes were deposited with the thermal evaporation of Cr (4 nm) and Au (40 nm) and the following e-beam lithography (channel length = 500 nm). The electrical properties of 10 FETs based on 2D PANI flakes were characterized (**Figure 8.17A and Figure 8.18**). Atomic force microscopy (AFM) analysis of 2D PANI flake positioned on a white square (**inset, Figure 8.17A**) disclosed that the average thickness of the sample was 8.0 ± 1.2 nm, revealing the multilayers of the 2D PANI were stacked as shown in **Figure 8.17B**. The pristine 2D PANI nanoflakes exhibited n -doped ambipolar behaviours with Dirac point of -37 ± 3 V (**Figure 8.17C**). Furthermore, the Ohmic contact behaviours between 2D PANI and source-drain electrodes were observed from the output curve (**Figure 8.19**). The average hole and electron mobilities were 0.047 ± 0.014 and 0.110 ± 0.019 $\text{cm}^2 \text{V}^{-1} \text{s}^{-1}$, respectively.

Figure 8.17D is the schematic diagram of the experimental set-up for doping 2D PANI with hydrochloric acid (HCl) in a Pyrex glass container equipped with a dopant loading reservoir. After evacuating the chamber, 5 mL HCl (35 %) was injected into the dopant loading reservoir. Then the glass chamber was heated to various temperature ranges (20 – 160 °C) for 1 h in order to vaporise HCl for gaseous doping. The electrical properties of the FET devices were characterized inside a vacuum probe station. The conductivity of the pristine 2D PANI (undoped) was 0.72 ± 0.04 S/cm, while pristine linear PANI (undoped) is an insulator (**Table 8.3**). After doping with HCl, 2D PANI showed dramatically increased electrical conductivity as shown in **Figure 8.17E**. With elevating the doping temperature to 160 °C, the conductivity of the HCl-doped 2D PANI was increased as high as $1.41 \pm 0.06 \times 10^3$ S/cm, indicating that the electrical conductivity was increased by a factor of ~ 1900 after doping (**Figure 8.17E**). This unprecedentedly high electrical conductivity of 2D PANI is approximately two orders of magnitude higher than the best performance of HCl-doped linear PANI reported to date ^[33]. To the best of our knowledge, this value is the record high conductivity ever reported for PANI (**Table 8.3**) ^[34]. In addition, as 2D PANI was doped, field-effect behaviours disappeared as shown in **Figure 8.20 and Figure 8.21**. The Ohmic contact between 2D PANI and source-drain electrodes was also maintained with changing doping temperature (**Figure 8.20**). From these temperature-dependent doping experiments, the lowest temperature for optimizing the conductivity was found to be approximately 100 °C (**Figure 8.17F**). Thus, 2D PANI can serve as a new class of soft 2D material with superior electrical properties.

8.4. Conclusion

In summary, we demonstrated that a new synthetic protocol for 2D PANI, which can be produced by ‘direct’ pyrolysis of organic HAB single crystals and has empirical formula of C_3N (three sp^2 C atoms sharing a tertiary N) at basal area. The atomic-level true 2D PANI structure was first realized, as confirmed by STM imaging. While DFT calculation suggested that 2D PANI had scant density of state at Fermi level as a metallic conductor, STS revealed intrinsic electronic nature of 2D PANI with a HOMO-LUMO gap of 2.7 eV. Upon doping with gaseous HCl at an elevated temperature (~ 160 °C), the 2D PANI flakes exhibited electrical conductivity of 1.41×10^3 S/cm which was two orders of magnitude higher than the best value of the doped linear PANI analogues reported to date. The structure of 2D PANI is quite striking, because it contains uniformly distributed nitrogen atoms for multifunctionality; hence, we expect that 2D PANI has strong potential from wet-chemistry to device applications beyond graphene and its linear analogue.

8.5. References

- [1] F. F. Runge, *Annalen der Physik* **1834**, 107, 65.
- [2] O. W. Brown, W. C. Frishe, *J. Phys. Colloid Chem.* **1947**, 51, 1394.
- [3] A. G. Macdiarmid, J.-C. Chiang, M. Halpern, W.-S. Huang, S.-L. Mu, L. D. Nanaxakkara, S. W. Wu, S. I. Yaniger, *Mol. Cryst. Liq. Cryst.* **1985**, 121, 173.
- [4] J. Stejskal, R. G. Gilbert, in *Pure Appl. Chem.*, Vol. 74, 2002, 857.
- [5] J.-C. Chiang, A. G. MacDiarmid, *Synth. Met.* **1986**, 13, 193.
- [6] A. G. MacDiarmid, L. S. Yang, W. S. Huang, B. D. Humphrey, *Synth. Met.* **1987**, 18, 393.
- [7] D. C. Trivedi, S. K. Dhawan, *Synth. Met.* **1993**, 59, 267.
- [8] C. Halvorson, Y. Cao, D. Moses, A. J. Heeger, *Synth. Met.* **1993**, 57, 3941.
- [9] H. L. Wang, A. G. MacDiarmid, Y. Z. Wang, D. D. Gebier, A. J. Epstein, *Synth. Met.* **1996**, 78, 33.
- [10] D. Dutta, T. K. Sarma, D. Chowdhury, A. Chattopadhyay, *J. Colloid Interface Sci.* **2005**, 283, 153.
- [11] M. M. Alam, J. Wang, Y. Guo, S. P. Lee, H.-R. Tseng, *J. Phys. Colloid Chem. B* **2005**, 109, 12777.
- [12] R. P. McCall, J. M. Ginder, J. M. Leng, K. A. Coplin, H. J. Ye, A. J. Epstein, G. E. Asturias, S. K. Manohar, J. G. Masters, E. M. Scherr, Y. Sun, A. G. Macdiarmid, *Synth. Met.* **1991**, 41, 1329.
- [13] N. V. Blinova, J. Stejskal, M. Trchová, G. Ćirić-Marjanović, I. Sapurina, *J. Phys. Colloid Chem. B* **2007**, 111, 2440.
- [14] R. J. Tseng, J. Huang, J. Ouyang, R. B. Kaner, Yang, *Nano Lett.* **2005**, 5, 1077.
- [15] B. E. Conway, V. Birss, J. Wojtowicz, *J. Power Sources* **1997**, 66, 1.
- [16] A. Bessière, C. Duhamel, J. C. Badot, V. Lucas, M. C. Certeat, *Electrochim. Acta* **2004**, 49, 2051.
- [17] A. Kalendová, D. Veselý, J. Stejskal, *Prog. Org. Coat.* **2008**, 62, 105.
- [18] G. K. S. Prakash, P. Suresh, F. Viva, G. A. Olah, *J. Power Sources* **2008**, 181, 79.
- [19] M.-Y. Chang, C.-S. Wu, Y.-F. Chen, B.-Z. Hsieh, W.-Y. Huang, K.-S. Ho, T.-H. Hsieh, Y.-K. Han, *Org. Electron.* **2008**, 9, 1136.
- [20] T. Mäkelä, J. Sten, A. Hujanen, H. Isotalo, *Synth. Met.* **1999**, 101, 707.
- [21] H. Gao, T. Jiang, B. Han, Y. Wang, J. Du, Z. Liu, J. Zhang, *Polymer* **2004**, 45, 3017.
- [22] S. Virji, J. Huang, R. B. Kaner, B. H. Weiller, *Nano Lett.* **2004**, 4, 491.
- [23] Y. Ma, J. Zhang, G. Zhang, H. He, *J. Am. Chem. Soc.* **2004**, 126, 7097.
- [24] D. Chaudhuri, S. Datar, R. Viswanatha, D. D. Sarma, H. Amenitsch, *Appl. Phys. Lett.* **2005**, 87, 093117.
- [25] Z. Wei, Z. Zhang, M. Wan, *Langmuir* **2002**, 18, 917.
- [26] G. Li, H. Peng, Y. Wang, Y. Qin, Z. Cui, Z. Zhang, *Macromol. Rapid Commun.* **2004**, 25, 1611.
- [27] J. Han, G. Song, R. Guo, *Adv. Mater.* **2007**, 19, 2993.

- [28]G. Ćirić-Marjanović, *Synth. Met.* **2013**, *177*, 1.
- [29]K. S. Novoselov, A. K. Geim, S. V. Morozov, D. Jiang, Y. Zhang, S. V. Dubonos, I. V. Grigorieva, A. A. Firsov, *Science* **2004**, *306*, 666.
- [30]A. K. Geim, K. S. Novoselov, *Nat Mater* **2007**, *6*, 183.
- [31]J. Mahmood, D. Kim, I.-Y. Jeon, M. S. Lah, J.-B. Baek, *Synlett* **2013**, *24*, 246.
- [32]J. Mahmood, E. K. Lee, M. Jung, D. Shin, I.-Y. Jeon, S.-M. Jung, H.-J. Choi, J.-M. Seo, S.-Y. Bae, S.-D. Sohn, N. Park, J. H. Oh, H.-J. Shin, J.-B. Baek, *Nat Commun* **2015**, *6*.
- [33]I. Y. Choi, J. Lee, H. Ahn, J. Lee, H. C. Choi, M. J. Park, *Angew. Chem. Int. Ed.* **2015**, *127*, 10829.
- [34]K. Lee, S. Cho, S. Heum Park, A. J. Heeger, C.-W. Lee, S.-H. Lee, *Nature* **2006**, *441*, 65.
- [35]P. Hohenberg, W. Kohn, *Phys. Rev.* **1964**, *136*, B864.
- [36]W. Kohn, L. J. Sham, *Phys. Rev.* **1965**, *140*, A1133.
- [37]G. Kresse, J. Furthmüller, *Phys. Rev. B* **1996**, *54*, 11169.
- [38]G. Kresse, J. Furthmüller, *Comput. Mater. Sci.* **1996**, *6*, 15.
- [39]J. P. Perdew, K. Burke, M. Ernzerhof, *Phys. Rev. Lett.* **1996**, *77*, 3865.

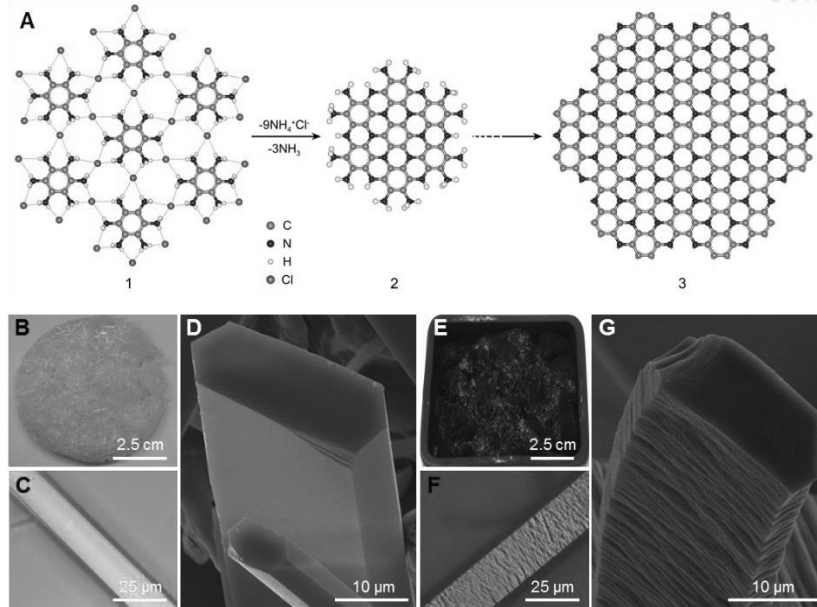


Figure 8.1. Schematic representation of 2D PANI formation. (A) Single-crystal X-ray packing structure of HAB (**structure 1**); structure of 2D PANI unit with edge groups (C_3NH , **structure 2**) and the spontaneous transformation of HAB crystal unit into the 2D PANI structure (**structure 3**).

Morphology changes of HAB crystals into 2D PANI frameworks. (B) Digital photograph of HAB crystals on butter paper. (C) Optical microscopy image of a needle-like HAB crystal before annealing. (D) SEM image of an HAB single crystal before annealing. (E) Digital image of HAB after annealing at 500 $^\circ\text{C}$. (F) Optical microscopy image of 2D PANI crystal after annealing at 500 $^\circ\text{C}$. (G) SEM image of a 2D PANI single crystal after annealing.

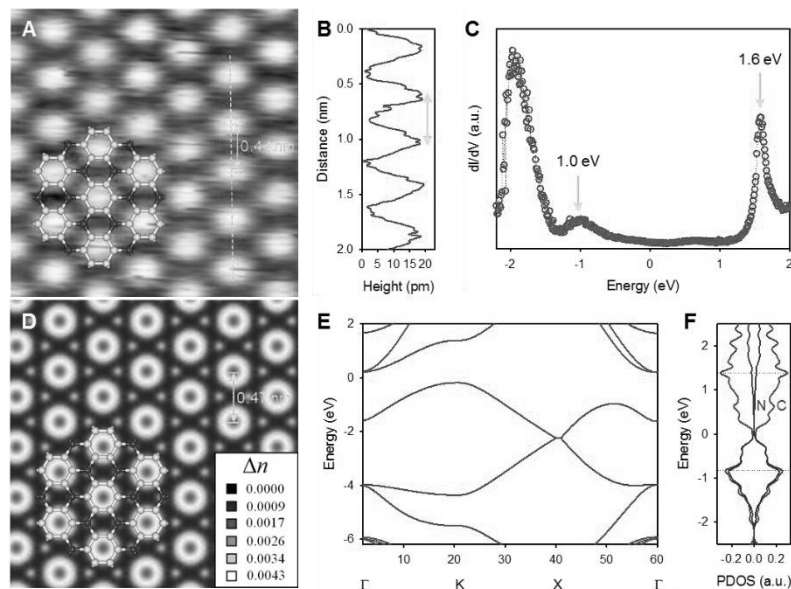


Figure 8.2. STM and theoretical studies of the 2D PANI structure. (A) STM image of a 2D PANI framework ($2.5 \times 2.5 \text{ nm}^2$, $V_s = -1.1 \text{ V}$, $I_t = 1.0 \text{ nA}$). Inset structure represents C_3N repeating unit with carbon atom (grey ball) and nitrogen atom (blue ball). (B) Topographic height profile along the cyan dot line marked in A. (C) Differential conductance (dI/dV) spectrum of a 2D PANI framework. (D)

Simulated STM image with superimposed structure of C_3N repeating unit. (E) Electronic band structure. (F) PDOS of the carbon (dark-red) and nitrogen (dark-blue) atoms.

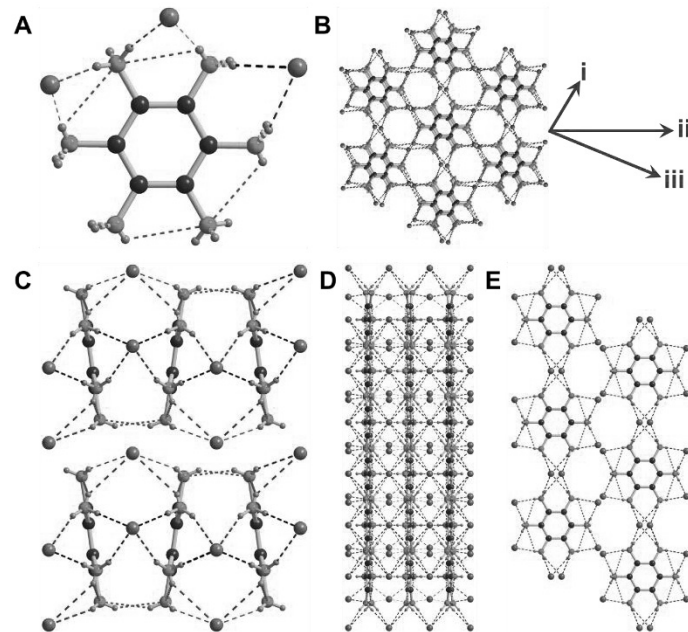


Figure 8.3. Single crystal structure of HAB. (A) The structure of HAB formula unit; (B) hydrogen-bonded three layers of HAB crystal; (C) hydrogen-bonded packing *i*-direction view in B; (D) hydrogen-bonded packing *ii*-direction view in B; (E) hydrogen-bonded packing *iii*-direction view in B.

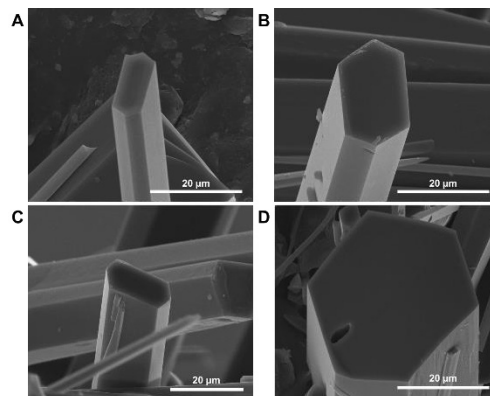


Figure 8.4. SEM images of the pure HAB crystals before pyrolysis. (A-D) Showing well-defined hexagonal rod like framework from different crystals.

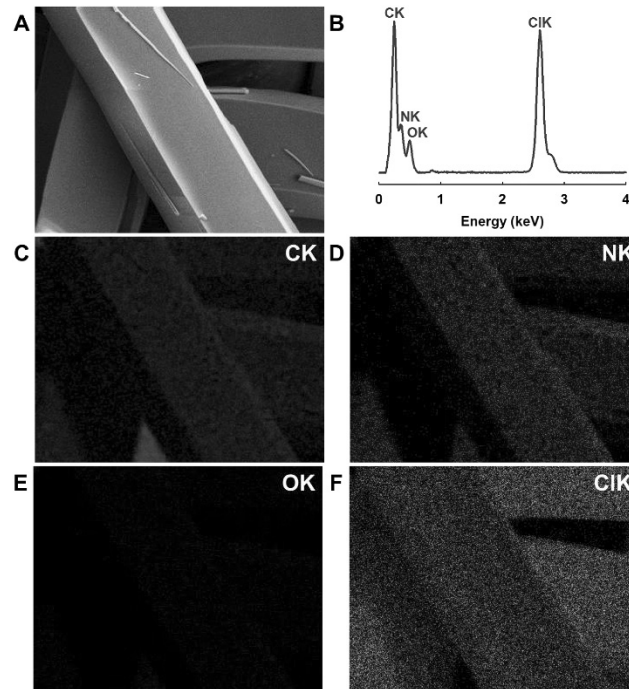


Figure 8.5. SEM EDS analysis of HAB crystals before pyrolysis. (A) SEM image; (B) SEM energy dispersive X-ray spectroscopy (EDS) showing the elemental composition of the hexaaminobenzene hydrochloride (HAB); (C) C-mapping; (D) N-mapping; (E) O-mapping; (F) Cl-mapping from the corresponding SEM image.

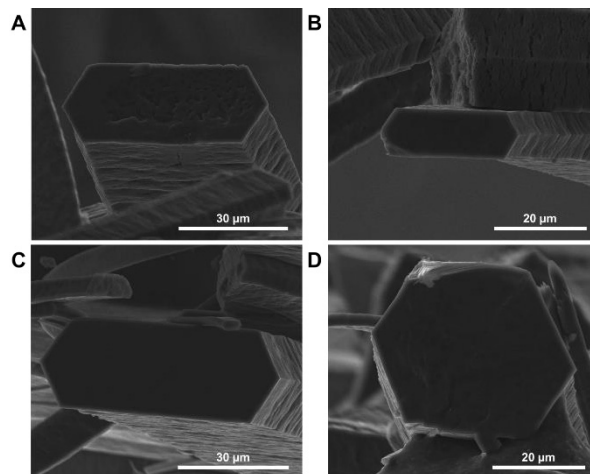


Figure 8.6. SEM images of the 2D PANI frameworks. (A-D) Showing the stacked layers and the prominent hexagonal rod like morphology is well maintained after annealing at 500 °C.

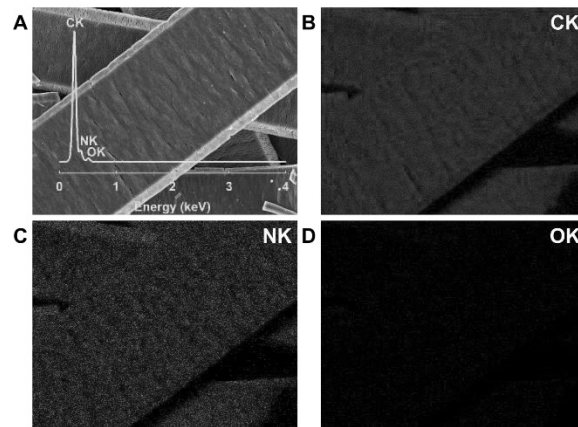


Figure 8.7. SEM EDS analysis of 2d PANI. (A) SEM image with energy dispersive X-ray spectroscopy (EDS) showing the elemental composition of the 2D PANI framework; (B) C-mapping; (C) N-mapping; (D) O-mapping from the corresponding SEM image, showing no chloride peak in the EDS spectrum.

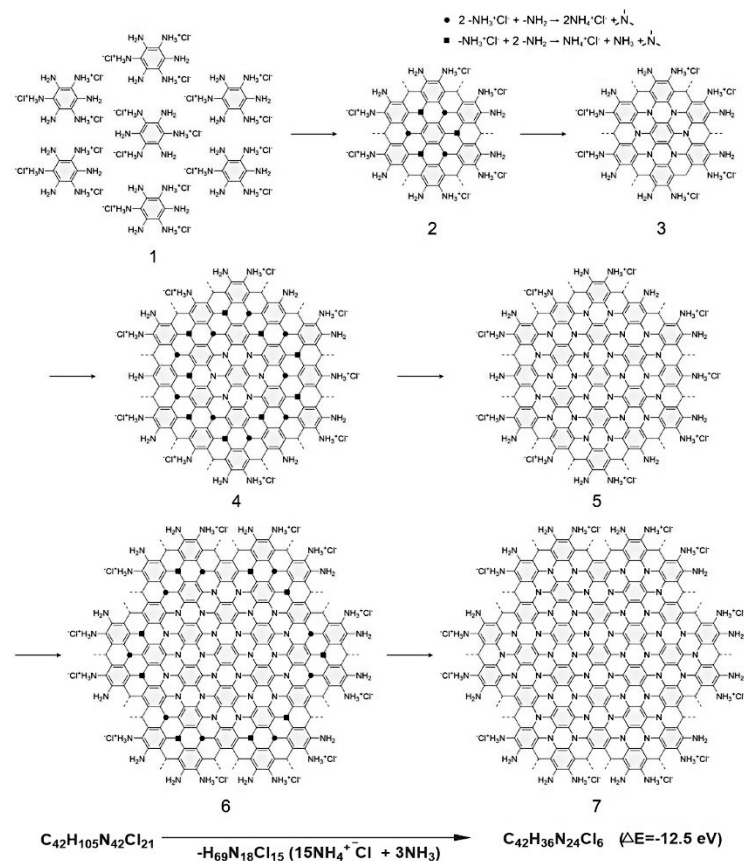


Figure 8.8. Mechanistic representation for the formation of the 2D PANI framework from HAB crystals *via* C₃NH structure with edge groups. The 2D PANI is formed spontaneously with the removal of ammonium chloride (NH₄Cl) and ammonia (NH₃). For clarification, we have assigned

dark blue color to the amine group ($-NH_2$) and the dark red color to the HCl attached amine ($-NH_3Cl$) group in the HAB molecule. When two blue and one red react and form tertiary nitrogen (N^+) linkage releasing two NH_4Cl molecules, represented by black dots (\bullet). When two reds and one blue react and form tertiary nitrogen (N^+) linkage, releasing one NH_4Cl and one NH_3 molecules, represented by black squares (\blacksquare). This reaction occurs spontaneously forming 2D PANI.

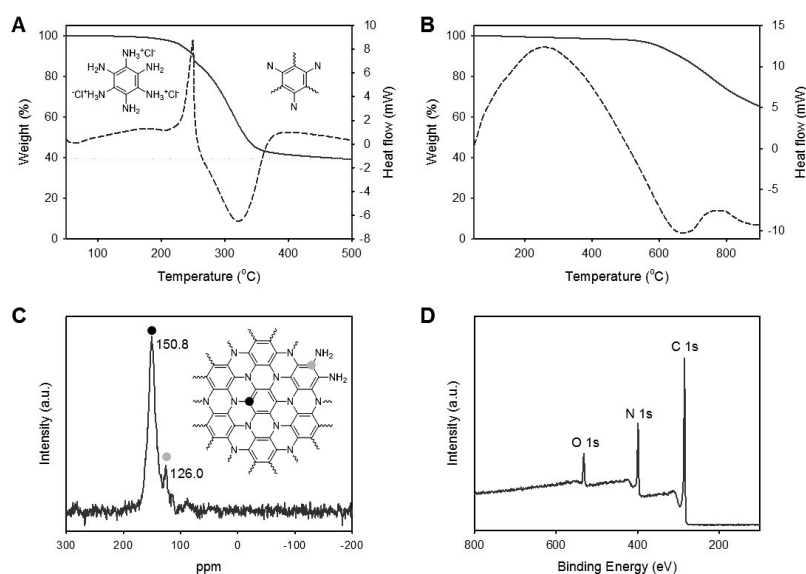


Figure 8.9. Characterisations of the 2D PANI structures. (A) TGA thermogram obtained from an HAB single crystals with a ramping rate of $10\text{ }^\circ\text{C}/\text{min}$ in argon. (B) TGA thermogram obtained from a 2D PANI framework with a ramping rate of $10\text{ }^\circ\text{C}/\text{min}$ in argon. TGA thermogram in air is presented in **Figure 8.12**. (C) Solid-state ^{13}C magic-angle spinning (MAS) NMR spectrum of 2D PANI framework showing only two carbon peaks. (D) XPS survey spectrum of 2D PANI framework. Its high-resolution XPS spectra are presented in **Figure 8.13**.

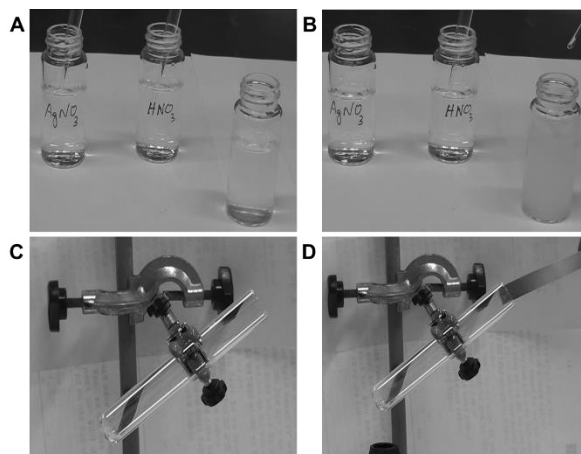


Figure 8.10. Detection of ammonium chloride. (A) Before addition of AgNO₃ to the sample solution (right vial); (B) after addition of AgNO₃, white precipitation appeared, indicating the presence of chloride ion $\text{HAB} + \text{HNO}_3 + \text{AgNO}_3 \rightarrow \text{AgCl}$ (white precipitation in water, right vial); (C) mixture of HAB and NaOH, before heating; (D) after heating the mixture, pH paper at the mouth of the test tube turn deep green, showing the release of ammonia gas as follow: $\text{NH}_4^+\text{Cl}^- + \text{Na}^+\text{OH}^- \rightarrow \text{NaCl} + \text{H}_2\text{O}\uparrow + \text{NH}_3\uparrow$. When the HAB monomer is annealed in a quartz tube furnace, ammonium chloride is released and deposited as ammonium chloride crystals, which have a melting point of 340 °C (sublimation), inside the tube and outside the heating zone. The deposited material was collected from the furnace tube and washed with chloroform to afford a white compound. Then, basic chemical tests were performed to detect ammonia and the chloride ion in the solution. The chloride ion was detected using a silver nitrate solution, because it forms a white precipitate after reaction with silver into silver chloride (AgCl) (Figure 8.10A and S7B). To identify ammonia, sodium hydroxide was added to the white crystals, which were then heated using a heat gun. Upon heating, ammonia is released and reacts with damp pH paper placed at the mouth of the test tube, turning it dark green (Figure 8.10C and S7D).

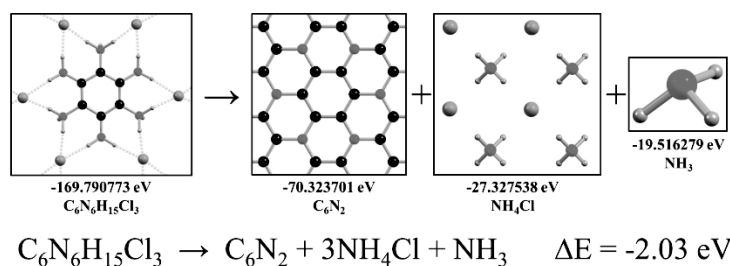


Figure 8.11. Estimation of the formation energy of 2D PANI structure. In this calculation, the two-dimensionally ionic-bonded lattice of C₆N₆H₁₅Cl₃ crystals, three-dimensional solid salt structures of ammonium chloride (NH₄Cl) and ammonia (NH₃) molecules are used for the reference of reactant and product. In this gauge, the energy gain per C₃N formula unit is calculated to be -2.03 eV in our DFT-PBE calculation.

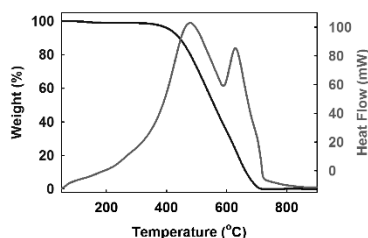


Figure 8.12. Thermal stability of 2D PANI in air. TGA thermogram obtained from a 2D PANI crystal after annealing (500 °C) with heating rate of 10 °C/min in air.

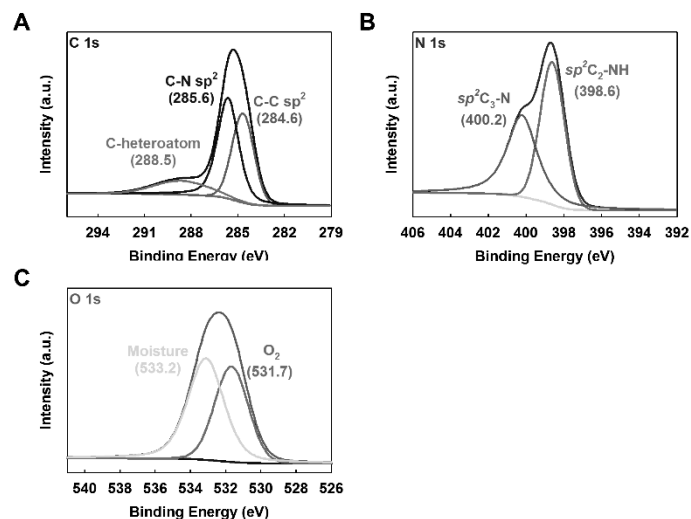


Figure 8.13. Bond nature in 2D PANI framework. High-resolution XPS survey spectra of 2D PANI framework. (A) C 1s; (B) N 1s; (C) O 1s. Little amount of oxygen content is originated from physically absorbed moisture and oxygen due to hygroscopic nature of 2D PANI.

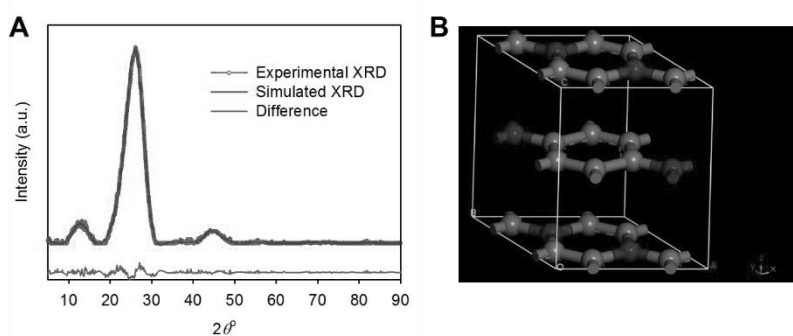


Figure 8.14. Powder XRD of the 2D PANI. (A) experimental PXRD pattern from the 2D PANI (dark green), simulated XRD after Pawley refinement (dark red) and the difference (dark blue); (B) unit cell of the 2D PANI with AB stacking.

The simulated XRD pattern was obtained by Pawley refinement of the PXRD pattern to optimize the lattice parameters until the R_p and R_{wp} values converge. The pseudo-Voigt profile function was performed for the whole profile fitting in the refinement processes. The final R_p and R_{wp} values were 6.32% and 3.50% (Table 8.2).

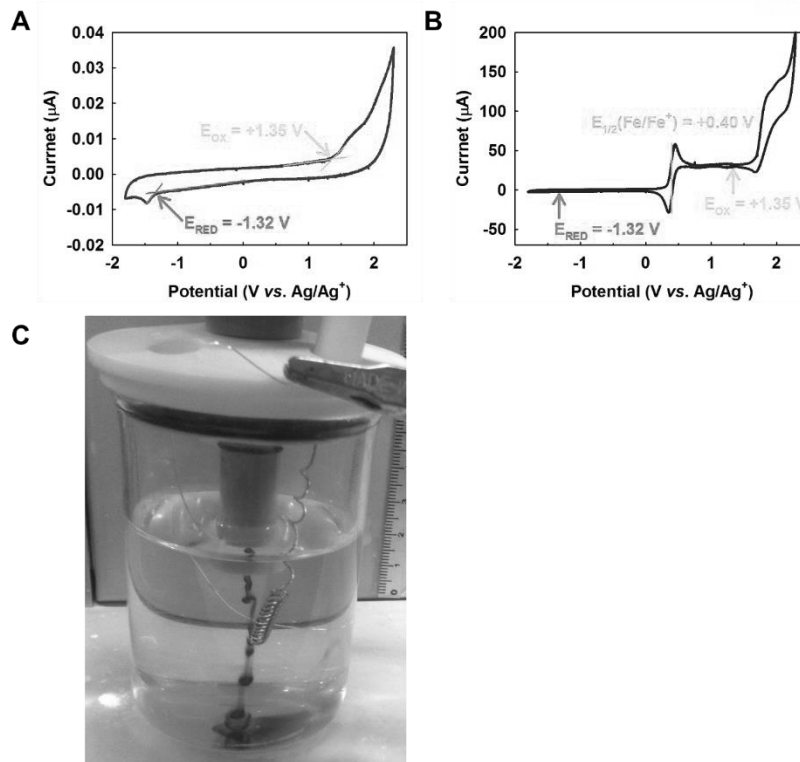


Figure 8.15. Electrochemical analysis of 2D PANI by cyclic voltammograms in acetonitrile containing 0.1 M TBAPF₆. (A) 2D PANI crystals; (B) 2D PANI crystal with Ferrocene; (C) pure HAB crystals were also tried to measure the electrochemical band gap, but HAB molecules were unstable in the electrochemical test condition. HAB decomposed during the process. Thus, it was not able to determine HOMO-LUMO gap by electrochemical method.

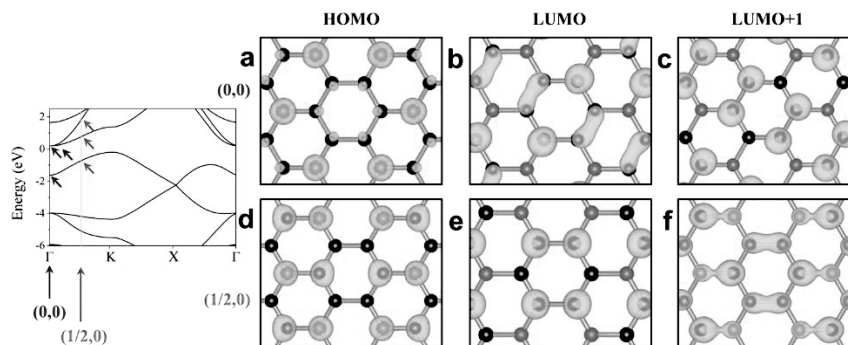


Figure 8.16. The band structure (Figure 8.2E) for the 2D triangular lattice of 2D PANI. (A) the valence band maximum state at Γ ; (B, C) the doubly degenerate conduction band minimum state at Γ ; (D) the valence band maximum state at M ($1/2,0$); (E, F) two low-lying state in the conduction band minimum at M.

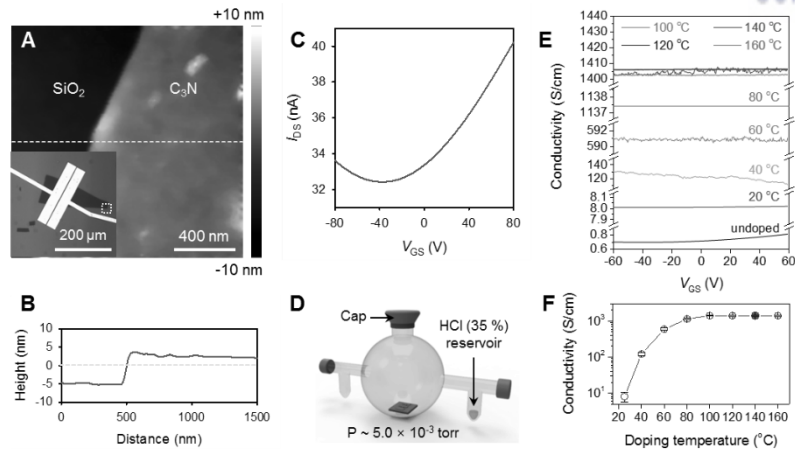


Figure 8.17. Electrical performance of 2D PANI and doping study with HCl gas. (A) AFM height image from the white square marked in the inset. Inset is optical microscope image of FET using 2D PANI as active materials on Si wafer with 300 nm SiO₂. Source and drain (channel length = 500 nm) were patterned by e-beam lithography ($W/L = 60 \mu\text{m} / 0.5 \mu\text{m} = 120$). (B) Thickness profile indicates a cross-section of a cyan-dashed line in A. (C) Transfer curve of pristine 2D PANI FET (without doping) as a function of gate voltage at $V_{DS} = 10 \text{ mV}$, measured under vacuum (5×10^{-6} torr). (D) Schematic diagram of the doping set-up for 2D PANI. (E) Conductivity changes as a function of gate voltage after doping with HCl gas. The solid black line represents the electrical property of the pristine 2D PANI (undoped). The doping temperature increased from 20 to 160 °C with a step of 20 °C. (F) An average conductivity (10 FET devices) changes as a function of the doping temperature.

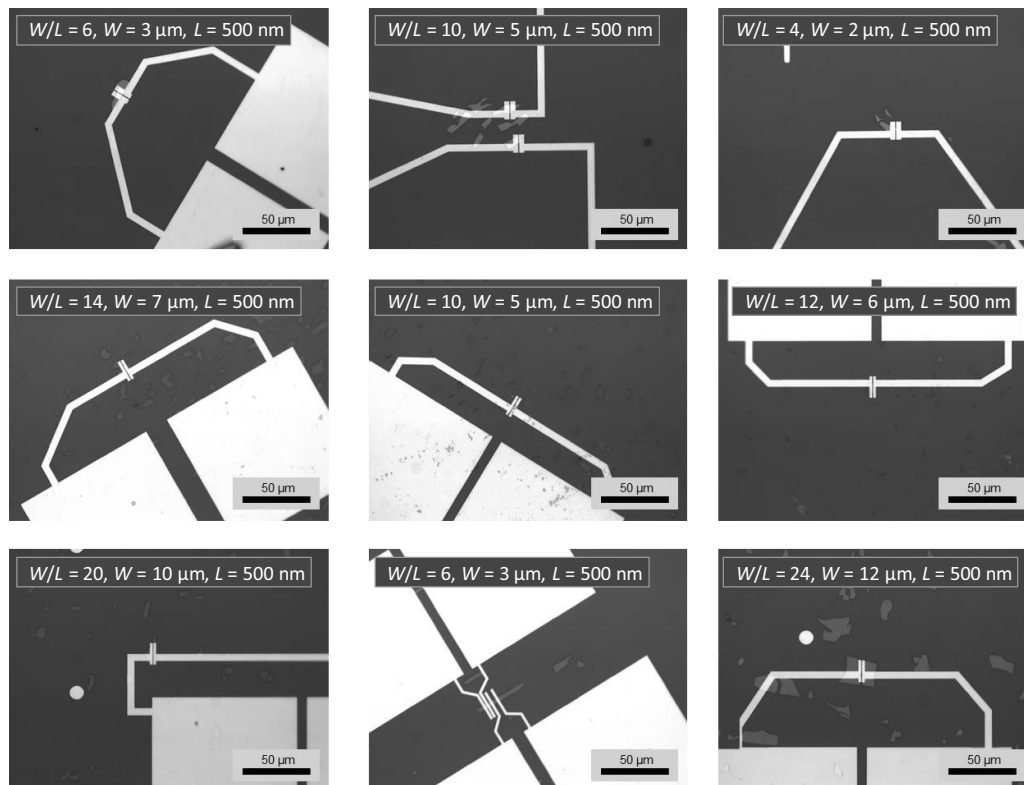


Figure 8.18. Optical microscope images of FET devices with channel length of 500 nm. Source and drain electrodes were defined by e-beam lithography.

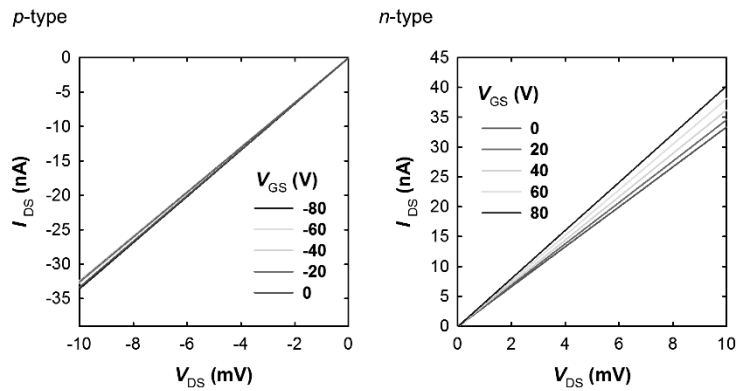


Figure 8.19. Output curves of 2D PANI FET measured under a pressure of 5×10^{-5} torr.

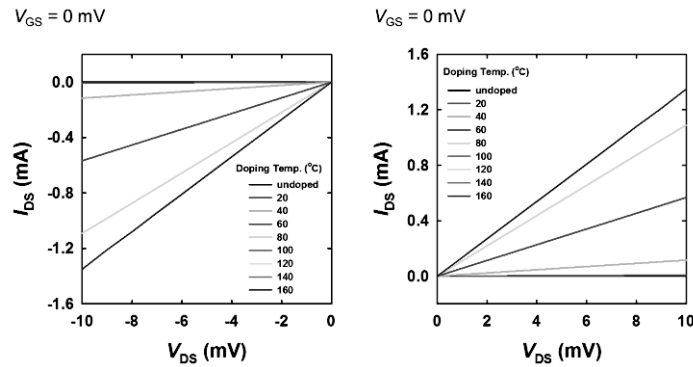


Figure 8.20. Current-voltage curves of 2D PANI measured under a pressure of 5×10^{-5} torr with increasing the doping temperature.

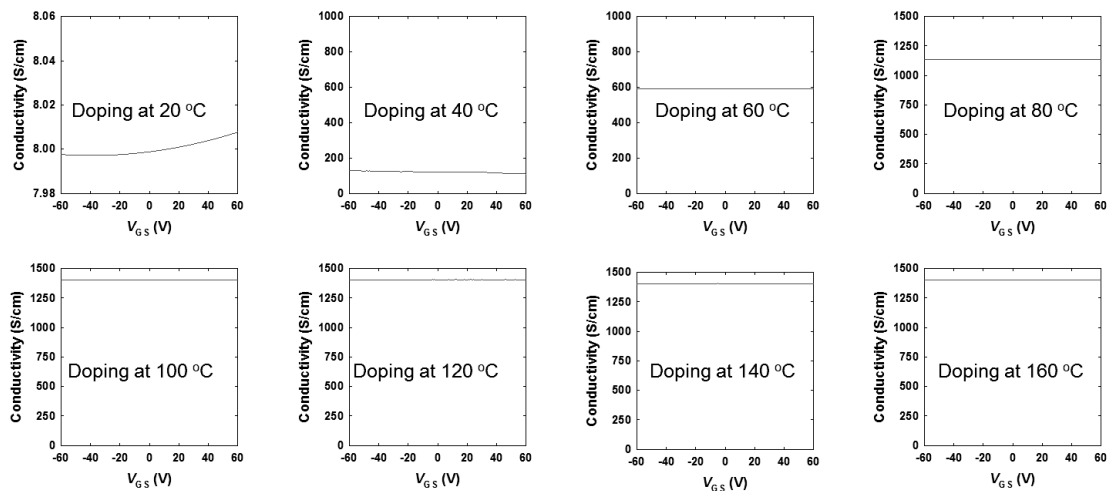


Figure 8.21. Transfer curves of 2D PANI as a function of doping temperature. Doping temperature was changed from 20 to 160 °C with a step of 20 °C.

Table 8.1. Elemental composition of the 2D PANI framework from different characterization techniques

Technique	C	H	N	O	Total
Theoretical (wt.%)	61.54	2.58	35.88	0	100
EA (wt.%)^a	59.74	1.92	26.16	11.31	99.13
SEM EDS (wt.%)	60.38	NA ^b	34.71 ^c	4.91 ^d	100

^a Elemental analysis (EA) is most reliable element counts for bulk sample. The more oxygen content could be detected because of the adsorbed moisture and oxygen. As the starting material is pure single crystal, so only possibility for oxygen content is adsorbed moisture and oxygen on the hygroscopic 2D PANI framework.

^b NA = Not available.

^{c,d} The increased nitrogen content and decreased oxygen content in EDS is due to removal of adsorbed moisture and oxygen under high vacuum condition in SEM.

Table 8.2. Atomistic coordinates for the refined unit cell parameters with AB stacking for the 2D PANI via Pawley refinement (space groups Triclinic P1, a=b=4.78 Å, c=6.81 Å, $\alpha=\beta=90^\circ$, $\gamma=120^\circ$)

Atom	x/a	y/b	z/c
C1	0.32726537	0.16363269	0
C2	0.16363269	0.32726537	0
C3	0.83636731	0.16363269	0
C4	0.16363269	0.83636731	0
C5	0.83636731	0.67273463	0
C6	0.67273463	0.83636731	0
C7	0.32726537	0.16363269	0.5
C8	0.16363269	0.32726537	0.5
C9	0.66666667	0.33333333	0.5
C10	0.33333333	0.66666667	0.5
C11	0.83636731	0.67273463	0.5
C12	0.67273463	0.83636731	0.5
N1	0.66666667	0.33333333	0
N2	0.33333333	0.66666667	0
N3	0.83636731	0.16363269	0.5
N4	0.16363269	0.83636731	0.5

Table 8.3. The comparison of conductivity of various materials, including metals, carbon-based materials, organic linear PANI and 2D PANI

Materials	Conductivity^a (S/cm)
Carbon (graphene)	1.00×10^6
Silver	6.30×10^5
Copper	5.96×10^5
Gold	4.10×10^5
Aluminum	3.50×10^5
Calcium	2.98×10^5
Tungsten	1.79×10^5
Zinc	1.69×10^5
PEDOT:PSS (solution-sheared, post-processed with organic solvent) ^{S(2)}	4.6×10^3
Carbon (graphite, basal plane)	3.00×10^3
2D PANI (HCl doped, this work)	1.41×10^3
PANI (HCl, self-stabilized dispersion polymerization) ^{S(3)}	1.3×10^3
PANI (ice template, HCl doped) ^{S(4)}	35
PEDOT:PSS	10
Carbon (graphite, ⊥basal plane)	3
2D PANI (undoped, this work)	0.72
PANI (doped by HBr)	4.60×10^{-7}
D.I water	5.50×10^{-8}
PANI (undoped)	6.28×10^{-11}

^a The conductivity table was cited from a website;

https://en.wikipedia.org/wiki/Electrical_resistivity_and_conductivity

Chapter 9. Summary and Perspectives

Demands for high performance of electronic devices and novel functionalities on the device such as flexibility, stretchability, light-weight, sensing of chemicals and integration of light detection and light emission are gradually elevated. The investigation of integration of light detecting and chemical sensing abilities in electronic human skin is a significant research that could promote the development of smart wearable electronic devices. In order to investigate the wearable electronic devices, novel electronic materials that are flexible and light-weight should be investigated as well as the mechanism behind the functionalities to be enhanced and fully exploit. An eventual goal of organic electronics is to fabricate large-area electronic devices and circuits on flexible and stretchable substrates. To achieve this target, high performance organic electronic materials and two-dimensional nanomaterials including graphene and transition metal dichalcogenide are worth to be studied and the combinatory investigations rising from the issues when those two materials put together in the electronic devices should be studied.

In this thesis, I have reported the studies on functional electronic devices for example, phototransistor, high performance field effect transistors based on graphene and organic dopants and graphene-like 2D nanomaterials. I have strived to give perceptions or practical research results for the development of soft nanoelectronic devices to widen possibilities for their practical use.

In Chapter 1, a brief introduction of the interface between 2D nanomaterials and organic electronic materials has been discussed. The methodologies of the synthesis for graphene and 2D nanomaterials in a large area was discussed as well as the electronic properties. Then, doping process and mechanism with respect to energy level were addressed. Among various doping technique, surface transfer doping has been used to dope 2D nanomaterials and organic semiconductors at the near-surface regime for nondestructive effects. In addition, organic field-effect transistors and organic phototransistors were introduced as representative applications utilizing 2D nanomaterials and organic electronic materials.

In Chapter 2, I have demonstrated monolayer graphene-based FET-type photodetectors with an ultrahigh responsivity of $\sim 1 \times 10^5 \text{ AW}^{-1}$ and a photoconductive gain of $\sim 3 \times 10^6$ at milliwatt optical intensities. Graphene-based photodetectors were functionalized using a 4-nm-thick photoactive ruthenium complex, which resulted in the generation of electron-hole pairs with long lifetime. The approach does not destroy the favorable electrical and optical properties of monolayer graphene, i.e., both the electron and hole mobilities further increased by functionalization with the photoactive compound, while maintaining the high optical transparency of monolayer graphene. Under illumination, the graphene-ruthenium complex hybrid phototransistors exhibited substantially enhanced electron current owing to the pronounced *n*-type doping effect engendered by electron transfer via MLCT from the ruthenium complex to graphene. The developed methodology opens a viable way for enhancing the photoresponsivity of graphene-based FET-type photodetectors.

In Chapter 3, a Ru-complex **1**-modified BPE-PTCDI phototransistor was fabricated by simple drop-casting of the transition metal complex. The resultant phototransistor exhibited a high photoresponsivity of ca. 3725 and 7230 AW^{-1} under an incident light intensity of $1.5 \mu\text{Wcm}^{-2}$ at $V_{\text{GS}} = 10$ and 80 V, respectively. Under illumination, the electrons were populated to the MLCT excited state from the ground state of Ru-complex **1** and were continually injected into the channel of the *n*-type BPE-PTCDI, which made the phototransistor highly photoresponsive. The EQE values of the Ru-complex **1**-modified BPE-PTCDI device were ca. 50000- and 3500-times higher than those of pristine BPE-PTCDI at $V_{\text{GS}} = 20$ and 80 V, respectively. This behavior stemmed from the long lifetime of electron-hole pairs ($\text{Ru}^{3+} - \text{e}^-$). The phototransistor had a high detectivity of 1.9×10^{13} Jones. Furthermore, functionalization of Ru-complex **1** on the BPE-PTCDI phototransistor array is feasible for the fabrication of large-area (10×10 phototransistor components), transparent optoelectronic devices with high flexibility and twistability.

In Chapter 4, I have fabricated ambipolar OFET arrays with well-balanced hole and electron mobilities via conventional photolithography using a chemically robust organic semiconductor **PTDPPSe-SiC4** and graphene electrodes. To the best of my knowledge, this is the first demonstration of fabrication of ambipolar OFET arrays with graphene electrodes using conventional photolithography to pattern a solution-processable organic semiconductor in a BGBC configuration on a flexible substrate. Owing to the high insolubility of **PTDPPSe-SiC4**, the organic semiconductor could be directly patterned by conventional photolithography. Graphene electrode devices showed higher carrier mobilities for both p-channel ($1.43 \text{ cm}^2 \text{ V}^{-1} \text{ s}^{-1}$) and n-channel operations ($0.37 \text{ cm}^2 \text{ V}^{-1} \text{ s}^{-1}$), compared to p-channel ($0.54 \text{ cm}^2 \text{ V}^{-1} \text{ s}^{-1}$) and n-channel mobilities ($0.009 \text{ cm}^2 \text{ V}^{-1} \text{ s}^{-1}$) of Cr/Au based devices on OTS-treated $\text{SiO}_2/\text{n}^+\text{Si}$ wafer. Because of the lower energetic barriers and favorable intermolecular interactions between graphene and **PTDPPSe-SiC4**, the contact resistance of the graphene device was much lower than that of the Cr/Au device. The **PTDPPSe-SiC4** OFETs operated normally after soaking in various solvents, and proved the chemical robustness of **PTDPPSe-SiC4**. As a further application, **PTDPPSe-SiC4** OFETs were used as a sensor platform for detecting acetone vapors.

In Chapter 5, a solution-processable organic *n*-type dopant was synthesized via a simple chemical reaction using PyB as an organic cation dye and NaBH_4 as a reducing agent. The synthesized organic cationic dye, rPyB, was applied to graphene FETs and OFETs with the N2200 polymeric *n*-type semiconductor. The rPyB dopant is highly effective to graphene due to the infinite conjugated system. Raman spectroscopy, KPFM and UPS confirmed that surface transfer rPyB doping on graphene and N2200 could be used to tune the WF of graphene and the charge transport of N2200 in the transistors. The electron mobility of graphene FETs with 4 times coating of rPyB were maintained up to 97.8 % for 90 days, resulting rPyB are highly stable. Finally, 16×16 graphene FET array was rPyB-doped using PDMS stamp. By touch the center of the PDMS stamp with a fingertip, only center area of 16×16 graphene FET array was selectively rPyB-doped.

In Chapter 6, In conclusion, I have studied the organic – inorganic interface between organic rPyB molecular dye with monolayer molybdenum diselenide. I have analyzed the photobehavior of doped monolayer TMDC by incorporating into phototransistor. The rPyB doped MoSe₂ phototransistor showed enormous enhancement compared to undoped MoSe₂ due to trion formation in doped system, coupled with the conformity of the dopant to MoSe₂ surface which facilitate smoother electron transfer across the interface.

In Chapter 7, a simple, but efficient and reliable, nitrogen-doping method *via* the reaction between the most commonly studied GO and primary amine containing molecules in a solution phase has been developed. This newly-developed doping method offers a powerful means to produce high-quality nitrogen-doped graphene nanoplatelets with the neutral point (Dirac point) located at around -16 V. Furthermore, the graphene nanoplatelets have a high hole and electron mobilities as high as 11.5 and 12.4 cm²V⁻¹s⁻¹, respectively, in the short channel length (500 nm). The process developed in this study provides a simple solution method for large-scale production of high-quality nitrogen-doped graphene nanoplatelets for n-type FETs.

In Chapter 8, a new synthetic protocol for 2D PANI, which can be produced by ‘direct’ pyrolysis of organic HAB single crystals has been demonstrated. The 2D PANI has empirical formula of C₃N (three *sp*² C atoms sharing a tertiary N) at basal area. The atomic-level true 2D PANI structure was first realized, as confirmed by STM imaging. While DFT calculation suggested that 2D PANI had scant density of state at Fermi level as a metallic conductor, STS revealed intrinsic electronic nature of 2D PANI with a HOMO-LUMO gap of 2.7 eV. Upon doping with gaseous HCl at an elevated temperature (~160 °C), the 2D PANI flakes exhibited electrical conductivity of 1.41 × 10³ S/cm which was two orders of magnitude higher than the best value of the doped linear PANI analogues reported to date. The structure of 2D PANI is quite striking, because it contains uniformly distributed nitrogen atoms for multifunctionality.

Soft nanoelectronics is a rising research area with great potential in the electronics sciences. 2D nanomaterials, organic semiconductors and carbon-based electronic materials are promising building blocks and key materials. Examples of tailored organic electronic materials for the enhancement of photoresponsivity or charge carrier mobility are addressed in this thesis. As with many other areas of scientific attempt, continuous investigation will require the integration of multiple disciplines, including chemistry, electrical engineering, optics and material science.

Acknowledgments

I am honored to receive my doctorate at Ulsan National Institute of Science and Technology (UNIST). I could not do all of these research results with my strength and knowledge alone. Because many people helped me, I could do it all the way of the doctoral course to the end without worrying about my degree. First of all, I am very grateful to Professor Joon Hak Oh, my supervisor. He gave me a lot of guidance during my graduate course with his lavish support and teaching. In addition, he gave me insightful answers on my research results and research process, and the direction of research on how these studies are meaningful for our research society. I would also like to thank Professor Jong-Beom Baek. He gave me a chance to do good research and I learned a lot about carbon materials through many collaboration with him. I would also like to thank Professor Byeong-Su Kim, my co-advisor. In addition, I would like to thank the rest of my thesis committee: Prof. Hyunhyub Ko, Prof. Sang Kyu Kwak for their encouragement and good advices.

During my Ph.D. course, if I did my research alone, it would remain impossible and I would have missed a tenth of what I have done so far. My driving force to study so far has been the encouragement of members of the Soft Nanomaterials and Devices Lab (SNDL) that helped me continue my research. We are from different backgrounds, but we have come together to become an expert in what we do. The past days of experimenting, laughing, and contemplating together to solve a problem for that goal pass like a panorama in my head. I particularly would like to thank Moonjeong Jang, my labmate. We have been working in the lab for the last 5 years and We have been able to solve difficulties with the encouragement together. I also like to thank my teammates Cheol Hee Park and Yong Hee Kim. When I had a lot of work to do, they helped me next to me, and they did things better than I did what I could not do alone.

During the last five years of graduate studies, I have published 11 SCI-grade scientific journals, including five journals as first author. I have published journals including *J. Am. Chem. Soc.*, *Angew. Chem. Int. Ed.*, *Nature Commun.*, *Adv. Funct. Mater.*, *Proc. Natl. Acad. Sci. USA* and *Adv. Mater.* to such a great journal publisher with the help of Professor Oh Joon Hak's guidance, help from co-worker and lab members. I could broaden my knowledge and gain my scientific knowledge through various national and international conferences. In addition, with the help of many people, I have been selected as the beneficiary of Global Ph.D. Fellowship of the National Research Foundation and can conduct research without financial difficulty during the degree course.

Finally, during my lifetime, I express my gratitude and love to God and my family, who have given me eternal love, support, and faith. My parents who always pray for me, Dong Un Lee, Young Sook Ju, and my sister, Joo Ri Lee, my sister, and Joo Sun Lee, thank you and love you. I realize that my doctoral degree has been fulfilled by their pray. Under God's plan, I want to move into another society. I will be a person who will be helpful to society without forgetting the valuable experience of my graduate school days.

감사의 글

지난 5년간의 대학원 생활을 생각하고 또한 이렇게 박사학위를 취득하게 되어 이 감사의 글을 쓰는 시점에서 감회가 새롭습니다. 처음 2012년에 대학원 과정을 시작할 때 끝나지 않을 것 같던 생활이 그리고 과연 내가 박사학위를 받을 수 있을까 라는 생각, 그 분야에서 내가 전문가가 될 수 있을까 라는 생각이 많이 들었습니다. 하지만 많은 분들의 도움으로 제가 이렇게 박사 학위를 받을 수 있게 된 것 같습니다.

먼저 저의 지도 교수님이신 오준학 교수님께 진심으로 감사를 표합니다. 처음에 2010년 UNIST 하계 연구장학생을 시작으로 당시 오준학 교수님과의 인연을 시작으로 UNIST에 2012년에 입학하기 까지 2010년 동계, 2011년 하계 동계 연구장학생을 매번 참가하면서 학부 시절 방학 때 마다 연구실 생활을 하였습니다. 처음에는 교수님께서 교수 임용되시고 연구실을 구축하는 초기 시절이어서 실험 할 수 장비가 없어 다른 연구실과 공동으로 실험을 진행하였는데, 어느덧 연구실에 장비가 많이 들어서고 또 그로부터 연구 결과 나오니 지금 와서 생각해 보면 이 모든 것이 감사합니다. 지금 이 글을 쓰는 시점에서 교수님을 안 지 횡수로 7년이란 시간이 지나왔고 7년동안 교수님께 연구를 배울수 있었던 것은 저에게 큰 축복이었습니다. 저에게 훌륭한 연구자가 되어라고 때로는 다정하게 때로는 엄하게 가르쳐 주셨지만, 그 속에 저에게 잘되라는 의미가 있었음을 다시 한번 깨닫게 됩니다. 모든 물심양면에 감사드리며 앞으로 모든 하는 일에 교수님의 가르침을 본받아 더욱 성장하여 훌륭한 연구자가 되도록 노력하겠습니다.

저의 공동 지도 교수님이신 김병수 교수님에게도 깊은 감사의 말씀 올립니다. 학위 과정에 많은 도움과 지도를 주시고 또한 학위 논문의 심사 위원이 되셔서 저에게 용기와 격려 주신 부분에 대해 정말 감사의 말씀 올립니다. 그리고 저에게 많은 공동 연구 기회를 주시고 저에게 좋은 연구 성과를 낼수 있게 가르침을 주신 백종범 교수님께 감사의 말씀 올립니다. 저의 전공이 탄소나노소재인데, 교수님과의 공동 연구가 없었더라면 저의 연구 지식과 배경이 정말 많이 한정되어 있었을 것입니다. 박사학위심사위원으로 함께 해주신 고현협 교수님, 광상규 교수님에게도 정말 감사의 말씀을 드립니다. 교수님께서 조언과 격려가 없었더라면 저의 연구 방향이 과연 올바른 방향으로 나아가고 있는지 돌아 볼 수 없었을 것입니다. 그리고 저와 같이 공동 연구를 진행한 Javed Mahmood 박사에게도 정말 감사의 마음을 표합니다.

저의 SNLD 입학동기인 문정이에게도 감사의 말을 전하고 싶습니다. 서로 다른 연구 주제로 연구를 진행 했지만, 각자의 자리에서 최선을 다하면 때로는 서로 돕고 연구에 대한 고충을 함께 이야기 나누었던 시간이 저에게 정말 큰 힘이 되었습니다.

그리고 우리 SNLD 멤버들. 저희 연구실의 초대 방장이면 우리 연구실의 기반을 다져 놓은 아름이. 긍정적인 힘과 웃음이 많은 호정이. 연구실의 군기 반장이며 나와 동갑내기 친구 지형이. 연구실의 만능 해결사 무열이, 개그 센스 넘치며 교수님께서 유일하게 재밌는 친구라고 칭찬 받은 윤호. 조용하면서도 아이디어 넘치며 저와 같이 실험을 진행 하면서 여러모로 많이 도와준 부사수 철희. 이제 연구실의 방장이 되어 바쁘겠지만, 자기 맡은 일에 최선을 다하는 해랑이. 조용하지만 믿음이 가는 인호. 연구실 만형이시며 남이 하지 않은 일에 과감하게 연구 잘하시는 오영 형님. 올해 같이 졸업을 하게 되며 예의 바른 착한 효은이. 항상 웃으며 나와 같이 MoSe₂ 연구를 진행한 mosquito, Hanum. 합성

연구와 배드민턴에 있어 정말 전문가이신 Xiabo 박사. 항상 웃으며 같은 학부 같은 군부대 출신인 열정적인 저의 또 다른 부사수 용희, 일을 너무 열심히 해 가끔씩 찢는 것을 잊고 출근하는 흥기, 예의 바르며 연구실의 로맨티가이인 상진이. 자기가 진짜 좋아하고 재미있을 연구를 찾고자 노력하는 종현이. 축구도 잘하고 연구도 열심히 하는 재환이. 그리고 이제는 졸업하고 사회에 나간 이전 SNDL 멤버들. 자연, 동영, Xien 교수님, 은엽, 유진이, 다정이. 모든 멤버들에게 감사의 마음을 표합니다.

그리고 제가 대학원 생활에 잘 적응하게 기도해 주신 정상균 목사님께 정말 감사의 말씀을 올립니다. 주일에 교회에서 만나보면 잘하고 있느냐는 그 한마디가 마음이 저의 마음에 깊은 감동을 주며 연구를 더욱 열심히 해야겠다는 마음을 주셨습니다. 그리고 성실순복음 교회 청년회 회원들. 성실순복음 교회 집사님, 권사님들께 감사의 마음을 표합니다. ‘연구는 체력이다’ 라는 말로 저를 극한으로 몰고가 저의 체력을 항상 시켜주신 이동후 아저씨, 수영과 스쿼시로 지칠 줄 모르는 체력을 함께 키울 수 있어 정말 감사드립니다. 항상 온화한 마음으로 교회 다니겠다 하지만 항상 나중에 다닌다는 저의 정신적 지주 되신 recovery 회수 형님, 그리고 저의 UNIST 동기 친구들 소현, 현지, 일영 모두 기억에 남고 감사드립니다. UNIST 에서 성경 공부를 인도하시며 함께 신앙을 공유해주시고 이제는 선교사님이 되신 정선희 선교사님 (교수님), 조형준 교수님, 학교 다니면서 그 분의 믿음을 같이 나눌 수 있었던 시간들은 결코 잊지 않을 것입니다. 그리고 POSTECH 에서 저의 옆에서 많은 조언과 기쁨, 신앙을 본받게 해준 현정이에게도 정말 감사의 마음을 표합니다. 포항중앙교회에서 만나게된 강지찬 목사님, 민영이, 윤정이, 시영이, 은정이, 혜연 누나, 린 누나, 세현이, 소리, 태식이, 명호, 은열이, 황태섭 집사님, 상욱형님, 재필 형님 모두 감사드립니다.

그리고 정말 사랑하는 우리 가족, 아버지, 어머니, 누나, 동생에게 정말 감사하다는 마음을 전하고 싶습니다. 저의 대학원 생활동안 다사다난한 일들이 집에 있었지만 서로가 기도와 사랑으로 잘 이겨내고 서로가 삶의 목적에 대해 명확히 나아가고 있음에 하나님께 너무 감사를 드립니다. 우리 모두가 영적으로 건강하고 하루 하루 살아가는 목적과 보람이 무엇인지를 정확히 알고 있으니, 저도 저의 자리에서 목적이 있는 삶을 살아가는 은광이가 되도록 하겠습니다. 마지막으로 이 모든 일에 저를 이끌어 주신 하나님께 모든 영광을 올립니다.

살아오면서 이렇게 내 인생의 목적이란 것을 생각해본 시간이 대학원 때이었음을 기억하게 됩니다. 어떻게 하면 내가 사회에 도움이 될 수 있는 사람인가를 고민하며 감사의 글을 마치겠습니다.

2017년 1월 11일

이 은 광

Curriculum Vitae

Eun Kwang Lee

Personal Details

Name Eun Kwang Lee
 Gender Male
 Date of Birth Feb. 09, 1987
 Nationality Republic of Korea
 Address School of Energy and Chemical Engineering, Ulsan National Institute of Science and Technology (UNIST), UNIST-gil 50, Ulsan 689-798, South Korea
 E-mail Address ekle@unist.ac.kr

Education

M.S. & Ph.D. Mar. 2012 – Feb. 2017
 Energy Engineering, School of Energy and Chemical Engineering, Ulsan National Institute of Science and Technology (UNIST)
 Research Advisor: Prof. Joon Hak Oh (POSTECH), Prof. Byeong-Su Kim (UNIST)
 Beneficiary of Global Ph.D. Fellowship (National Research Foundation)
 B. S. Mar. 2005 – Feb. 2012
 Chemical Engineering, Pusan National University
 (Military service, Apr. 2006 – Jun. 2008)

Publication

1. E. K. Lee,[†] C. H. Park,[†] J. Lee, H. R. Lee, C. Yang,* J. H. Oh,* "Chemically Robust Ambipolar Organic Transistor Array Directly Patterned by Photolithography". *Adv. Mater., in press* (2017). [[†]Contributed equally]
2. J. Mahmood,[†] E. K. Lee,[†] M. Jung, D. Shin, H. J. Choi, J. M. Seo, S. M. Jung, D. Kim, F. Li, M. S. Lah, N. Park,* H. J. Shin,* J. H. Oh,* J. B. Baek,* "Two-dimensional polyaniline (C3N) from carbonized organic single crystals in solid state". *Proc. Natl. Acad. Sci. U. S. A.* **113**, 7414-7419 (2016). [[†]Contributed equally]
3. X. Liu,[†] E. K. Lee,[†] D. Y. Kim, H. Yu, J. H. Oh,* "Flexible Organic Phototransistor Array with Enhanced Responsivity via Metal-Ligand Charge Transfer". *ACS Appl. Mater. Interfaces* **8**, 7291-7299 (2016). [[†]Contributed equally]
4. M. Y. Lee, J. Hong, E. K. Lee, H. Yu, H. Kim, J. U. Lee, W. Lee, J. H. Oh,* "Highly Flexible Organic Nanofiber Phototransistors Fabricated on a Textile Composite for Wearable Photosensors". *Adv. Funct. Mater.* **26**, 1445-1453 (2016).

5. X. Shang, H. Yu, W. Choi, E. K. Lee, J. H. Oh,* "Effects of microwave-assisted annealing on the morphology and electrical performance of semiconducting polymer thin films". *Org. Electron.* **30**, 207-212 (2016).
6. J. Park, H. Song, E. K. Lee, J. H. Oh, K. Yong,* "ZnO nanowire based photoelectrical resistive switches for flexible memory". *J. Electrochem. Soc.* **162**, H713-H718 (2015).
7. J. Mahmood, E. K. Lee, M. Jung, D. Shin, I. Y. Jeon, S. M. Jung, H. J. Choi, J. M. Seo, S. Y. Bae, S. D. Sohn, N. Park, J. H. Oh,* H. J. Shin,* J. B. Baek,* "Nitrogenated holey two-dimensional structures". *Nat. Commun.* **6**, 6486 (2015).
8. X. Liu,[†] E. K. Lee,[†] J. H. Oh,* "Graphene-ruthenium complex hybrid photodetectors with ultrahigh photoresponsivity". *Small* **10**, 3700-3706 (2014). [[†]Contributed equally]
9. S. M. Jung, E. K. Lee, M. Choi, D. Shin, I. Y. Jeon, J. M. Seo, H. Y. Jeong, N. Park, J. H. Oh, J. B. Baek,* "Direct solvothermal synthesis of B/N-doped graphene". *Angew. Chem., Int. Ed.* **53**, 2398-2401 (2014).
10. J. H. Oh,* A.-R. Han, H. Yu, E. K. Lee, M. J. Jang, "Tuning Polarity and Improving Charge Transport in Organic Semiconductors", *Proceedings of SPIE 2013*, **8331**, 883112 (2013).
11. D. W. Chang,[†] E. K. Lee,[†] E. Y. Park, H. Yu, H. J. Choi, I. Y. Jeon, G. J. Sohn, D. Shin, N. Park, J. H. Oh,* L. Dai,* J. B. Baek,* "Nitrogen-doped graphene nanoplatelets from simple solution edge-functionalization for n-type field-effect transistors". *J. Am. Chem. Soc.* **135**, 8981-8988 (2013). [[†]Contributed equally]

Patents

1. J. H. Oh, E. K. Lee, X. Liu, "금속 착화합물 및 이를 포함하는 그래핀-금속 착화합물 복합체 (Metallic Complex and Graphene-Metallic Complex Hybrid Including The Same)"
KR 10-1656878 (09-06-2016)

Presentation (International)

1. E. K. Lee, H. Abdullah, J. H. Oh, "Highly Enhanced Optoelectronic Properties in MoSe₂ with Reduced Organic Dye Molecular N-Dopant", IUPAC-PSK40, Jeju, Korea, Oct. 04-07, **2016**
2. E. K. Lee, C. H. Park, Y. Kim, J. H. Oh, "Transparent and Low Work Function Electrodes with Stretchable Graphene and Metal Grid", IUPAC-PSK40, Jeju, Korea, Oct. 04-07, **2016**.
3. E. K. Lee, X. Liu, D. Y. Kim, C. H. Park, J. H. Oh, "Carbon-Based Hybrid Flexible Photodetector Array Functionalized with a Ruthenium Complex", Materials Research Society (MRS) Fall Meeting, Boston, MA, USA, Nov. 29-Dec. 4, **2015**.
4. E. K. Lee, X. Liu, D. Y. Kim, C. H. Park, J. H. Oh, "Carbon-Based Hybrid Photodetectors Functionalized with a Ruthenium Complex", IUPAC-2015, Busan, Korea, Aug. 9-14, **2015**.

5. E. K. Lee, X. Liu, D. Y. Kim, C. H. Park, J. H. Oh, “Carbon-based hybrid photodetectors functionalized with a ruthenium complex”, 31st International Conference of the POLYMER PROCESSING SOCIETY, Jeju Island, Korea, Jun. 7-11, **2015**.
6. E. K. Lee, C. H. Park, J. H. Oh, “Effects of Molecular Dual Doping and Doping Location in Graphene Field Effect Transistors”, Materials Research Society (MRS) Fall Meeting, Boston, MA, USA, Dec. 01-06, **2013**. [RR15.107]

Presentation (Domestic)

1. E. K. Lee, X. Liu, D. Y. Kim, C. H. Park, J. H. Oh, “Flexible Hybrid Photodetectors Based on the Graphene and Organic Semiconductor Functionalized with a Ru-complex”, The Korean Institute of Chemical Engineers Fall Meeting, Goyang, Korea, Oct. 21-23, 2015.
2. E. K. Lee, X. Liu, D. Y. Kim, J. H. Oh, “Hybrid photodetectors geared with a photoactive ruthenium complex”, The Korean Society of Industrial and Engineering Chemistry Spring Meeting, Busan, Korea, Apr. 30-May. 1, 2015.
3. E. K. Lee, E. Y. Park, C. H. Park, O. Y. Kwon, J. H. Oh, “Effects of Doping Location in Graphene Field-Effect Transistors”, The Korean Society of Industrial and Engineering Chemistry Spring Meeting, Busan, Korea, Apr. 30-May. 1, 2015.
4. E. K. Lee, X. Liu, H. Abdullah, J. H. Oh, “Graphene-Ru complex photodetectors with ultrahigh photoresponsivity”, The Korean Society of Industrial and Engineering Chemistry Spring Meeting, Busan, Korea, Apr. 30-May. 1, 2015.
5. E. K. Lee, X. Liu, J. H. Oh, “Graphene-ruthenium complex hybrid photodetectors with ultrahigh photoresponsivity”, The Polymer Society of Korea Spring Meeting, Daejeon, Korea, Apr. 09-11, 2014.
6. E. K. Lee, C. H. Park, J. H. Oh, “Bandgap Control of Bilayer Graphene Using Self-assembled Monolayer and Graphene Oxide”, The Polymer Society of Korea Fall Meeting, Changwon, Korea, Oct. 10-11, 2013.
7. E. K. Lee, E. Y. Park, C. H. Park, J. H. Oh, “Effects of Molecular Dual Doping and Doping Location in Graphene Field-Effect Transistors”, The Polymer Society of Korea Spring Meeting, Daejeon, Korea, Apr. 11-12, 2013.